



INTERIM REPORT

Model roundup and extension for the current- and wave-induced burial, re-exposure, mobilization and migration of UXO and DMM

SERDP Project MR21-1081

JANUARY 2024

Peter Menzel (lead PI)
Corvus Works UG

Daniel Klembt
Mirko Rummelhagen
Karsten Breddermann
Helen Morrison
Corvus Works UG

Richard Whitehouse
Sebastian Escobar
Michiel Knaapen
Nick Tavouktsoglou
Tommaso Attili
HR Wallingford

Version: 1.0

Date: 2/10/2024



Table of Contents

1	Abstract	17
2	Objective	17
3	Technical Approach	18
3.1	Area of Interest: Fort Pierce	18
3.2	Available Data on the AoI	20
3.2.1	Bathymetry.....	23
3.2.2	Geomorphology	24
3.2.3	Currents.....	25
3.2.4	Wave data	26
3.2.5	Sediment composition.....	28
3.3	Objects of Interest.....	30
3.4	Basics and Wave Models.....	31
3.5	Mobilization Model	37
3.6	Burial Models	40
3.6.1	DRAMBUIE 2.0	40
3.6.2	DRAMBUIE 3.0	44
3.7	Analyzing the existing models	56
3.8	Combination of the Mobilization and Burial Model	60
3.9	The Lattice Boltzmann Method (rejected).....	61
3.10	TELEMAC Simulations	62
3.10.1	TELEMAC 2D.....	62
3.10.2	TOMAWAC	62
3.10.3	GAIA	64
3.10.4	Model discretizations	66
3.10.5	Model Setup.....	66
3.10.6	Conclusion	68
3.11	Including migrating bedforms	69
3.12	Determining the coefficients	72
3.12.1	Wind tunnel experiments	72
3.12.2	Numerical Simulation using CFD.....	80
3.12.3	Drag crisis	82
3.12.4	Added mass.....	83
3.12.5	Boundary Element Method to quantify the Added mass coefficient.....	84
3.13	Software.....	85



3.13.1	Requirements	86
3.13.2	Analysis of the existing software	87
3.13.3	Development	88
3.13.4	Software-Architecture	88
3.13.5	Core-Plugin Scheme	92
3.13.6	Input Interfaces	94
3.13.7	Output Interface and SimOutput Class	98
3.13.8	Simulation Configuration	99
3.13.9	C++-style Interfaces	99
3.13.10	Templates	100
3.13.11	Multithreading	101
3.13.12	Bazel Build System	102
3.13.13	Continuous Integration	103
4	Results and Discussion	105
4.1	Combining the Burial and Mobilization models	106
4.2	Implementation of seabed morphology	107
4.3	Dimensionless coefficients	108
4.3.1	Drag and lift from the wind tunnel experiments	108
4.3.2	Drag and lift from CFD	110
4.3.3	Comparison of CFD and the wind tunnel experiments	113
4.3.4	Calculation of the polynomials for drag and lift	114
4.3.5	Added mass coefficient	117
4.3.6	Conclusion on drag and lift and added mass	118
4.3.7	Rolling resistance coefficient	120
4.4	TELEMAC Simulations	120
4.4.1	Currents	120
4.4.2	Waves	125
4.4.3	Sediments	127
4.4.4	Simulation of monthly metocean and morphodynamics conditions of 2016 129	
4.4.5	Conclusion	131
4.5	Examples of the model-classification	132
5	Conclusions to Date	133
6	Literature Cited	136
Appendix A.	The Lattice Boltzmann Method (rejected)	144





List of Tables

Tab. 1: Objects of Interest	30
Tab. 2: Equations of the linear wave theory.....	34
Tab. 3: Equations of Stokes' third-order wave theory.	35
Tab. 4: Scheme for the choice of the flow regime to compute the wall shear stress. ..	41
Tab. 5: Equations to predict the equilibrium burial depth (Friedrichs, et al., 2018). ...	44
Tab. 6: Sediment fractions.....	68
Tab. 7: Data of the models in the original and in the wind tunnel.	78
Tab. 8: Scaling of the velocity from original scale to wind tunnel scale.	79
Tab. 9: Procedure for measurement in the wind tunnel.....	80
Tab. 10: Boundary conditions of the numerical simulations.....	81
Tab. 11: Polynomials for the added mass coefficients.	118



List of Figures

Fig. 1: Location of the Offshore Obstacle Area at the Fort Pierce U.S. Naval Amphibious Training Base.....	18
Fig. 2: Example of a beach fortification in the Normandy.....	19
Fig. 3: The boundaries of the Fort Pierce AoI, alongside the locations of the relevant environmental data.....	21
Fig. 4: Indian River Lagoon System.....	22
Fig. 5: The inlets near the AoI: Sebastian (top); Fort Pierce (middle); and St Lucie (bottom).	23
Fig. 6: The processed bathymetry data in (2016 Lidar data) and around (1930 lead line data) the AoI.....	24
Fig. 7: The Florida current runs offshore of the area of interest.	25
Fig. 8: Monthly wave conditions off Fort Pierce, measured between 2006 and 2020. Top, significant wave height. Bottom, Peak wave period. The boxplots feature the monthly means (white dots), the first and the third quantiles of the available data (grey boxes). The violin plots feature the approximate - kernel density- distribution of the monthly measured data.	27
Fig. 9: The annual wave rose for Fort Pierce.	27
Fig. 10: Grain size at various sample locations (from the seafloor downwards), obtained from four different locations within the AoI (“Grab” and “PushCorer” sites in Fig. 3).	29
Fig. 11: Technical drawings of the OoI.....	31
Fig. 12: Characteristic quantities of a surface wave.....	32
Fig. 13: Orbits of waves in different water depths.	33
Fig. 14: Regions of validity of the different wave theories, modified according to (Habel, 2001), (CERC, 1984) and (Le Méhauté, 1976).	37
Fig. 15: Loads on a cylindrical object in a symmetrical scour trough due to waves....	37
Fig. 16: Downhill-slope force (a) and friction force (b).....	39
Fig. 17: Procedure to calculate the time series of scour burial depth of free settling objects.	48
Fig. 18: Example of the scour burial depth evolution for a current-only (top) and wave-current (bottom) flow using several time steps Δt	49
Fig. 19: Correlation analysis between all considered variables.	50
Fig. 20: GPR model performance.....	52
Fig. 21: MLPNN model performance	53
Fig. 22: Comparison of existing ANN model against existing empirical models for an increasing wave height and no current.	54
Fig. 23: Comparison of existing ANN model against existing empirical models for an increasing wave height and a 0.4 m/s current.....	55
Fig. 24: Comparison of existing ANN model against dataset reserved for validation. Effects of increasing wave height.....	55
Fig. 25: Comparison of existing ANN model against dataset reserved for validation. Effects of increasing wave height.....	56
Fig. 26: Process flow of the combined burial-mobilisation-simulation.	61
Fig. 27: Computed sediment settling velocity.....	65
Fig. 28: Model domain and bathymetry.	66



Fig. 29: Model layout. Boundary conditions were retrieved from global currents (HYCOM), wind, air pressure and waves (ERA5) models. These were imposed on the open boundaries (blue lines) of the TELEMAC-2D and TOMAWAC models, which modeled local conditions of the East Coast of Florida..... 67

Fig. 30: Model distribution of mean sediment particle size. 68

Fig. 30: Time scales of the simulation components. 69

Fig. 31: Coordinates and scales. 70

Fig. 32: NetCDF Data Format. 71

Fig. 33: Design of the Göttingen type wind-tunnel of MariKom..... 73

Fig. 34: Drawing of the arrangement of the end plate within the test section of the wind-tunnel. 74

Fig. 35: Vertical velocity profile in the wind-tunnel..... 74

Fig. 36: Direction of the calibration weights..... 75

Fig. 37: Relative uncertainty of the wind velocity $U^*(u)/u$ in the wind tunnel..... 77

Fig. 38: Technical drawing of the model of a 1000 lb GP bomb. 77

Fig. 39: Model of the 1000 lb GP Bomb on the measuring plate in the wind tunnel... 78

Fig. 40: Simulation Domain and Boundary Conditions. 81

Fig. 41: Mesh convergence for the 500 lb GP Bomb at a burial depth of $z_b/D = 0.3$ 82

Fig. 42: Drag coefficient of a Sphere for a smooth and a rough surface of the sphere..... 83

Fig. 43: Basic Software Architecture Overview..... 88

Fig. 44: UML Representation of main components of the Business Logic. 89

Fig. 45: GUI Example. 91

Fig. 46: GUI Layout. 91

Fig. 47: Example of a force comparison simulation displaying graphs in the GUI. 92

Fig. 48: Core-Plugin Scheme. 93

Fig. 49: Possible derived Inputs. 94

Fig. 50: UML Representation of the Object Data Interface. 95

Fig. 51: UML Representation of the Wave Data Interface. 96

Fig. 52: UML Representation of the Morphology Data Interface..... 96

Fig. 53: UML Representation of the Environment Data Interface..... 97

Fig. 54: UML Representation of the Object Library..... 97

Fig. 55: UML Representation of the MorphologyNCModel..... 98

Fig. 56: UML Representation of the Output Concept. 99

Fig. 57: Thread Pool Scheme. 101

Fig. 58: Jenkins CI Setup..... 104

Fig. 59: Preliminary mobilization return time analysis, showing the model can be applied in the AoI. 105

Fig. 60: Burial depth and point of mobilization for artificial, increasing wave action. 106

Fig. 61: Burial depth for artificial, increasing wave action and a change of the seabed level..... 107

Fig. 62: Measured drag coefficient of the 1000 lb GP Bomb. 109

Fig. 63: Measured drag coefficient of the 155 mm, HE 107..... 109



Fig. 64: Measured drag coefficient of the Tiny Tim Rocket..... 110

Fig. 65: Drag coefficient of the 1000 lb GP Bomb from CFD..... 110

Fig. 66: Drag coefficient of the 500 lb GP Bomb from CFD..... 111

Fig. 67: Drag coefficient of the 155 mm, HE 107 from CFD. 111

Fig. 68: Lift coefficient of the 1000 lb GP Bomb from CFD..... 112

Fig. 69: Lift coefficient of the 500 lb GP Bomb from CFD..... 112

Fig. 70: Lift coefficient of the 155 mm, HE 107 from CFD. 113

Fig. 71: Comparison of the results from CFD and the experiments for the 1000 lb
GP Bomb 113

Fig. 72: Polynomials for the drag coefficient from CFD of the 1000 lb GP Bomb. .. 114

Fig. 73: Classification of the functions into the coefficients a, b and c. 115

Fig. 74: Determined polynomial for the coefficient a at different burial depths..... 115

Fig. 75: Determined polynomial for the coefficient b at different burial depths. 115

Fig. 76: Determined polynomial for the coefficient c at different burial depths..... 116

Fig. 77: Mesh convergence for the 500 lb GP Bomb at a burial depth of $z_b/D=0.05$. 117

Fig. 78: Added mass coefficients. 118

Fig. 79: Lift and drag coefficient during a single wave cycle. 119

Fig. 80: Loads on an object during a single wave cycle..... 120

Fig. 81: Locations of measurement stations used in the tidal levels comparison..... 121

Fig. 82: Comparison of water levels predicted by the model and by the NOAA tidal
predictions at Cape Canaveral, Cocoa Beach and Patrick Airforce Base. 122

Fig. 83: Comparison of water levels predicted by the model and by the NOAA tidal
predictions at Canova, Sebastian Inlet and Vero Beach. 123

Fig. 84: Comparison of water levels predicted by the model and by the NOAA tidal
predictions at North Beach, Fort Pierce and Ankona. 124

Fig. 85: Comparison of water levels predicted by the model and by the NOAA tidal
predictions at Jensen Beach and Seminole Shores. 125

Fig. 86: Location of the Waverider buoy offshore of Fort Pierce. 126

Fig. 87: Comparison between measured and predicted significant wave height (top);
peak period (middle) and wave direction (bottom). 126

Fig. 88: Comparison between measured and predicted significant wave spectrum... 127

Fig. 89: Qualitative comparison of measured bed elevation changes(left) and
modelled bed evolution (right). The sources for the measurements data are:
(OCM-Partners, 2023b) and (OCM-Partners, 2023a). 128

Fig. 90: Quantitative comparison of longshore bed evolution from measurements
and model results. Top, bed evolution profile, the solid lines are the zonal
average and the shaded areas are the standard deviation. Bottom, local
coordinates and sample polygons used to calculate the zonal statistics. The
sources for the measurements data are: (OCM-Partners, 2023b) and (OCM-
Partners, 2023a). 129

Fig. 91: Modelled and measured wave conditions at the Fort Pierce station, Florida,
throughout 2016. Top: significant wave height. Middle: peak wave period.
Bottom: mean wave direction..... 130

Fig. 92: Monthly total bed evolution modelled for 2016. 131

Fig. 93: Model review classification table (v4) showing example of burial model. .. 132



Fig. 94: Model review classification table (v4) showing example of mobilization model. 133

Fig. 95: D2Q9 lattice with corresponding velocity vectors \mathbf{c}_i 144

Fig. 96: The resulting bathymetry in the extended AoI after post-processing the two lead line datasets from 1930 (H05027 and H05032) and transforming the UTM coordinates to a uniform x-y grid. 153

Fig. 97: Water level (m) at $t=2580$ s, obtained from the LABSWE test simulation using the extended AoI around Fort Pierce. The black contours visualize the bathymetry. 153

Fig. 98: Velocity vectors, scaled by a factor of 400, at $t=2580$ s, obtained from the LABSWE test simulation using the extended AoI around Fort Pierce. The underlying contour plot shows the bed elevation \mathbf{z}_e , (m) 154



Notation

Latin symbols

a	approximation of the wave amplitude	m
a_r	coefficient	[-]
a_{WT}	Ratio of the nozzle cross-section areas	[-]
A	wave amplitude	m
A_1, A_2	cross sections of the nozzle of the wind tunnel	m^2
A_e	empirically calculated value	[-]
A_{CS}	cross section	m^2
$A_{CS,obj}$	cross section of an UXO object	m^2
A_F	Area	m^2
A_1	coefficient for the drag	[-]
A_2	coefficient for the drag	[-]
B	empirically calculated value	[-]
c	celerity	m/s
c_a	added mass coefficient	[-]
c_l	added lift coefficient	[-]
c_d	drag coefficient	[-]
$\downarrow c_{d,mean}$	mean drag coefficient	[-]
$\downarrow c_{d,max}$	maximum drag coefficient	[-]
$\downarrow c_{dr}$	drag coefficient for current for rough turbulent flow	[-]
$\downarrow c_{ds}$	drag coefficient for current for smooth turbulent flow	[-]
c_r	rolling resistance coefficient	[-]
c_s	speed of sound	m/s
\vec{c}_i	normalized vectors of discretized lattice velocities	[-]
C	depth-averaged concentration	% vol
C_b	bed friction coefficient	[-]
C_i	scaling factor	[-]
C_z	Chezy constant	[-]
C_{zref}	near-bed concentration of sediment	% vol
d	grain size	m
d_e	depth	m
d_0	reference grain diameter	m
d_{50}	median grain diameter	m
D	diameter of cylinder	m
D_s	sediment deposition rate	
D_P	mean direction from which the energy is coming at peak wave period	[-]
D_{bathy}	bathymetry	m
D^*	dimensionless grain size	m
D_0	diffusion constant	[-]
E_{0i}	Partheniades constant parameter	
\vec{e}	unit vector	[-]
f_i	distribution function	[-]
f_w	wave friction factor	[-]
f_{wr}	wave friction factor for rough turbulent flow	[-]



f_{ws}	wave friction factor for smooth turbulent flow	[-]
F	force	N
F_b	hydrostatic buoyancy	N
F_g	weight force	N
F_l	hydrodynamic lift	N
F_r	rolling resistance	N
$F_{\alpha,slope}$	bed slope force	N
g	acceleration due to gravity	m/s^2
g_i	distribution functions of the LB/AD model	[-]
h	water depth	m
h_i	proportion of higher moments of the f_i (KBC model)	[-]
H_s	significant wave height	m
H_0	fixed reference level	m
k	wave number	$1/m$
k_i	kinetic part of the f_i (KBC model)	[-]
l_i	Side length of wind tunnel nozzle cross-section area	m
L	characteristic length	m
m	mass	kg
m_0	first moment of the sea state spectrum	m^2
n_b	Manning's coefficient	[-]
p	pressure	N/m^2
p_{baro}	Ambient barometric pressure difference	N/m^2
p_{diff}	Static pressure difference	N/m^2
P	fitting coefficient	[-]
q	number of discrete velocity vectors	[-]
q_0	maximum discharge	m^3/s
r	radius	m
$R_{specific}$	Specific gas constant	0.287 kJ/(kgK)
s	ratio of sediment density to water	[-]
s_i	shear stress component of the f_i (KBC model)	[-]
S	current scour depth	m
S_h	source or sink of fluid	m/s^2
S_x	source term	m/s^2
S_y	source term	m/s^2
SST	sea surface temperature	K
t	time	s
t_i	lattice specific constants	[-]
T	characteristic time-scale for scour or period of water wave	s
T_a	average wave period	s
T_p	peak wave period	s
T_w	period of water wave	s
u	velocity component	m/s
u_τ	shear velocity	m/s
\ddot{u}	acceleration of the water	m/s^2
U	characteristic velocity	m/s
U^*	uncertainty of a measured variable	[-]
U_0	incident velocity	m/s



\bar{U}	depth-averaged current velocity	m/s
U_m	maximum combined wave and current velocity	m/s
U_w	wave orbital velocity amplitude at seabed	m/s
v	velocity component	m/s
V	volume	m^3
w	velocity component	m/s
w_s	settling velocity	m/s
x	direction	[-]
\vec{x}	location vector $\vec{x} = (x, y, z)^T$	
y	direction	[-]
y^+	dimensionless wall distance	[-]
z	direction	[-]
z_b	burial depth	m
z_e	seafloor elevation	m
z_s	free surface elevation	m
z_{max}	maximum depth of scour pit	m
z_{ref}	position of the interface between bed load and suspended load	m
z_0	bed roughness length	m
z_∞	depth of scour pit after infinite time	m

Greek symbols

α	maximum slope	°
α_{obj}	orientation angle of the object's main axis to the wave direction	[-]
ε_s	turbulent diffusivity of the sediment	
γ	relaxation time (KBC model)	s
λ	wavelength	m
ν	kinematic viscosity	m^2/s
ν_t	Momentum diffusion coefficient	m^2/s
ϑ	Absolute temperature	K
ρ	density of the water	kg/m^3
ρ_a	density of the air	kg/m^3
ρ_p	particle density	kg/m^3
ρ_s	sediment density	kg/m^3
ζ	arbitrary quantity	[-]
τ	relaxation time	s
τ_b	bed shear stress	pa
τ_c	current-only bed shear-stress	pa
τ_{ci}	Critical bed shear stress for erosion parameters	pa
τ_m	mean bed shear-stress during a wave cycle, combined waves and currents	pa
τ_{mr}	mean bed shear-stress rough-turbulent flow	pa
τ_{ms}	mean bed shear-stress smooth-turbulent flow	pa
τ_{max}	max. bed shear-stress during a wave cycle, combined waves and currents	pa
τ_s	total bed shear stress	pa
τ_{rs}	root-mean-square bed shear-stress under combined waves and currents	pa
τ_w	amplitude of oscillatory bed-shear-stress, combined waves and currents	pa
φ	phase angle of the wave	[-]



φ_d	angle of deflection	[-]
φ_g	grain size, given in phi units	[-]
φ_{wc}	angle between wave and current direction	[-]
ζ	volume fraction	[-]
Φ	ratio of the wave speed to the lattice speed	[-]
ω	wave frequency	Hz
Ω	collision operator	[-]

Special indices

<i>obj</i>	Related to the object
<i>rot</i>	Related to the rotation
\perp	Perpendicular



Dimensionless numbers

Ur	Ursell number	$Ur = \left(\frac{H}{\lambda}\right) \left(\frac{\lambda}{h}\right)^3$
Re	Reynolds number	$Re = \frac{U \cdot L}{\nu}$
↳ Re_c	current Reynolds number	$Re_c = \frac{\bar{U} \cdot h}{\nu}$
↳ Re_w	wave Reynolds number	$Re_w = \frac{U_w^2 \cdot T_w}{2\pi \cdot \nu}$
Sh	Shields parameter	$Sh = \frac{\tau}{(\rho_S - \rho_F)gd_{50}}$
↳ Sh_{crit}	critical Shields parameter	$Sh_{crit} = \frac{0.3}{1 + 1.2d^*} + 0.055[1 - e^{-0.02d^*}]$
Sc	Schmidt number	$Sc = \frac{\nu}{D_o}$
Fr	Froude number	$Fr = \frac{u}{\sqrt{gh}}$
KC	Keulegan Carpenter number	$KC = \frac{U_w \cdot T_w}{D}$



List of abbreviations

ADCP	Acoustic Doppler Current Profiler
ANN	Artificial neural network
AoI	Area Of Interest
BEM	Boundary element method
BGK	Bathnagar–Gross–Krook
BM	Burial Model
CAD	Computer-Aided Design
CDIP	Coastal Data Information Program
CEHNC	U.S. Army Engineering and Support Center, Huntsville
CESAJ	U.S. Army Corps of Engineers, Jacksonville District
CZMIL	Coastal Zone Mapping and Imaging Lidar
DEM	Digital Elevation Model
DMM	Discarded Military Munitions
DRAMBUIE	Defense Research Agency Mine Burial Environment
FOV	Field Of View
GDAL	Geospatial Data Abstraction Library
GPR	Gaussian process regression
GRZ	Grain-Size Analysis
HyCOM	Hybrid Coordinate Ocean Model
JANET	Joint Army Navy Experimental and Testing Board
JONSWAP	Joint North Sea Wave Observation Project
KBC	Karlin Bösch Chikatamarla
LABSWE	Lattice Boltzmann Model for Shallow Water Equations
LB/AD	Lattice Boltzmann/Advection-Diffusion
LBM	Lattice Boltzmann Method
MEC	Munitions and Explosives of Concern
MLPNN	multi-layer perceptron neural network
MLW	Mean Low Water
MM	Mobilization Model
MVC	Model-View-Controller design pattern for software architecture
NATB	Naval Amphibious Training Base
NCEI	National Centers for Environmental Information
NDBC	National Data Buoy Center
netCDF	Network Common Data Form
NOAA	National Oceanic and Atmospheric Administration
NWPS	Nearshore Wave Prediction System
OoI	Objects Of Interest
PPDFs	Particle Probability Distribution Functions
SERDP	Strategic Environmental Research and Development Program
USACE NCMP	U.S. Army Corps of Engineers National Coastal Mapping Program
UTM	Universal Transverse Mercator
UXO	Unexploded Ordnance Devices



Acknowledgements

This research was supported wholly (or in part) by the U.S. Department of Defense, through the Strategic Environmental Research and Development Program (SERDP). The authors would like to thank Sarah Barlow for her great support, the Munitions Response Program Manager David Bradley as well as the technical advisors to the Munitions Response Program. A special thanks go to Kelly Enriquez, Wendell Hardwick, Michael Richardson, Andrew Schwartz (alphabetical order) for their very productive support. We would like to thank the scientific community within the SERDP Munitions Response Program for their critical questions, their support and the very beneficial discussions. Last but not least, we would like to thank the administration teams at DOD and SERDP, HR Wallingford and Corvus Works.



1 Abstract

This Interim Report describes the outcomes from the research performed within the period from 05/01/2021 to 01/31/2023, i.e. year 1 and year 2 of the SERDP Project MR21-1081. During this time, the administrative and organizational structure of the project was set up. The Area of Interest (AoI) as well as the Objects of Interest (OoI) were defined and characterized. The environmental and technical information were collected, imported and analyzed. A site meeting at Fort Pierce was held on 8th December 2022 in close cooperation with CEHNC and CESAJ to define requirements and deliverables.

The existing mobilization model was applied on the AoI and OoI and the weaknesses and strengths of the existing model were found. It is shown that the mobilization model can be combined with the burial model of Whitehouse, with which the first Go/No-Go-Decision point was passed successfully.

As Dr. Helen Morrison left the project, the Lattice Boltzmann Simulations were not continued. Instead of these, TELEMAC was successfully implemented and used to model the currents, tides, waves and the morphodynamics in the Area of Interest. First test simulations were validated successfully.

The UXOmob software was completely re-designed and set up in C++ to increase the performance and allow for spatial analysis of long huge time series. An algorithm that considers a local vertical change of the seabed due to morphodynamics including erosion and accumulation of sediment was included and tested. Thus, the second Go/No-Go-Decision point was passed successfully.

From available burial data, a sensitivity study was done to quantify the importance of the variables, influencing the burial process of UXO. The most important variables were used to set up a neural network which, after training, will be validated within the framework of the existing DRAMBUIE model.

For a systematic cross comparison of the existing burial and mobilization models, a classification procedure was developed and described. For this purpose, the relevant literature was reviewed and first examples of the classification are shown.

2 Objective

Unexploded Ordnances (UXOs) and Discarded Military Munitions (DMMs) are found in many coastal regions. They are present in US coastal waters that coincide with former test firing ranges or underwater dump sites and cause a potential risk to personnel as the ammunition or explosive was not detonated. These objects are constantly exposed to environmental influences such as saltwater, which causes corrosion, and waves and currents as well as mobile seabed sediments. Thus, the management and risk assessment of the potentially numerous and diverse object types is a big challenge. For site managers, the location of the objects, along with their type and condition, are of particular interest. Even if these pieces of information were known from surveys, the horizontal and vertical (with respect to the seafloor) locations of particular objects may vary due to continuous environmental influences. Thus, at the least where objects of interest are known to remain on or in the seabed, a scheduled program of monitoring is needed. The project aims to quantify the influence of currents and waves on the mobilization and migration of objects of interest, including the role played by migrating bedforms. This quantification also includes analysis of the (self-)burial and re-exposure of objects. Ultimately, the critical conditions for mobilization need to be identified, along with a probability of occurrence within the area of interest and analysis of how far objects subsequently migrate. This will allow for informed decisions to be made regarding ongoing



monitoring, significantly reducing the frequency of repeated and expensive surveys for those locations where the risk of object migration is demonstrated to be low under the prevailing environmental conditions.

3 Technical Approach

3.1 Area of Interest: Fort Pierce

Together with the U.S. Army Engineering and Support Center Huntsville (CEHNC), the decision was made to focus on an area of interest (AoI) close to Fort Pierce. In addition to the main AoI, an alternative AoI (Flamenco Bay on the Island of Culebra, Puerto Rico) was agreed upon for optional later improvements and validation.

The Fort Pierce U.S. Naval Amphibious Training Base (NATB) was established in 1942 for training of the Naval Underwater Demolition Team. This included the use of bulk high explosives, high explosive rockets, bombs, anti-aircraft guns and small arms. The total size of the training base was 19,280.48 acres on North and South Hutchinson Island, including submerged lands in the Indian River. The north-south extension was about 25 miles. In 1943 the Joint Army Navy Experimental and Testing Board (JANET) was established to develop methods for breaching and removing beach fortification. The main purpose of these activities was to prepare for invasions in Europe and Japan. Thus, besides several more land-based activities, on North Hutchinson Island beach fortifications were built in the regions of South Beach to test ordnances, containing quantities of high explosives. This area of 3895 acres, shown in Fig. 1, is called Offshore Obstacle Area and referenced as Project 05 in the Inventory Project Report of the US Army Corps of Engineers (Army, 2012).

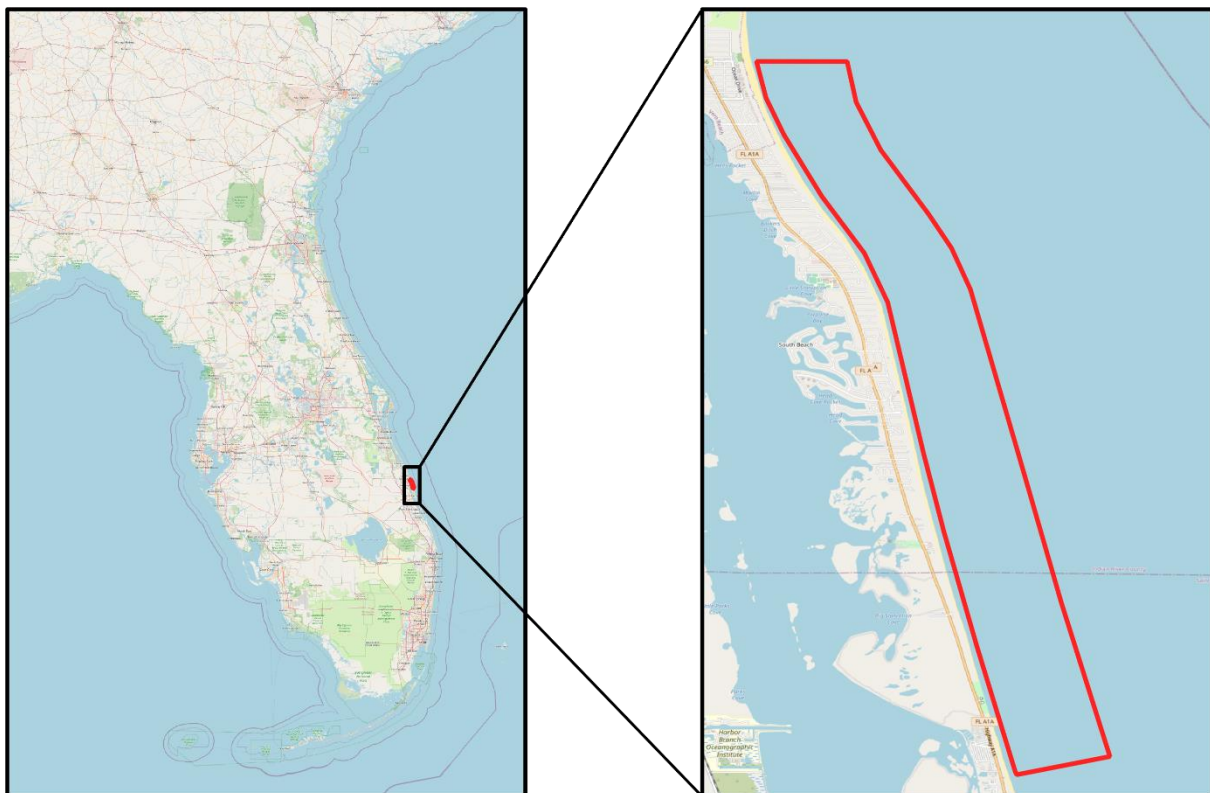


Fig. 1: Location of the Offshore Obstacle Area at the Fort Pierce U.S. Naval Amphibious Training Base.

According to (CEHNC, 2007), the activities focused on:

- “Reddy Fox (10” diameter metal tubes, loaded with explosives in length of 100’, towed by landing craft) attacks against man-made water obstacles and sand bars”
- “Remotely-controlled or remotely-detonated landing craft loaded with explosives directed against land and water obstacles”
- “Mechanical equipment for detonating underwater mines”
- “Aerial bombardment against beach obstacles”
- “Tank rocket launcher attacks against beach obstacles”
- “Tank dozer operations”
- “Demolition rockets fired from a variety of landing craft”
- “Smoke laying operations from unmanned watercraft”
- “Placing of steel rails by jetting”

However, in 1946 the land was cleaned up and returned to its original owners. The cleanup included the removal of buildings and the disposal of munition, which was dumped about 15 miles offshore at about 1500 ft water depth in the Atlantic Ocean.

Since that time, the area was strongly developed and now includes residential, commercial, governmental and educational facilities. Several activities, e.g. (Army, 2012), (McDonald, et al., 1998), (USACE, 1998) and (CEHNC, 2021) have taken place to evaluate the risk of hazards. As the facility was built to simulate the inventory of the Atlantic Wall as shown in Fig. 2, similar installations were made. It is proven that especially horned scullies were installed. As the fortifications in Europe also consisted of similar items, it is speculative if also simple log posts, log ramps, Czech hedgehogs and maybe Belgian doors were installed. The findings of the beach barrier removal project from 1998 (USACE, 1998) indicated that, besides horned scullies (including concrete), simple rails were also used. The activities of (McDonald, et al., 1998) show that also a lot of anti-tank mines were found, which leads to the assumption that those may also have been used for training or simulation of a real barrier.

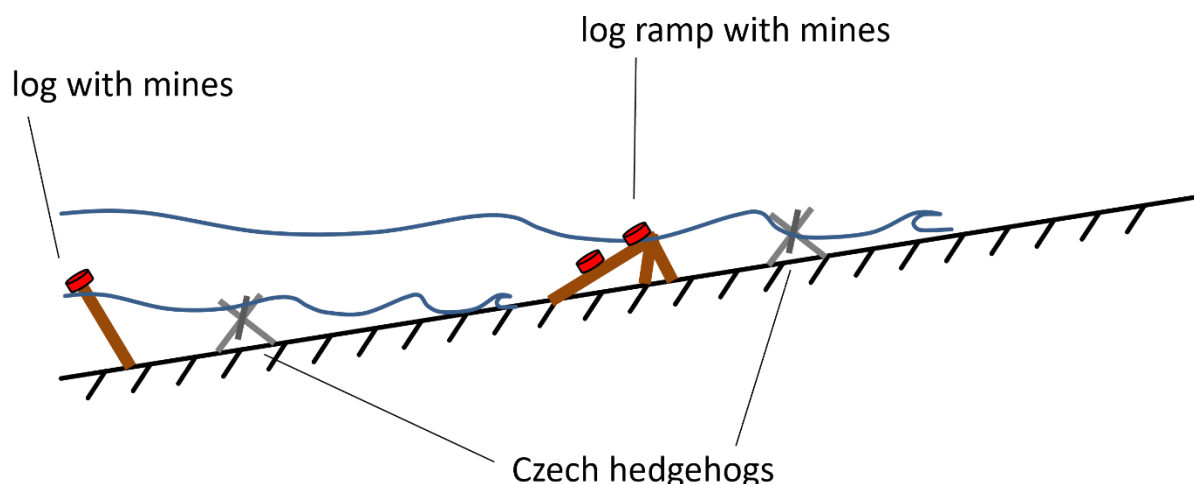


Fig. 2: Example of a beach fortification in the Normandy

(CEHNC, 1996) reports about 10 findings of ordnance items, related to NATB, on land sites in the time period of 1951 to 1996. During the Beach Barrier Removal Project (USACE, 1998), about 160 tons of material was removed from the beach and shallow water up to 3 m



water depth. During this campaign, some C-2 plastic explosives, a Mk 5 Barrage Rocket, a 81 mm Mortar and a 1,000 lb Bomb were found. According to (CEHNC, 2021), a 500 lb and a 1,000 lb Bomb was found in 2013, as well as three 500 lb Bombs, two 7.2-inch demolition rockets and four Tiny Tim Rockets in 2015. Another Tiny Tim rocket is reported from a land-based incident. Furthermore, a total of 10 mines of different types were found in 2018 as well as a 7.2-inch rocket motor in 2020. During an EM-Survey in 2017, two JATO M3A2, an M6 mine and a T37 rocket motor were found. All items were buried by about 30 inches. It is worth mentioning that the EM Survey was able to cover slightly more than 1% of the whole area of Project 05. From this report, two citations need to be mentioned:

- *“Additional Munitions and Explosives of Concern (MEC) may be located on the seafloor or below the seafloor in areas that were not investigated.”*
- *“The marine environment is subject to sediment erosion and deposition due to ocean currents, tidal patterns, storm events, and near-shore processes. In the marine environment, MEC tend to undergo scour burial during typical flow conditions. During high intensity conditions, such as storm events, MEC may be uncovered, moved by the currents, and then reburied when typical flow conditions return. The possibility exists that additional MEC may be present in areas not investigated or may become exposed due to natural processes, such as by storm surge and deposition or erosion of the sand/sediment.”*

This supports the necessity of the research done in this project. The reported UXO findings prove that the Offshore Obstacle Area of Fort Pierce NATB is an area with potential risk due to UXO.

3.2 Available Data on the AoI

The AoI is on the East Coast of Florida, along the coast of both Indian River County and St. Lucie County. It encloses an area approximately 12 km long, along the shoreline, and extends approximately 1.3 to 1.4 km offshore. Environmental data available in the AoI and its vicinity consist of wave measurements, on the waverider buoy of Fort Pierce, and sediment core samples from the from the Florida Department of Environmental Protection and its Reconnaissance Offshore Sand Search Inventory (ROSSI) (Coor, et al., 2015).

The shoreline is approximately straight along most of the AoI (see Fig. 3), but with a slight kink at monument IR R-105. Between monuments SL R-012 and IR R-105, it is oriented 16 degrees anticlockwise from the north direction, and between IR R-105 and IR R-090, the orientation is 28 degrees.

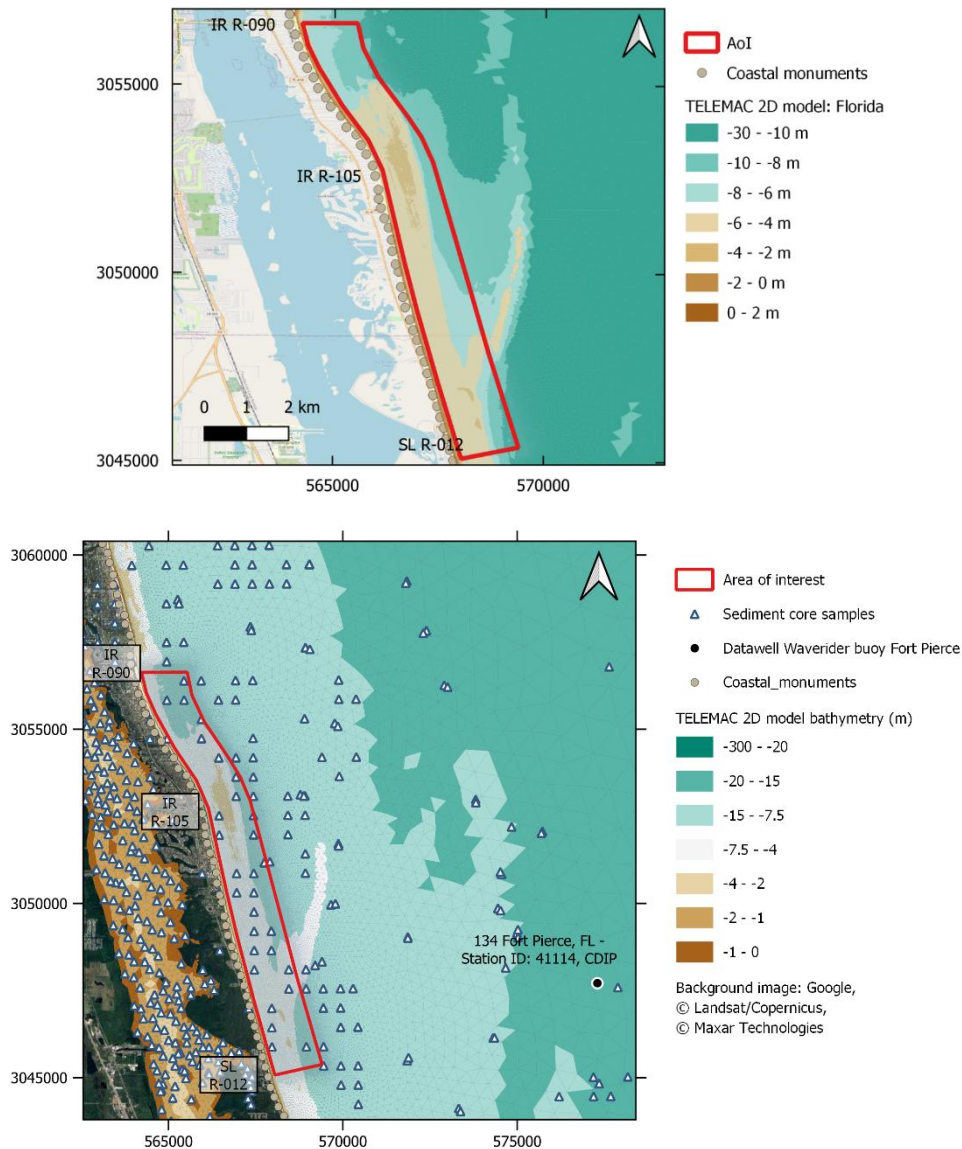


Fig. 3: The boundaries of the Fort Pierce AoI, alongside the locations of the relevant environmental data.

There are multiple bars and low-relief flats in the nearshore and on the berm. This topography, and the fine sediments ($d_{50} = 0.3$ mm), makes the beach along the AoI dissipative and with a low wave reflectivity (Benedet, et al., 2003).

West of the AoI is the Indian River Estuary, which flows parallel to the East Coast of Florida for approximately 250 km. The estuary consists of three separate lagoons: Mosquito Lagoon; Indian River Lagoon; and Banana River Lagoon (Fig. 4). The largest of these, and most important because it is the closest to the AoI, is the Indian River Lagoon. This Lagoon is connected to the Atlantic Ocean through three inlets, shown in Fig. 5: Sebastian, Ft. Pierce and St. Lucie inlet. The geometry along the Indian River Lagoon is intricate with many canals, sinuous distributaries, numerous land abutments protruding into the water and the federally maintained Atlantic Intracoastal Waterway (Bilskie, et al., 2019).

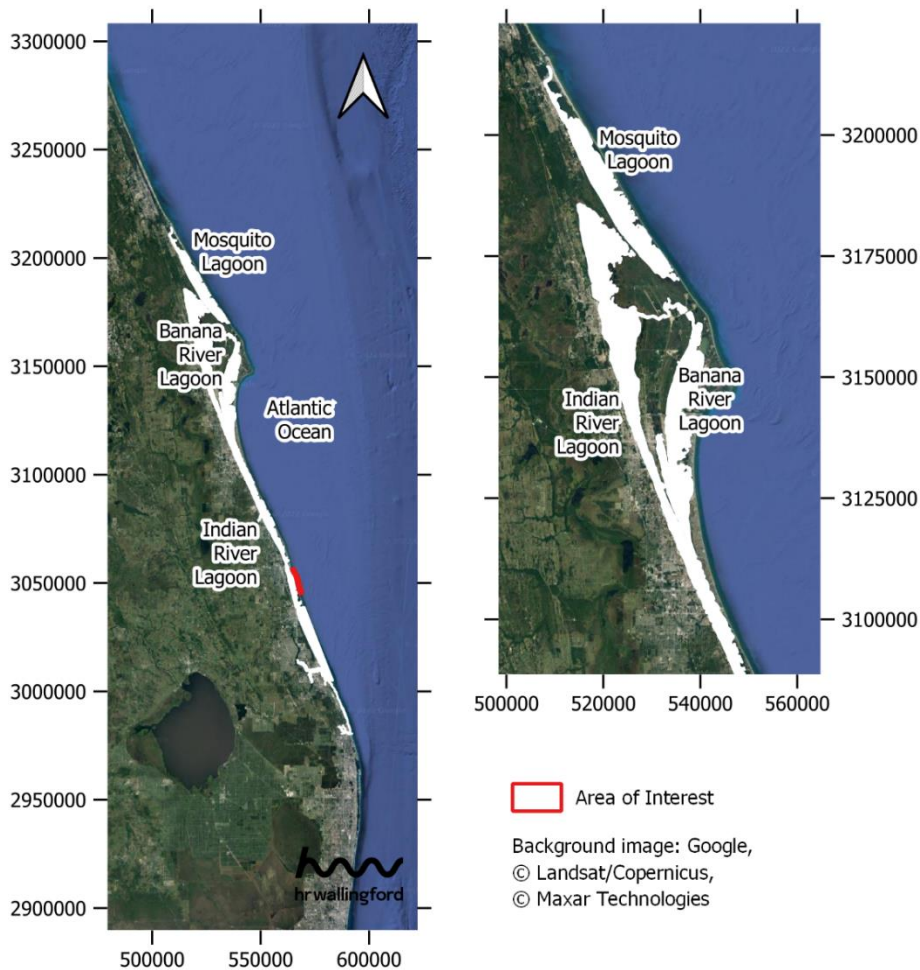


Fig. 4: Indian River Lagoon System.

Fort Pierce is the nearest inlet to the AoI. It is located 6 km south of the AoI. Its navigation channel is 6.5 m deep, with two jetties separated by 274 m. The north jetty is 549 m long and the south jetty is 366 m (Rodríguez & Dean, 2009). Sebastian inlet is located approximately 27 km north of the area of interest. Its navigation channel is 2.4 m deep, protected by a north jetty extending 182 m from the shore and a south jetty 152 m long from the shore. This inlet has a steel bulkhead next to the north jetty and it protrudes 1370 m into the ocean in a northwest to southeast direction. The farthest inlet is St Lucie, 46 km away south from the AoI, along the navigation channel depths range from 5 to 3 m. The inlet is protected by jetties on its north and south banks (NOS, 2021) and a detached breakwater south of the northern jetty.

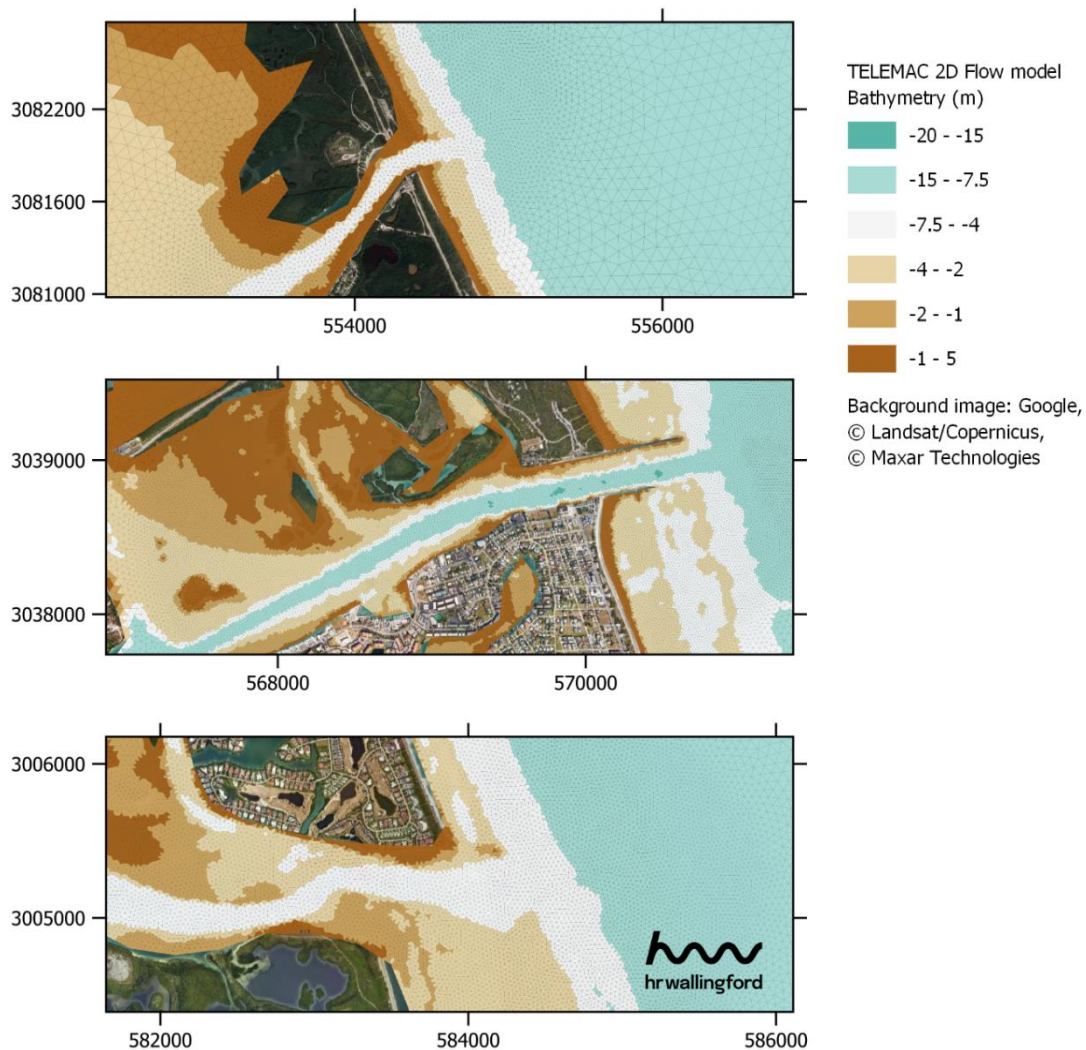


Fig. 5: The inlets near the AoI: Sebastian (top); Fort Pierce (middle); and St Lucie (bottom).

3.2.1 Bathymetry

There are a range of different bathymetry datasets available via NOAA’s National Centers for Environmental Information (NCEI) that cover the region in and around the AoI. The area directly within the AoI boundaries is, for example, included in the “2016 USACE NCMP Topobathy Lidar: Florida East Coast” dataset, which is well resolved at a pixel size of 0.0315’’ x 0.0315’’ (approximately 0.87 m x 0.87 m). The data was recorded using the Coastal Zone Mapping and Imaging Lidar (CZMIL) system, which is able to record both topographic and bathymetric data. The horizontal position is provided as latitude/longitude in NAD83(NSRS2007) and meets an accuracy of $3.5 + 0.05d_e$ m at 95% confidence level, where d_e is the depth. The depth is given in NAVD88 meters and compiled to meet $\sqrt{(0.2)^2 + (0.0075d_e)^2}$ m vertical accuracy at 95% confidence level for the shallow FOV data and $\sqrt{(0.3)^2 + (0.013d_e)^2}$ m vertical accuracy at 95% confidence level for the deep FOV data[1].

[1] Information available at (USACE NCMP Topobathy Lidar, 2022)

Understandably, the highly resolved Lidar data is only available close to the shore and thus does not extend much beyond the Fort Pierce AoI. In order to understand the potential effects of waves and seabed morphodynamics on the AoI, bathymetry data is also required for areas further offshore. As there is a waverider buoy located close to the AoI, the area of data collection was extended to include its location. For this, two further datasets were acquired, namely H05027[2] and H05032[3], which both contain lead line data from 1930 with the depth given in mean low water (MLW). The contained datapoints can be seen in Fig. 3. Along the survey lines, the points are approximately 50 m apart, whereas the distance between the individual survey lines can be up to 300 m. The points of the two datasets were hence converted into two grids, both with a resolution of 0.0005 degrees (approximately 50 m). These grids were then merged into one, using bilinear interpolation and a blending function for the overlap with a blending distance of 0.01 degrees. The subsequent gaps were filled using GDAL's "fill nodata" with a maximum search distance of 10 pixels (see definition of a pixel in Section 3.10.4) for the required interpolation and the resulting dataset was then finally cropped to the required extent.

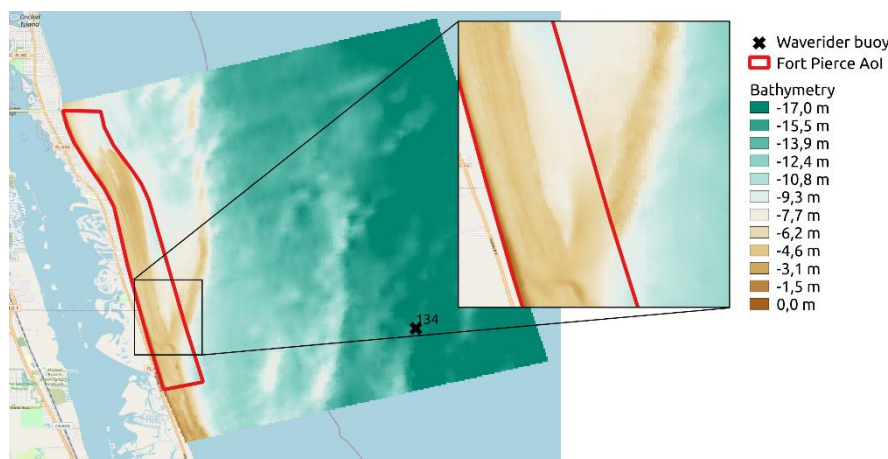


Fig. 6: The processed bathymetry data in (2016 Lidar data) and around (1930 lead line data) the AoI

Fig. 6 shows the Lidar data from 2016 in the Fort Pierce AoI and the resulting dataset obtained from the 1930s lead line data for the area outside of the AoI. The datums of the datasets (NAVD88 and MLW, respectively) only vary by about 0.76 m and therefore no correction was made to either dataset at this point. The close-up panel emphasizes the difference in resolution between both datasets across the Fort Pierce AoI boundary. Nevertheless, it is worth pointing out that although the datasets were obtained more than 80 years apart, there is little discrepancy between them, thus suggesting that there are no major net changes to the seabed taking place. At the same time, there is a prominent sandbar present just offshore of the AoI, which might be affected by seasonal variations and will thus be a focus of future work within the project.

3.2.2 Geomorphology

The continental shelf dips towards the East and its width varies between 5 km to 120 km along the East Coast of Florida. The cross-shore slope is generally gentle (1/80), characterized by inner plateaus, shoals and reefs. The shoreface zone consists of a terrace of unconsolidated sediments reaching up to 3 m below the water sediment interface. Characteristic widths of the

[2] Information available at (National Centers for Environmental Information, 2022)

[3] Information available at (National Centers for Environmental Information, 2022)

shoreface range between 150 m towards the South and 1000 m towards the North (Ousley, et al., 2014). Offshore is the inner shelf, outer shelf and the shelf break. The limit between these areas is determined by changes in slope and sediment bed morphology. The inner shelf is characterized by sandy flats and localized changes in depth along shoals, sand ridges and reef structures. The outer shelf is rocky, with coral reef patches and its slope drops until the shelf break; sediments are predominantly medium to coarse sands, fine to medium quartz and fine to gravel-sized carbonates, calcarine and broken shells. The particle sorting is poor and the content of silt and clay is varied, although not abundant. (Coor, et al., 2015) (Ousley, et al., 2014). There are also hard bottom areas along the shoreface (McCarthy, et al., 2020) which will limit the sediment supply and morphology change where they occur.

3.2.3 Currents

The Tide in the US East Coast is of semi-diurnal type, dominated by the M2 component (period of 12.42 h), with amplitudes as small as 0.186 m in Key West, to 0.6–1 m from Florida to New York, and approx. 1.38 m in Boston and Portland (Ezer, 2020).

The Florida Current, in the subtropical North Atlantic Ocean at 27°N, has an important role in climate due to its transport of heat and other tracers (Duerr & Dhanak, 2012). It can reach velocities in the 1–2.5 m/s range and is characterized by cyclonic eddies that travel eastwards and northwards, along the continental margin (Kourafalou & Kang, 2012). Fig. 7 shows an example of the strength of the Florida current.

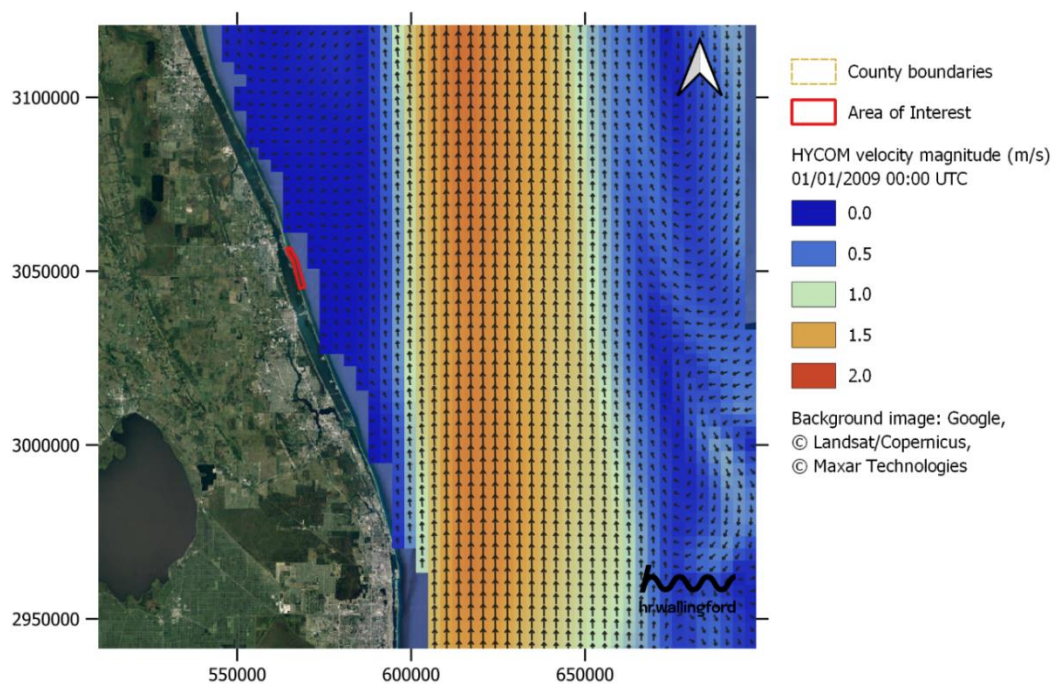


Fig. 7: The Florida current runs offshore of the area of interest.

Tides and ocean currents are not the main drivers of morphodynamics along the beach, but these dominate the exchange of water within the Indian River Lagoon. Fort Pierce Inlet transports 50% of the intertidal volume of the Lagoon, whereas Sebastian Inlet and St. Lucie Inlet exchange approximately 30% and 20% (Bilskie, et al., 2019).



3.2.4 Wave data

The Coastal Data Information Program (CDIP) maintains a spherical directional waverider buoy (NDBC 41114; 134 – Fort Pierce, FL) at 27.551 N 80.217 W[4]. It measures wave energy, wave direction and sea temperature. Hence, the provided datasets[5] deliver significant wave height (H_s), peak wave period (T_p), mean direction from which the energy is coming at peak wave period (D_p), average wave period (T_a) and sea surface temperature (SST) at a 30 minute rate.

While the data provides fairly extensive insight into the statistical wave information at the station dating back to 2006, it is unfortunately only of limited value to research within the Fort Pierce AoI. As previously mentioned, and as can be seen in Fig. 6, the waverider buoy is located approximately 11 km offshore and therefore well outside the AoI. Furthermore, the water depth at the location of the buoy is recorded as 16.49 m and is thus considerably deeper than the average depth within the AoI (~ 6 m). Hence, some form of modelling is required to obtain a realistic estimate of the temporally and spatially resolved waves from the waverider buoy data. In principle, NOAA's Nearshore Wave Prediction System (NWPS) provides such model data, though it has proven rather difficult to obtain highly resolved data for the AoI over an extended timeframe.

Ocean swells and wind-generated waves are the main factors affecting beach morphodynamics along East Florida. The coupling of tropical storms, north eastern, and other wind and swell events results in a highly dynamic nearshore system. Waves vary seasonally, with the strongest events taking place during autumn (see top panel of Fig. 8). The typical significant wave heights are about 0.5 m in summer, increasing to about 1 m in autumn, winter and spring. During storms the significant wave height can increase to 2 to 3 m in summer; 3 to 4 m in winter and spring; and 6 m during autumn. The significant wave heights in autumn are correlated to the intensity of the hurricanes in the area.

For almost all months, the peak wave period has a bi-distribution mode with wind waves (typically about 5 s period) and swell (typically about 10 s period). The only exceptions happen during autumn (see bottom panel of Fig. 8), where the swell (10 s) is the dominant frequency of most wave activity. The wave direction is consistent throughout the year, most waves (66.5%) come from the sector between northeast and east (Fig. 9).

[4] Information available at (Coastal Data Information Program (CDIP), 2022)

[5] Information available at (National Data Buoy Center, 2022)

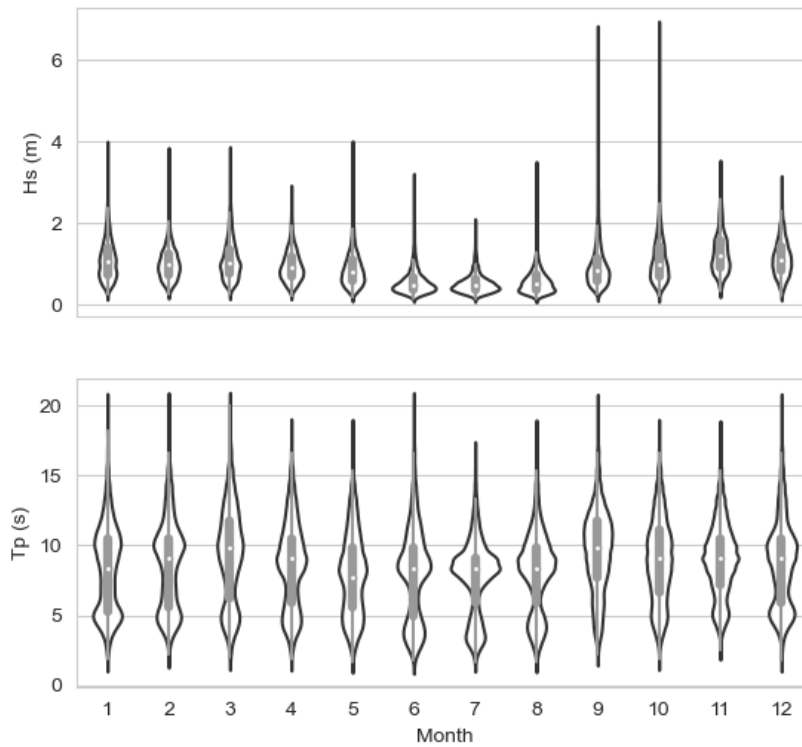


Fig. 8: Monthly wave conditions off Fort Pierce, measured between 2006 and 2020. Top, significant wave height. Bottom, Peak wave period. The boxplots feature the monthly means (white dots), the first and the third quantiles of the available data (grey boxes). The violin plots feature the approximate -kernel density- distribution of the monthly measured data.

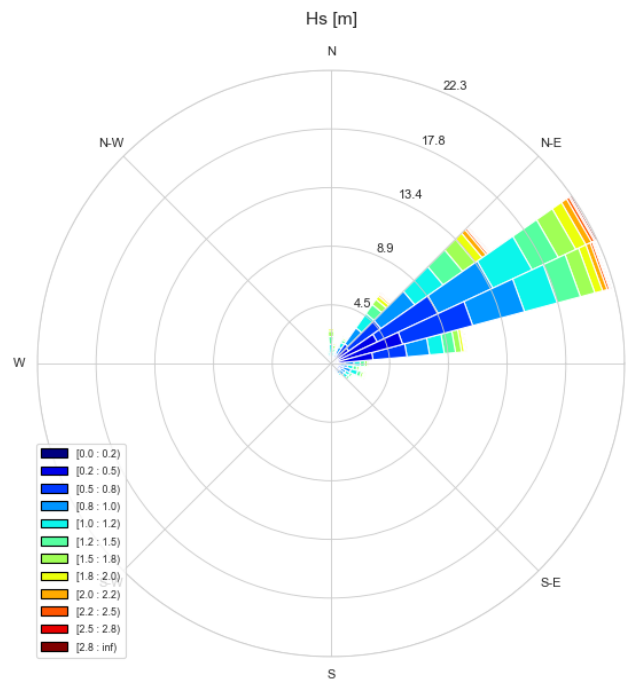


Fig. 9: The annual wave rose for Fort Pierce.



3.2.5 Sediment composition

Information on the sediment composition in the AoI is provided by usSEABED (Buczowski, et al., 2020). Various datasets are available, which provide insight into different aspects of the sediment composition, covering textural, statistical, geochemical, geophysical, dominant component, and color data as well as information on facies and selected components. While some of these datasets (denoted “US9_EXT”) contain extracted data from quantitative measurements, other datasets were obtained by parsing written descriptions. According to the usSEABED website and the provided metadata, these include:

- “US9_PRS”: “parsed data on grain size, sediment texture, color, age, and other information about the seafloor derived from written descriptions from cores, grabs, photographs, and videos”;
- “US9_CMP”: “numeric data about selected components (for example, minerals, rock type, microfossils, and benthic biota) and sea-floor features (for example, odors)”;
- “US9_FAC”: “concatenated information about components (minerals and rock type), genesis (metamorphic, carbonate, terrigenous), and other appropriate facies or groupings of information about the seafloor parsed from written descriptions from cores, grabs, photographs, and videos”.

Furthermore, datasets denoted as “US9_CLC” contain “data created through the application of known relationships between analytical values or empirical relationships (calculated data)” and “US9_SRC” refers to the original data before being incorporated into usSEABED.

The average grain size, for example, is best obtained via the extracted quantitative data. Fig. 3 shows the location of all such datasets in the AoI and within the direct vicinity. Samples in the database are labeled with the respective device that was used to obtain the sediment probe (“Grab”: grab sampler; “VibroCorer”: vibrocorer; “PushCorer”: push corer; “UnidDevice”: unidentified device). Of these, only the four datasets from the grab samplers and the push corer provide data regarding the grain size, given in phi units:

$$\varphi_g = -\log_2 \frac{d}{d_0} \quad [1]$$

where d is the grain size in mm and $d_0 = 1$ mm is the reference diameter. The standard deviation of the grain size is also provided in phi units. All four sets of data were obtained between 1994 and 1998.

Fig. 10 shows the measured grain sizes (standard deviation of the single samples) at the different vertical sample locations (from the seafloor downwards) of all four datasets, whereas only the data of the data type denoted as “GRZ” (= grain-size analysis) were considered. The error bars for the grain sizes are given by the standard deviation in phi units, resulting in varying negative and positive errors depending on the average value of the grain size. The error bars for the sample locations on the other hand are given by the respective top and bottom of the sample locations. One data point (at $d = 0.93$ mm) exhibits a comparably large standard deviation, which is most likely due to the fact that the corresponding sample contained 16% gravel (and 84% sand), while all other samples contained only a maximum of 6% gravel. Those that



contained 100% sand and that were sampled at less than 2 m below the seafloor (15 of the 23 samples depicted) all provided similar grain sizes between 0.2 mm and 0.7 mm. The average grain size of all 23 considered samples was 0.41 mm, which will thus be used as the average grain size for the models within this project. The grain size is a little bit coarser than in the burial model used. For this reason, a connection with the Shields parameter is made and therefore a use in the model is possible.

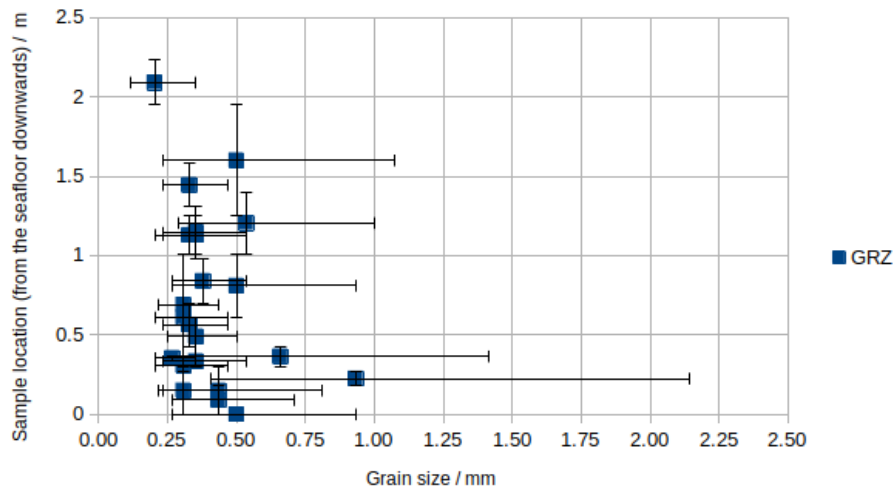


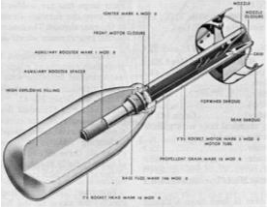
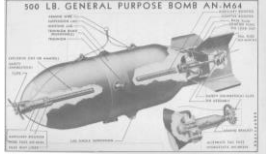
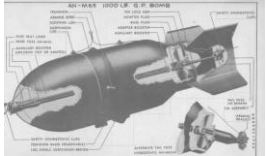
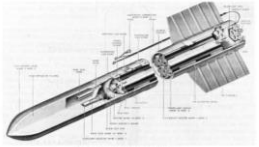

Fig. 10: Grain size at various sample locations (from the seafloor downwards), obtained from four different locations within the AoI (“Grab” and “PushCorer” sites in Fig. 3).

Fig. 10 shows the mean values in grain size in mm for the measured phi. Mean phi plus the standard deviation gives the maximum value in the diagram. Mean phi minus the standard deviation gives the minimum value in the diagram. The calculation was done with equation [1], for this reason it is not a symmetrical minimum or maximum value of the grain size.

3.3 Objects of Interest

In close coordination with the U.S. Army Engineering and Support Center Huntsville (CEHNC) and in accordance with the findings, four Objects of Interest (OoI) were defined.

Tab. 1: Objects of Interest

name	diameter [cm]	length [cm]	mass in air [kg]	image
7.2-inch Demolition Rocket	5.7	88.9	27.2	
500 lb GP Bomb	36.1	114.3	232.3	
1000 lb GP Bomb	47.8	134.9	437.3	
Tiny Tim Rocket	29.9	312.4	568.4	
Tiny Tim Rocket Warhead	29.9	119.4	272.2	
155 mm, HE 107	15.5	58.4	34.2	 Image: MR-2320

In addition to these objects, we decided to consider the 155 mm, HE 107 projectile as it has already been investigated intensively by other SERDP-projects and thus, validation data are available. The list of OoI is shown in Tab. 1. During the project, the burial, mobilization and re-exposure of the five OoI will be investigated. Thus, numerical simulations will be done to determine the hydrodynamic coefficients. For this purpose, simplified CAD-models were designed as shown in Fig. 11.

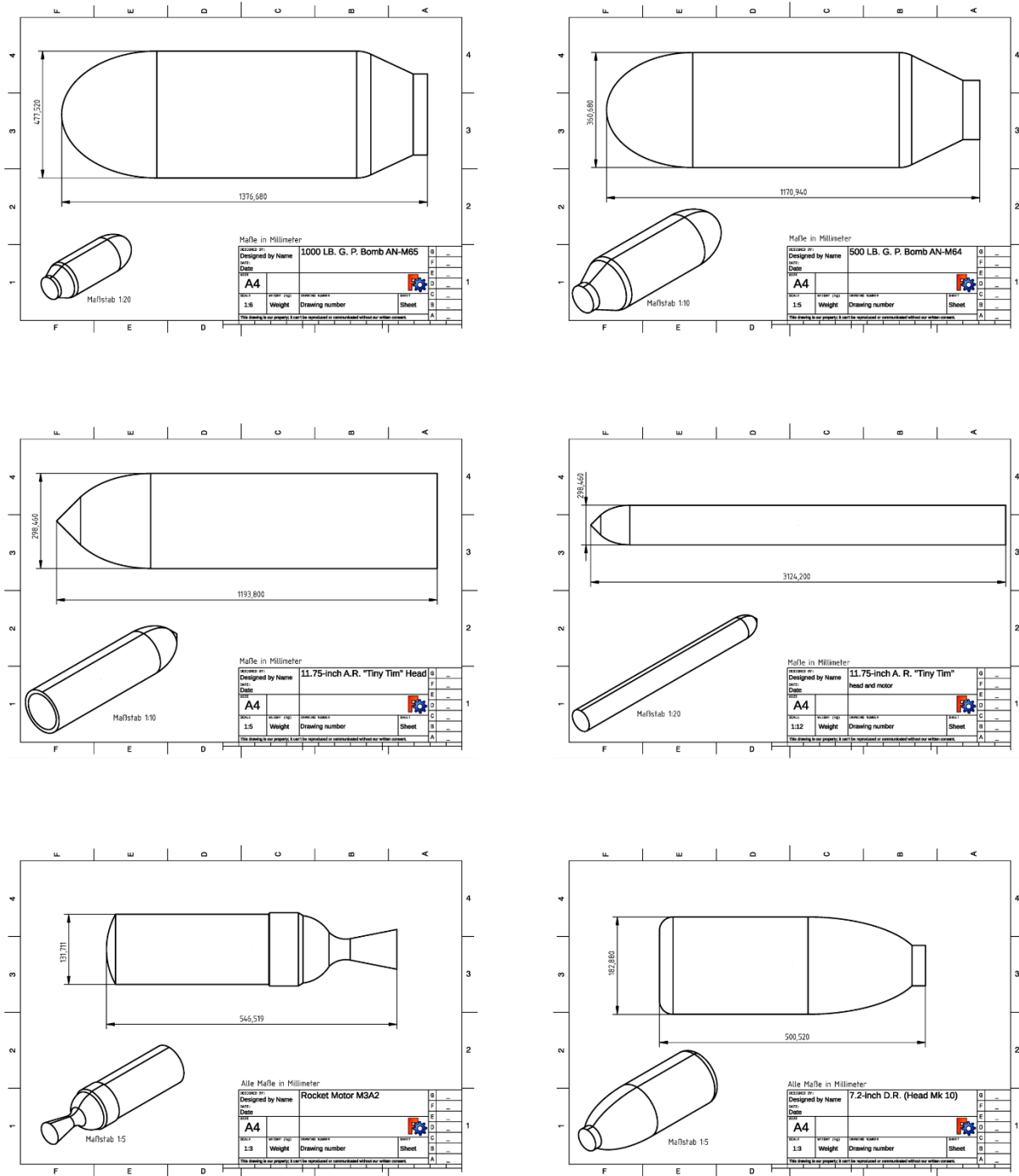


Fig. 11: Technical drawings of the OoI.

As the actual state of the objects on the seafloor is not exactly known, different options are considered as can be seen for the Tiny Tim Rocket. However, during the project, this will be defined more precisely.

3.4 Basics and Wave Models

The implementation of a OoI mobilization model requires the kinematics from the waves to be defined, and hence a description of wave phenomena is introduced here. From the physical point of view, waves are characterized as a periodic change of a physical quantity with a spatial propagation. Within an ocean environment one distinguishes between transverse and

oscillatory waves. Idealising a surface wave as a sinusoidal oscillation we assume only energy transport but no net transport of matter in the direction of wave propagation. Water particles are assumed to purely travel on closed orbits. Realistically, ocean surface waves represent a combination of transverse and longitudinal waves.

To describe surface waves, the wavelength λ , the wave amplitude A , the period T and the water depth h are used. A graphic demonstration of these quantities and their relations is shown in Fig. 12.

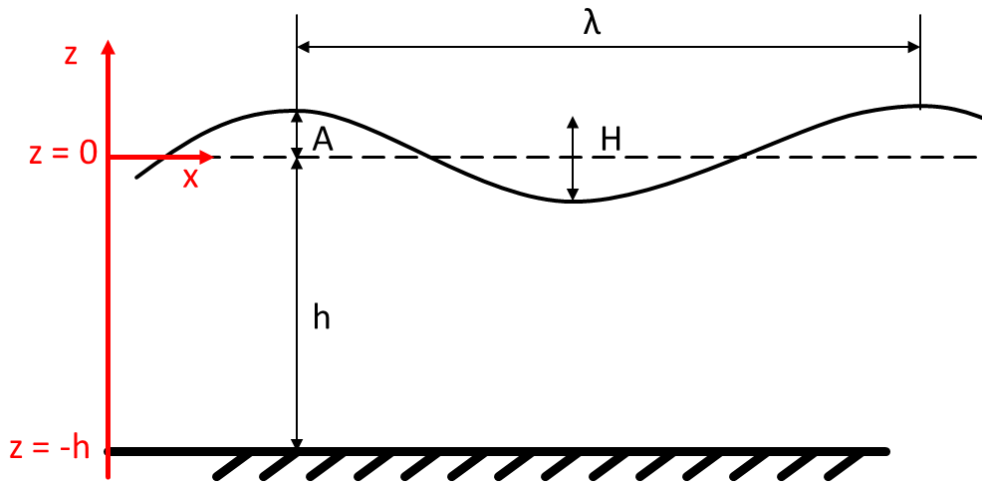


Fig. 12: Characteristic quantities of a surface wave.

From these quantities the speed of wave propagation, the so-called wave celerity,

$$c = \frac{\lambda}{T}, \quad [2]$$

the wave number

$$k = \frac{2\pi}{\lambda}, \quad [3]$$

the angular wave frequency

$$\omega = \frac{2\pi}{T}, \quad [4]$$

as well as the phase angle of the wave

$$\varphi = kx - \omega t. \quad [5]$$

with the distance x (in the direction of wave propagation) and the time t can be defined.

Besides these basic quantities, additional variables are often used in practice. The wave height is normally used as $H = 2A$, whereas the significant wave height H_s is mostly used in coastal and ocean engineering and in oceanography. The significant wave height was defined by (Munk, 1944) as the arithmetic mean of the maximum third of all waves measured in a continuous natural (irregular) sea state. H_s is a statistical value that directly relates to the energy contained in a natural sea state via

$$H_s = 4\sqrt{m_0} \quad [6]$$

where m_0 is the first moment of the so-called sea state spectrum. As an irregular sea state can be seen as a superposition of a number of sinusoidal waves with different periods, wave heights and phase angles, the sea state spectrum is its spectral representation. This spectrum is assumed to follow a Rayleigh distribution. Common spectral distributions are the Pierson-Moskowitz-spectra (Pierson & Moskowitz, 1964) and the JONSWAP-spectra, representing specific sea state features common in the North Sea. For the sake of completeness, the wave steepness H/λ , the relative water depth h/λ and the relative wave height H/h are specified. However, the maximum wave height H_{max} can be derived from the significant wave height as

$$H_{max} = H_s \cdot \sqrt{\frac{\ln N}{2}}, \quad [7]$$

Using the number N of wave cycles within a statistical time series.

Considering the movement of a single water molecule, this is extremely complex in natural conditions due to the superposition of a large number of waves of different wavelength, periodic times and phase angles in different water depths. Thus, simplifications and assumptions are made to yield an approximate conclusion. Common wave theories used to describe oscillatory waves distinguish between shallow water, transitional water and deep water waves, which are shown schematically in Fig. 13. The discrimination is realized by the relative water depth. In deep water, the orbits of the water molecules are circular, and the radius decreases with increasing water depth and there is no interaction with the sea floor. Within this region, a significant influence of the waves on objects on the sea floor or the sea floor itself is not expected. However, transitional waves will induce a force on the sea floor itself as well as on objects located on the sea floor. As the velocity close to the sea floor has to be solely parallel to the bottom, also the orbits above are elliptic. With increasing depths, the vertical velocity component of the elliptic orbits w decreases faster than the horizontal velocity component u . The horizontal velocity close to the sea floor is lower than the horizontal velocity at the surface. In contrast to this, the horizontal velocity component in shallow water waves is nearly constant and independent of the water depth. In this way, the impact of the surface waves on objects on the sea floor or the sea floor itself achieves its maximum in shallow water.

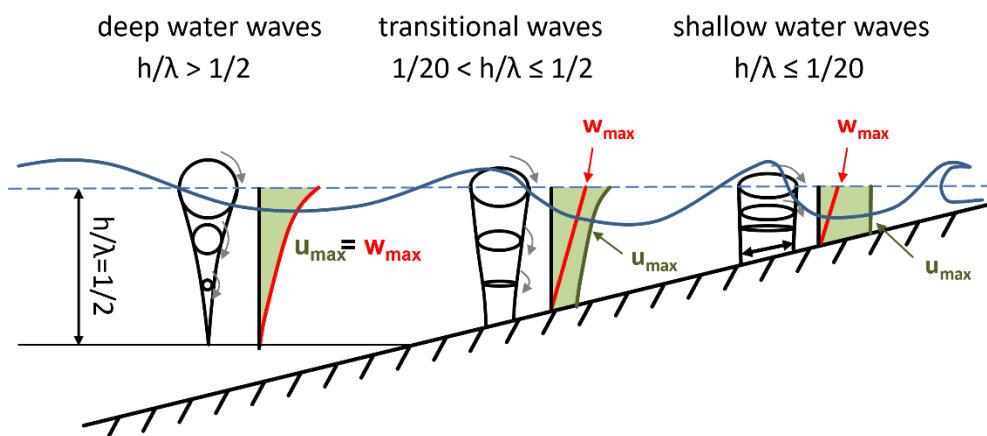


Fig. 13: Orbits of waves in different water depths.



Assuming a sinusoidal wave of a single wavelength and wave period, the orbits of the water molecules can be described by the linear wave theory of (Airy, 1845) and (Laplace, 1776).

Tab. 2: Equations of the linear wave theory.

	deep water $h/\lambda > 1/2$	transitional water $1/20 < h/\lambda \leq 1/2$	shallow water $h/\lambda \leq 1/20$
u	$A\omega e^{kz} \cos \varphi$	$A\omega \frac{\cosh k(z+h)}{\sinh kh} \cos \varphi$	$A\omega \frac{1}{kh} \cos \varphi$
w	$A\omega e^{kz} \sin \varphi$	$A\omega \frac{\sinh k(z+h)}{\sinh kh} \sin \varphi$	$A\omega \left(1 + \frac{z}{h}\right) \sin \varphi$
Δx	Ae^{kz}	$A \frac{\cosh k(z+h)}{\sinh kh}$	$\frac{A}{kh}$
Δz	Ae^{kz}	$A \frac{\sinh k(z+h)}{\sinh kh}$	$A \left(1 + \frac{z}{h}\right)$

The equations for the fluid velocity components u and w as well as the equations for the semi-minor and the semi-major of the orbits, given in Tab. 2, are valid for waves with low amplitude, small relative wave height and small steepness. Within these equations the total water depth h is positive, whereas the vertical position within the water column z is negative with $z = -h$ at the sea floor and $z = 0$ at the water surface as shown in Fig. 12. Tab. 2 highlights the equations for horizontal (u) and vertical (w) water particle velocities as well as the length of the semi-major (Δx) and -minor (Δz) axes for each particle orbit, depending on the water depth.

Typical ocean waves often strongly differ from the ideal of a sinusoidal function, which restricts the applicability of the linear wave theory. Due to these restrictions, several nonlinear wave theories have been established, whereas the theory of (Stokes, 1847) may be the most familiar one. This theory also includes the nonlinear part of the Bernoulli equation, hence also making it applicable for steeper waves. The equations of Stokes' third-order wave theory are shown in Tab. 3, with \dot{u} and \dot{w} being the horizontal and vertical water particle accelerations, respectively.

Tab. 3: Equations of Stokes' third-order wave theory.

	deep water	shallow water incl. transitional regime
	$h/\lambda > 1/2$	$h/\lambda \leq 1/2$
u	$A\omega e^{kz} \cos \varphi$	$c \left[ka \frac{\cosh[k(z+h)]}{\sinh(kh)} \cos \varphi \right. \\ + \frac{3}{4} k^2 a^2 \frac{\cosh[2k(z+h)]}{\sinh^4(kh)} \cos(2\varphi) \\ + \frac{3}{64} k^3 a^3 \frac{11 - 2 \cosh(kh)}{\sinh^7(kh)} \cosh[3k(z+h)] \cos(3\varphi) \left. \right]$
w	$A\omega e^{kz} \sin \varphi$	$c \left[ka \frac{\sinh[k(z+h)]}{\sinh(kh)} \sin \varphi \right. \\ + \frac{3}{4} k^2 a^2 \frac{\sinh[2k(z+h)]}{\sinh^4(kh)} \sin(2\varphi) \\ + \frac{3}{64} k^3 a^3 \frac{11 - 2 \cosh(kh)}{\sinh^7(kh)} \sinh[3k(z+h)] \sin(3\varphi) \left. \right]$
\dot{u}	$a\omega^2 e^{kz} \sin \varphi$	$c \left[k\omega a \frac{\cosh[k(z+h)]}{\sinh(kh)} \sin \varphi \right. \\ + \frac{3}{2} k^2 \omega a^2 \frac{\cosh[2k(z+h)]}{\sinh^4 kh} \sin(2\varphi) \\ + \frac{9}{64} k^3 \omega a^3 \frac{11 - 2 \cosh(2kh)}{\sinh^7 kh} \cosh[3k(z+h)] \sin(3\varphi) \left. \right]$
\dot{w}	$-a\omega^2 e^{kz} \cos \varphi$	$c \left[-k\omega a \frac{\sinh[k(z+h)]}{\sinh(kh)} \cos \varphi \right. \\ + \frac{3}{2} k^2 \omega a^2 \frac{\sinh[2k(z+h)]}{\sinh^4 kh} \cos(2\varphi) \\ - \frac{9}{64} k^3 \omega a^3 \frac{11 - 2 \cosh(2kh)}{\sinh^7 kh} \sinh[3k(z+h)] \cos(3\varphi) \left. \right]$



The parameter a serves as a first approximation to the wave amplitude A . For a proper estimation of this parameter, according to (EAK, 1993), a is implicitly given as

$$H = 2a + \frac{3}{32}k^2a^3 \cdot \left(\frac{1 + 8 \cosh^6(kh)}{\sinh^6(kh)} \right), \quad [8]$$

which does not lead to a practical solution. According to (EAK, 1993), the wave velocity can be computed as

$$c = \sqrt{\frac{g}{k} \tanh(kh) \cdot \left[1 + k^2a^2 \frac{8 + \cosh(kh)}{8 \sinh^4(kh)} \right]}. \quad [9]$$

A first theory for shallow water waves was presented by (Korteweg & de Vries, 1895) and is known as the Cnoidal theory. In contrast to Stokes' theory, Cnoidal theory is also able to describe an increase of the wavelength with increasing water depth. The equations of the Cnoidal theory are notoriously difficult to solve due to the use of elliptic Jacobi-functions. Cnoidal theory is not used and can therefore be disregarded.

Detailed information on the different wave theories and their derivation can be found in (Zanke, 2002), (EAK, 1993), (CERC, 1984), (Le Méhauté, 1976) and (Malcherek, 2010). Regarding the resulting assumptions for the different theories, it can be found that some of these partially contradict each other. These contradictions, especially between the theories of (Airy, 1845) and (Lord Rayleigh F.R.S., 1876), were investigated by (Ursell F.R.S., 1953). He found that both theories have their individual range of validity, which can be distinguished by the wave steepness and the relative water depth. Hence, the Ursell parameter

$$Ur = \left(\frac{H}{\lambda} \right) \left(\frac{\lambda}{h} \right)^3 = \frac{H\lambda^2}{h^3} \quad [10]$$

was defined. For small values of the Ursell parameter, the linear wave theory is applicable, whereas the nonlinear theories should be used for large values. As a critical value for the discrimination between the linear wave theory and the Cnoidal theory $Ur = 25$ is usually used, whereas the threshold to the theory of solitary waves is generally accepted to be at $Ur = 500$. The boundary for validity between Stokes' theory and the Cnoidal theory was defined by (Hedges, 1995) to be $Ur = 40$, whereas (Massel, 1999) published it to be at $Ur = 75$. According to (Le Méhauté, 1976) (see Fig. 14) the wave steepness (y-axis) is plotted against the relative water depth (x-axis). Based on this figure, a suggestion of the applicability of the different wave theories can be given, whereas the boundaries are considered to be approximations.

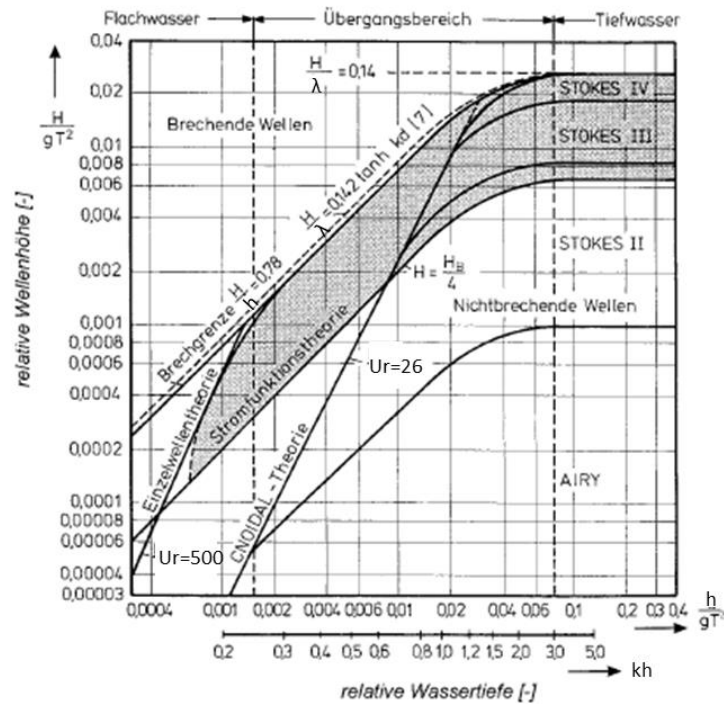


Fig. 14: Regions of validity of the different wave theories, modified according to (Habel, 2001), (CERC, 1984) and (Le Méhauté, 1976).

3.5 Mobilization Model

The mobilization model is based on integrating the offset-position of an object from its original, partially buried, position over time. This is done by deriving the position from the acceleration of the object, which again is derived from the loads on the object. These loads are computed via the Morison equation.

The loads on a cylindrical object in a symmetrical wave-induced seabed scour profile are shown in Fig. 15. Here, the seabed elevation is approximated to be sinusoidal with a maximum slope of α . The maximum slope is related to the sediment properties. The burial depth is given by z_b .

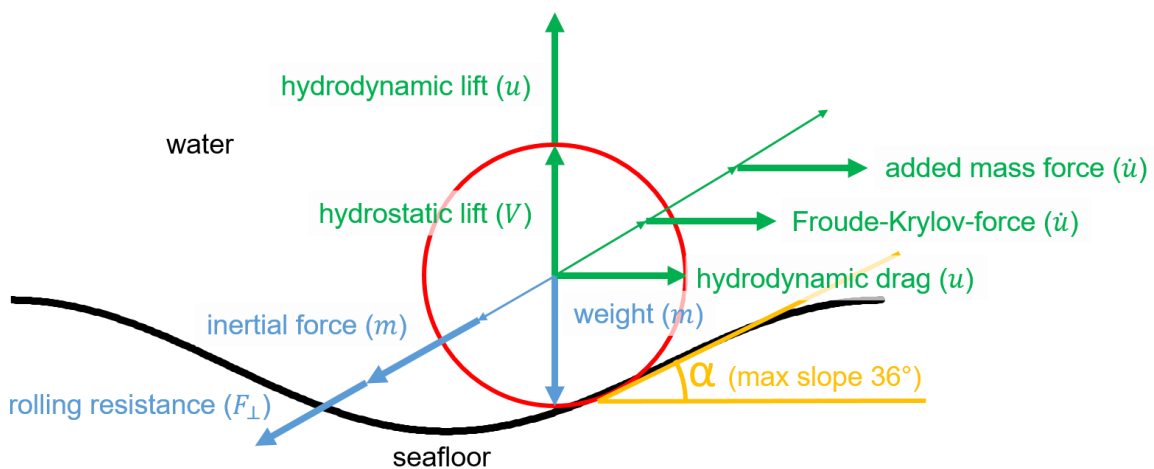


Fig. 15: Loads on a cylindrical object in a symmetrical scour trough due to waves.



An equation for the dynamic loads on a moving body in an oscillatory flow was published by (Morison, et al., 1950) and later was called the Morison equation. For the horizontal load, the Morison equation can be written as

$$\frac{3}{2}m\dot{u}_{obj} = \rho V_{obj}\dot{u} + \rho c_a V_{obj}(\dot{u} - \dot{u}_{obj}) + \frac{\rho}{2}(u - u_{obj})|u - u_{obj}|c_d A_{cs,obj} \quad [11]$$

with m being the mass of the object, V_{obj} and $A_{cs,obj}$ the volume and the cross section of the object, u and \dot{u} the velocity and acceleration of the water, u_{obj} and \dot{u}_{obj} the velocity and acceleration of the object, ρ the density of the water, c_a the added mass coefficient and c_d the drag coefficient. On the left-hand side we find the inertia, including the rotation. As the mass distribution of the objects is not completely known, a homogeneous mass distribution is assumed. The equivalent mass for the rotary inertia is

$$m_{rot} = \frac{\varphi_d}{r^2} \quad [12]$$

with r being the radius of the object and

$$\varphi_d = \frac{1}{2}mr^2 \quad [13]$$

Thus,

$$m_{rot} = \frac{1}{2}m \quad [14]$$

can be added to the pure inertia as

$$m + m_{rot} = \frac{3}{2}m \quad [15]$$

as it is written in Eq.[11] on the left-hand side.

The first term on the right-hand side of Eq.[11] is called the Froude-Krylov force, which is induced by the horizontal pressure gradient due to surface waves. The second term is the hydrodynamic mass force, which can be interpreted to be caused by the energy that is needed to build up the boundary layer at the walls of the object during the relative acceleration of the fluid. The third term is the hydrodynamic drag, which is caused by the wall shear stress at the object's surface and the flow-induced pressure difference between the front and the wake of the object. In practice, the hydrodynamic mass can be written on the left-hand side

$$\left(\frac{3}{2}m + \rho c_a V_{obj}\right)\dot{u}_{obj} = \rho V_{obj}\dot{u}(1 + c_a) + \frac{\rho}{2}(u - u_{obj})|u - u_{obj}|c_d A_{cs,obj}. \quad [16]$$

The vertical forces on the object will be handled separately as they will result in a horizontal force due to the slope of the seafloor. Due to this, the horizontal force

$$F_x = \cos \alpha F_{\parallel} = \cos \alpha \sin \alpha (F_g - F_b - F_l) \quad [17]$$

has to be derived in dependency of the instantaneous angle α as shown in Fig. 16a.

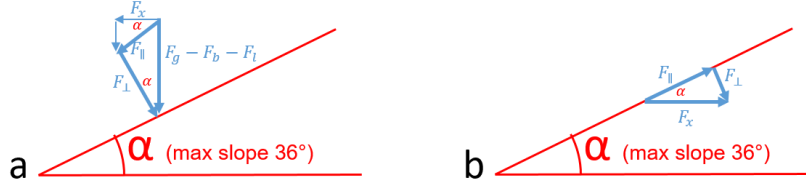


Fig. 16: Downhill-slope force (a) and friction force (b).

Inserting the weight F_g , the hydrostatic buoyancy F_b and the hydrodynamic lift F_l , Eq. [17] develops as

$$F_g - F_b - F_l = (m - \rho V_{obj})g - \frac{\rho}{2}(u - u_{obj})|u - u_{obj}|c_l A_{cs,obj} \quad [18]$$

and Eq. [16] can be written as

$$\begin{aligned} & \left(\frac{3}{2}m + \rho c_a V_{obj}\right) \dot{u}_{obj} \\ & = \rho V_{obj} \dot{u}(1 + c_a) + \frac{\rho}{2}(u - u_{obj})|u - u_{obj}|c_d A_{cs,obj} \\ & + \cos \alpha \sin \alpha \left\{ (m - \rho V_{obj})g \right. \\ & \left. - \frac{\rho}{2}(u - u_{obj})|u - u_{obj}|c_l A_{cs,obj} \right\}. \end{aligned} \quad [19]$$

From these horizontal loads, the force component perpendicular to the surface can be derived as

$$F_{\perp} = F_x \sin \alpha, \quad [20]$$

which is shown in Fig. 16b. The rolling resistance, $F_{r\parallel}$, which is parallel to the surface, then can be calculated using the rolling resistance coefficient, c_r , via

$$F_{r\parallel} = c_r F_x \sin \alpha \quad [21]$$

and the horizontal component is defined as

$$F_{rx} = c_r F_x \sin \alpha \cos \alpha. \quad [22]$$

Inserting Eq. [22] into Eq. [19] in which the horizontal force is written on the right side, the final equation can be written as

$$\begin{aligned}
 \dot{u}_{obj} = & [1 + c_r \sin \alpha \cos \alpha] \left[\rho V_{obj} \dot{u} (1 + c_a) \right. \\
 & + \frac{\rho}{2} (u - u_{obj}) |u - u_{obj}| c_d A_{cs,obj} \\
 & + \cos \alpha \sin \alpha \left\{ (m - \rho V_{obj}) g \right. \\
 & \left. \left. - \frac{\rho}{2} (u - u_{obj}) |u - u_{obj}| c_l A_{cs,obj} \right\} \right] \\
 & \cdot \left(\frac{3}{2} m + \rho c_a V_{obj} \right)^{-1}
 \end{aligned} \tag{23}$$

Inserting the wave-induced velocity and acceleration of the water, which is shown in Tab. 2 for the linear wave theory and in Tab. 3 for the 3rd order Stokes's wave theory, the instantaneous horizontal component of the acceleration of the object can be derived. Adding the vertical force components, the full acceleration of the object is obtained. This is used to simulate the velocity and to integrate the position of the object. This simulation is used regardless of whether the object is moved out of the scour hole or not. By simulating this for different burial depths, water depths, wave lengths and wave heights, the critical parameters can be found.

3.6 Burial Models

Within the project, several approaches for Burial Models were investigated, improved and combined. As the existing DRAMBUIE model, of (Whitehouse, 1998) was invented to predict current-induced scour burial, it needed to be improved to handle waves. This improved DRAMBUIE 2.0 was used as the basis for the first simulations.

In a second step, DRAMBUIE 2.0 was strongly improved and then is called DRAMBUIE 3.0. DRAMBUIE in general consists of two main parts. An equilibrium burial model and a time evolution model. Both parts were completely re-invented in DRAMBUIE 3.0.

3.6.1 DRAMBUIE 2.0

According to (Soulsby, 1995), (Soulsby, 1997), (Whitehouse, 1998) and (Whitehouse, et al., 2000), the burial depth of a cylindrical object on a sandy seafloor is derived by

$$z_b = z_{b\infty} \left\{ 1 - e^{-\left(\frac{t}{T}\right)^P} \right\}, \tag{24}$$

with $z_{b\infty}$ being the final or equilibrium burial depth for the time $t \rightarrow \infty$. The characteristic burial time-scale factor T governs the rate of burial, whereas P is a fitting coefficient, given as constant $P = 0.6$ in (Whitehouse, 1998). The value of $z_{b\infty}$ can be derived as

$$\begin{aligned}
 z_{b\infty} &= 0 & \text{for } 0 \leq \sqrt{Sh/Sh_{crit}} < 0.75 \\
 z_{b\infty} &= z_{b_{max}} \left(2\sqrt{Sh/Sh_{crit}} - 1.5 \right) & \text{for } 0.75 \leq \sqrt{Sh/Sh_{crit}} < 1.25 \\
 z_{b\infty} &= z_{b_{max}} & \text{for } 1.25 < \sqrt{Sh/Sh_{crit}}
 \end{aligned} \tag{25}$$

with the critical Shields parameter Sh_{crit} and the Shields parameter Sh , whereas



$$z_{b_{max}} = 1.15 \cdot D \quad [26]$$

depends on the diameter D of the object. The critical Shields parameter Sh_{crit} for initial sediment mobilization is evaluated empirically via

$$Sh_{crit} = \frac{0.3}{1 + 1.2d^*} + 0.055[1 - e^{-0.02d^*}] \quad [27]$$

with the dimensionless grain size

$$d^* = d_{50} \sqrt[3]{(s - 1) \cdot \frac{g}{\nu^2}} \quad [28]$$

Here, d_{50} is the median sediment grain size and

$$s = \frac{\rho_s}{\rho} \quad [29]$$

is particle specific gravity. The characteristic time-scale for burial can be calculated as:

$$T = \frac{A_e \cdot Sh^B D^2}{\sqrt{(s - 1)gd_{50}^3}} \quad [30]$$

Here, A_e and B are empirically calculated values, given in (Whitehouse, 1998) as $A_e = 0.095$ and $B = -2.02$. The Shields parameter is calculated as

$$Sh = \frac{\tau}{(\rho_s - \rho)gd_{50}} \quad [31]$$

with the total hydraulic shear stress τ being derived from the shear stresses induced by wave action, τ_w , and the shear stress induced by the current, combined with the mean wave-induced shear stress, τ_m , via

$$\tau = \sqrt{(\tau_m + \tau_w |\cos \varphi_{wc}|)^2 + (\tau_w |\sin \varphi_{wc}|)^2} \quad [32]$$

Several cases are then conceivable for the calculation of τ . Only the case relevant to this study is discussed below. The cases differ fundamentally by the different averaged current velocities \bar{U} and wave orbital velocities U_w . According to this distinction, in some cases the flow is divided into the typical flow regime with the help of special Reynolds numbers (wave Reynolds number and current Reynolds number). Only the fourth case (combined wave and current flow) is relevant to this study; the other cases are listed in detail in (Soulsby, 1997).

Tab. 4: Scheme for the choice of the flow regime to compute the wall shear stress.

1	No flow case ($\bar{U} = 0$ and $U_w = 0$)
	$\tau_m = \tau_{max} = 0$
2	Current-only flow case ($\bar{U} > 0$ and $U_w = 0$)
	↳ $Re_c \leq 2000$ <i>laminar case</i>

$$\tau_m = \tau_{max} = \frac{3\rho v \bar{U}}{h}$$

↳ $Re_c > 2000$ *turbulent case*

$$\tau_{mr} = \rho \cdot c_{dr} \cdot \bar{U}^2, \tau_{ms} = \rho \cdot c_{ds} \cdot \bar{U}^2, \tau_m = \tau_{max} = \max(\tau_{mr}, \tau_{ms})$$

3 Wave-only flow case ($\bar{U} = 0$ and $U_w > 0$)

↳ $Re_w \leq 1,5 \cdot 10^5$ *laminar case*

$$\tau_m = 0, \tau_{max} = \rho \cdot \frac{1}{\sqrt{Re_w}} \cdot U_w^2$$

↳ $Re_w > 1,5 \cdot 10^5$ *turbulent case*

$$\tau_m = 0, \tau_{wr} = \frac{1}{2} \rho \cdot f_{wr} \cdot U_w^2, \tau_{ws} = \frac{1}{2} \rho \cdot f_{ws} \cdot U_w^2, \tau_{max} = \max(\tau_{wr}, \tau_{ws})$$

4 Combined wave and current flow ($\bar{U} > 0$ and $U_w > 0$)

↳ $Re_c \leq Re_{c,crit}$ and $Re_w \leq Re_{w,crit}$ *laminar case*

$$\tau_w = \rho \cdot \frac{1}{\sqrt{Re_w}} \cdot U_w^2, \tau_{max} = \sqrt{(\tau_m + \tau_w |\cos \varphi_{wc}|)^2 + (\tau_w |\sin \varphi_{wc}|)^2}$$

↳ $Re_c > Re_{c,crit}$ or $Re_w > Re_{w,crit}$ *turbulent case*

- $\tau_{max,r} \leq \tau_{max,s}$ a smooth turbulent wave-plus-current shear-stress flow
- $\tau_{max,r} > \tau_{max,s}$ rough-turbulent wave-plus-current shear-stresses flow

To distinguish between the laminar and the turbulent case in Tab. 4, different Reynolds numbers are used. Here, the current-Reynolds number

$$Re_c = \frac{\bar{U} \cdot h}{\nu} \quad [33]$$

and the wave Reynolds number

$$Re_w = \frac{U_w^2 \cdot T_w}{2\pi \cdot \nu} \quad [34]$$

are defined. The corresponding critical values for the current Reynolds number

$$Re_{c,crit} = 2000 + (5.92 \cdot 10^5 \cdot Re_w)^{0.35} \quad [35]$$

and the wave Reynolds number



$$Re_{w,crit} = 1.5 \cdot 10^5 \quad [36]$$

are used. In this study, the flow is turbulent and is therefore described in more detail. Thus τ_m and τ_w can be calculated as

$$\tau_m = \rho \cdot c_{d,max} \cdot \bar{U}^2 \quad [37]$$

and

$$\tau_w = \frac{1}{2} \rho \cdot f_{wr} \cdot U_w^2 \quad [38]$$

with the maximum grain drag coefficient

$$c_{d,max} = \sqrt{\left[\left(c_{d,mean} + T_3 \cdot \frac{U_w}{\bar{U}} \cdot \sqrt{\frac{f_{wr}}{2}} \cdot |\cos \varphi_{wcl}| \right)^2 + \left(T_3 \cdot \frac{U_w}{\bar{U}} \cdot \sqrt{\frac{f_{wr}}{2}} \cdot |\sin \varphi_{wcl}| \right)^2 \right]} \quad [39]$$

and the wave friction factor for rough turbulent flow

$$f_{wr} = 1.39 \left(\frac{U_w \cdot T}{2\pi \cdot z_0} \right)^{-0.52} \quad [40]$$

The coefficient T_3 in Eq. [39] will be treated later. The bed roughness length

$$z_0 = \frac{d_{50}}{12} \quad [41]$$

is derived from the mean grain size d_{50} . The mean grain drag coefficient in Eq. [39]

$$c_{d,mean} = \left[\sqrt{A_1^2 + A_2} - A_1 \right]^2 \quad [42]$$

is derived, using the coefficients

$$A_1 = \frac{T_3 \cdot [\ln(T_2) - 1]}{2 \cdot \ln(T_1)} \quad [43]$$

and

$$A_2 = \frac{0.40 \cdot T_3}{\ln(T_1)} \quad [44]$$

The used coefficients



$$T_1 = \max \left\{ a_r \cdot \sqrt{\frac{f_{wr}}{2}} \cdot \left(\frac{A}{z_0}\right), 12 \right\} \quad [45]$$

with

$$a_r = 0.24, \quad [46]$$

$$T_2 = \frac{h}{T_1 \cdot z_0} \quad [47]$$

and

$$T_3 = \left[(c_{dr})^2 + \left(\frac{f_{wr}}{2}\right)^2 \left(\frac{U_w}{\bar{U}}\right)^4 \right]^{1/4} \quad [48]$$

with the grain drag coefficient for the rough turbulent flow

$$c_{dr} = \left[\frac{0.40}{\ln\left(\frac{h}{z_0}\right) - 1} \right]^2 \quad [49]$$

are derived.

3.6.2 DRAMBUIE 3.0

DRAMBUIE 2.0 already is able to predict the burial by currents and waves. In the new approach, both fundamental part, the equilibrium burial model and the time evolution model were improved.

3.6.2.1 Time evolution model

As the time evolution model is of critical importance, this was improved significantly by implementing the empirical equations proposed by (Friedrichs, et al., 2018) as shown in Tab. 5. Here, the characteristic time-scale for burial still is calculated from Eq. [30]

Tab. 5: Equations to predict the equilibrium burial depth (Friedrichs, et al., 2018).

1 No flow case ($\bar{U} = 0$ and $U_w = 0$)		
$z_{b\infty} = 0$		
2 Current-only flow case ($\bar{U} > 0$ and $U_w = 0$)		
Cylinders with $D < 2.6$ cm	$Sh < 0.038$	$z_{b\infty} = 2800 \cdot D \cdot Sh^{2.6}$
	$Sh \geq 0.038$	$z_{b\infty} = 3.4 \cdot D \cdot Sh^{0.54}$

Cylinders with $D \geq 8.6$ cm	$Sh < 0.042$	$z_{b\infty} = 830 \cdot D \cdot Sh^{2.4} \cdot 0.89 \cdot s_{obj}^{0.12}$
	$Sh \geq 0.042$	$z_{b\infty} = 1.3 \cdot D \cdot Sh^{0.36} \cdot 0.89 \cdot s_{obj}^{0.12}$
Spheres	$Sh \geq 0.04$	$z_{b\infty} = 1.1 \cdot D \cdot Sh^{0.36}$
3 Wave-only and wave-current flow case ($\bar{U} = 0$ and $U_w > 0$)		
Cylinders	$\cos \alpha_{obj} > 0.6$	$z_{b\infty} = 0.1 \cdot D \cdot (KC^{0.51}) \cdot \exp\left(-1.1 \cdot \left(\frac{\bar{U} \cdot \cos \varphi_{wc} }{U_{wc}}\right)\right) \cdot \exp\left(-3.4 \cdot (\cos \alpha_{obj} - 0.6)\right) \cdot 1.8 \cdot Sh^{0.33}$
	$\cos \alpha_{obj} \leq 0.6$	$z_{b\infty} = 0.1 \cdot D \cdot (KC^{0.51}) \cdot \exp\left(-1.1 \cdot \left(\frac{\bar{U} \cdot \cos \varphi_{wc} }{U_{wc}}\right)\right) \cdot 1.8 \cdot Sh^{0.33}$
Tapered cylinders	$\cos \alpha_{obj} > 0.6$	$z_{b\infty} = 0.1 \cdot D \cdot (KC^{0.51}) \cdot \exp\left(-1.1 \cdot \left(\frac{\bar{U} \cdot \cos \varphi_{wc} }{U_{wc}}\right)\right) \cdot \exp\left(-3.4 \cdot (\cos \alpha_{obj} - 0.6)\right) \cdot 3.6 \cdot Sh^{0.33}$
	$\cos \alpha_{obj} \leq 0.6$	$z_{b\infty} = 0.1 \cdot D \cdot (KC^{0.51}) \cdot \exp\left(-1.1 \cdot \left(\frac{\bar{U} \cdot \cos \varphi_{wc} }{U_{wc}}\right)\right) \cdot 3.6 \cdot Sh^{0.33}$
Conical frustums	$\cos \alpha_{obj} > 0.6$	$z_{b\infty} = 0.0077 \cdot D \cdot (KC^{0.78}) \cdot \exp\left(-1.1 \cdot \left(\frac{\bar{U} \cdot \cos \varphi_{wc} }{U_{wc}}\right)\right) \cdot \exp\left(-3.4 \cdot (\cos \alpha_{obj} - 0.6)\right)$
	$\cos \alpha_{obj} \leq 0.6$	$z_{b\infty} = 0.0077 \cdot D \cdot (KC^{0.78}) \cdot \exp\left(-1.1 \cdot \left(\frac{\bar{U} \cdot \cos \varphi_{wc} }{U_{wc}}\right)\right)$
Spheres		$z_{b\infty} = 0.1 \cdot D \cdot (KC^{0.51}) \cdot \exp\left(-1.1 \cdot \left(\frac{\bar{U} \cdot \cos \varphi_{wc} }{U_{wc}}\right)\right) \cdot 1.4 \cdot Sh^{0.33}$

In Tab. 5, KC is the Keulegan Carpenter number,

$$KC = \frac{U_{wc} T_w}{D}, \quad [50]$$

α_{obj} is the angle of the object main axis relative to U_w , U_{wc} is the maximum combined wave and current velocity and φ_{wc} is the angle between the wave and current direction.

For current-only flows, the shear stress $\tau = \tau_c$ can be estimated as

$$\tau_c = \rho \cdot u_\tau^2, \quad [51]$$

where u_τ is the shear velocity. The latter is related to the current velocity U observed at the height z above the bed as (Friedrichs, et al., 2018)

$$\frac{U}{u_\tau} = \frac{1}{0.41} \cdot \ln\left(\frac{z}{2.5d_{50}}\right) + B_s. \quad [52]$$

In Eq. [52], B_s is an empirical function defined as (Friedrichs, et al., 2018)

$$B_s = 8.5 + \left[2.5 \cdot \ln\left(u_\tau \cdot \frac{2.5d_{50}}{\nu}\right) - 3\right] \cdot \exp\left(-0.121 \left[\ln\left(u_\tau \cdot \frac{2.5d_{50}}{\nu}\right)\right]^{2.42}\right), \quad [53]$$

with the kinematic viscosity of water ν . The threshold value of Sh distinguishing clear-water to live-bed scour conditions was assumed as $Sh = 0.04$ by (Friedrichs, et al., 2018). In the present study, the threshold values have been mathematically derived from the intersection of the relative power laws, resulting in $Sh = 0.038$ for $D < 2.6$ cm and $Sh = 0.042$ for $D \geq 8.6$ cm (Tab. 5). In addition, the equilibrium burial depth depends on the object specific gravity

$$s_{obj} = \frac{\rho_{obj}}{\rho}, \quad [54]$$

for $D \geq 8.6$ cm.

In the case of wave-only and combined wave-current flows, (Friedrichs, et al., 2018) suggested to calculate the total bed shear stress according to Eq. [38] as

$$\tau_w = 0.5 \cdot \rho \cdot f_w \cdot U_{wc}^2, \quad [55]$$

where f_w is the wave friction factor and U_{wc} is the maximum combined wave-current velocity. According to (Friedrichs, et al., 2018), U_{wc} and f_w can be derived as

$$U_{wc} = \sqrt{U_w^2 + \bar{U}^2 + 2U_w\bar{U} \cdot |\cos \varphi_{wc}|}, \quad [56]$$

$$\frac{0.32}{f_w} - 1.64 = \left\{ \ln\left(\frac{6.36f_w^{0.5}A}{2.5d_{50}}\right) - \ln\left[1 - \exp\left(-0.0262 \frac{Re_w f_w^{0.5}}{\left[\frac{A}{(2.5d_{50})}\right]}\right) + \frac{4.71 \left[\frac{A}{2.5d_{50}}\right]}{Re_w f_w^{0.5}}\right]\right\}^2. \quad [57]$$

Here, U_w is the wave orbital velocity, \bar{U} the depth-averaged current flow velocity, φ_{wc} the angle between the wave and current direction and.

3.6.2.2 Time stepping approach

Based on Eq. [24], a time-stepping approach was derived to predict the scour burial time evolution under unsteady flows (Whitehouse, 1998). By assuming a quasi-steady flow over a time interval dt , an increment dz_b can be calculated as



$$\frac{dz_b}{dt} = \frac{p(z_{b\infty} - z_b)}{T \left[-\ln \left(\frac{z_{b\infty} - z_b}{z_{b\infty}} \right) \right]^{\frac{1}{p}-1}}. \quad [58]$$

The scour burial depth can be derived at a certain time t by numerically integrating Eq. [58] as

$$z_b(t) = z_b(t - \Delta t) + \frac{p(z_{b\infty}(t) - z_b(t - \Delta t))}{T(t) \left[-\ln \left(\frac{z_{b\infty}(t) - z_b(t - \Delta t)}{z_{b\infty}(t)} \right) \right]^{\frac{1}{p}-1}} \Delta t. \quad [59]$$

In Eq. [59], Δt is the time step, $T(t)$ is defined in Eq. [30] and $z_{b\infty}(t)$ can be calculated as presented in Tab. 5.

For $t = \Delta t$, given that Eq. [59] cannot be applied, $z_{b\infty}(\Delta t)$ can be evaluated with Eq. [24] (Whitehouse, 1998).

For $t > \Delta t$, all the relevant parameters can be calculated for each time t and Eq. [59] can be applied.

When $z_b(t - \Delta t) \geq z_{b\infty}(t)$, Eq. [59] would lead to meaningless predictions, such that it is assumed $\Delta z_b(t) = 0$ and $z_b(t) = z_b(t - \Delta t)$. Fig. 17 summarises the entire procedure for the calculation of the scour burial evolution of free settling objects, where t_{end} is the duration of the test.

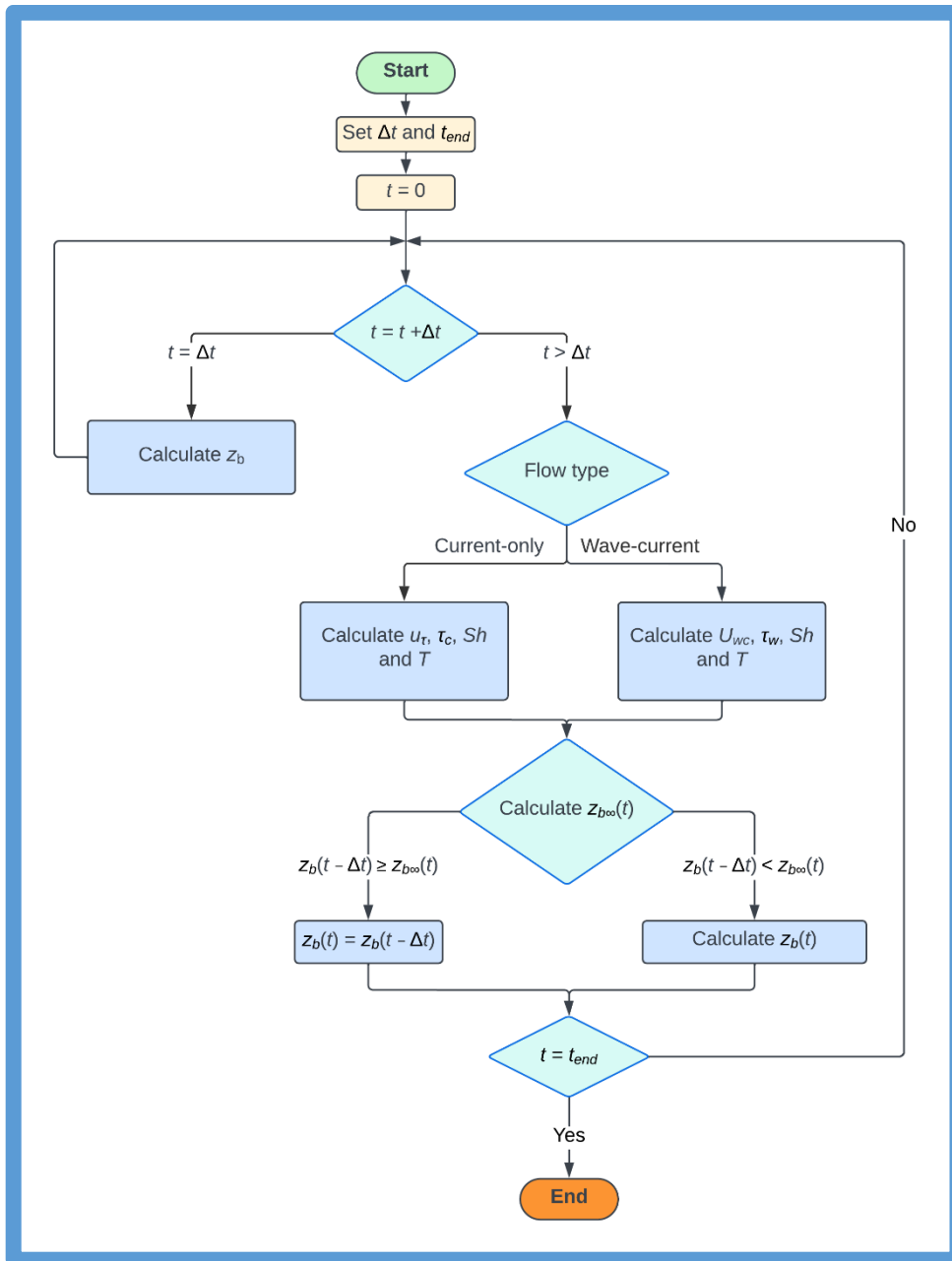


Fig. 17: Procedure to calculate the time series of scour burial depth of free settling objects.

This model has been applied to predict the scour burial depth evolution for 2 tests, investigating the effect of the time resolution (see Fig. 18). The top subfigure of Fig. 18 shows the results for a cylindrical object under a current-only flow with $D = 0.038$ cm, $d_{50} = 0.135$ mm and $s_{obj} = 2.65$. The flow consisted of a reversing current with maximum velocity of 0.29 m/s and period $T_c = 480$ s. On the other hand, the scour depth of a cylinder due to a wave-current flow with $\bar{U} = 0.152$ m/s, wave height $H = 0.131$ m and $T_w = 2$ s is shown in the bottom subfigure of Fig. 18.

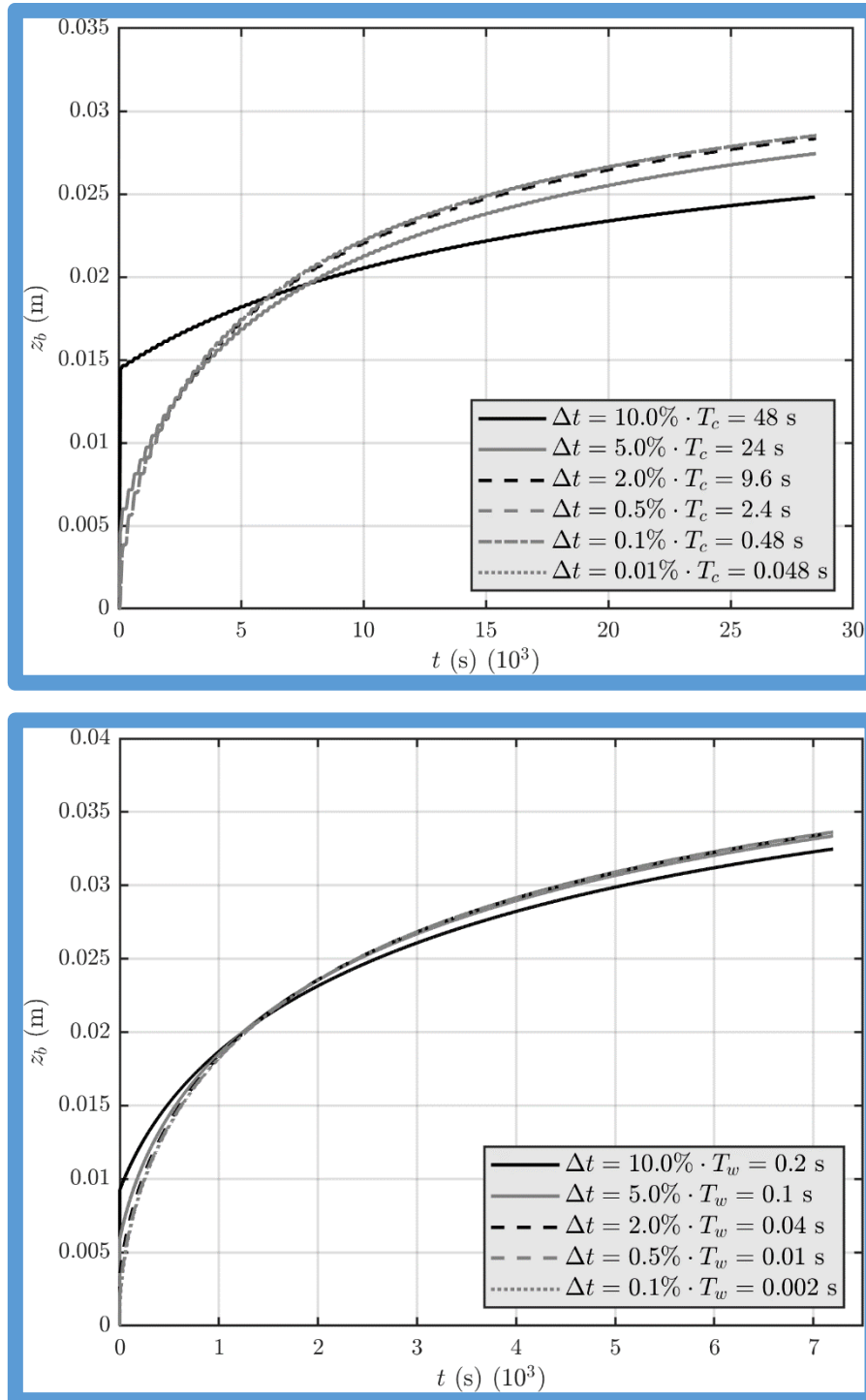


Fig. 18: Example of the scour burial depth evolution for a current-only (top) and wave-current (bottom) flow using several time steps Δt .

The next steps are to compare the burial model with published/unpublished laboratory observations and to reach out to the SERDP community for laboratory and field validation datasets.

3.6.2.3 Equilibrium burial model using ANNs

As part of this project an Artificial neural network (ANN) model capable of predicting the equilibrium burial of UXOs was developed. The advantages of the machine learning algorithms are threefold:

1. Has the tendency to pick up physical processes such as backfilling due to wave action.
2. Can easily be updated by including additional training data-sets as they become available.
3. While most existing models provide envelope predictions, the current model provides a best fit prediction which can be used for probabilistic predictions.

In the present study, machine learning algorithms were utilised to develop prediction models to predict the equilibrium burial depth of UXOs. The prediction models were developed using both Gaussian process regression (GPR) algorithm as well as the multi-layer perceptron neural network (MLPNN). For each machine learning algorithm, two types of prediction models were trained using non-dimensional predictors and dimensional predictors respectively. As part of feature selection, a sensitivity analysis was performed to evaluate the relative importance of the non-dimensional and dimensional predictors. The influence of various proportions of data partitioning on the model performance was investigated as well.

Correlation analysis is an instrumental component of the feature selection process used for optimising the feature space. In particular, reducing the dimensionality of the feature space will lower the computational cost required to train machine learning models. Moreover, proper feature selection can also yield better performing models (Li, et al., 2017). Therefore, it is useful to understand the correlation between various predictors and targets in order to identify the variables that should be omitted from the training process. To that end, the Pearson correlation coefficient provides an indication of the direction and strength of the linear relationship between two sets of variables (Zhou et al., 2016). The correlation coefficient ranges from -1 to 1, where a coefficient of 1 indicates strong positive correlation between two variables, while a coefficient of -1 indicates strong negative correlation. Since predictors with strong linear correlation can be expressed by each other, omitting either one of them will help to reduce the dimensionality of the feature space. The mathematical formulation of the Pearson correlation coefficient (r) is used and the correlation matrix in Fig. 19 is the outcome of the analysis.

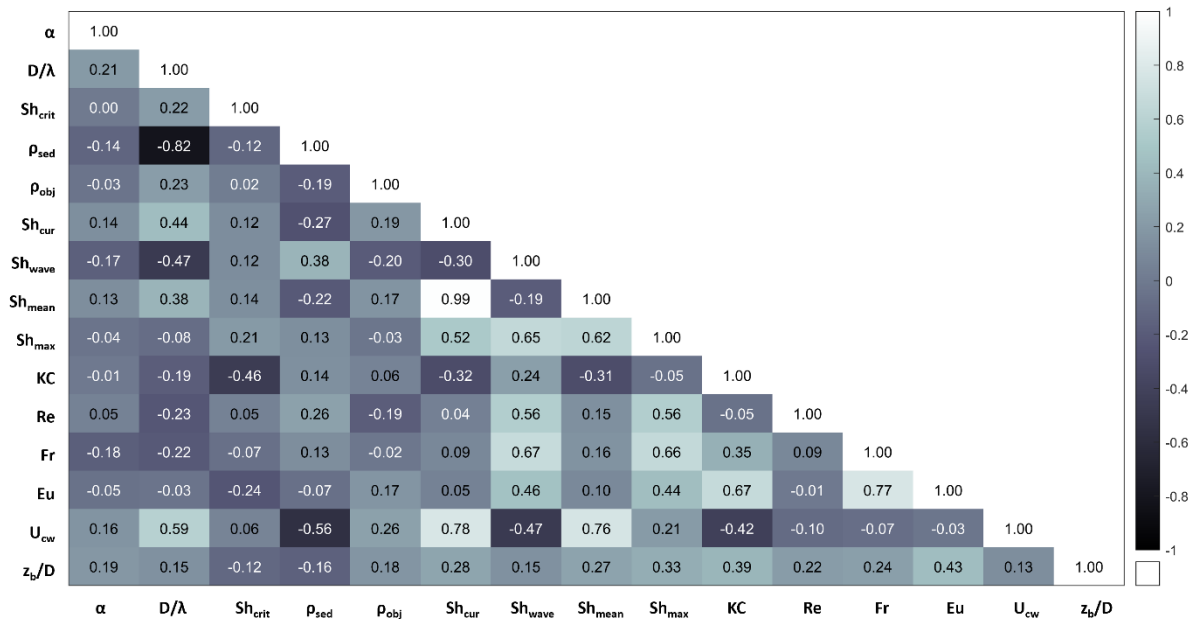


Fig. 19: Correlation analysis between all considered variables.

As shown in Fig. 19, the correlation analysis based on the Pearson correlation coefficient reveals that there is strong linear correlation between the variable pairs:

- $Sh_{mean} - Sh_{cur}$
- $Sh_{max} - Sh_{wave}$
- $Sh_{max} - Sh_{cur}$
- $Fr - Sh_{max}$
- $Fr - Sh_{wave}$
- $Eu - Fr$
- $Eu - KC$
- $U_{cw} - Sh_{cur}$
- $U_{cw} - Sh_{mean}$

Based on the information above and the fact that

$$Sh_{mean} \text{ and } Sh_{max} = f(Sh_{wave}, Sh_{cur}),$$

Sh_{wave} and Sh_{cur} can be discarded as input variables as the remaining variables that have strong correlation pairs are ultimately a function of these two variables. Further it can be observed that the following pair of variables have very low correlation with the target output (z_b/D):

- Sh_{crit}
- ρ_{sed}
- This is due to the limited range of sediments tested throughout all of the acquired data sets which used sediment with very similar densities and median diameters. Despite this, the critical shields number (Sh_{crit}) was included in the final ANN architecture to provide the ability for the model to be re-trained once additional datasets with larger sediment property variations become available. The final observation is that the predictor with the strongest correlation to the target is Eu which is the non-dimensional form of the pressure gradient induced by the flow on the UXO. The pressure gradient around a cylinder can be determined using the approach described in (Tavouktsoglou, et al., 2017).

Based on the above, the machine learning training process makes use of the following variables:

$$\frac{z_b}{D} = f\left(\alpha, \frac{D}{\lambda}, \rho_{obj}, Sh_{max}, Sh_{mean}, Sh_{crit}, KC, Eu, Re, Fr\right) \quad [60]$$

The results of this exercise revealed that the prediction models developed with the GPR algorithm have significantly better performance as compared to the MLPNN models. Additionally, the performance of the GPR models trained with non-dimensional predictors was significantly superior to the GPR models trained with dimensional predictors. The best performing non-dimensional GPR model was able to produce reliable burial predictions under current, wave-current and wave-only regimes (Fig. 20).

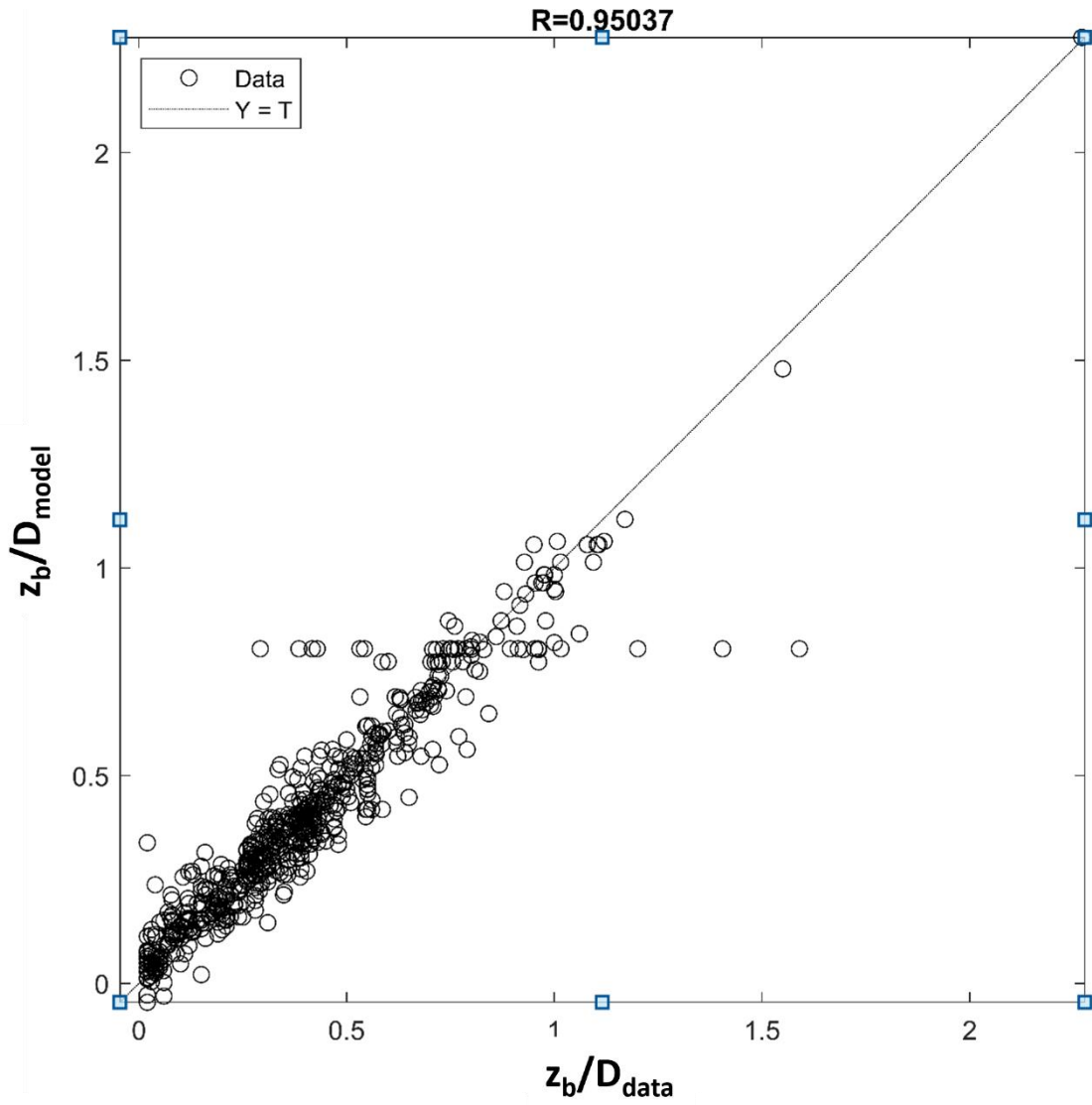


Fig. 20: GPR model performance

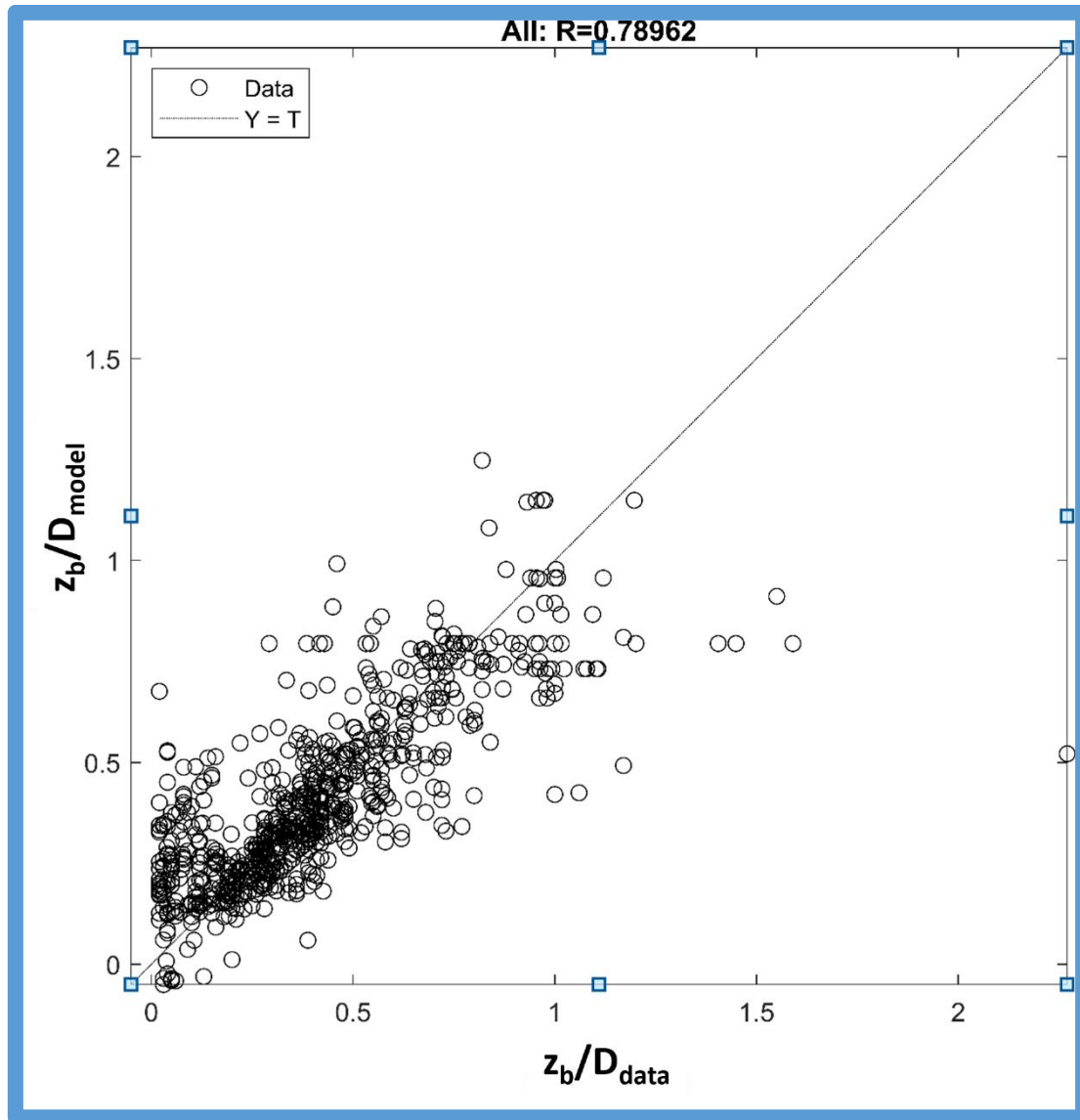


Fig. 21: MLPNN model performance

The derived ANN GPR model was further validated:

1. By comparing the model against existing prediction models; and,
2. Against a reserved dataset that was not used for training purposes.

The present ANN model was compared to three well empirical models that have been extensively tested and validated in literature. These are:

- DRAMBUIE 2.0
- (Cataño-Lopera, et al., 2007). Which is an empirical model derived based on experimental data for waves and currents
- (Voropayev, et al., 2003). Which is an empirical model derived based on experimental data for waves and currents.

The results of the comparison are presented in Fig. 22 and Fig. 23. The figures show the burial depth predicted by the different models for an increasing wave height and no current (Fig. 22) and a 0.4 m/s current imposed (Fig. 23). The results show that the present model follows the

same general trend as the existing models although it has a tendency to produce smaller burial depth values. This is because the aforementioned empirical models are calibrated to produce envelope predictions while the current model yields best fit predictions.

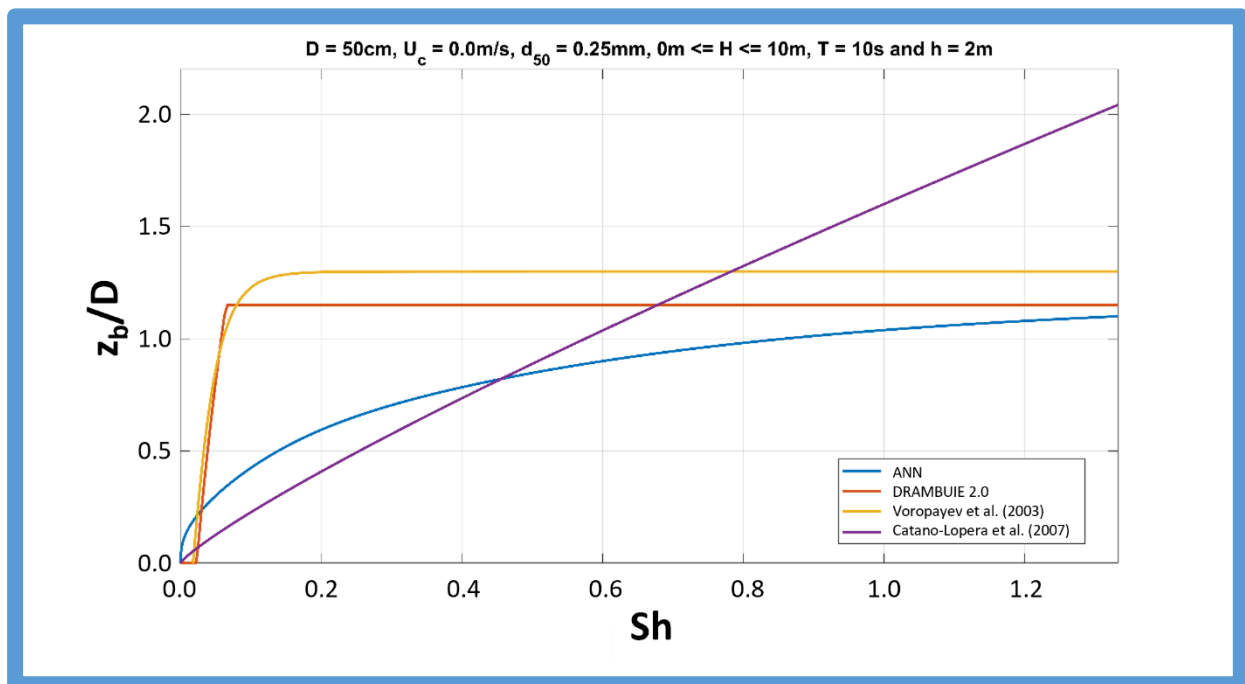


Fig. 22: Comparison of existing ANN model against existing empirical models for an increasing wave height and no current.

Fig. 23 presents the effect an imposed current would have on the burial. An interesting outcome of the ANN is that it shows a reduction of the burial depth for small wave heights. This behaviour is consistent with scour observations around marine structures which suggest that small amplitude wave trains have the ability to backfill scour holes thus reducing the overall scour depth.

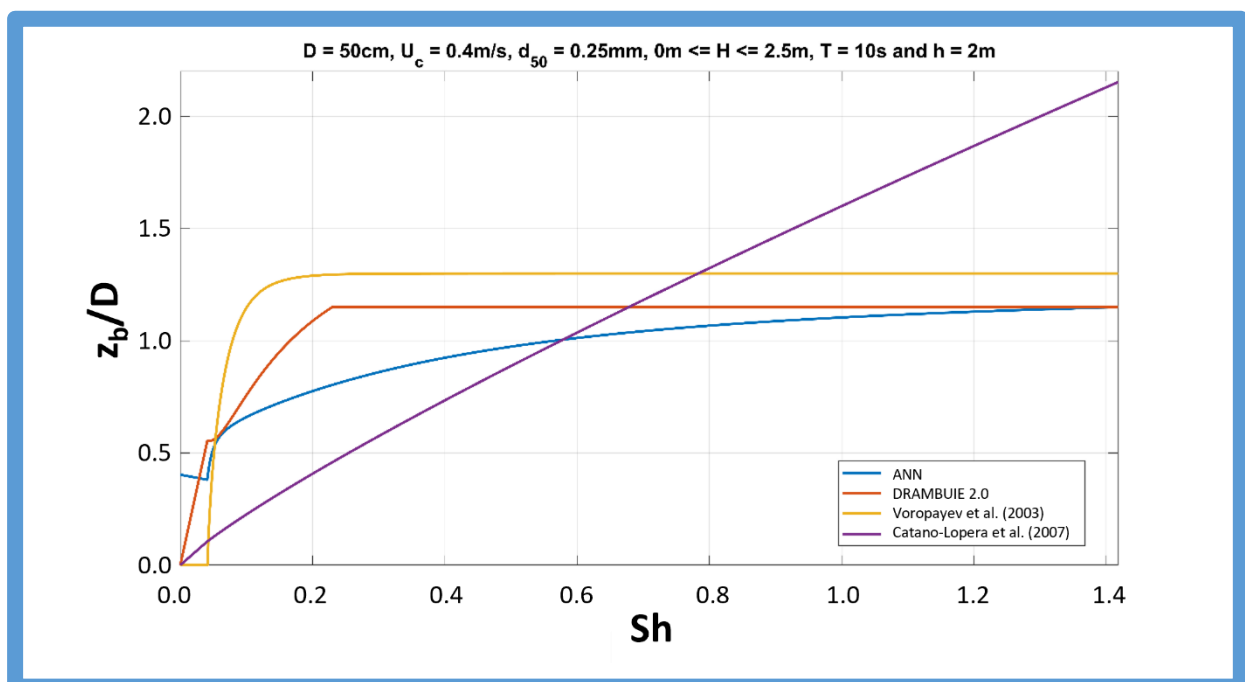


Fig. 23: Comparison of existing ANN model against existing empirical models for an increasing wave height and a 0.4 m/s current

Fig. 24 and Fig. 25 show the effect an increasing wave height and wave period have on the equilibrium burial of UXOs. The predictions of the ANN show good agreement with the validation dataset with the model predicting well for small wave heights and slightly overpredicting for higher wave heights.

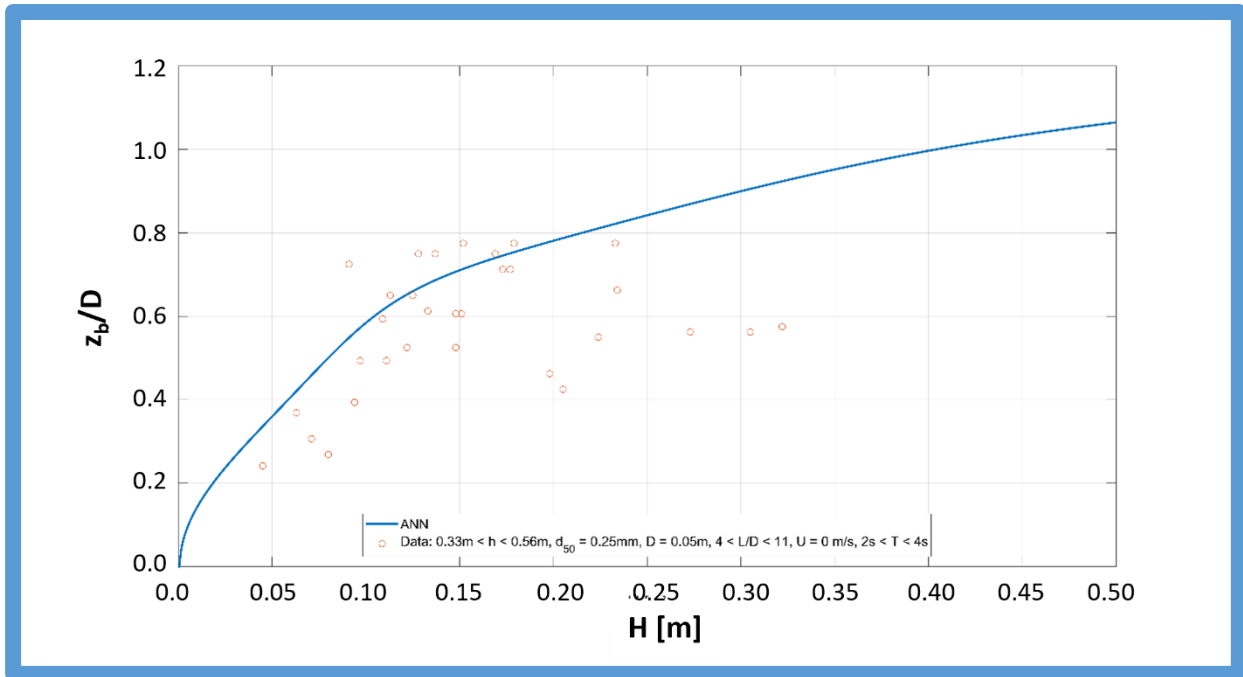


Fig. 24: Comparison of existing ANN model against dataset reserved for validation. Effects of increasing wave height

Similarly to Fig. 24, Fig. 25 presents the predictions of the ANN for an increasing wave period. With the exception of one outlier the ANN predicts the burial accurately for wave periods smaller than 4 s while for larger periods tends to overpredict the burial.

As can be concluded, the model tends to reduce in accuracy for larger values of wave height and period. This is explained by the low density of training data associated with these values. Future experimental campaigns targeting these data ranges would help reduce the accuracy of the model.

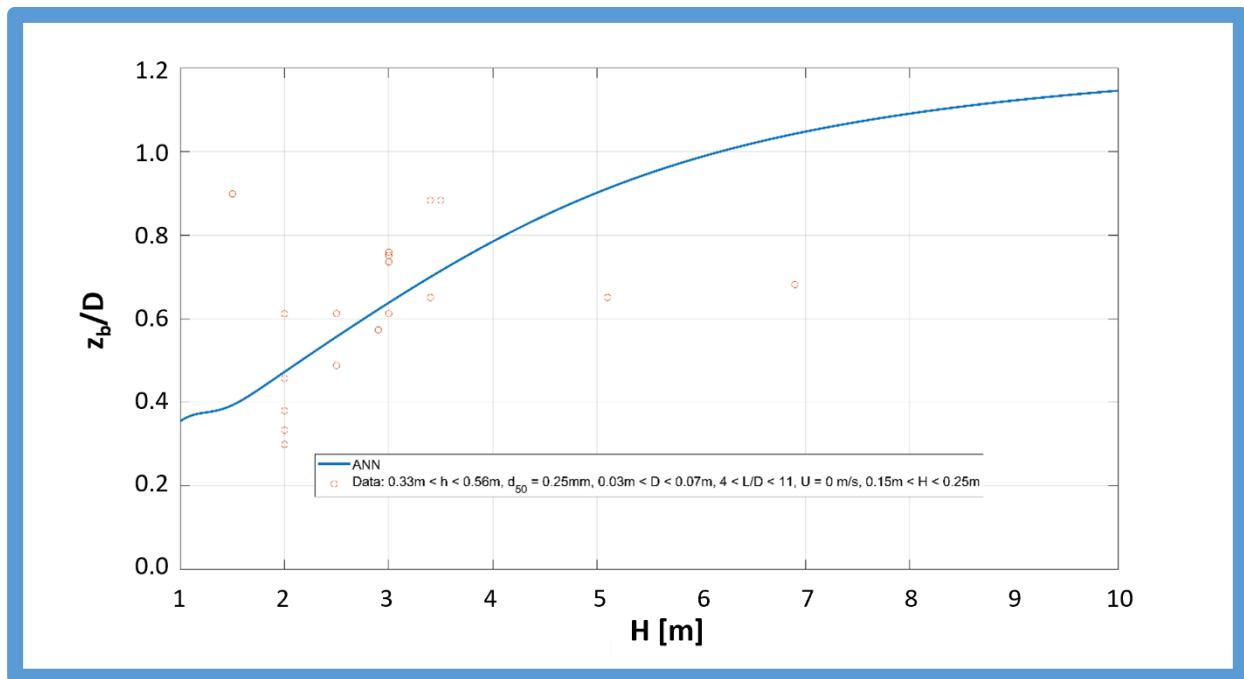


Fig. 25: Comparison of existing ANN model against dataset reserved for validation. Effects of increasing wave height

3.7 Analyzing the existing models

This section of the report discusses the general parameters of scour burial and object mobilization models. Models for object burial and mobilization/migration were analyzed previously in the IEEE Special Issue (Wilkins & Richardson, 2007), (Friedrichs, et al., 2016), (Rennie, et al., 2017) and Menzel et al. (Menzel, et al., 2018) (Menzel, et al., 2019). An updated listing of models is under preparation formed around a classification procedure that places the intercomparison of models on a common set of variables and definitions. This is required to allow a systematic cross-comparison of the models.

The existing munitions burial and migration literature has been reviewed to provide a cross-cutting basis for the improvement of the burial model DRAMBUIE (Whitehouse, 1998) in the combined burial and mobilization model.

To achieve a common basis of comparison for the models, and to ensure a broad field of comparison, the key variables have been worked up during the first year of the project and summarized as follows.

The **Model type** is subdivided into two categories of burial and mobilization, with a third category of migration for those mobilization models that track the movement of objects once they have been mobilized.

The **Object type** covers the main shape categories of cylinder, bomb, sphere, tapered cylinder and conical frustum, with another category for objects not covered.

For the **Burial model (BM)**:

BM1-Process: this covers the type of model whether it is an impact model, scour burial or liquefaction model, i.e. local processes leading to change of elevation of the object with



respect to the seabed, and external processes independent of the object related to the movement of the shoreline and migration of bedforms.

BM2-Forcing: this covers the driving forces for the burial process. For scour burial unidirectional currents, tidal (reversing) currents and surface waves, with or without currents in addition, can all create sediment transport on the seabed, flow interaction with the object and local scouring. As well as leading to scour burial, waves and breaking waves may also promote liquefaction of the seabed which reduces the bearing capacity of the soil. At the shoreline the swash zone experiences shallow oscillatory flows which may promote burial. In environments with soft soils and no forcing by waves or currents, the object may settle into the bed due to gravity alone.

BM3-Basis: this relates to whether the burial model is deterministic, i.e. it takes a single input of (e.g.) current or wave operating for a specified period of time to predict the burial degree after that time. Alternatively, it may be a model that predicts the maximum burial after a very long period of time as a target burial depth without a time development component that restricts the degree of burial. Alternatively, a time-varying model is one where there is a continuously varying time-series of wave, current and water level inputs driving the scour evolution. This type of model utilizes a target maximum scour depth predictor and an expression for the burial timescale which are both a function of the Forcing. A time-varying model would then sum up the changes in scour resulting from the changes in Forcing, and knowledge of the changing position of the object during the scour evolution.

BM4-Object density explicit: As well as key variable related to the dimensions and shape of the object, the density (or specific gravity) is a key variable as it can alter the way the object relates to the burial process. Light (low density) objects are less likely to become buried than heavy (high density) objects.

BM5-Object orientation to flow: This relates to the direction the object is heading with respect to the direction the forcing is approaching the object. When the object (such as a cylinder) is at 90 degrees to the flow (i.e. with maximum projected area to the flow) the blockage will be maximized and the scour process will be more vigorous than when the object is flow aligned (0 degrees to the flow). If the object is not buried initially then it may maximise its projected area to the flow (Munk moment).

The initial heading at the start of the period of Forcing is a key variable, although during the scour burial process non-cylindrical shaped objects (e.g. tapered cylinders) may adjust their angle as the scour process develops asymmetrically at both ends. Of course, related to the implementation of a combined Burial and Mobilization model, if the object is mobilized it can change its position and heading. A variable orientation based on the Forcing heading and object response may be required in a time-varying Burial model.

BM6-Soil: The main categories of soil considered are granular and cohesive soils. Both categories can contain mixtures of grain sizes depending on the environment of deposition from which they originated and on the deposition history. Cohesive soils will experience different degrees of self-weight consolidation and compaction that effect the inherent shear strength of the soil. With granular soils, the veneer thickness overlying stiffer cohesive soils or rock may provide a limit on Object burial depth requiring more complex input data on Soil for the model.



BM7-Morphology: This variable relates to the inherent sediment transport environment sands forming rippled bed morphology under wave and current Forcing. Flat bed morphology is potentially more prevalent in laboratory conditions than the field, although storm conditions may lead to ripple wash out in the sheet flow regime associated with intense near-bed sediment transport during the storm, with ripples likely to reform on the waning energy phase of the storm. Megaripples and dunes are more likely to form in current dominated environments but can be modified during storms, reforming again during the post-storm current dominated environment once again. On the shoreface there will be a range of features, firstly the main nearshore profile and secondly bars and berms of various shapes and sizes providing periodic features at different locations on the mean profile. The key role of morphology is to provide modulation of current and wave fields and to provide time-varying global changes in bed elevation external to the local scaled forcing-object-sediment interaction.

BM8-Scour feature: The nature of the burial model varies and may capture different features of the scour associated with the object. A key variable that is required is the scour depth at the object as this will control the potential for lowering below the bed. The lateral extent of the scour profile around the object will influence the degree of sheltering that is experienced and will be controlled by the Forcing, its heading with respect to the Object orientation of the flow to the object interaction and the angle of friction of the Soil. If a complete description is included of the depth and extent with a shape then the scour feature is described by its profile.

BM9-Object settlement: This variable in the classification relates to the interaction between the Process model, for scour for example, which changes the elevation of the bed around the Object. The model may predict the scour formation around the Object and assume the lowest elevation of scour and settlement of the Object tracks down at the same rate, or include a more complex process of scour and settlement as coupled but distinct processes. This means the scour process may be continuous whereas the settlement can take place in a step-wise or continuous fashion.

BM10- Soil failure process: The scour burial process takes place by settlement of the object into the Soil. The way this takes place may be parameterized in terms of the Object density and the Soil response due to bearing capacity under the Object due to Scour reducing the contact area or Liquefaction providing loss of bearing capacity and sinking of an Object into the Soil when the specific gravity of the Object exceeds the specific gravity of the (partially) liquefied Soil.

BM11-Validated: The Burial model may be validated with laboratory and/or field data that was not used in the original determination of the model. Validation data is important as it demonstrates the model performance under different test conditions, and for models based on the parameterization of the results of laboratory experiments the comparison with field data can be used to confirm the margins of the model and their applicability in real world scenarios.

For the **Mobilization model (MM):**

MM1-Forcing: this covers the driving forces for the mobilization process. Forcing may be applied by unidirectional currents, tidal (reversing) currents and surface waves, with or without currents in addition. Waves and breaking waves may be asymmetric in shallow water and in the swash zone with characteristically faster forward flow under the crest but potentially smaller but longer duration trough associated flows. At all times on a sloping bed associated



with the Morphology, whether during flow Forcing events or during low energy periods, the force of gravity may modify or cause Mobilization on a downslope portion of the seabed.

MM2-Basis: this relates to whether the Mobilization model is deterministic, i.e. it takes a single input of (e.g.) current or wave of specified magnitude to predict whether an Object of known properties can be mobilized by overcoming the Resistance.

Alternatively, a time-varying model is one where there is a continuously varying time-series of wave, current and water level inputs to check whether the Resistance is overcome at a given time leading to mobilization of the Object.

MM3-Object density explicit: As well as key variable related to the dimensions and shape of the object, the density (or specific gravity) is a key variable as it alters the susceptibility for mobilization. Light (low density) objects are more likely to move whereas heavy (high density) objects will have more resistance to movement.

MM4-Object orientation to flow: This relates to the direction the Object is heading with respect to the direction the forcing is approaching the object. When the Object (such as a cylinder) is at 90 degrees to the flow (i.e. with maximum projected area to the flow) the applied force will be maximized to overcome the resistance. If the Object is not buried initially and not at 90 degrees then it may maximize its projected area to the flow (Munk moment).

Whilst the initial heading at the start of the period of Forcing is a key variable, the scour development may lead to changes in orientation, e.g. for tapered cylinders that may adjust their angle as the scour process develops asymmetrically at both ends. Of course, related to the implementation of a combined Burial and Mobilization model, if the object is mobilized it can change its position and heading. A variable orientation based on the Forcing heading and Object response may be required in a time-varying Burial model.

MM5-Soil: The main categories of soil considered are granular and cohesive soils. The Soils will provide a different interface roughness depending on their grain size population and control the Resistance between the Object and the Soil. For the Mobilization model a specific category of fixed bed is included as this captures studies with concrete beds in the laboratory or rock beds which do not feature in a Burial model but could be a key bed type for mobilization. It could be argued that the fixed bed category (e.g. rock) should be included in the Burial model classification of Soil as burial would not be expected to occur and this would act as a switch-off of that model in areas where rock outcrops at the seabed.

MM6-Morphology: This variable relates to the inherent sediment transport environment, sands forming rippled bed morphology under wave and current Forcing. Flat bed morphology is potentially more prevalent in laboratory conditions than the field, although storm conditions may lead to ripple wash out in the sheet flow regime associated with intense near-bed sediment transport during the storm, with ripples likely to reform on the waning energy phase of the storm. Megaripples and dunes are more likely to form in current dominated environments but can be modified during storms, reforming again during the post-storm current dominated environment once again.

On the shoreface there will be a range of features, firstly the main nearshore profile and secondly bars and berms of various shapes and sizes providing periodic features at different locations on the mean profile. The key role of the morphology is to provide modulation of



currents and wave fields, such that deep water waves or open water currents will need to be transformed to apply in shallow water, and to provide time-varying global changes in bed elevation external to the local scaled forcing-object-sediment interaction.

In some seafloor environments the bed may be net erosional leading to the formation of furrows which will provide a particular configuration for the sheltering of Objects.

MM7-Initial condition: This relates to the configuration of the Object with respect to the seabed profile around the object. This may be specified in terms of percentage of the Object which is buried where the Soil contacts the Object across the whole external area which lies below the seabed. Alternatively the percentage of the Object buried may be specified with a parameterized shape to the scour profile. On hard substrates there may be no burial and hence the Initial condition may be a fixed geometry between the Object and the Soil governed by the type of Object being considered.

MM8-Resistance: The resistance mechanism needs to be described which may be a characteristic of particular Object types on specific assumptions about Morphology and Initial condition. If the Morphology is flat the resistance may be from sliding or rolling, or by overcoming suction forces between the Object and the Soil.

Where the Soil is locally scoured and deposited the Object may gain Resistance from the pivot angle required to lift the Object out of the scour hole. This may be also the case on furrowed beds when the Object is lying within the furrow or if the seafloor roughness is high compared to the characteristic diameter of the Object.

MM9-Mobilization step: The description of the Mobilization step of the model is important as it may be defined in a number of ways. It may be described deterministically by comparing integrated variables of the Forcing such as significant wave height and period and predict whether object movement did or did not occur. This can lead to discrimination of whether a specified wave field can move a specified Object type and density.

More detailed analysis is possible using a phase-resolved approach where the specific profile of wave kinematics is modelled and used to determine whether an individual wave within a specified sea-state can mobilize the Object and if so at what phase through the wave this takes place. A phase-resolving approach is more versatile than the deterministic method but requires more detailed sets of inputs for Forcing.

The extension of the Mobilization step is to model the migration of the object based on the initial configuration and to predict how far and in what direction movement takes place.

MM10-Validated: The Mobilization model may be validated with laboratory and/or field data that was not used in the original determination of the model. Validation data is important as it demonstrates the model performance under different test conditions, and for models based on the parameterization of the results of laboratory experiments the comparison with field data can be used to confirm the margins of the model and their applicability in real world scenarios.

3.8 Combination of the Mobilization and Burial Model

The methods from Sections 3.4, 3.5 and 3.6 were combined in a single software, whereas the input data are delivered via csv-files that contain all environmental data, all object data and

the wave information, which may be delivered as single waves or statistical wave information such as the significant wave height H_s and the peak wave period T_p . For each location, the software runs through all objects and for all objects through all statistical wave entries. From a statistical wave entry, the maximum wave height and the number of single waves is derived to form a time series. In a subsequent development a spectral distribution for the waves is going to be considered. In the model each single wave is discretized into 360 phase angles to compute the individual wave-induced bottom near current velocities. These wave-induced current velocities as well as the background current velocity then are applied in the mobilization model to derive the acceleration and thus the displacement of the object. If the object is not mobilized within the single wave cycle, the burial model is applied to compute a new burial depth. Thus, the mobilization model is applied on a phase resolved basis, whereas the burial model is applied on a single wave basis (i.e. phase-averaged). The process flow of the simulation is shown in Fig. 26.

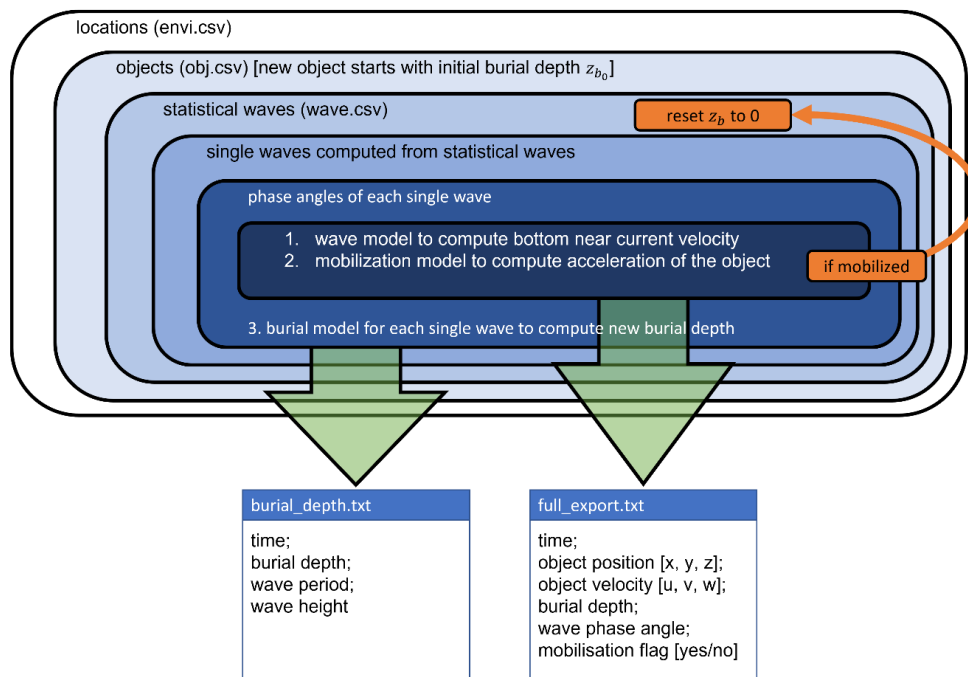


Fig. 26: Process flow of the combined burial-mobilisation-simulation.

Here also the termination criterion is shown. As soon as the object leaves the scour trough, which is defined as a sine-function with a critical slope angle defined in the environmental input file, the simulation will be terminated for the individual statistical wave-entry. As the position of the object is an object specific variable, the simulation then continues with the same object with a burial depth of $z_b = 0$. The assumption here is that the same object may have been mobilized at a very close location and may have migrated to the current position. Thus, the simulation is already prepared to handle spatial analysis and processes of migration, which will be implemented later in the project.

3.9 The Lattice Boltzmann Method (rejected)

During the first phase of the project, the applicability of the Lattice Boltzmann Method (LBM) was investigated. It was shown that the method could be used but still requires massive improvements to keep up with current methods like TELEMAC and Delft3D. Unfortunately,



one of the very rare specialists in the Lattice Boltzmann Method, Dr. Helen Morrison, who was working on this project, left the team in early 2022. As it seemed to be impossible to find an adequate replacement to continue the work without creating a huge delay to the whole project, the decision was made to proceed without Lattice Boltzmann but with TELEMAC. The use of TELEMAC opens several advantages for the project. TELEMAC is already able to simulate the development of waves, entering shallow water and interacting with the seafloor. Furthermore, the system is well tested and widely proved in environmental current, wave and morphodynamics modelling and handling of huge input datasets from operational models. As HR Wallingford is using and developing TELEMAC continuously, the expertise was already available and could be applied to the project very fast without any additional training period. It was thus decided that the resources planned for the Lattice Boltzmann Simulation would now be used for the TELEMAC simulation and a more professional and sustainable implementation of the UXOmob software. Information on the work done on the LBM during the project can be found in Appendix A.

3.10 TELEMAC Simulations

The open source TELEMAC software (version V8p2r0) is used in this work to predict temporal and spatially varying outputs for key parameters including: morphodynamics, sea level variations, and wave characteristics. The model setup consists of the TELEMAC-2D, TOMAWAC and GAIA modelling train, where TELEMAC-2D calculates hydrodynamics, TOMAWAC the waves variables, and GAIA the morphodynamics (Tassi, et al., 2022).

3.10.1 TELEMAC 2D

Water propagation is determined through solution of the continuity equation and the momentum balance equations (Saint-Venant equations). It is assumed that the water is incompressible, the equations are depth averaged and the results correspond to the horizontal plane with its x-axis corresponding to the west-east direction, and the y-axis is the south-north direction. Source terms for these equations are bottom friction, Coriolis force, wind shear, and wave radiation stresses.

$$\frac{\partial h}{\partial t} + u \cdot \nabla(h) + h \operatorname{div}(u) = S_h \quad [61]$$

$$\frac{\partial u}{\partial t} + u \cdot \nabla(u) = -g \frac{\partial z_s}{\partial x} + S_x + \frac{1}{h} \operatorname{div}(h \nu_t \nabla u) \quad [62]$$

$$\frac{\partial v}{\partial t} + u \cdot \nabla(v) = -g \frac{\partial z_s}{\partial y} + S_y + \frac{1}{h} \operatorname{div}(h \nu_t \nabla v) \quad [63]$$

Here, h is the water depth, u and v are the velocity components, g is the gravitational acceleration, ν_t is the momentum diffusion coefficient, z_s is the free surface elevation, t is the time, x and y are the horizontal coordinates, S_h is the source or sink of fluid and S_x and S_y are source terms.

3.10.2 TOMAWAC

Waves are addressed through the spectral approach in the TOMAWAC module. The wave field is modelled through the directional spectrum of wave action balance equation:

$$\frac{\partial N}{\partial t} + \dot{x} \frac{\partial N}{\partial x} + \dot{y} \frac{\partial N}{\partial y} + \dot{k}_x \frac{\partial N}{\partial k_x} + \dot{k}_y \frac{\partial N}{\partial k_y} = Q(x, y, k_x, k_y, t) \quad [64]$$

Where N is the directional spectrum of wave action, the dot over the variables denotes the time transfer rates of each variable, given by the linear wave theory (Cavaleri & Rizzoli, 1981) (Komen, et al., 1996) (Madsen & Sørensen, 1993) (Tolman, 1991), $k = (k_x, k_y)$ is the wave number vector which follows the dispersion relation:

$$\omega^2 = gk \tanh(kh) \quad [65]$$

ω being the intrinsic angular frequency, observed in a coordinate system moving at the velocity of the flow current.

TOMAWAC takes into account the following source terms:

- wind-driven wave generation (Komen, et al., 1996),
- whitecapping dissipation (Komen, et al., 1984),
- bottom friction (Hasselmann, et al., 1973),
- quadruplet interactions (Hasselmann, et al., 1985),
- and depth-induced breaking (Battjes & Janssen, 1978).

The bed shear stress resulting from the waves is calculated following (Jonsson, 1966) and (Toffolon & Vignoli, 2007) with a quadratic law of the form:

$$\begin{aligned} \tau_w &= \frac{1}{2} \rho C_w U_w^2 \\ U_w &= \frac{H_s \omega}{2 \sinh(kh)} \\ C_w &= \begin{cases} 0.3 & \left[\text{if } \frac{U_w T_a}{2\pi} \leq 1.57 \right] \\ \exp \left[-6 + 5.2 \left(\frac{U_w T_a}{2\pi} \frac{1}{k_s} \right) \right] & \left[\text{if } \frac{U_w T_a}{2\pi} > 1.57 \right] \end{cases} \end{aligned} \quad [66]$$

Where, H_s is the significant wave height calculated from the moment of order zero (m_0) of the wave spectrum, T_a is the mean wave period calculated from the moments of order -1 (m_{-1}) and 0 (m_0) of the wave spectrum:

$$\begin{aligned} H_s &= 4\sqrt{m_0} \\ T_m &= \frac{m_{-1}}{m_0} \\ m_0 &= \int_0^\infty \int_0^{2\pi} N \omega \, d\theta \, df \\ m_{-1} &= \int_0^\infty \int_0^{2\pi} \frac{N}{f} \omega \, d\theta \, df \end{aligned} \quad [67]$$

θ and f are the discrete direction and frequency.

3.10.3 GAIA

Suspended sediment transport is modelled in GAIA/SISYPHE through the two-dimensional advection-diffusion equation:

$$\frac{\partial hC}{\partial t} + \frac{\partial huC}{\partial x} + \frac{\partial hvC}{\partial y} = \frac{\partial}{\partial x} \left(h\varepsilon_s \frac{\partial C}{\partial x} \right) + \frac{\partial}{\partial y} \left(h\varepsilon_s \frac{\partial C}{\partial y} \right) + E - D \quad [68]$$

$C = C(x, y, t)$ is the depth-averaged concentration (in % volume), (u, v) are the depth-averaged components of the velocity, ε_s is the sediment turbulent diffusivity. In this work, only non-cohesive sediments are taken into account. Thus the sediment deposition rate can be computed from Krone's law:

$$D_s = w_s C_{zref} \quad [69]$$

w_s is the settling velocity and C_{zref} is the near-bed concentration, evaluated at the interface between the bed load and the suspended load, $z = z_{ref}$. The erosion law is:

$$E_i = \begin{cases} E_{0i} \left(\frac{\tau_b}{\tau_{cei}} - 1 \right) & \text{if } (\tau_b > \tau_{cei}) \\ \tau_{cei} & \text{if } (\tau_b \leq \tau_{cei}) \\ 0 & \end{cases} \quad [70]$$

E_{0i} is the Partheniades constant parameter, τ_b is the bed shear stress, τ_{cei} the critical bed shear stress for erosion parameter. The sediment bed evolution is tracked through the Exner equation:

$$\rho_s (1 - \lambda_p) \frac{\partial (\beta E_m)}{\partial t} + \frac{\partial q_{bx}}{\partial x} + \frac{\partial q_{by}}{\partial y} + S_e - S_d - S_F = 0 \quad [71]$$

and the bed load empirical formulation

$$Q_b = A_b U \left[\left(U^2 + \frac{0.018}{C_D} U_w^2 \right)^{0.5} - U_{cr} \right]^{2.4} \quad [72]$$

When modelling suspended sediment transport. The first variable that depends on the size is the sediment settling velocity. TELEMAC 2D – SISYPHE, make use of the following hybrid formula to account for this:

$$w_s = \begin{cases} \frac{(s-1)gd_{50}^2}{18v} & \text{if } (d_{50} > 10^{-4}) \\ \frac{10v}{d_{50}} \left(\sqrt{1 + 0.01 \frac{(s-1)gd_{50}^3}{v^2}} - 1 \right) & \text{if } (10^{-4} \leq d_{50} \leq 10^{-3}) \\ 1.1\sqrt{(s-1)d_{50}} & \text{else} \end{cases} \quad [73]$$

Which leads to a behaviour, shown in Fig. 27.

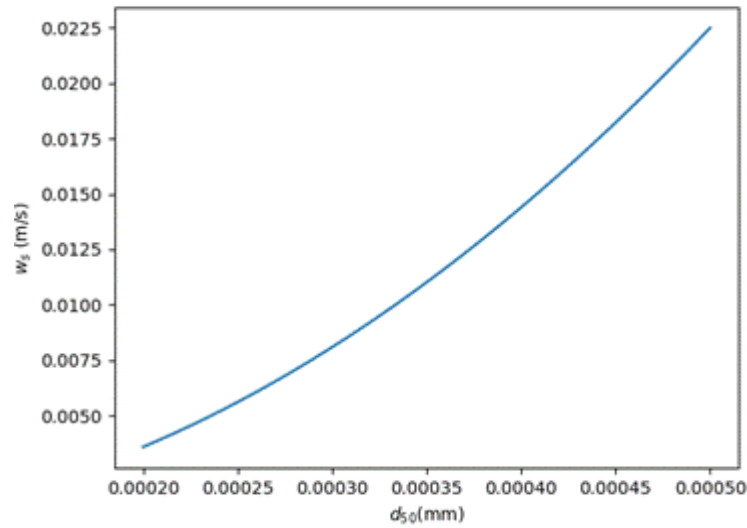


Fig. 27: Computed sediment settling velocity.

The computed settling velocity values are needed to determine the non-dimensional settling lag:

$$\tau = w_s \frac{d_{50}}{D_z} \quad [74]$$

Large particles have large -non-dimensional- lag, as though they have increased drag. The consequence of this is that the ratio between near-bed and depth-average concentration decreases for large particles, meaning these have lower deposition fluxes and remain more time in suspension, which leads in the end to larger suspended sediment concentrations throughout the modelling domain.

$$\beta(\tau) = \frac{2\tau}{\pi} (1 - 2\tau^2)e^{-\tau^2} - E(\tau) + \beta_s D_z w_s^{-2} (4\tau^2 (1 + \tau^2) E(\tau)) \quad [75]$$

3.10.4 Model discretizations

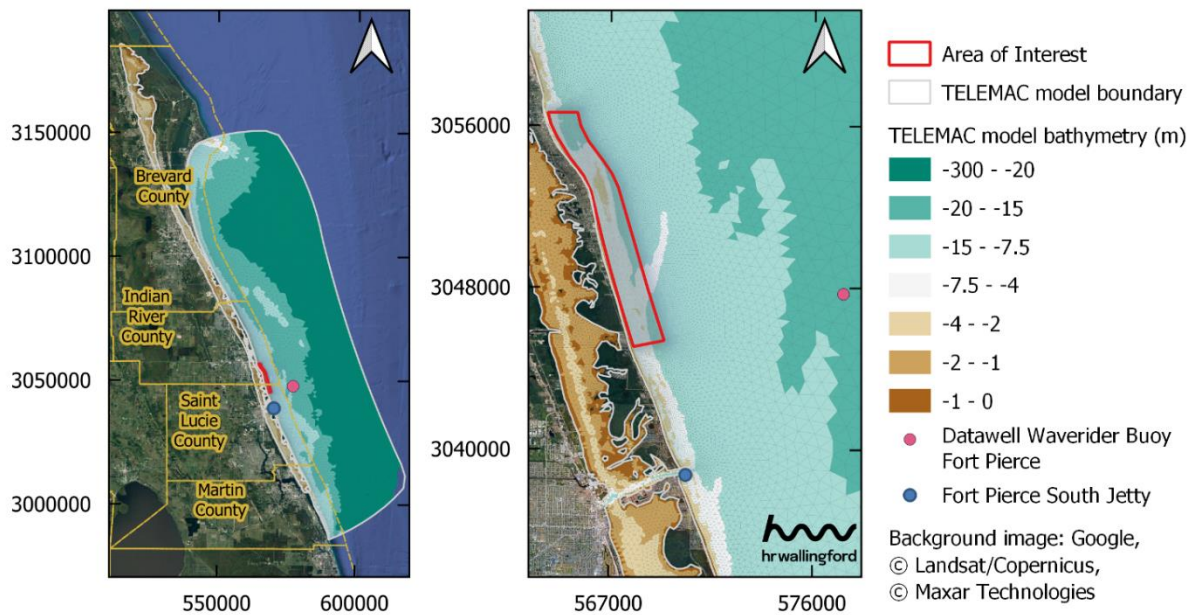


Fig. 28: Model domain and bathymetry.

The bathymetry was derived from datasets available via NOAA’s National Centers for Environmental Information (NCEI) that cover the region in and around the AoI. The area directly within the AoI boundaries and offshore is, for example, included in the “2016 USACE NCMP Topobathy Lidar: Florida East Coast” dataset, which is well resolved at a pixel size of 0.0315’’ x 0.0315’’ (approximately 0.87 m x 0.87 m). The data was recorded using the Coastal Zone Mapping and Imaging Lidar (CZMIL) system, which is able to record both topographic and bathymetric data. For the Indian River Lagoon part of the domain, the bathymetry is derived from the Central Florida 1/3 arc-second NAVD 88 Coastal Digital Elevation Model. Grid spacings for the DEMs range from 1/3 arc-second (~10 meters) to 3 arc-seconds (~90 meters).

The spectral discretization (of the waves module) included 30 frequencies and 24 directions. The discretization frequencies were geometrically distributed with a step that follows the distribution: $f_n = f_1 q^{(n-1)}$. With f_n being the n^{th} discretization frequency, f_1 the first frequency bin (0.04 Hz) and $q=1.1$ the frequential ratio.

3.10.5 Model Setup

The model setup links global-scale atmospheric and hydrodynamic processes with county-scale morphodynamics (see Fig. 29). Free surface water elevations (NAVD88) and flow velocity components were retrieved from the Hybrid Coordinate Ocean Model (HYCOM) (Bleck, 2002), Gulf of Mexico (GoM) regional analysis (experiment_32.5) (Chassignet, et al., 2007), and imposed onto the TELEMAC-2D model open boundary nodes. Spatially varying wind velocities and atmospheric pressure from the European Centre for Medium-Range Weather Forecasts (ECMWF) ERA5 dataset were imposed over each mesh node TELEMACTELEMAC-2D and TOMAWAC models. The offshore wave boundary conditions were also retrieved from the ERA5 dataset. The wave energy was imposed on the boundaries as a two-dimensional wave variance spectrum, variable in time and space, discretised over 30

frequencies and 24 directions. More about the model setup can be found in (Escobar, et al., 2023).

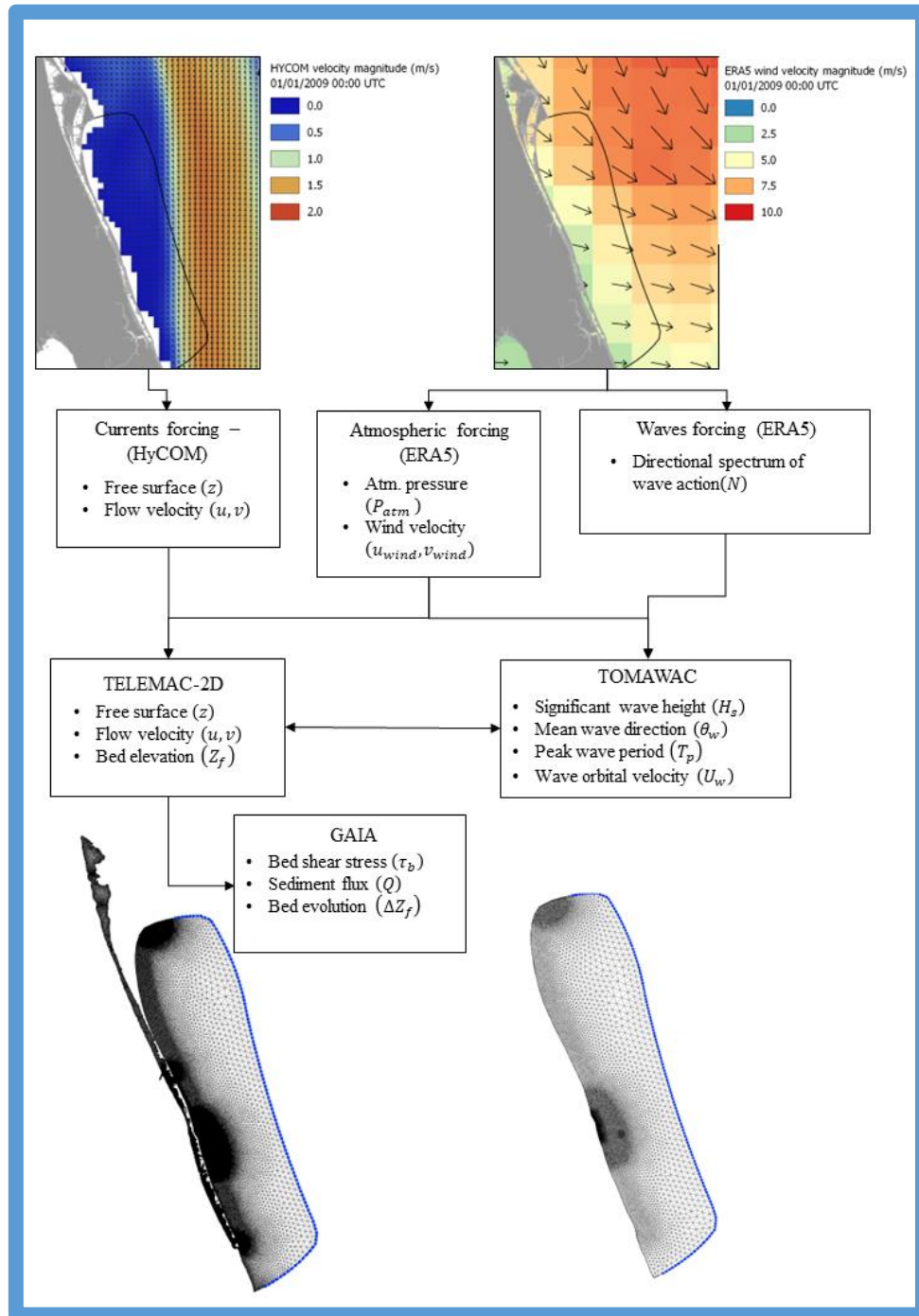


Fig. 29: Model layout. Boundary conditions were retrieved from global currents (HYCOM), wind, air pressure and waves (ERA5) models. These were imposed on the open boundaries (blue lines) of the TELEMAC-2D and TOMAWAC models, which modeled local conditions of the East Coast of Florida.

The bed composition for the model domain is defined by 5 fractions with the grain sizes listed in Tab. 6. These discrete fractions cover the prevalent fine sand-sized quartz to fine gravel-sized sediment of the area (Ousley, et al., 2014). They were derived from particle size distributions reported in the usSEABED (Buczowski, et al., 2020) and the ROSSI (Coor, et al., 2015) databases. Also, the availability of each fraction in space was accounted for through

relative abundance maps calculated from the spatial coordinates of the particle size distributions (Buczowski, et al., 2020) (Coor, et al., 2015). Fig 30 visualises the variation in the mean model grain size based on the modelled fractions.

Tab. 6: Sediment fractions.

Sediment class number	Grain size (mm)	Classification
1	0.05	Silt (non-cohesive)
2	0.15	Fine sand
3	0.30	Medium sand
4	0.60	Coarse sand
5	4.00	Fine gravel

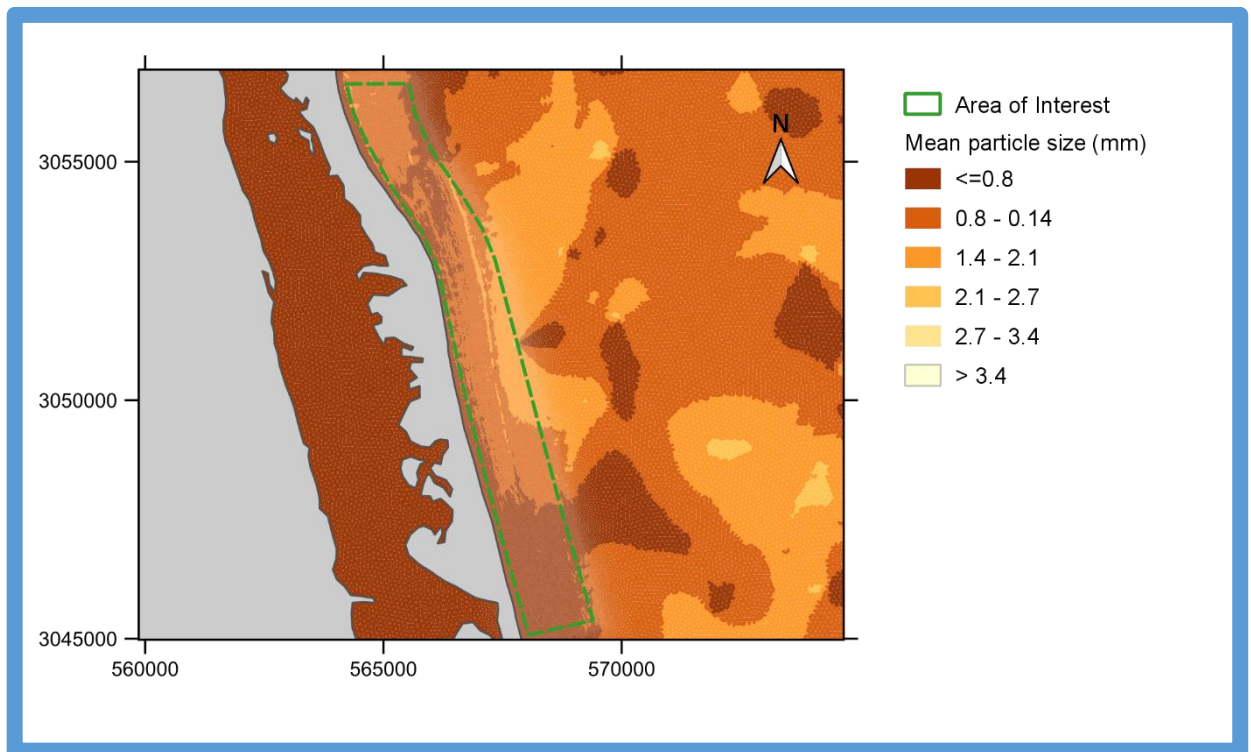


Fig. 30: Model distribution of mean sediment particle size.

3.10.6 Conclusion

A large scale model of the East Coast of Florida was implemented to simulate metocean processes and morphodynamics near Fort Pierce. It was implemented in the TELEMAC software, which is able to simulate the development of waves and currents entering shallow water and interacting with the seafloor. The TOMAWAC module is a third-generation wave model that simulates the generation of waves due to winds and offshore climates, it also

simulates wave propagation into shallow water. The TELEMAC-2D module is a two dimensional in the horizontal (2DH) shallow water flow model that simulates currents in large areas of sea, estuaries and along inter-tidal zones. The GAIA module solves the equations of sediment transport and bed evolution. The coupling of these three modules enables long-term morphodynamics modelling.

3.11 Including migrating bedforms

The seabed morphodynamics were simulated at HR Wallingford using TELEMAC (Section 3.10). The outcome of those simulations are datafiles with spatially resolved time series of morphodynamics, sea level variations, and wave characteristics. The time resolution of those time series is typically in the order of minutes to hours. The time scales of the mobilization calculation (Section 3.5), burial calculation (Section 3.6) and morphology data are depicted in Fig. 31.

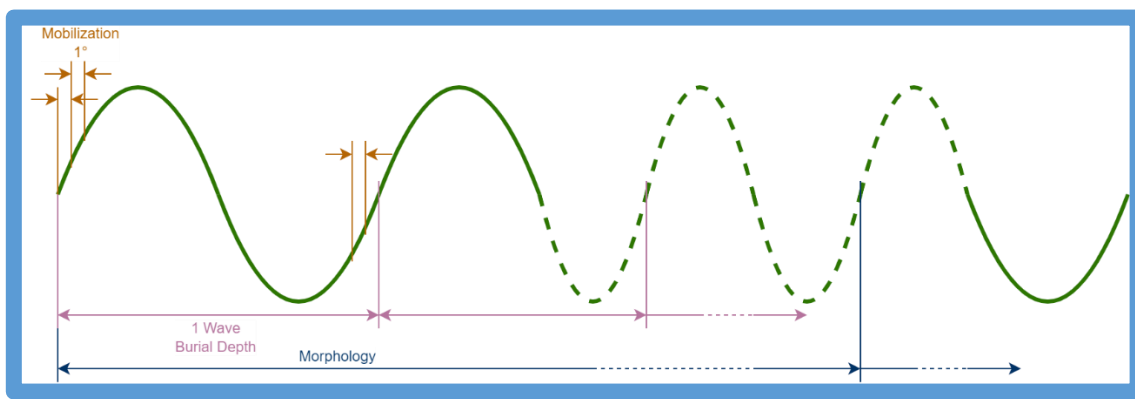


Fig. 31: Time scales of the simulation components.

Matching the timescales of the mobilization and burial calculations to the timescale of the morphology imposes significant challenges due to their large differences. Mobilization and burial simulations need to be integrated over a large period, which significantly increases complexity and computational effort. An overview about influencing parameters and their coordinates is given in Fig. 32.

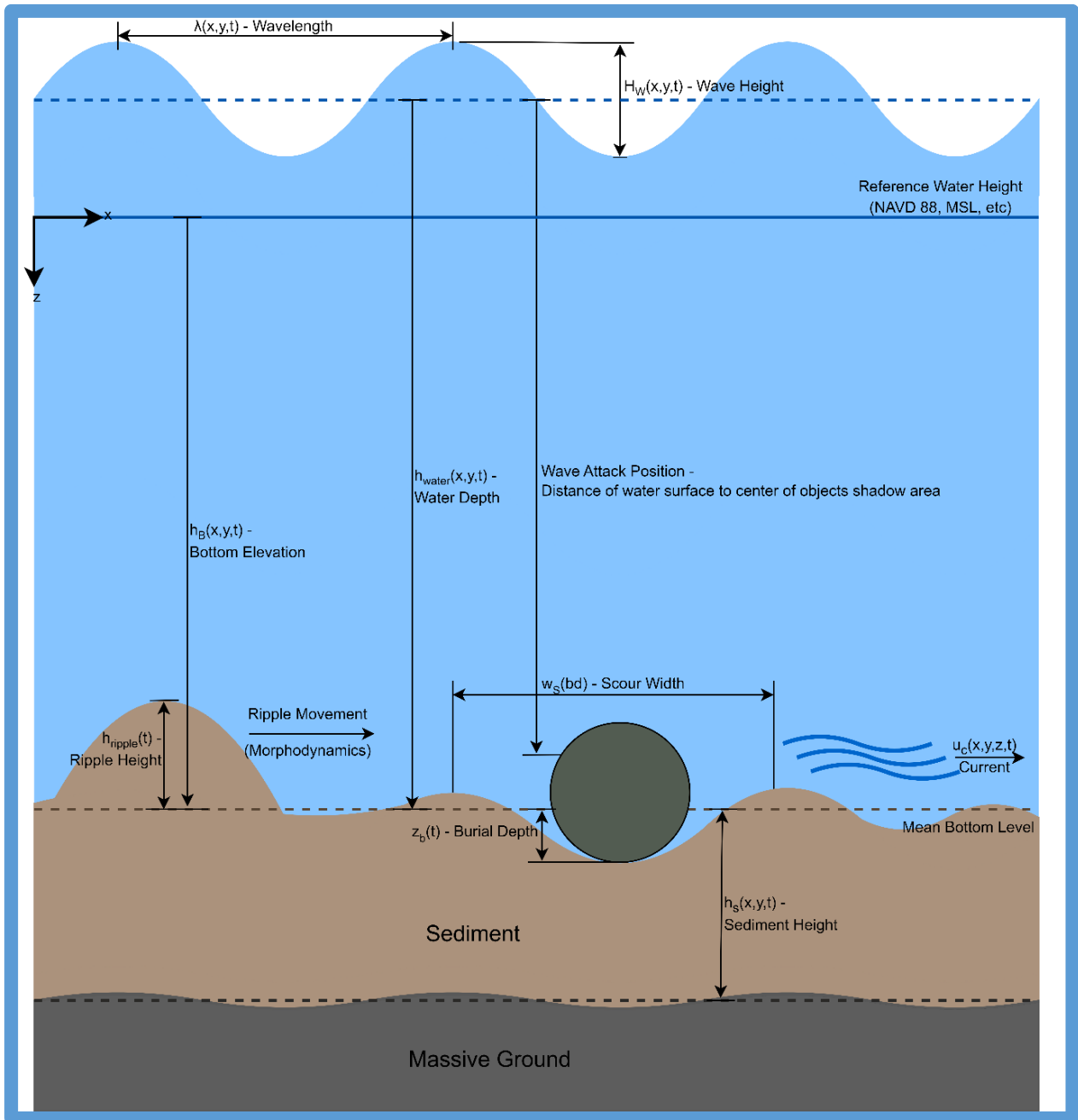


Fig. 32: Coordinates and scales.

Transferring multiple spatially and temporal varying datasets with appropriate resolution imposes challenges on the data transfer. For data exchange the usage of netCDF files has been defined. A netCDF (Network Common Data Form) file is a self-describing data format used for storing multidimensional scientific data. It is a binary file format that allows for efficient access to large amounts of data, while also providing a flexible and standardized way of representing and storing complex data structures. In a netCDF file, data is organized into variables, each of which can have one or more dimensions. The dimensions define the size and shape of the data, while the variables store the actual data values (Fig. 33).

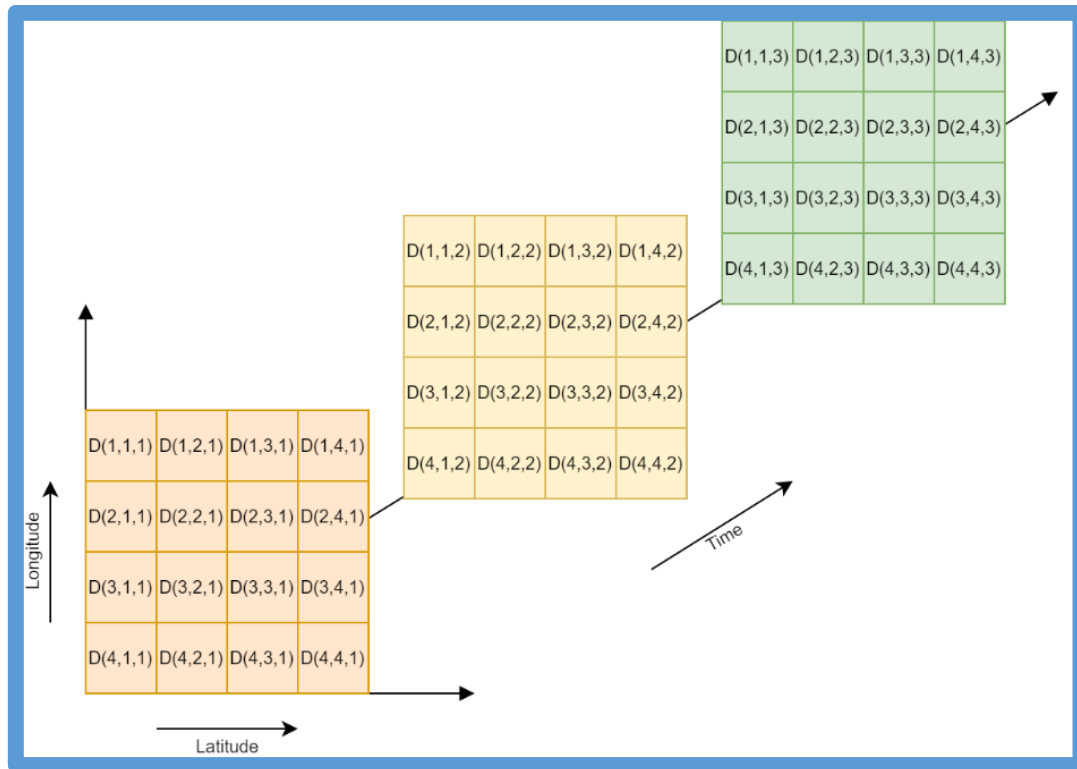


Fig. 33: NetCDF Data Format.

In addition to the data, a netCDF file can also contain metadata, such as units, variable names, and other information that describes the data. The netCDF file used in this project describes at least the morphology (water depth and bottom elevation) over time in a geolocation grid. The dataset also inherits environmental and wave properties.

The simulation starts with modelling the mobilization process at a configurable phase-resolved wave resolution. For each full wave the burial process is simulated (Section 3.8). Subsequently, the current bathymetry is interpolated from the data within the netCDF file (Section 3.13.6.5), applied to the simulation and the entire process recommences with the simulation of the mobilization process.

With an average wave period of 6 seconds, the simulation necessitates the execution of 300 waves and burial processes within the span of 2 morphology data points (with a 30-minute morphology resolution). This translates to 108,000 mobilization calculations within this half-hour window. Extrapolating these figures to a month-long simulation period, the numbers escalate to 155.5 million mobilization calculations and 432,000 burial calculations. Importantly, it's crucial to note that these substantial computations pertain to a singular object at a specific location.

To overcome these computational challenges the algorithms developed in Section 3.8 were highly optimized (Section 3.13.2). In addition to general optimizations a multithreading component (Section 3.13.11) has been implemented, which allows to highly parallelize simulations optimizing for synchronous execution. As objects and locations do not influence each other during simulations those calculations are easily parallelizable taking advantage of modern multi-processor architectures.

The software is able to handle vertical changes of the seabed together with the burial and mobilization model. Thus it was shown that it is possible to match the time scales of the mobilization model, the burial model and the model for seabed morphology.

3.12 Determining the coefficients

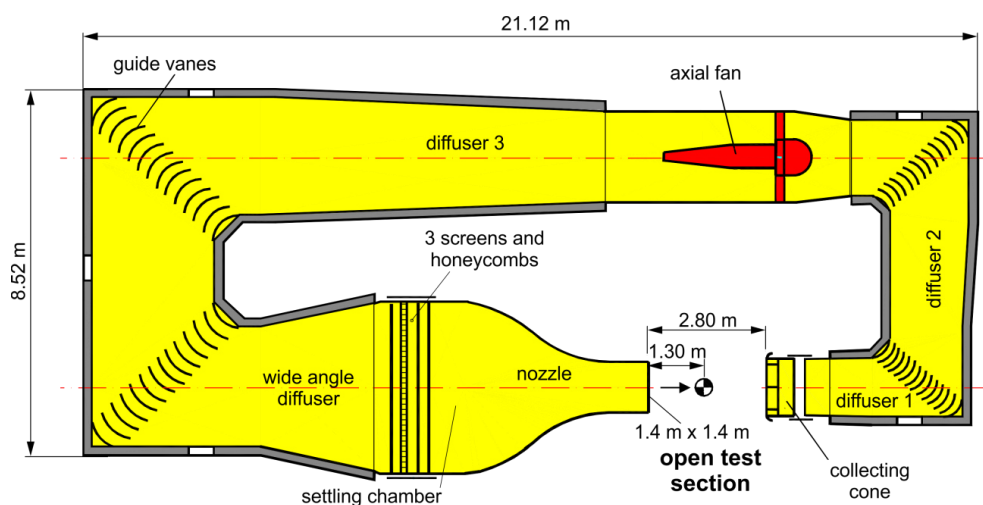
Numerical and experimental investigations were used to determine the drag and lift coefficients and the added mass coefficient of the OoI (see Section 3.5 for the loads on an object). The lift coefficient c_l and the drag coefficient c_d are dimensionless coefficients. They are used to characterize the dynamic lift of a body, or to quantify the drag or resistance of an object in a fluid environment. Both coefficients depend on various parameters such as the shape of the body, the Reynolds number and the roughness of the surface. Both coefficients are essential for the calculation of the mobilization of an object on the seafloor. A good knowledge about these coefficients is important and thus they were measured in numerical simulations and experiments.

Through the experimental and numerical investigations, polynomials for the coefficients were derived. These polynomials represent the dependence of the individual coefficient on the object's burial depth and the Reynolds number. The investigations were done with wind tunnel experiments and Computational Fluid Mechanics (CFD).

Another dimensionless coefficient is the added mass coefficient. This is calculated using the boundary element method and explained in the corresponding chapter.

3.12.1 Wind tunnel experiments

The goal of the wind-tunnel experiments was to determine the vertical and horizontal components of the fluid dynamic loads on the objects. Conserving of the Reynolds number during scaling of the objects from original scale to model scale guarantees that the turbulence structures in the wake of the object are comparable to those in original scale. Furthermore, the flow separation takes place at the same position. Thus, the pressure-induced loads are similar to the real ones. To transfer the data from laboratory scale into real (full) scale, the forces were typically converted into the dimensionless drag coefficient c_d and the lifting coefficient c_l .



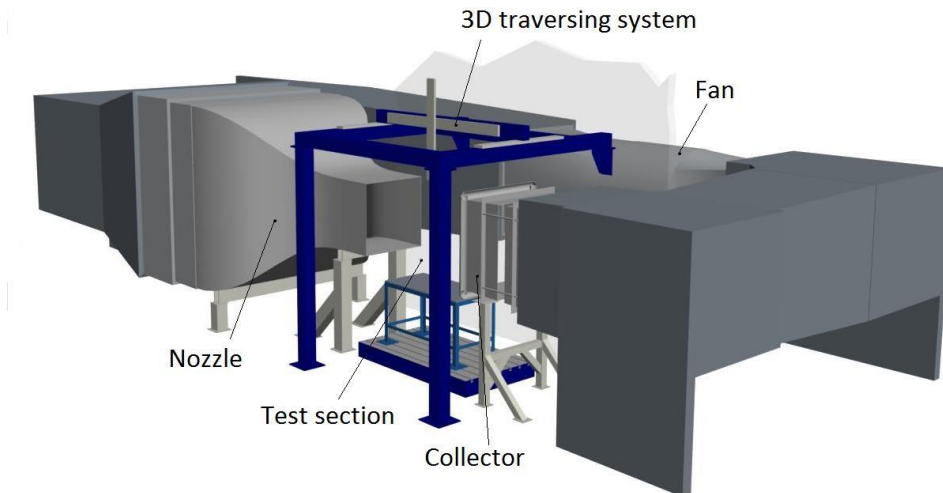


Fig. 34: Design of the Göttingen type wind-tunnel of MariKom.

The certified Göttingen type wind-tunnel of MariKom has a fan power of 200 kW and reaches a maximum velocity of 64 m/s with a degree of turbulence of less than 0.4 %. The open test section with a cross section of 1.4 m x 1.4 m and a length of 2.8 m is arranged horizontally. The overall design of the wind-tunnel is shown in Fig. 34. Within the measuring section a horizontal end plate is installed to simulate the sea floor. The objects were mounted on a 6-component force balance, which was mounted under the horizontal endplate. The velocity within the test section was derived from the difference of the static pressure between the settling chamber and the outlet of the nozzle. Since both, viscosity and density of the air depend on the air temperature, the humidity and the atmospheric pressure, these environmental parameters were permanently monitored to determine both, the respective dynamic viscosity and density. Both parameters were used to determine the Reynolds number.

The end plate within the test section was mounted horizontally and arranged like shown in Fig. 35. The shaft of the 6-component force balance, which was aligned under the end plate, was located 1300 mm downstream of the exit of the nozzle.

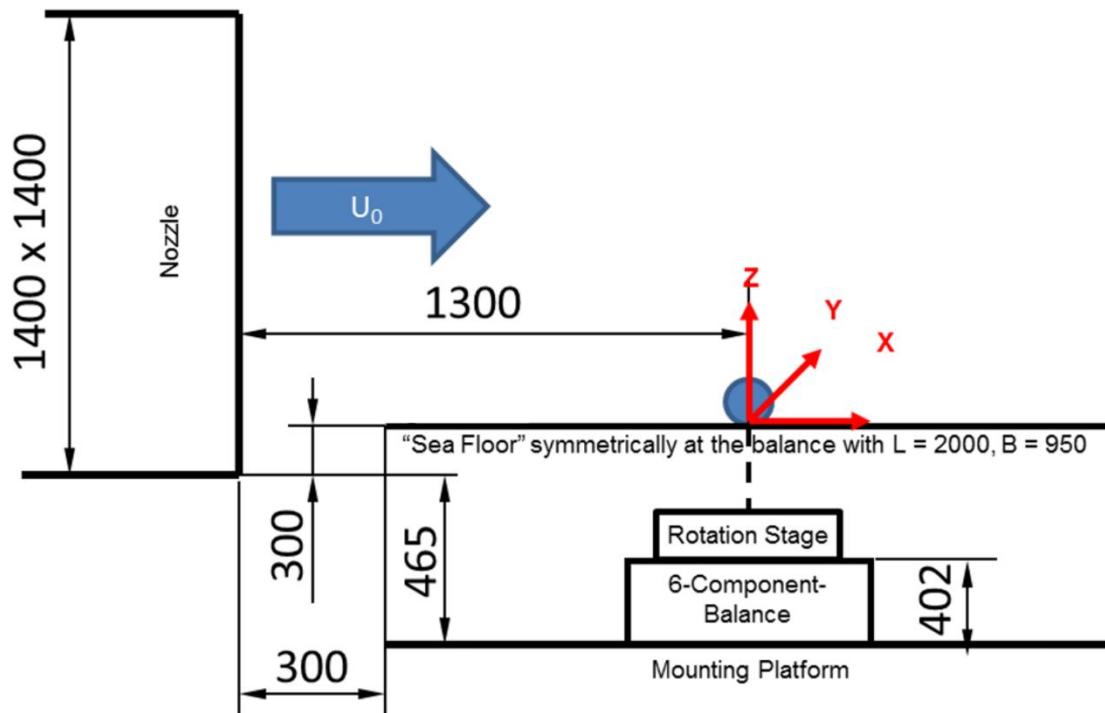


Fig. 35: Drawing of the arrangement of the end plate within the test section of the wind-tunnel.

The vertical profile of the velocity was measured with a hot wire anemometer inside the test section 5 cm upstream of the center position. This measurement was done in the empty wind tunnel section i.e., without any installed model. Based on these measurements, Fig. 36 shows the true profile for the incident velocities of most interest.

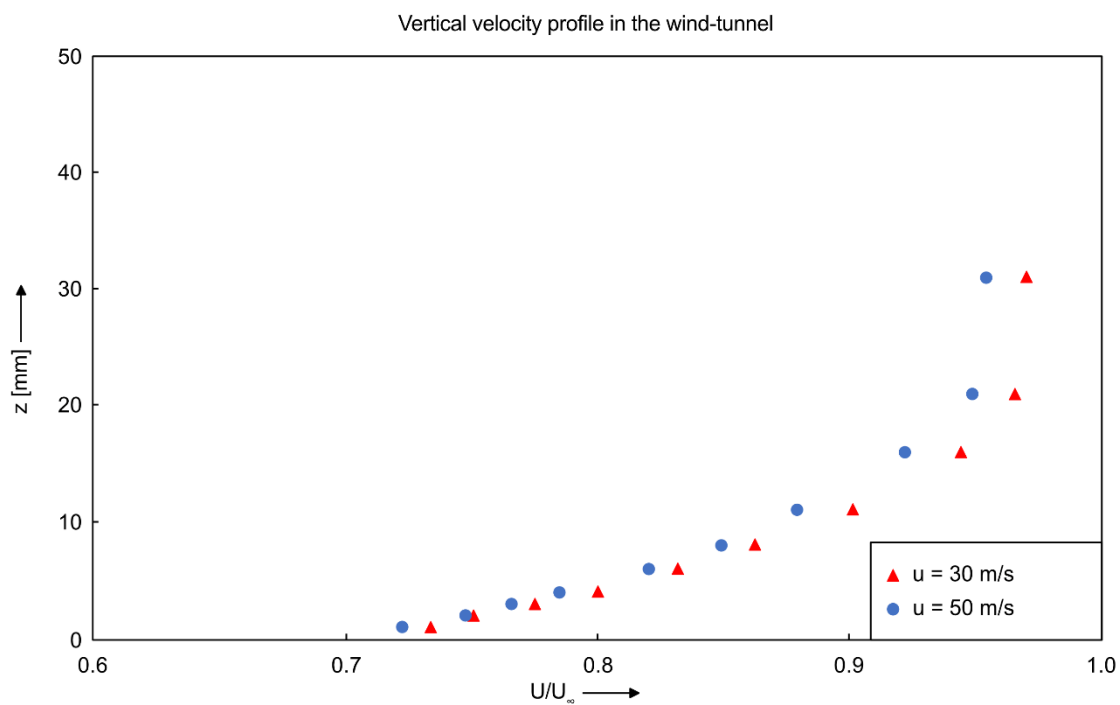


Fig. 36: Vertical velocity profile in the wind-tunnel.

For the correct measurement of the lift and drag force, the measurement technology in the wind tunnel was calibrated and, if necessary, corrected and adjusted. The calibration and

setup of the 6-component force balance and the velocity measurement technology was particularly relevant. The calibration of the balance was carried out with different measuring weights (see Fig. 37).

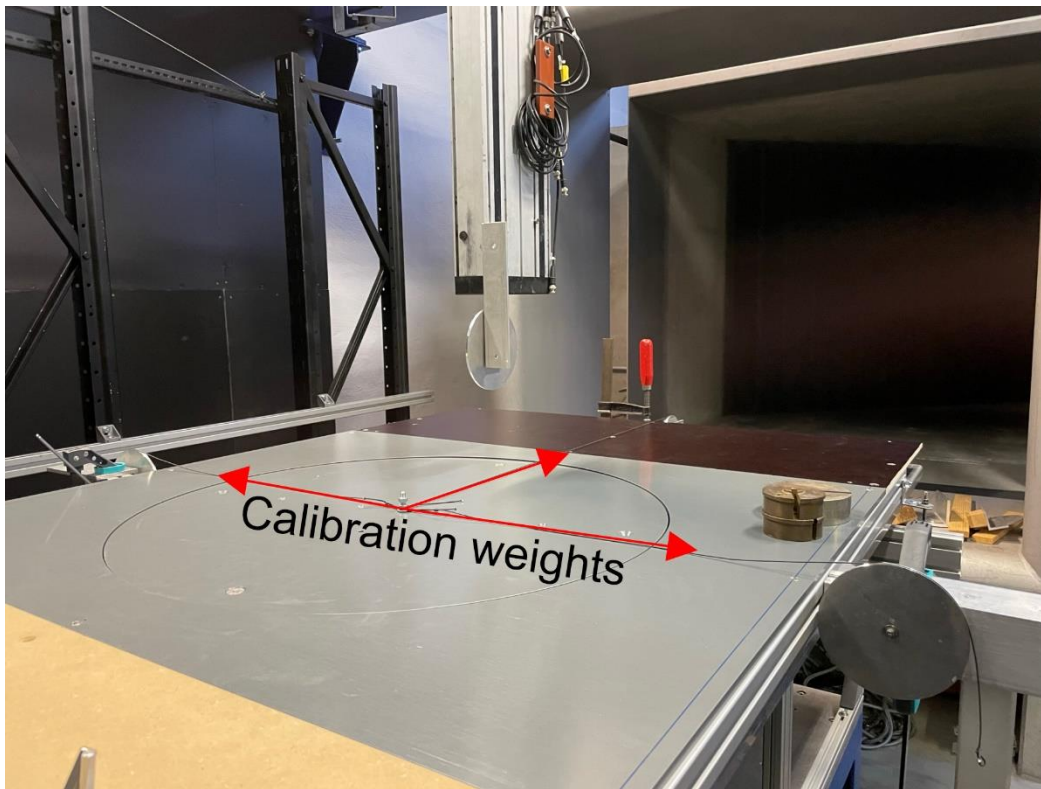


Fig. 37: Direction of the calibration weights.

The adjustment of the force measurement of the measuring scale was then made with masses of 50 g, 100 g, 250 g, 500 g, 1 kg, 2 kg, 5 kg and 10 kg. The measurement curve was then used as an adjustment for the further measurements.

The wind velocity is calculated as

$$u = \sqrt{\frac{2 \cdot p_{diff}}{\rho_a \cdot \left(1 - \frac{1}{a_{WT}^2}\right)}} \quad [76]$$

with p_{diff} being the measured difference of the static pressure at the inlet and the outlet of the nozzle, where two circumferential pressure lines were mounted on the outside of the nozzle to measure the averaged static pressure over the cross-sections. a_{WT} is the cross-section of the inlet related to the outlet of the nozzle. The density ρ_a of the air in the tunnel is derived from the ideal gas law as

$$\rho_a = \frac{p_{baro}}{R_{specific} \cdot \vartheta} \quad [77]$$

using the ambient barometric pressure p_{baro} , the absolute temperature ϑ and the specific gas constant $R_{specific} = 0.287 \text{ kJ}/(\text{kg} \cdot \text{K})$. An accurate measurement of the wind velocity was of utmost importance during the experiments.

Following the rules of linear error propagation (Walter & Herms, 2004) the uncertainty of the wind velocity due to the accuracy of the measurement devices was quantified. The uncertainty of a variable Y is denoted with $U^*(Y)$. Identifying the dependencies from Eq. [76], the relative uncertainty of the wind velocity is given as

$$\frac{U^*(u)}{u} = \left| \frac{\partial u}{\partial p_{diff}} \cdot \frac{U^*(p_{diff})}{u} \right| + \left| \frac{\partial u}{\partial \rho} \cdot \frac{U^*(\rho)}{u} \right| + \left| \frac{\partial u}{\partial a_{WT}} \cdot \frac{U^*(a_{WT})}{u} \right|. \quad [78]$$

Taking the derivative of Eq. [76] with respect to the variables it follows

$$\begin{aligned} \frac{\partial u}{\partial p_{diff}} \cdot \frac{1}{u} &= \frac{1}{2 \cdot p_{diff}} \\ \frac{\partial u}{\partial \rho} \cdot \frac{1}{u} &= -\frac{1}{2 \cdot \rho} \\ \frac{\partial u}{\partial a_{WT}} \cdot \frac{1}{u} &= \frac{1}{a_{WT}} - \frac{a_{WT}}{a_{WT}^2 - 1} \end{aligned} \quad [79]$$

The relative uncertainty of the density is given by

$$\frac{U^*(\rho)}{\rho} = \left| \frac{\partial \rho}{\partial p_{baro}} \cdot \frac{\Delta p_{baro}}{\rho} \right| + \left| \frac{\partial \rho}{\partial \vartheta} \cdot \frac{\Delta \vartheta}{\rho} \right| \quad [80]$$

with the derivatives

$$\begin{aligned} \frac{\partial \rho}{\partial p_{baro}} \cdot \frac{1}{\rho} &= \frac{1}{p_{baro}} \\ \frac{\partial \rho}{\partial \vartheta} \cdot \frac{1}{\rho} &= -\frac{1}{\vartheta} \end{aligned} \quad [81]$$

and p_{baro} and $\Delta \vartheta$ being the accuracies of the associated measurements. It is assumed that $R_{specific}$ is sufficiently exact and its uncertainty is negligible. The ratio

$$a_{WT} = \frac{A_1}{A_2} = \frac{l_1^2}{l_2^2} \quad [82]$$

is derived from the cross sections A_1 and A_2 , which are derived from the side lengths l_i of the square cross-section. The relative uncertainty $U^*(a_{WT})/a_{WT}$ of the area ratio can be expressed by

$$\begin{aligned} \frac{U^*(a_{WT})}{a_{WT}} &= \left| \frac{\partial a_{WT}}{\partial l_1} \cdot \frac{\Delta l_1}{a_{WT}} \right| + \left| \frac{\partial a_{WT}}{\partial l_2} \cdot \frac{\Delta l_2}{a_{WT}} \right| \\ \frac{U^*(a_{WT})}{a_{WT}} &= \left| 2 \cdot \frac{\Delta l_1}{l_1} \right| + \left| -2 \cdot \frac{\Delta l_2}{l_2} \right| \end{aligned} \quad [83]$$

with the accuracy of the length measurement Δl_i . The accuracies and uncertainties of the measuring equipment was found in the data sheets. The relative uncertainty of the wind velocity $U^*(u)/u$ is shown in Fig. 38. The unsteadiness in the chart is a consequence of the use of two different pressure transmitters for different pressure ranges. However, for wind velocity of more than 3 m/s the uncertainty of the velocity reading will be below $\pm 3\%$.

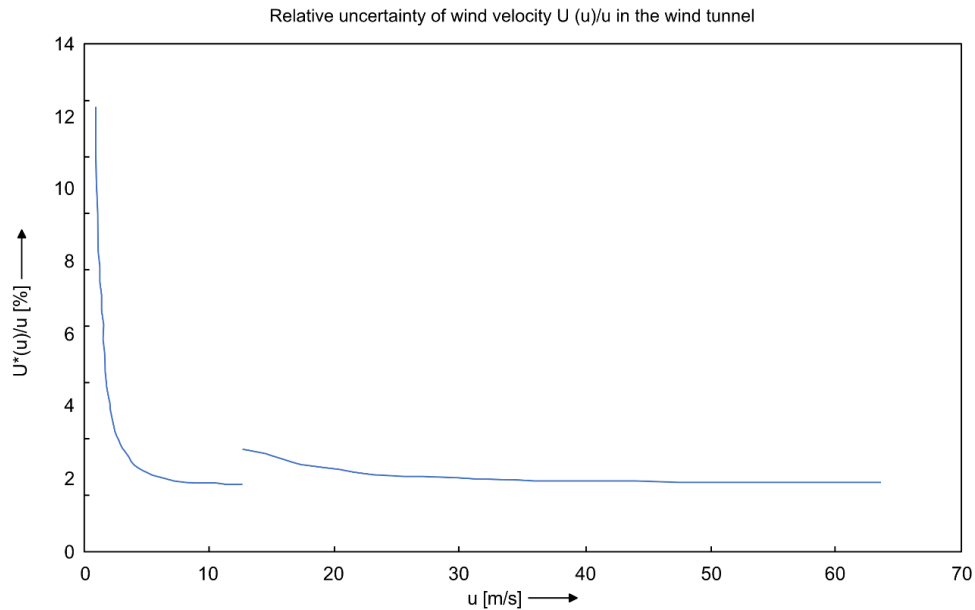


Fig. 38: Relative uncertainty of the wind velocity $U^*(u)/u$ in the wind tunnel.

The objects used, as well as their corresponding adaptations regarding different burial depths are shown below. Fig. 39 exemplarily shows a drawing of the 1000 lb GP Bomb. Based on this, four models were produced. By simply cutting the models, four different burial depths were simulated. Models of the 155 mm, HE 107 and the Tiny Tim Rocket were built in the same way.

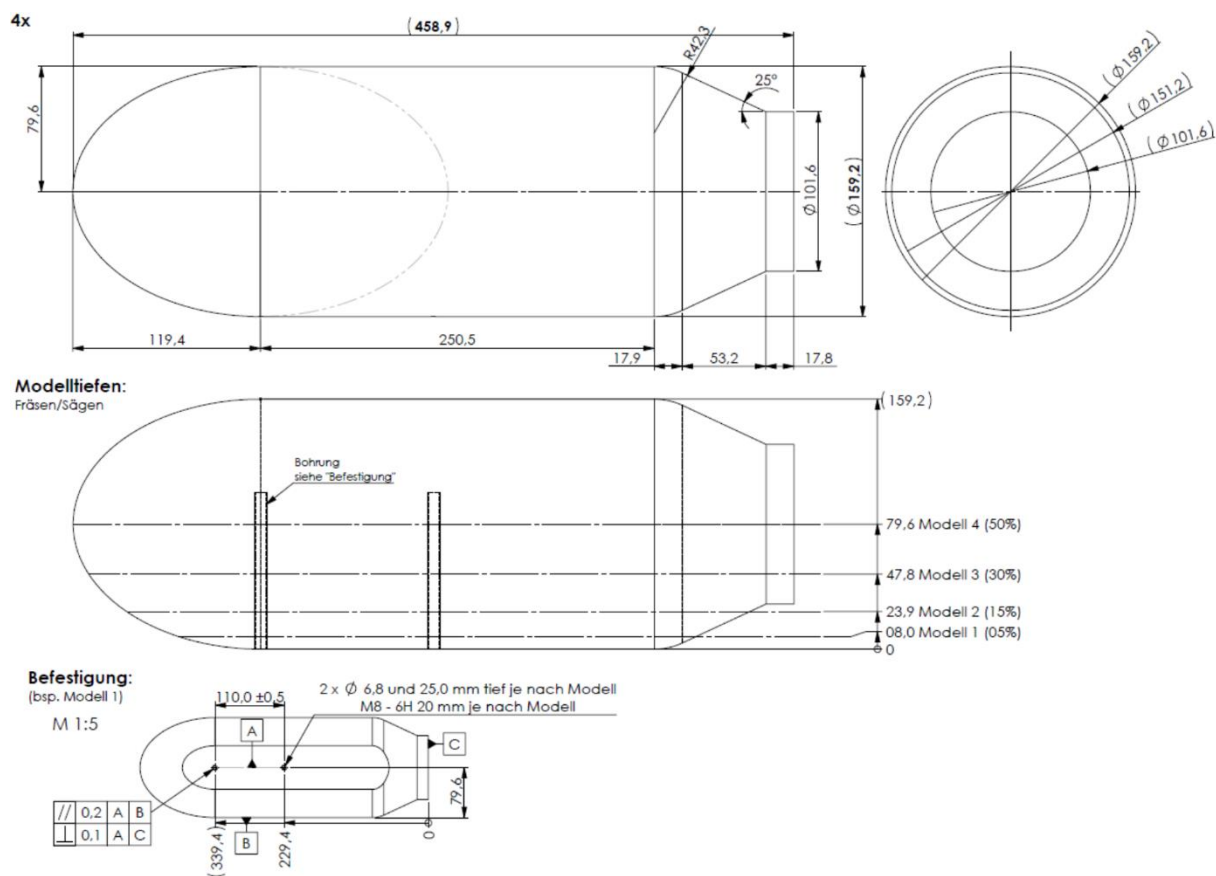


Fig. 39: Technical drawing of the model of a 1000 lb GP bomb.

In summary, 12 different models were produced for the wind tunnel. Tab. 7 shows an overview of the corresponding sizes and the applied size scale factor.

Tab. 7: Data of the models in the original and in the wind tunnel.

Object	Original [mm]		z_b/D	Wind tunnel [mm]		scale factor
	length	height		Length	height	
1000 lb GP Bomb	1349	478	0.05	458.9	151.2	1:3
			0.15	458.9	135.3	
			0.30	458.9	111.4	
			0.50	458.9	79.6	
155 mm, HE 107	584	155	0.05	292.1	71.8	1:2
			0.15	292.1	64.3	
			0.30	292.1	52.9	
			0.50	292.1	37.8	
Tiny Tim Rocket	3124	298	0.05	624.8	56.7	1:5
			0.15	624.8	50.7	
			0.30	624.8	41.8	
			0.50	624.8	29.9	

Fig. 40 shows the 1000 lb GP Bomb, mounted on the measuring plate in the wind tunnel at the various burial depths.

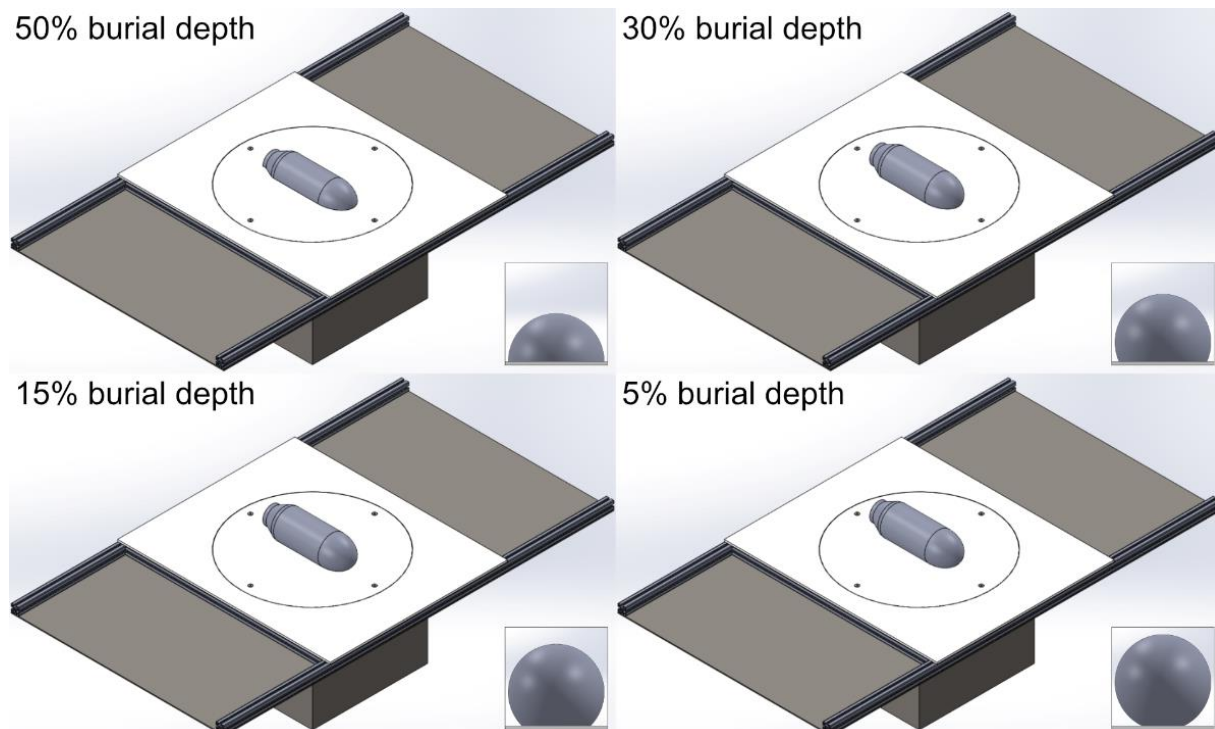


Fig. 40: Model of the 1000 lb GP Bomb on the measuring plate in the wind tunnel.

Conserving the Reynolds number



$$Re = \frac{U_0 \cdot D}{\nu} \quad [84]$$

in down scaled wind tunnel experiments leads to a new corresponding incident velocity U_0 . As the models, used in CFD, were original scale models with incident velocities of 0.2, 0.6, 1.0, 2.0, and 4.0 m/s, the incident velocities in the wind tunnel are based on those. The Reynolds numbers and incident velocities in the wind tunnel are exemplarily shown in Tab. 8 for the 1000 lb GP Bomb at $z_b/D = 0.3$.

Tab. 8: Scaling of the velocity from original scale to wind tunnel scale.

Model	z_b/D	Original U_0 [m/s]	Re	Wind tunnel U_0 [m/s]
1000 lb GP Bomb	0.30	0.2	$7.31 \cdot 10^4$	6.62
		0.6	$2.19 \cdot 10^5$	19.86
		1.0	$3.66 \cdot 10^5$	33.10
		2.0	$7.31 \cdot 10^5$	66.20
		4.0	$1.46 \cdot 10^6$	132.39

As the maximum velocity of the wind tunnel is limited to 60 m/s, only the first three velocities can be investigated in the wind tunnel, representing incident velocities up to 1 m/s in real scale.

To minimize the effect of a potential gap between the object and the end-plate (seafloor) in the wind tunnel, the objects were mounted on a turntable without any gap. The turntable then was attached to the loads balance. The additional drag forces, affecting the turntable were derived from loads measurements without any object being installed. These loads then were subtracted from the measurements with an object being attached to the turntable. This setup allowed to change the incident flow angel of the objects, whereas 0 deg was defined with the incident flow direction being perpendicular to the main axis of the object. Tab. 9 exemplarily shows the variety of the parameters during the wind tunnel experiments with the 1000 lb GP Bomb.



Tab. 9: Procedure for measurement in the wind tunnel.

$z_b/D = 0.5$		$z_b/D = 0.3$		$z_b/D = 0.15$		$z_b/D = 0.05$	
U_0 [m/s]	Angle [°]	U_0 [m/s]	Angle [°]	U_0 [m/s]	Angle [°]	U_0 [m/s]	Angle [°]
7	-90	7	-90	7	-90	7	-90
	-45		-45		-45		-45
	0		0		0		0
	45		45		45		45
	90		90		90		90
19	-90	19	-90	19	-90	19	-90
	-45		-45		-45		-45
	0		0		0		0
	45		45		45		45
	90		90		90		90
36	-90	36	-90	36	-90	36	-90
	-45		-45		-45		-45
	0		0		0		0
	45		45		45		45
	90		90		90		90
45	-90	45	-90	45	-90	45	-90
	-45		-45		-45		-45
	0		0		0		0
	45		45		45		45
	90		90		90		90

Thus, at least 80 measurements were performed for each object. The duration of each single measurement as well as the sampling frequency were defined the way that unsteady phenomena are resolved and enough cycles are covered to guarantee a sufficient averaging time. Subsequently, 24000 samples (sampling frequency 1200 Hz, sampling time 20 s) were recorded during each individual measurement and then averaged. The dimensionless drag coefficients

$$c_d = \frac{2F_x}{\rho U_0^2 A_{cs,obj}} \quad [85]$$

and lift coefficient

$$c_l = \frac{2F_z}{\rho U_0^2 A_{cs,obj}} \quad [86]$$

were derived from the measured loads F_x and F_y , the incident velocity U_0 and the objects' cross section $A_{cs,obj}$.

3.12.2 Numerical Simulation using CFD

Several numerical simulations by CFD for the 500 lb GP Bomb, the 1000 lb. GP Bomb, the Tiny Tim Rocket and the 155 mm, HE 107 were performed to derive the drag and lift coefficients. The different models were set up in a numerical domain with the dimensions of

13 x 22 x 30 m (H x W x D), consisting of 60 million mesh elements with a maximum cell size of 4 mm. The simulations were then checked for mesh independency and the results were evaluated. In some cases, the mesh was subsequently adjusted. The determined drag and lift coefficients were plotted over the Reynolds number and a regression polynomial was created.

3.12.2.1 Boundary conditions and models for the numerical simulation

The Numerical Simulations were performed with the free, open source CFD software OpenFOAM. The used methods were RANS and URANS with the $k-\omega$ -SST turbulence model. Automatically generated unstructured grids of tetrahedrons with prismatic boundary layers were used in the simulation domain. The dimensionless wall distance was kept at $y^+ < 1$ for all simulations. Fig. 41 shows a sketch of the simulation domain.

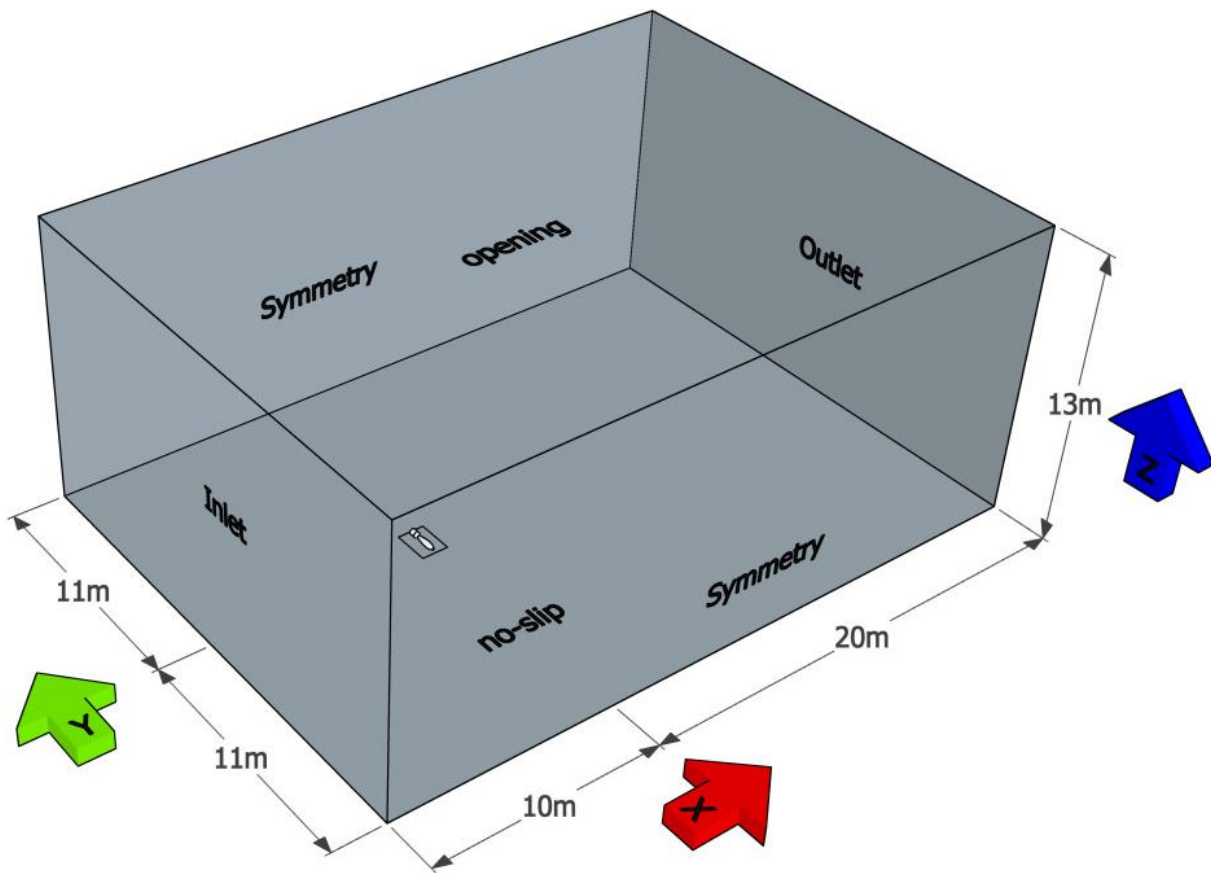


Fig. 41: Simulation Domain and Boundary Conditions.

The exact values of the boundary conditions of the numerical simulation are shown in Tab. 10.

Tab. 10: Boundary conditions of the numerical simulations.

inlet:	block profile, 5% turbulence intensity, fully developed boundary layer at the object
sides:	Symmetric
top:	Opening
bottom and object:	element size on object: 4 mm
mesh elements:	approx. 60 mio mesh elements
fluid:	water, $\rho = 1000 \text{ kg/m}^3$, $T = 8^\circ\text{C}$

Since grid generation near the point of contact between a cylindrical object and the seafloor is very difficult, this edge was assumed to have a small but measurable slope. This slope was assumed to have an angle of 45° . This assumption does not change the results significantly however it reduces the effort for the grid construction and stabilizes the convergent evolution of the results. Necessary studies concerning the grid independency of the results as well as a permanent monitoring of the convergence of the results were done as a matter of course (for example see Fig. 42).

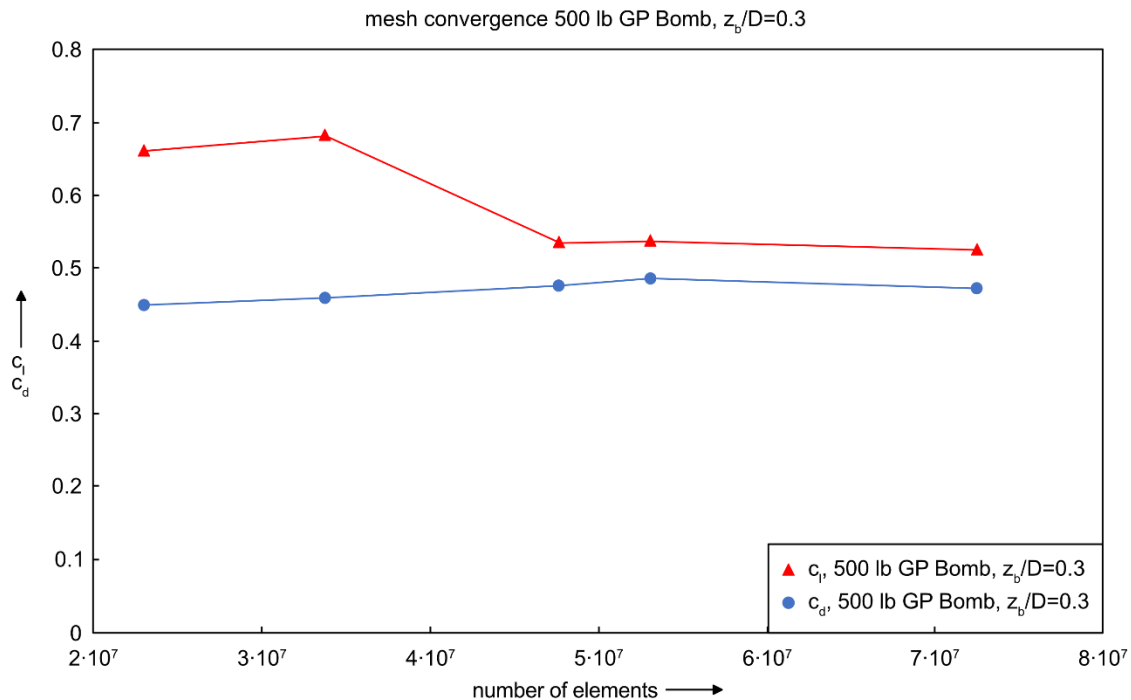


Fig. 42: Mesh convergence for the 500 lb GP Bomb at a burial depth of $z_b/D = 0.3$.

The simulations were performed for the real scale size in water (full scale) and for model size in air (wind tunnel scale). The wind tunnel sized simulations were solely used for validation purposes. For all simulations, the vertical velocity profile was monitored at the position of the object.

3.12.3 Drag crisis

In fluid dynamics, the drag crisis (also known as the Eiffel paradox) is a phenomenon in which the drag coefficient drops off suddenly as the Reynolds number increases. This effect is well known and well-studied, especially for cylindrical and spherical objects. The typical Reynolds number range for this effect to occur is about $Re = 3 \cdot 10^5$ (see also Fig. 43). This corresponds to the range where the flow pattern changes, leaving a narrower turbulent wake. The behavior is highly dependent on small differences in the condition of the surface of the object.

Drag of a Sphere

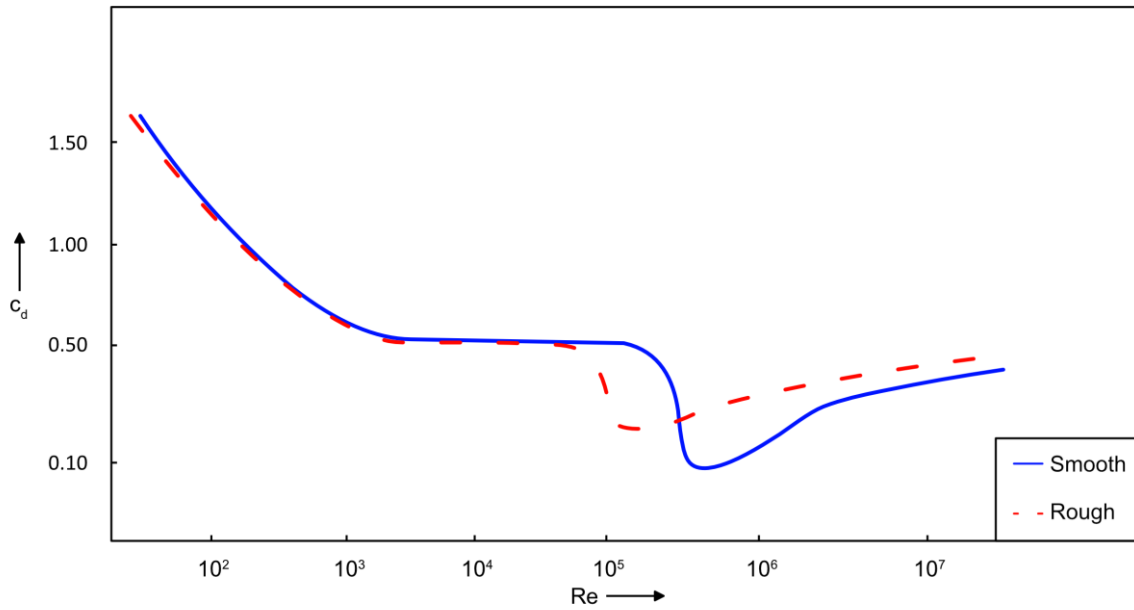


Fig. 43: Drag coefficient of a Sphere for a smooth and a rough surface of the sphere.

The drag crisis is associated with a transition from a laminar to a turbulent boundary layer flow adjacent to the object. For cylindrical structures, this transition is associated with a transition from well-organized vortex shedding to randomized shedding behavior for super-critical Reynolds numbers, eventually returning to well-organized shedding at a higher Reynolds number with a return to increasing drag coefficients.

3.12.4 Added mass

A fundamental principle of classical physics says: no body exists where another already exists. In the case of a moving body surrounded by a fluid, the latter must therefore experience an impulse. Added masses m_{jk} (effect in direction j when moving in direction k) are to be understood as a conceptual equivalent for the fluid mass m_{Fl} to be accelerated in this way. As a result, the surrounding fluid volume V_{Fl} of density ρ_{Fl} must be accelerated out of its equilibrium. According to Newton's 1st law it experiences a force and according to Newton's 3rd law it counteracts the acceleration of the body. An interpretation of this situation ultimately allows the statement that the body will act slower due to the fluid. According to (Clauss, et al., 1992) the order of magnitude of m_{jk} in the x-direction is illustrated by the example of a $l = 1\text{ m}$ long cylinder.

The added mass or virtual mass is the inertia added to a system because an accelerating or decelerating body must move (or deflect) some volume of surrounding fluid as it moves through it. The virtual mass was calculated for each object and assigned to the different axes. The objects were created with a construction program and then the STL file was meshed. The meshes created were checked and adjusted using a mesh independence study. Finally, the added mass coefficient was calculated using the Boundary Element Method (BEM).

$$m_{xx} = \rho_{Fl} \cdot V_{Fl} = \rho_{Fl}(\pi \cdot l \cdot R^2) \quad [87]$$

For a quantified indication of m_{jk} (Kornev, 2009) first considers a potential flow within a friction-free validity range. Starting from the kinetic energy of the fluid and using the Laplace equation Eq. [88] as well as several mathematical transformations, he succeeds in linking m_{jk} to a location-dependent body movement potential ϕ . With any movement in three-dimensional space \mathcal{E} it makes sense to provide a single potential ϕ_k for each of the six degrees of freedom. Through a discretization of the body surface \mathcal{S} , the aforementioned connection can finally be specified with

$$\nabla^2 \cdot \phi(x) = 0 \quad [88]$$

$$m_{jk} = -\rho_{Fl} \oint_{\mathcal{S}} \phi_j \cdot \frac{\partial \phi_k}{\partial \vec{n}} d\mathcal{S} \quad [89]$$

As shown, the determination of the added masses for an arbitrary body is subject to the assumption that the potential distribution over its surface as well as its directional derivation to \vec{n} must be known. However, it is noteworthy that, if the Laplace equation needs to be fulfilled and known boundary conditions for this problem are compiled only information on limitations exists. It is therefore obvious to formulate the search for the added masses as a boundary value problem (BVP).

$$BVP = \begin{cases} \nabla^2 \cdot \phi(x) = 0, & \text{in } \mathcal{E} \\ \frac{\partial \phi}{\partial \vec{n}} = x, & \text{on } \mathcal{S} \end{cases} \quad [90]$$

According to (Korotkin, 2009) and (Lewandowski, 2004) the second boundary condition can be summarized with the directional cosines and the unit vectors $\vec{e}_x, \vec{e}_y, \vec{e}_z$ as:

$$\vec{\mathcal{E}}_{\mathcal{S}} = \begin{pmatrix} \mathcal{E}_{\mathcal{S},1} \\ \mathcal{E}_{\mathcal{S},2} \\ \mathcal{E}_{\mathcal{S},3} \end{pmatrix} = \begin{pmatrix} \cos(\vec{n}_{\mathcal{S}}, \vec{e}_x) \\ \cos(\vec{n}_{\mathcal{S}}, \vec{e}_y) \\ \cos(\vec{n}_{\mathcal{S}}, \vec{e}_z) \end{pmatrix} \quad [91]$$

$$\frac{\partial \phi}{\partial \vec{n}} \Big|_{\mathcal{S}} = \begin{cases} \mathcal{E}_{\mathcal{S},k}, & f \text{ or } k = 1, 2, 3 \\ (\vec{r} - \vec{\mathcal{E}}_{\mathcal{S}})_{k-3}, & f \text{ or } k = 4, 5, 6 \end{cases} \quad [92]$$

3.12.5 Boundary Element Method to quantify the Added mass coefficient

A suitable numerical tool to solve Eq. [90] is the boundary element method (BEM). As (Hartmann, 1987) confirms, the decisive advantage of the BEM lies in the fact that only information about the edge must be available, because only there unknowns occur. For a three-dimensional problem, this means nothing less than a reduction to a two-dimensional task. Consequently, only limiting surfaces and not the volumes involved have to be discretized. In the end, a result is achieved inside, outside or on the actual boundary surface. In contrast to other methods (FDM, FEM, FVM), the BEM is strictly subject to the restrictions of the ordinary (ODE) or partial differential equations (PDE) to be solved. The reason for this is the use of so-called fundamental solutions G as analytical and thus exact solutions for the given BVP.

A key element of the BEM is the replacement of the PDE Eq. [88] by an equivalent integral equation. Mathematically speaking, it is the transfer of the BVP to the edge. Following this step, the potential ϕ can be calculated at any point on the surface by the formula

$$\frac{1}{2}\phi = \oint_S \phi \cdot \frac{\partial G}{\partial \vec{n}} dS - \oint_S \frac{\partial \phi}{\partial \vec{n}} \cdot G dS \quad [93]$$

Obviously, the required variable occurs on both sides of the equation. Here another basic concept of BEM comes into play: the formation of a linear equation system (LES) with the help of so-called integral operators in equations. [95] and [96]. The fundamental solutions used for this are alternatively also called “Green’s function” and were determined for various differential equations in (Gaul, et al., 2003). In the case of the Laplace equation, it depends solely on the position vectors of the observer \vec{r}_0 and source points \vec{r}_s , which in turn describe S in their entirety.

$$G = \frac{1}{4\pi|\vec{r}_0 - \vec{r}_s|} \quad [94]$$

It can be noted that Eq. [93] characterizes the effect of a source at \vec{r}_s on any point at \vec{r}_0 . Physically, for example, this corresponds to the attraction in a gravitational field or induction in an electrostatic field. Therefore, both \mathcal{L} and \mathcal{M} can be calculated for a given geometry.

$$\{\mathcal{L}\}_S = \int_S G dS \quad [95]$$

$$\{\mathcal{M}\}_S = \frac{\partial \{\mathcal{L}\}_S}{\partial \vec{n}} = \int_S \frac{\partial G}{\partial \vec{n}} dS \quad [96]$$

The use of integral operators also allow the simplification of the notation of Eq. [93] and the execution of a numerical discretization in Eq. [97] for a finite number of elements N . Finally, the variables are re-sorted using the unit matrix \mathbf{I} , resulting in an LES, shown in Eq. [98], of the form $\mathbf{Ax} = \mathbf{b}$. On its right side, the known boundary conditions from Eq. [92] are inserted and then solved with the help of a written MATLAB program.

$$\frac{1}{2}\phi_i = \sum_{j=1}^N \{\mathcal{M}_{ij} \cdot \phi_j\} \cdot \vec{r}_j - \sum_{j=1}^N \left\{ \mathcal{L}_{ij} \cdot \frac{\partial \phi_j}{\partial \vec{n}_j} \right\} \vec{r}_j \quad [97]$$

$$\left(\mathcal{M} - \frac{1}{2}\mathbf{I} \right) \phi = \mathcal{L} \cdot \frac{\partial \phi}{\partial \vec{n}_j} \quad [98]$$

In a last step, the resulting potential distribution and the applied boundary conditions for [92] are used in Eq. [89] and the added masses are calculated as a function of ρ_{FI} .

3.13 Software

The software presented in Section 3.8 successfully showed the integration of phase resolved wave- and mobilization-simulations with the wave resolved burial simulation. This software was written in DELPHI, with a strong focus on procedural functions solving the simulation algorithms.



The actual Go/No-Go decision point was:

Is it possible to match the timescales of the mobilization model, the burial model and the model for seabed morphology?

imposes implicit requirements, like performance, extensibility and testability, needed to be reflected in the upcoming software development process.

3.13.1 Requirements

To achieve the second Go/No-Go decision point, the task was to match the timescales of seabed morphology (in the order of months) and those of the existing mobilization and burial model (in the order of seconds). Matching these timescales poses a huge difficulty as the timescales are quite different. The only applicable solution to match the timescales is to integrate the mobilization and burial model outputs over a very large period of time, which has the following effects:

- Increased complexity: Matching the timescales of different models adds complexity to the software, as it requires the implementation of specialized algorithms and data structures to represent and manipulate the different timescales.
- Increased computation: Matching the timescales of different models will also require additional computation, as it involves the integration, aggregation, or interpolation of data from the different models, which will add to the overall computational load of the software.
- Increased testing and validation: Matching the timescales can also make the software more difficult to test and validate, as it may require the development of specialized test cases and evaluation criteria to ensure that the timescales are matched correctly and that the results of the models are consistent and reliable.
- Increased risk of errors and inconsistencies: Matching the timescales can increase the risk of errors and inconsistencies in the software, as it can be challenging to ensure that the timescales are matched accurately and consistently across the different models and data sources.

In addition, the simulation software shall feature a user-friendly interface for intuitive navigation and configuration of simulation parameters. Users should be able to tailor simulations to specific contexts, adjusting e.g. object properties, environmental conditions, and simulation time frames. The software shall support a wide range of input formats for describing objects, waves, environments, or morphology. Output flexibility enables users to specify varied output formats and data types, while robust data logging captures detailed information for post-simulation analysis. Visualization tools shall empower users with graphical representations and visualizations to aid in interpreting and communicating simulation outcomes. Finally, the software shall be capable of including a variety of calculation models and to offer meaningful possibilities for comparison.

Furthermore, a future-proof software foundation shall be developed, which can satisfy a range of use cases. Therefore, the following non-functional requirements shall be considered in the software development process:



- **Extensibility:** refers to the ability of a software system to be extended or modified to add new features, functions, or capabilities without significant effort or disruption. Extensibility enables systems to evolve and adapt over time to meet changing user needs and requirements, and to incorporate new technologies and innovations.
- **Modifiability/Maintainability:** refers to the ease with which a software system can be modified or changed to correct errors or improve performance. Modifiability enables systems to be updated and improved over time to meet changing user needs and requirements, and to address bugs or other issues that may arise during its operation. Maintainability enables a system to be supported and maintained over its lifespan, and it can help to reduce the cost and effort required to keep the system running reliably.
- **Scalability:** refers to the ability of a software system to handle increased workloads or data volumes without degrading its performance. Scalability is an important non-functional requirement for many software systems, as it enables the system to accommodate growth and change over time, and to continue to deliver its intended functionality and benefits even as its usage and requirements evolve.
- **Testability:** refers to the ease with which a software system can be tested to ensure that it meets its specified requirements and behaves as expected. Testability enables the system to be validated and verified before it is deployed, and it can help to identify and fix problems with the system early in its development cycle.
- **Reliability:** refers to the ability of a software system to operate consistently and correctly over time, without experiencing errors or failures. Reliability ensures that the system continues to deliver its intended functionality and benefits even in the face of unexpected or adverse conditions.
- **Performance:** refers to the speed, efficiency, and responsiveness of a software system. Performance is an important requirement, as it enables the system to deliver its intended functionality and benefits in a timely and effective manner, and it can help to ensure that the system is usable and satisfying for its users.

3.13.2 Analysis of the existing software

There are a few potential disadvantages to procedural programming. One of the main disadvantages is the difficulty to manage and maintain large and complex programs. Due to the software composition of many individual procedures or functions, each of which performs a specific task, it becomes difficult to keep track of the interaction of those functions. In procedural programming, the emphasis is on breaking a program down into small, independent functions, rather than on creating modular, self-contained units of code (such as classes or objects) that can be easily reused in different contexts. As a result, it can be more difficult to reuse, modify or understand code written in a procedural style, and it can also be more challenging to manage the dependencies between different parts of the code.

DELPHI is a high-level programming language that is generally considered to be easy to use, whereas low-level programming languages, like C++, are more complex and powerful. In terms of performance, C++ is generally considered to be faster and more efficient than Delphi, especially for applications that require a lot of processing power. When it comes to

complex mathematical algorithms, C++ has an advantage over DELPHI in terms of performance because C++ can be more closely optimized for such algorithms.

Therefore, the decision was made to rewrite the software in object-oriented C++.

3.13.3 Development

The software development started with two parallelized approaches. While a basic software architecture was designed, the existing DELPHI software has been ported to C++ for a rapid prototyping approach.

Rapid prototyping allows developers to quickly test and evaluate different design ideas and approaches, helping to make informed decisions about the software architecture and design of the project. It enables developers to gather feedback from users and stakeholders early in the development process, which helps to ensure that the final product meets expectations. Rapid prototyping helps to reduce the overall time and cost of development, as it allows developers to identify and fix problems at an early development stage which avoids costly changes in a later stage.

The software architecture is the high-level structure of the software system, which defines the system's components, their relationships, and principles which govern their design and evolution. Having a well-defined software architecture can have several advantages in software development, including:

- clear, consistent, well-structured, and maintainable framework
- clearly defined relationships
- independent, modular, and reusable code
- reusability in different contexts
- identification of potential design issues early in the development process
- more informed decisions about the design and implementation of the software
- providing a clear understanding of the system's overall structure

3.13.4 Software-Architecture

The Software Architecture follows the basic MVC (Model-View-Control) design pattern.

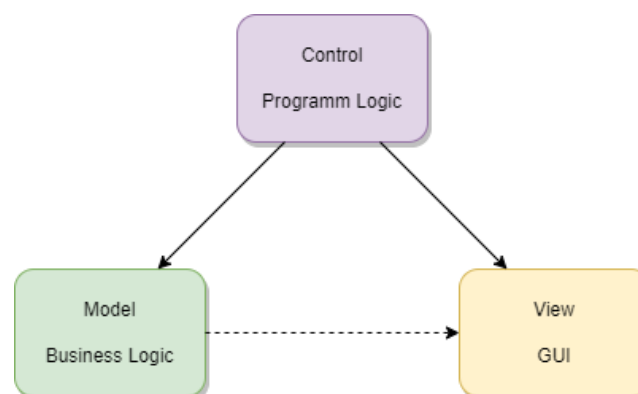


Fig. 44: Basic Software Architecture Overview.

The Model-View-Controller (MVC) design pattern (Fig. 44) is a software architectural pattern that is commonly used for developing user interfaces that divide the application into three interconnected parts. These parts are the model, the view, and the controller. The main

advantage of the MVC design pattern is that it separates the application into three distinct parts, each with its own responsibility. This separation of concerns makes it easier to develop and maintain the application, as well as to extend and modify it in the future. Furthermore, the separation allows easy porting of the business logic into different contexts, like running headless on a server or utilizing different GUI frameworks. Other advantages include an increased flexibility, testability, and code reuse.

The model is responsible for managing the data and the business logic of the application. It represents the state of the application and performs operations on the data.

The view is responsible for presenting the user interface and displaying the data to the user. It receives user input and sends it to the controller.

The controller is responsible for receiving user input and deciding how to handle it. It updates the model and the view as needed.

3.13.4.1 Business Logic

Business Logic refers to the part of the application that implements the rules and processes that define how the application operates. This includes the algorithms and rules that govern the manipulation of data, the operations that the application performs and how the application should respond to different inputs and events.

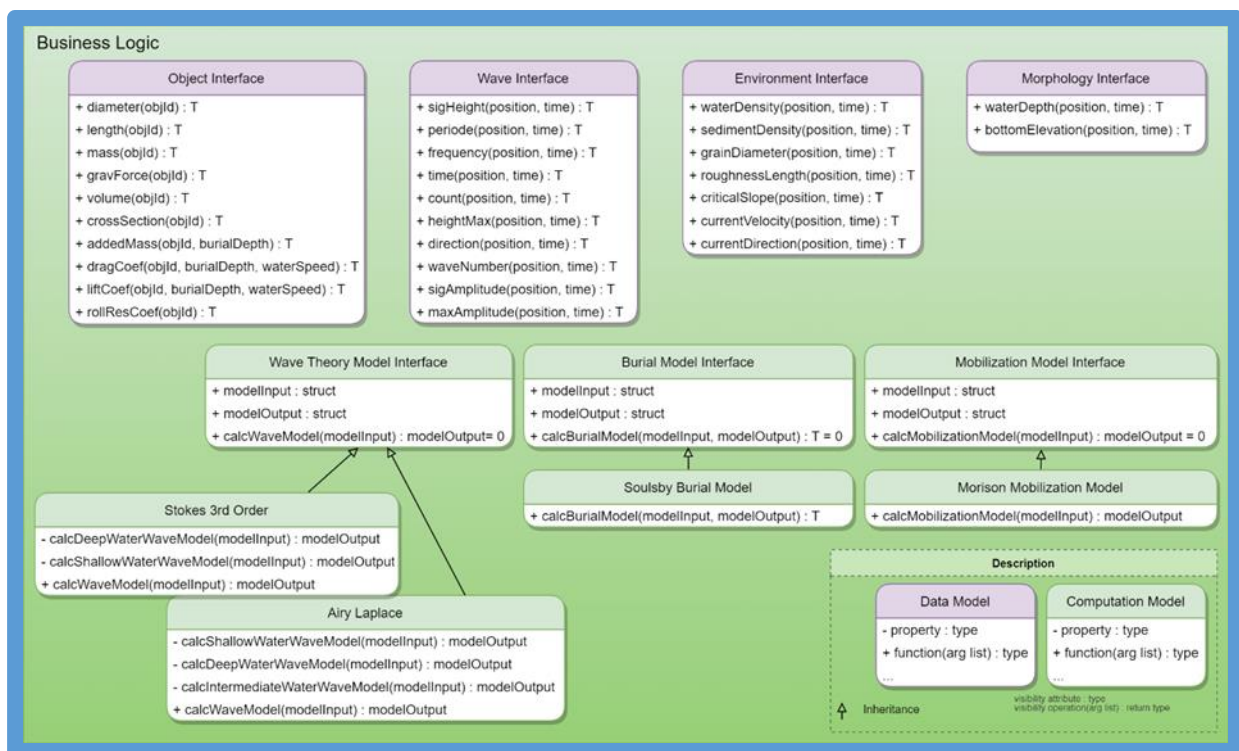


Fig. 45: UML Representation of main components of the Business Logic.

The business logic (Fig. 45) provides necessary objects for storing and for manipulating data. The data model objects (purple in Fig. 45) are primarily concerned with storing and organizing data in a consistent manner. These models provide interfaces (Section 3.13.8) for accessing single data properties. The classes are templated (Section 3.13.10) and functions return the according template type T. Data with spatial or temporal resolution can be accessed with the according position and time. However, interface implementations can choose to ignore



the arguments, e.g. in cases where data is only available as fixed values. There are several advantages to using data classes in software design. These advantages include:

- Encapsulation: Data classes provide a way to group related data and to hide the implementation details of the data from the rest of the program
- Type safety: Data classes provide a way to define the types of data that can be stored in the class, which helps to prevent errors and ensure that the data is used consistently throughout the program (see also Section 3.13.10)
- Extensibility: Data classes can be easily extended or subclassed to add new functionality or to specialize the data for specific purposes
- Performance: C++ provides special support for data classes like vector or map, which can improve the performance of the program

Computational classes (green in Fig. 45) are classes in a software program that are primarily concerned with performing computations and operations on data. The advantages of using computational classes include:

- Encapsulation/Abstraction: Computational classes provide a way to group related computations together and to hide the implementation details of the computations from the rest of the program (see also chapter 3.13.7)
- Extensibility: Computational classes can be easily extended or subclassed to add new functionality or to specialize the computations for specific purposes
- Performance: Specialized classes can be highly optimized to improve the performance

The further software design and the interaction between the components is described in Section 3.13.5.

3.13.4.2 Program Logic

The program logic is responsible for handling the external interfaces of the program. These include for example user interfaces or file interfaces. Therefore, the program logic provides a set of tools for data and event handling across various entities. Data management involves the import, provisioning, conversion, processing, storage, and visualization of information. The term 'data' extends beyond input and output data, encompassing persistent settings, configurations, and internal objects.

3.13.4.3 Graphical User Interface

Due to the capsulated software design any graphical user interface framework can be used. The GUI can also be completely omitted and replaced by a command line interface or network interfaces. Currently the Qt Framework is used for GUI development. The GUI is programmed using the Qt Modeling Language (QML). GUI elements are hierarchically structured where each element can be reused to compose new elements. Fig. 46 depicts an example view of the GUI with Fig. 47 describing the corresponding layout.

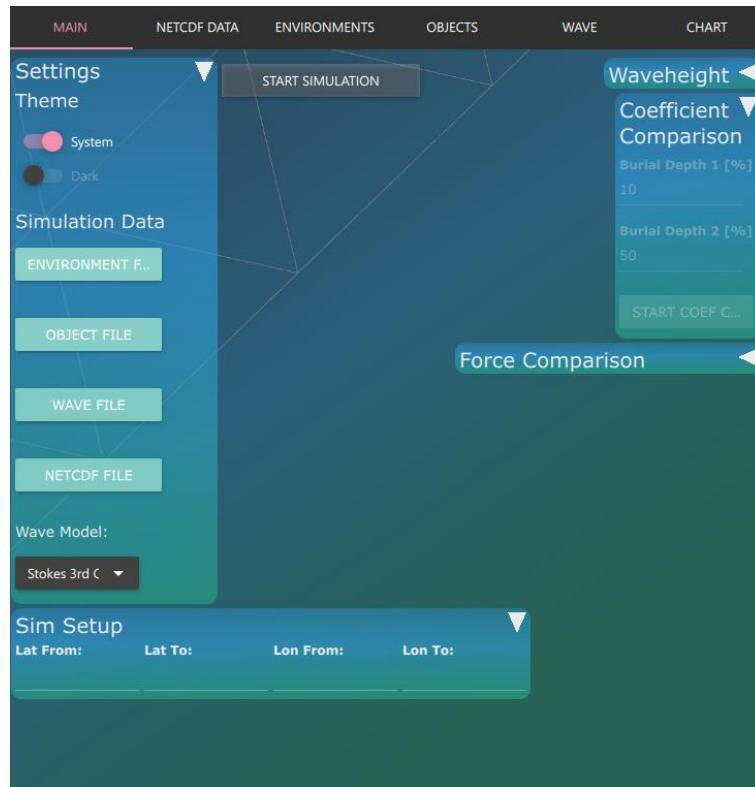


Fig. 46: GUI Example.

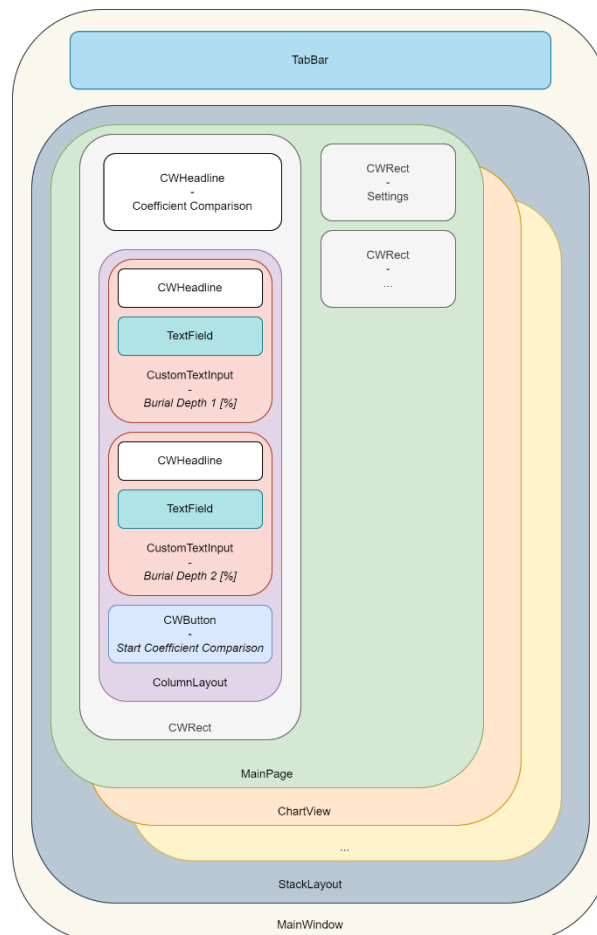


Fig. 47: GUI Layout.

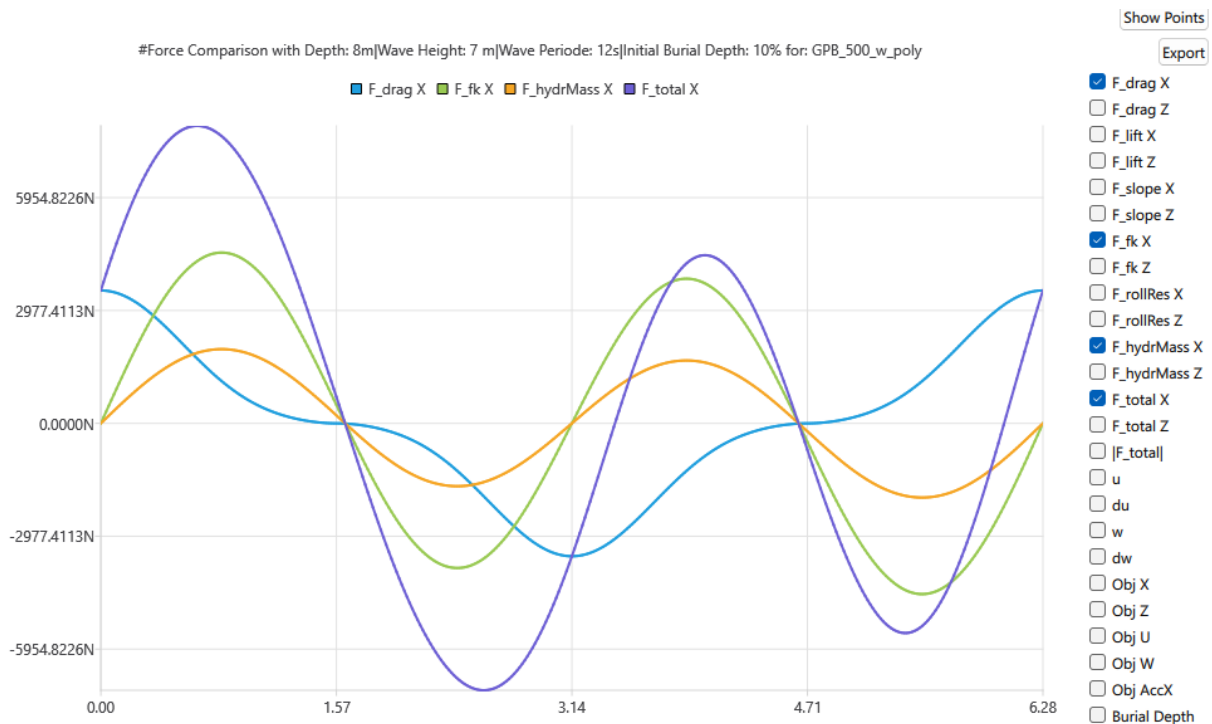


Fig. 48: Example of a force comparison simulation displaying graphs in the GUI.

Fig. 48 displays an example view of the GUI which is able to display recorded graphs during simulation. Which graphs shall be shown is configurable and the graphs can be freely zoomed.

3.13.5 Core-Plugin Scheme

The Business Logic is designed as a Core-Plugin scheme (Fig. 49). The core of the system constitutes the fundamental processes of the system. It abstracts the simulation from implementation details. The implementation details depend on specific demands in the Plugin System. The core system with its adjacent interfaces defines the requirements for those plugins.

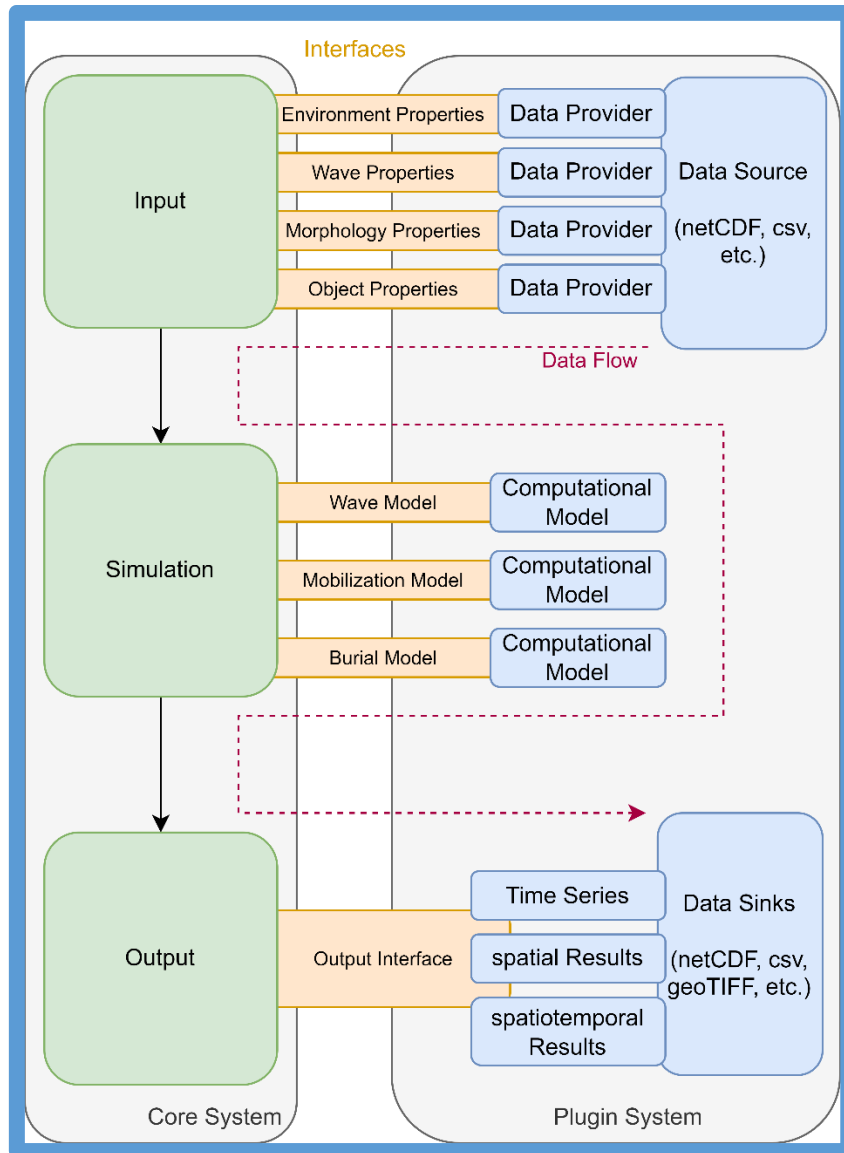


Fig. 49: Core-Plugin Scheme.

The Core comprises three integral components: Input, Simulation, and Output. The input component serves as the gateway to external data sources, defining interfaces for a variety of data formats. Its role is to facilitate seamless interaction between the core system and external data sources (Section 3.13.6).

The simulation component establishes interfaces for wave-, mobilization-, and burial models. This component adopts a modular approach to streamline the integration of new simulation models, enhancing adaptability and scalability.

The output component defines the output interface, allowing the attachment of multiple data sinks simultaneously (Section 3.13.7).

This design architecture facilitates the dynamic addition of functionality, efficient data management, and versatility in handling diverse data sources and output formats. A user-friendly graphical interface empowers users to effortlessly select their preferred data sources, simulation models, and output formats, enhancing accessibility and user experience.

3.13.6 Input Interfaces

Fig. 50 depicts the Input Interfaces (green) as well as possible derived objects. The method of accessing essential data for the simulation is encapsulated within these Input Interfaces. They ensure uniformity, irrespective of the specific implementation details. Simultaneously, a simulation object exclusively interacts with these standardized interfaces. The versatility of this approach is underscored by its capacity to accommodate diverse methods or functionalities in the actual implementation, granted that they adhere to the specified interface requirements.

Advantages of this framework include enhanced adaptability, as the simulation remains insulated from changes in the underlying implementation. This promotes ease of maintenance, allowing for the incorporation of varied techniques without disrupting the overall functionality. Additionally, the standardized interfaces foster modularity, enabling efficient collaboration among different components within the simulation system. This approach not only streamlines the development process but also facilitates future enhancements and updates.

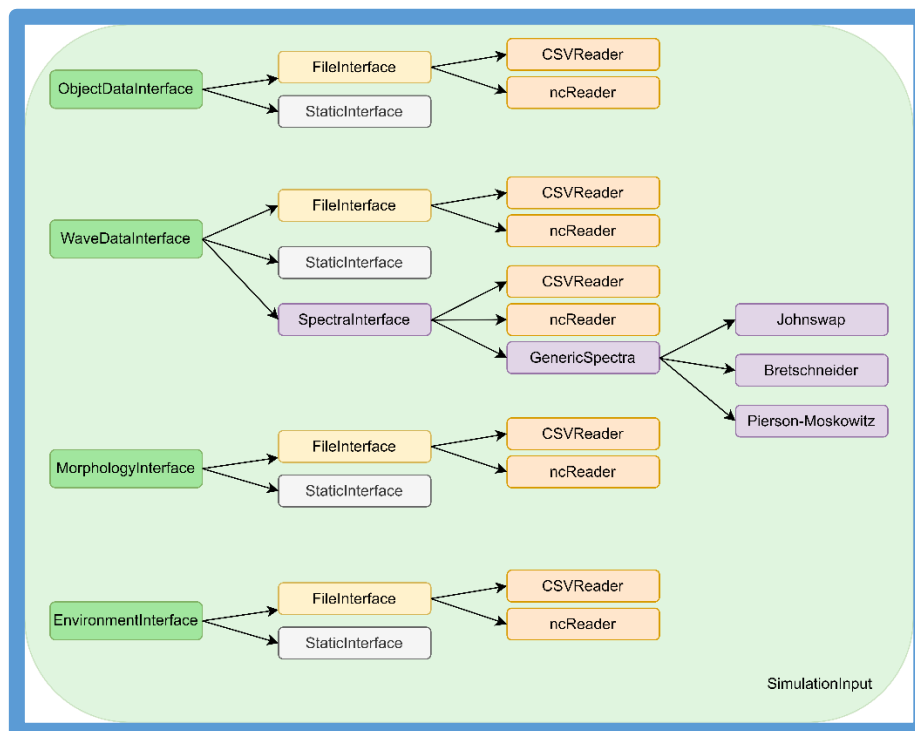


Fig. 50: Possible derived Inputs.

3.13.6.1 Objects

Objects are essentially defined by their inherent characteristics. The Object Data Interface lays out a specific set of data requirements that implementations need to meet. This interface is like a data hub, and the input section of the simulation relies on it. While the interface doesn't explicitly specify the type of data to be returned, it assumes a common return type (T) for all properties.

For every property request made through this interface, an object ID needs to be provided as an argument. Since simulations often involve a mix of different objects, an Object Data implementation has the flexibility to provide properties based on the unique object ID.

Implementations can also choose to focus on just one object's properties, ignoring the object ID argument when necessary. This adaptability makes the system more versatile and customizable to various simulation scenarios.

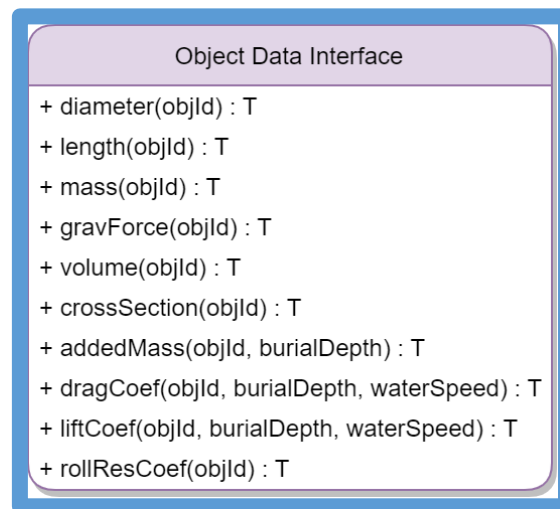


Fig. 51: UML Representation of the Object Data Interface.

The coefficients related to added mass, drag, and lift of objects are not static properties; they dynamically depend on the object's state. Consequently, the interface introduces extra parameters for the current burial depth and water speed. Implementations can leverage these additional parameters for enhanced flexibility and accuracy.

3.13.6.2 Wave Data Interface

The Wave Data Interface (Fig. 52) defines a template interface class named `WaveDataInterface`, specifically crafted to facilitate access to diverse properties of wave data. Functioning as a template class, `WaveDataInterface` accommodates any data type `T`, such as float or double. Within the Wave Data Interface, several pure virtual functions demand implementation by any class inheriting from it. These functions requires two parameters: a `LatLon<T>` structure denoting a geographical location with latitude and longitude coordinates, and a `std::chrono::time_point<std::chrono::utc_clock>` representing a specific point in time.

The primary objective of the functions encapsulated in the Wave Data Interface class is to provide various properties of wave data at a specified location and time. These properties include significant wave height (`sigHeight`), wave period (`periode`), wave frequency (`frequency`), averaging time for statistical data (`time`), count of waves averaged for statistical analysis (`count`), maximum wave height (`heightMax`), wave direction (`direction`), wave number (`waveNumber`), significant wave amplitude (`sigAmplitude`), and maximum wave amplitude (`maxAmplitude`).

In essence the `WaveDataInterface` class delivers a versatile and expandable interface for accessing wave data. Any class aiming to provide wave data can inherit from `WaveDataInterface` and tailor its functions to appropriately return the relevant data. This design promotes adaptability, allowing seamless integration of diverse data sources and properties within the domain of wave analysis.

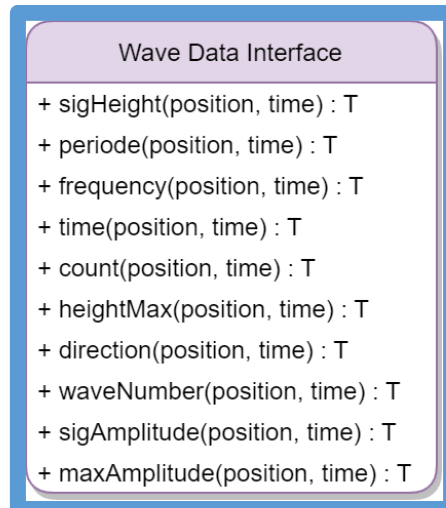


Fig. 52: UML Representation of the Wave Data Interface.

3.13.6.3 Morphology Data Interface

The Morphology Data Interface (Fig. 53) provides the definition of how to provide bathymetry data. The bathymetry data needs to include the underwater topography information water depth and bottom elevation (see Fig. 32) for the simulation. Basic implementations of the interface can choose to omit the position and/or the timestamp to provide simple inputs for the simulation. For simulations representing real world applications a water depth and bottom elevation should be given with an appropriate spatial and temporal resolution.

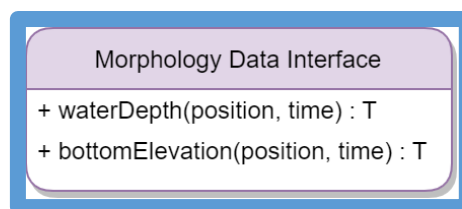


Fig. 53: UML Representation of the Morphology Data Interface.

3.13.6.4 Environment Data Interface

The Environment Data Interface (Fig. 54) is a flexible class designed for accessing environmental data at specified geographical locations and times. It establishes a standard framework through pure virtual functions, mandating that inheriting classes implement these functions. The functions take two parameters: a LatLon structure representing geographical coordinates and a `std::chrono::time_point<std::chrono::utc_clock>` indicating a specific time. Importantly, these parameters are flexible, potentially allowing implementations to ignore them if not relevant. The functions include diverse environmental properties such as water density, sediment density, grain diameter, roughness length, critical slope, current velocity, and current direction. This design ensures adaptability, allowing inheriting classes to seamlessly integrate and provide specific data based on their unique requirements.

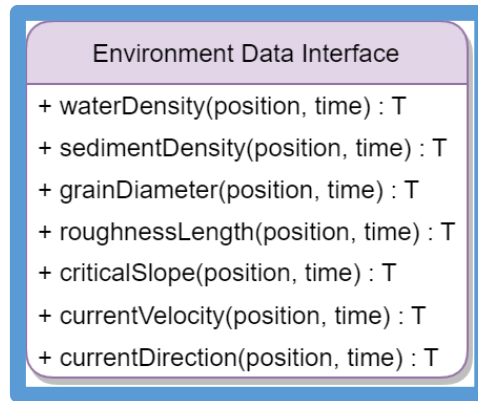


Fig. 54: UML Representation of the Environment Data Interface.

3.13.6.5 Input Data Implementations

The Interfaces described in 3.13.6.1 to 3.13.6.4 can be implemented using standard tools provided by the Program Logic (3.13.4.2) of the Software Architecture. These tools also include file readers, like CSV and NetCDF reader or provide data handling algorithms. Some examples of implementations are presented below.

The Object Library

The Object Library (Fig. 55) is an implementation of the object data interface. It encapsulates known objects and their properties. Therefore, the class provides functions to dynamically add objects based on different representations. Each function returns the id of the object within the object library.

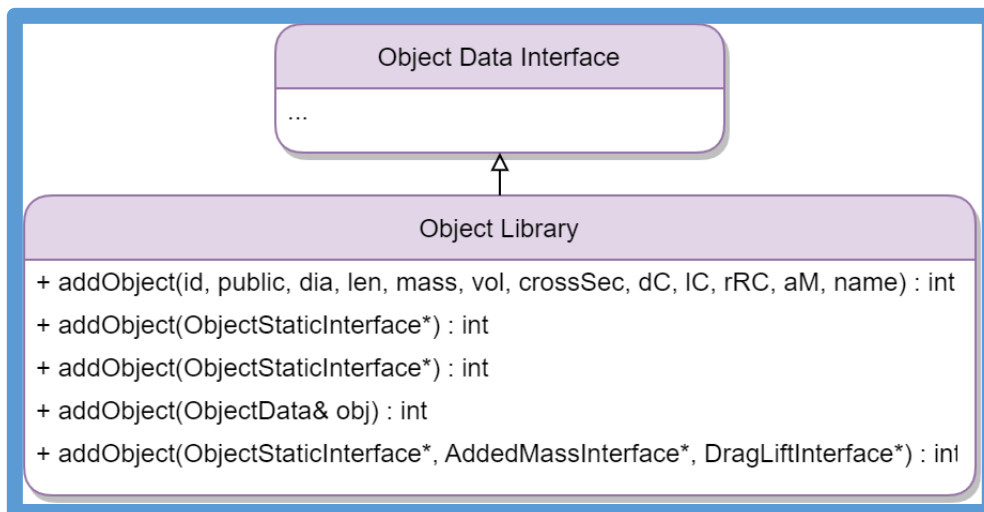


Fig. 55: UML Representation of the Object Library.

The Object CSV Model

The Object CSV Model provides an implementation for loading object properties from a CSV file. A CSV (Comma Separated Values) file is a tabular data format, where individual records are represented by rows and each column corresponds to a specific field or attribute. These files serve as a straightforward means to exchange simple data between diverse software applications, owing to their simplicity and extensive compatibility. However, when it comes to

more intricate data, such as information with temporal and spatial resolutions, CSV files prove unsuitable for efficient sharing or provisioning.

The MorphologyNCModel

The MorphologyNCModel (Fig. 56) class provides a way to interact with morphology data stored in NetCDF format. It inherits from Morphology Data Interface and NCInterface to provide a specific implementation for NetCDF files. It uses NetCDFHandler objects and functions from the NCInterface to handle the actual reading of the files, and interpolating data. The MorphologyNCModel implements the functions defined by the Morphology Data Interface to access the water depth and bottom elevation.

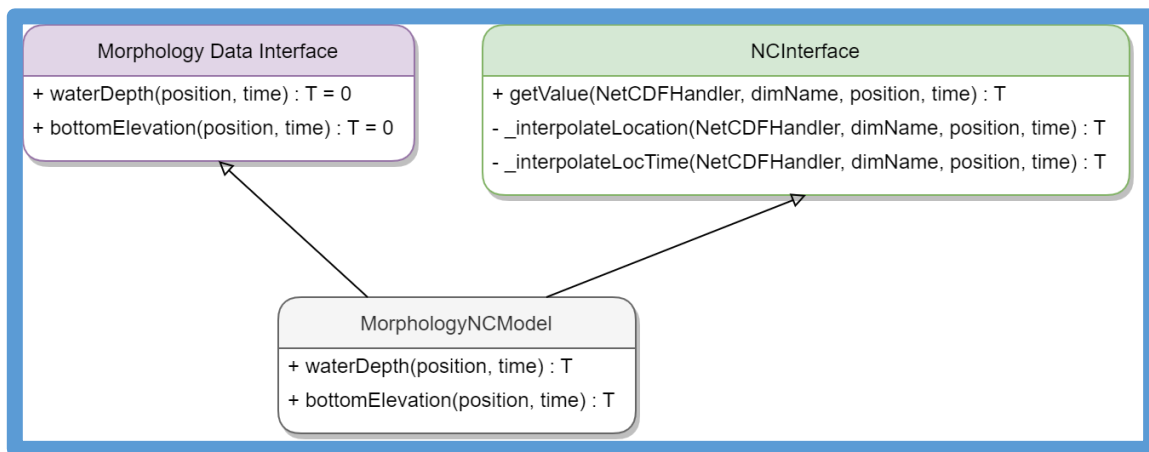


Fig. 56: UML Representation of the MorphologyNCModel.

3.13.7 Output Interface and SimOutput Class

The output concept involves the storage of simulation data through the SimOutput class designed to interface with multiple output interfaces (see Fig. 57). The class is templated, accommodating various data types (T) that align with the simulation output. It features a flexible vector for storing multiple Output Interfaces. The copy constructor is deleted in the SimOutput class to prevent potential data corruption issues by limiting access to the output interfaces. The critical function, 'store,' is responsible for storing data of type T, associating it with specific attributes like location, time, output type, and object ID. To ensure thread safety, the class utilizes private data members: a vector (_outList) containing output interfaces and a mutex (_dataMutex) to synchronize access to these interfaces.

The OutputInterface concept establishes a template interface class designed for storing and retrieving diverse output data types. Its templated nature allows adaptation to various data types (T), aligning with the context of the output data. The class incorporates an enum (VALUE_TYPE) categorizing different types of output data. Two crucial pure virtual functions, 'store' and 'getValue,' define the interface's core functionality. 'Store' associates a value of type T with specific data attributes, including output type, dataset, location, and time. 'getValue' retrieves a value based on specified parameters. OutputInterface, by providing a flexible framework, enables inheriting classes to implement necessary functions for storing and retrieving data according to their unique requirements.

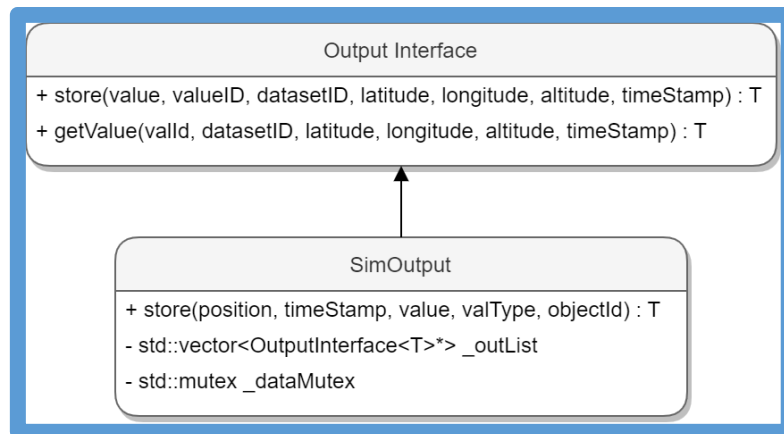


Fig. 57: UML Representation of the Output Concept.

3.13.8 Simulation Configuration

The SimConfig class serves as a robust and versatile tool for managing configuration data in a simulation environment. Templated to fit the simulation with various data types (T), it encapsulates key aspects of simulation configuration through nested structures. The SIM_ID structure encapsulates a unique identifier for a simulation, while the SIM_TYPE enumeration defines different simulation types, such as ALL, OBJECTS, and WAVE_HEIGHT.

Within the SimConfig class, the SIM_TIME structure encapsulates temporal aspects of the simulation configuration. It efficiently represents the simulation timeframe by utilizing two std::chrono::time_point<std::chrono::utc_clock> instances (start and end).

The SIM_GRID structure serves as a pivotal component, defining the spatial boundaries and resolution of the simulation grid. It employs two LatLon<T> structures (upperLeft and bottomRight) to delineate the geographical bounds of the grid. The Vector3D<T> structure (resolution) complements this by specifying the desired resolution of the simulation. This spatial resolution does not necessarily need to fit the resolution of given input data.

The SIM_OPTIONS structure encompasses various configuration options essential for tailoring the simulation. These options include waveDiscretion, providing control over the phase resolution of waves for mobilization calculations; initialBurialDepth, governing the starting depth for burial processes; skipSimMobilization, allowing flexibility in mobilization simulations; and optimizeSim, offering optimization capabilities for the simulation process. By encapsulating these features, SimConfig provides a comprehensive and organized approach to configuring simulations, enabling users to tailor various aspects of the simulation environment.

An optional Shape class can be set in the SimConfig. This class allows to refine the SIM_GRID by defining an area using multiple points. Only locations within the defined shape will be simulated.

3.13.9 C++-style Interfaces

The main parts of the software are completely encapsulated and provide their functionality using C++-style interfaces. An interface is a set of related functions that define a specific behavior or contract. In the C++ programming language, interfaces are implemented using abstract classes, which are classes that contain at least one pure virtual function. Some of the advantages of using interfaces in C++ include:



- polymorphism (the ability of different objects to respond to the same message in different ways)
- clear and well-defined contract between different components of the system or between systems
- modular and independent components
- readability and understandability: by creating abstractions that hide details of the implementation
- flexibility, extensibility and portability: interfaces can be implemented by different classes (from different programming languages), which helps to improve the flexibility and extensibility of the system
- reduce code duplication and improve the overall maintainability: by defining common functionality that can be shared by multiple classes
- interoperability: interfaces can be implemented by classes from different modules or libraries
- testability: a clear separation between the interface and the implementation of a class helps to improve the testability of the code by allowing mocks or stubs
- reliability and stability: defining the public API of a class, helps to improve the reliability and stability of the system by preventing clients from accessing or modifying the internal state of a class

3.13.10 Templates

The business- as well as the program logic is mostly templated. In C++, a template is a mechanism that allows an object to work with any data type. Templates are typically used to implement algorithms or data structures that can be used with different types of data without having to write separate versions of the code for each type. The templates in this software allow to decide between calculating the algorithms in single- or in double precision at run-time. Some other advantages of using templates in C++ include:

- Performance:
 - compile-time polymorphic code, which can be optimized by the compiler for the specific data type used at runtime
 - efficient and generic code without the need to use runtime reflection or dynamic dispatch
 - generic code that can be optimized by a compiler (compared to using runtime polymorphism or generic programming techniques)
- Reliability:
 - type-safe, as the type-checking is done at compile time, rather than at runtime
- Flexibility, reusability, extensibility:
 - code that can work with different data types, without the need to write separate versions of the code for each data type
 - write generic algorithms and data structures that can be used with a wide range of data types, without the need to write specialized versions for each data type

- easy extension to support new data types, without the need to modify the existing code

3.13.11 Multithreading

In computer programming, multithreading is the ability of a scheduler (provided by an operating system) to provide multiple threads of execution concurrently. This allows a program to perform multiple tasks simultaneously within a single process. The operating system is responsible for distributing the threads on multi-processor systems.

Multithreading has an important role on the responsiveness of a system. Multithreading allows the program to continue executing other tasks even if one or more threads are blocked or waiting for a slow operation to complete. This improves the overall responsiveness of the program, as it can continue to respond to user input or perform other tasks while waiting for the blocked thread to finish.

Furthermore, by executing multiple threads concurrently, a program can make better use of the CPU's processing power and memory resources, leading to improved performance. This is especially useful when the program needs to perform multiple tasks simultaneously, such as performing (multiple) calculations and handling user input at the same time. Especially for simulations with a lot of inputs (like different objects or environments), concurrently running those simulations will improve the overall processing time heavily.

Multithreading is implemented using the thread pool pattern. A thread pool is a collection of worker threads that are used to perform tasks concurrently. The idea behind a thread pool is to have a pre-allocated group of worker threads that are available to perform tasks as they are submitted. This can be more efficient than creating a new thread for each task, as creating and destroying threads can be time-consuming. When a task is submitted to a thread pool, it is placed in a queue. A worker thread from the pool retrieves the task from the queue and executes it. Once the task is complete, the worker thread returns to the pool and waits for the next task to be added to the queue.

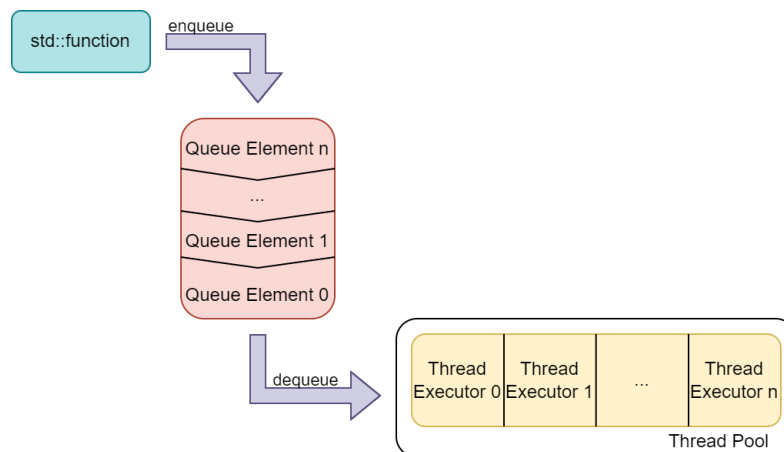


Fig. 58: Thread Pool Scheme.

Fig. 58 shows the principle of the implemented multithreading component. The tasks are added to a queue in form of a C++ `std::function`. Each thread executor waits for a new task using the C++ `std::condition_variable`. If a new task arises or the queue is still not empty a thread executor dequeues the `std::function` and executes it. The work done in these functions



are parallelizable calculations of mobilization, burial and morphology changes for e.g. different objects or different locations. Every work which does not depend on the outcome of a previous calculation can be easily parallelized. Dependencies of functions are synchronized between threads using `std::mutex` and `std::lock_guard`.

As the software performs a lot of expensive computations, the scalability can also be improved by using caching and pre-computation. By storing the results of expensive computations in memory, recomputing can be avoided which will greatly improve the performance.

3.13.12 Bazel Build System

Bazel is a powerful and versatile build system addressing complex needs of large-scale software development projects. Renowned for its efficiency and scalability, Bazel excels in managing the build and test processes for projects with diverse languages and dependencies. One of its key strengths lies in its ability to build projects incrementally, significantly reducing build times by intelligently determining which parts of the codebase need recompilation. Bazel also provides a unified and consistent build environment across different platforms, ensuring reproducibility and reliability. Furthermore, Bazel promotes code sharing and collaboration by enabling the creation of hermetic and shareable build configurations.

Structuring a code base with Bazel involves defining a set of rules and dependencies that specify how the project components are organized and interact. Bazel uses a BUILD file for each directory to declare targets, such as libraries or binaries, and their dependencies. This declarative approach allows developers to explicitly express the relationships between different modules, making it easier to understand and maintain the project structure. Overall, the process of structuring a code base with Bazel emphasizes clarity, modularity, and efficient dependency management, contributing to a more maintainable and scalable software project. Within the Bazel build system, the BUILD file emerges as a foundational component, serving as a blueprint for the systematic organization and construction of code within a designated directory. The structure of a BUILD file will be explained with the following example:

```
cc_library(  
    name = "moduleB",  
    srcs = glob(["moduleB/*.cpp"]),  
)  
  
cc_library(  
    name = "moduleA",  
    srcs = glob(["moduleA/*.cpp"]),  
    deps = [  
        ":moduleB",  
    ],  
)  
  
cc_test(  
    name = "moduleA_test",  
    srcs = ["moduleA/moduleA_test.cpp"],  
    deps = [  
        ":moduleA",  
    ],  
)
```



```
    ],  
  )  
  
  cc_binary(  
    name = "executable",  
    srcs = ["main.cpp"],  
    deps = [  
      ":moduleA",  
    ],  
  )
```

Library ModuleB:

The `cc_library` rule defines a C++ library target named `moduleB`. This target encapsulates source files, denoted by the `glob(["moduleB/*.cpp"])` directive, within the `moduleB` directory.

Library ModuleA:

Subsequently, another `cc_library` rule is employed to define a C++ library target named `moduleA`. This library encompasses source files from the `moduleA` directory and declares a dependency on `moduleB` with the reference `":moduleB"` within the `deps` attribute.

Test Target for ModuleA:

A `cc_test` rule is introduced to define a C++ test target named `moduleA_test`. This target includes test source files, indicated by the `srcs` attribute (`"moduleA/moduleA_test.cpp"`), and declares a dependency on `moduleA` with the reference `":moduleA"` within the `deps` attribute.

Executable Target:

Additionally, a `cc_binary` rule is presented, defining a C++ binary target named `executable`. This target is linked with source files from `"main.cpp"` and is explicitly dependent on `moduleA` through the `deps` attribute.

This configuration adheres to established best practices in software architecture, where libraries encapsulate reusable components, and binaries depend on these libraries to facilitate executable functionality. The modular structure enables maintainability, code reuse, and a clear delineation of dependencies within the project.

3.13.13 Continuous Integration

Continuous integration (CI) is a software development practice in which code changes are regularly merged into a central repository and verified against automated tests and other checks on the resulting codebase. The goal of CI is to detect and prevent conflicts and other issues early in the development process. In this CI workflow, changes are committed to the central GIT repository on a frequent basis. Whenever a new commit is made, the CI system automatically builds the code and runs a suite of automated tests to ensure that the changes have not introduced any regressions or other problems. If the tests pass, the code is considered stable and other CI jobs like deployment or building of installers are triggered.

The CI system is implemented using Jenkins⁶, an open-source continuous integration (CI) and continuous delivery (CD) tool that is widely used for automating the build, test, and deployment of software.

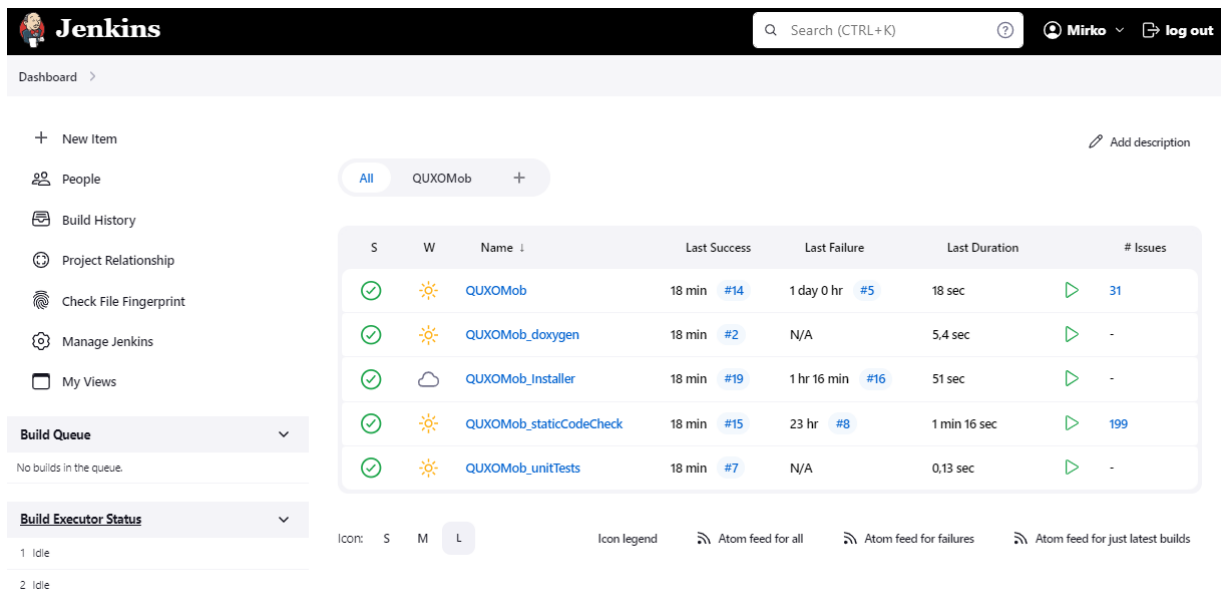


Fig. 59: Jenkins CI Setup.

Fig. 59 displays the main Jenkins jobs at the current project stage. The QUXOMob job regularly polls the main GIT repository for newly committed changes. In case of new commits the software is built on the appropriate build executor. The build output is analyzed for errors and warnings. These errors and warnings are stored for each build for comparing of build and progress analysis.

A successful QUXOMob job triggers the static code checks and unit test jobs. The static code check job uses cppcheck⁷ which is an open-source static code analysis tool for C and C++ code. It is designed to detect bugs, defects, and other issues in C and C++ code that may not be easily found by other methods, such as testing or debugging. Cppcheck works by analyzing the source code of a program and checking it against a set of rules that are designed to identify common coding errors, such as memory leaks, buffer overflows, uninitialized variables, and other issues. It can also check for compliance with coding standards and best practices, such as the C++ Core Guidelines⁸. These issues are stored into an xml file which is analyzed and visualized by Jenkins. The issues are stored for each job run and can be compared between jobs.

Unit tests are small, individual tests that are designed to test the functionality of a specific piece of code, such as a function or a method. By regularly running unit tests it can be ensured that the code is correct and works as intended. The unit tests are composed utilizing the Google Test framework and executed through the Bazel test command within the Continuous Integration System. This practice ensures a systematic evaluation of individual software components. Google Test offers a versatile set of features, including test fixtures, parameterized tests, and assertions, contributing to the comprehensive testing of the codebase. The integration

⁶ <https://www.jenkins.io/>

⁷ <https://cppcheck.sourceforge.io/>

⁸ <https://isocpp.github.io/CppCoreGuidelines/CppCoreGuidelines>

of Google Test with Bazel and Jenkins streamlines the testing procedures, fostering an efficient and reliable software testing environment. The graphical representation of test outcomes, accessible through Jenkins, provides a clear and concise overview of job statuses.

After the test jobs successfully finish, they trigger the deployment phase. For now, an installer is built (QUXOMob_Installer) and the documentation is generated (QUXOMob_doxygen) at the end of the continuous integration chain. Future extensions could include the automated build of installers for different platforms or the deployment of build artifacts into other builds or software.

4 Results and Discussion

During previous work, a mobilization model to compute the mobilization return time of UXO was developed. In a first step, this model was applied on the AoI and OoI, using artificial dimensionless coefficients for the OoI. The waves applied to the model were taken from the waverider buoy about 10 km offshore of the AoI. As no wave transformation model was currently available to be applied to the waverider data (in year 1 of the project), these waves were directly applied on the AoI. Hence, this does not represent a physically correct boundary condition, but the procedure is justified in that it was used to check if the bathymetry and wave data as well as the objects data were compatible with the UXOmob 4.0 model, confirming this procedure was justified. The mobilization return times from the initial run of the model for the 7.2 inch Demolition Rocket were thus shown in Fig. 60. Here the color shows the return time, which is a purely statistical value describing the mean time between two mobilizations. As can be seen, the existing model is applicable to the AoI but the values are absolutely not realistic. The reason for this is mainly found in the wave data, which as discussed above are not realistic in shallow water nearshore and with the use of the artificial dimensionless coefficients, of which specific values will be derived in year 2 of the project in Task 1.2.

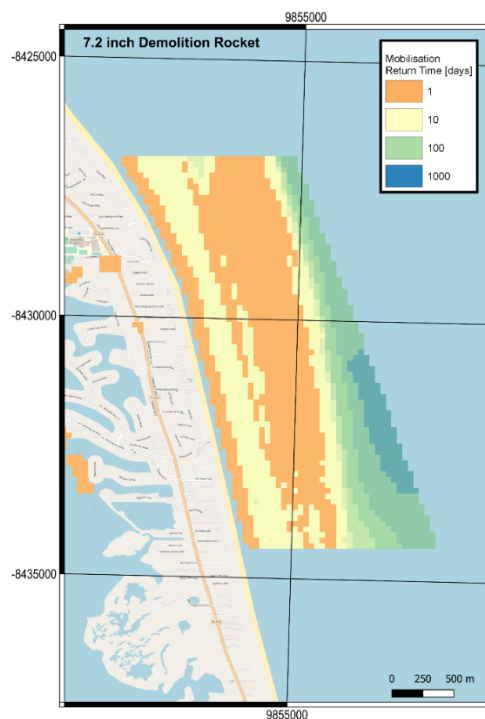


Fig. 60: Preliminary mobilization return time analysis, showing the model can be applied in the AoI.

For the wave data, further analyses are necessary as no wave data with high (smaller than 100 m) spatial resolution are available from NOAA and other public sources. Thus, it was

decided to consider whether additional simulations could be made by the project team. Furthermore, we asked U.S. Army Engineering and Support Center Huntsville (CEHNC) whether there were any additional near shore measurements, using waverider and/or ADCP measurements inside the AoI. No additional data was available at this time.

Furthermore, the return time approach in itself is not ideal regarding the requirements of the CEHNC as this value provides a good input to a mobilization planning tool but does not fulfil the requirements during monitoring. Additionally, it will be difficult to apply the return time method on time-evolution of object burial and migration paths of mobilized objects.

4.1 Combining the Burial and Mobilization models

In Section 3.8, the new combined software was described in detail. In a first test simulation to prove the functionality, artificial (non-realistic) wave data and environmental data were applied. The object data are used from Tab. 1, whereas the dimensionless coefficients are still preliminary values from similar objects. As mentioned, the correct values will be utilised later in the project for the final report. The results of the test simulation are shown in Fig. 61. Here the red stepped graph shows the maximum wave height, derived from H_s , and the black stepped graph shows the corresponding peak wave period. The burial depth of the different objects is shown by the colored graphs, noting that the initial burial depth was set to 50% of the diameter of the objects. The stars show the mobilization of the individual objects. As the 7.2 inch Demolition Rocket is not mobilized at all, no star is shown for this object. The burial time under the simulation is about 1.5 hours from 50% to full burial which seems quite fast and the time-evolution aspect was further analyzed in year 2 of the project.

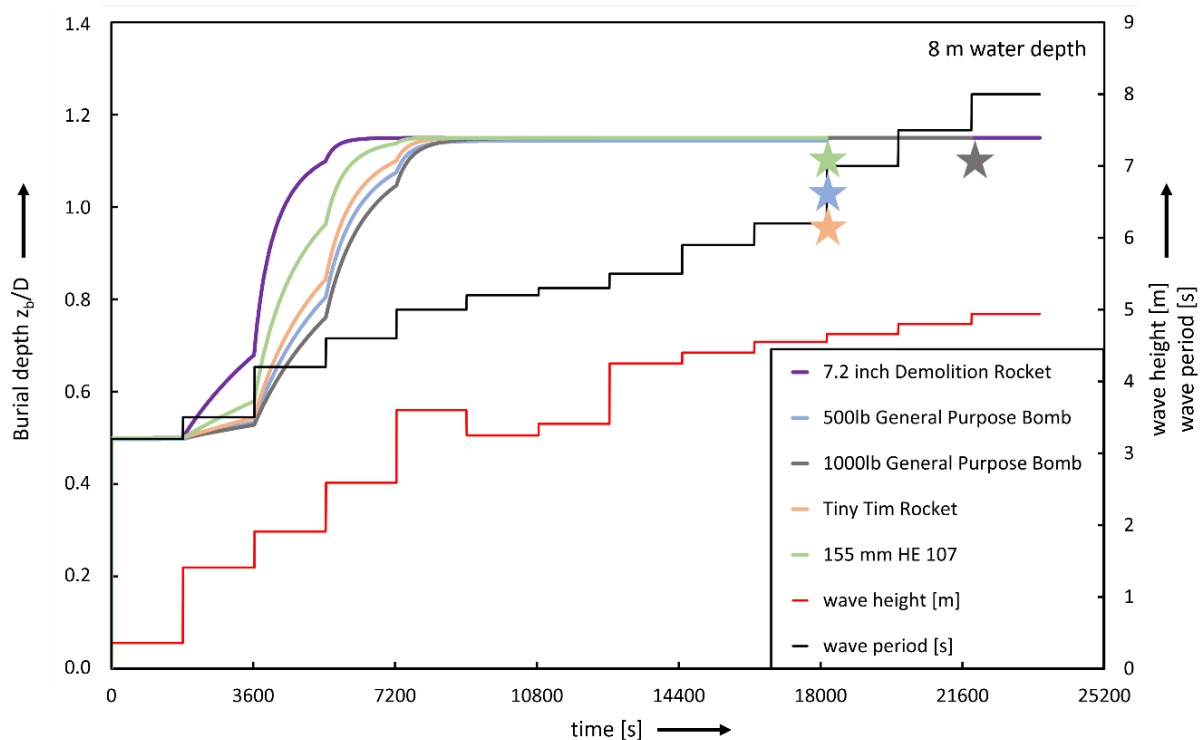


Fig. 61: Burial depth and point of mobilization for artificial, increasing wave action.

As already mentioned earlier, the **first Go/No-Go Decision was set to Go**. Further improvements of the model are nevertheless necessary such as:

- Including wave spectra
- Including the real dimensionless coefficients

- Multi-Threading for later application on spatial data
- Improved scour-burial time-development
- Include seabed level change
- Including spatial data and spatial seabed level change
- Include migration

These improvements have been made and will be further supported by the findings from the literature reviews and simulations that are also under simultaneous development in this project.

4.2 Implementation of seabed morphology

The implementation of the seabed morphology is crucial for the acceptance of the model for the application on live sites. Thus, the morphodynamics is computed in TELEMAC and included into the UXOmob simulation software. As shown in Section 3.13, the software was completely re-designed to significantly improve the performance and thus allow the handling of spatial data and huge time series. As a proof of concept, a local seabed change was applied to the burial and mobilization analysis, already shown in Fig. 61. The result is shown in Fig. 62 for just two objects for a better understanding. Here again, different artificial wave heights (red) and wave periods (black) were applied to the objects. Additionally, the change of the seabed level dz , starting at 8 m water depth is shown in the yellow line in the graph.

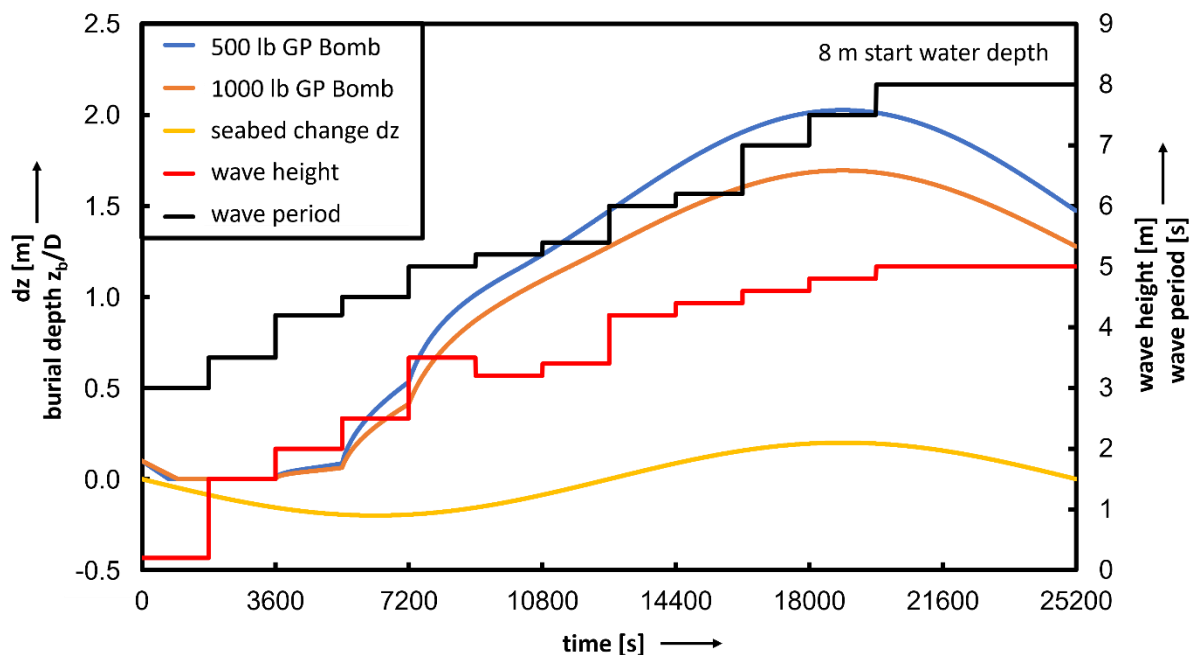


Fig. 62: Burial depth for artificial, increasing wave action and a change of the seabed level.

The seabed change was defined by sine function, starting with an erosion of up to 20 cm of sediment, followed by an accumulation of up to 20 cm of sediment. As the burial depth of the objects starts with $z_b/D = 0.1$, an erosion of sediment will lead to a reduction of the burial depth until it reaches $z_b/D = 0.0$ and if the wave action is small and does not cause scour burial. Further erosion then cannot reduce the burial depth but lead to a vertical displacement of the object, following the seafloor as it drops. Increasing wave action will start the burial



process at the individual seabed level. Additional accumulation of sediment will support the burial process and finally may lead to a burial depth, which may be larger than the equilibrium burial depth of the self burial process in DRAMBUIE (i.e. $z_b/D = 1.15$). This effect can be seen in the plot after about 10,000 seconds. As soon as the burial depth exceeds $z_b/D = 1.15$ due to morphodynamics action, the burial and mobilization simulation equations are not solved to reduce the computing time. In realistic scale it is assumed that the scour hole then is completely backfilled with sediment and the object is no longer exposed to the current. This behavior is assumed to remain until the erosion of sediment by morphodynamics reaches the object and thus the burial depth reaches $z_b/D = 1$. As soon as this situation is achieved, it is assumed that the scour hole develops again very fast, depending on the wave conditions, and thus the burial and mobilization equations start running again.

However, Fig. 62 demonstrates the proof of concept for the implementation of seabed morphodynamics and waves. The UXOmob is now able to read a spatial and temporal list of seabed level data and wave data from TELEMAC and compute the burial, re-exposure and mobilization of objects on the seafloor.

Thus, the second Go-No-Go decision point was completed successfully.

Within the remaining project time, the software will be improved for better performance and usability and the time series from the TELEMAC simulation will be processed. Furthermore, it may be considered to run the simulation automatically on the output files of TELEMAC or any other source for morphodynamics data. It also may be considered to implement a drift model for UXO.

4.3 Dimensionless coefficients

4.3.1 Drag and lift from the wind tunnel experiments

From the wind tunnel experiments, in general, decreasing drag coefficients are found with an increasing Reynolds number, except for a certain range of the so-called drag crisis. The drag crisis was specifically investigated and is described in Section 3.12.2. In Fig. 63 to Fig. 65, the measured drag coefficient and the corresponding Reynolds number are plotted for different burial depths and for the incident flow angle being perpendicular to the main axis of the objects (0 deg).

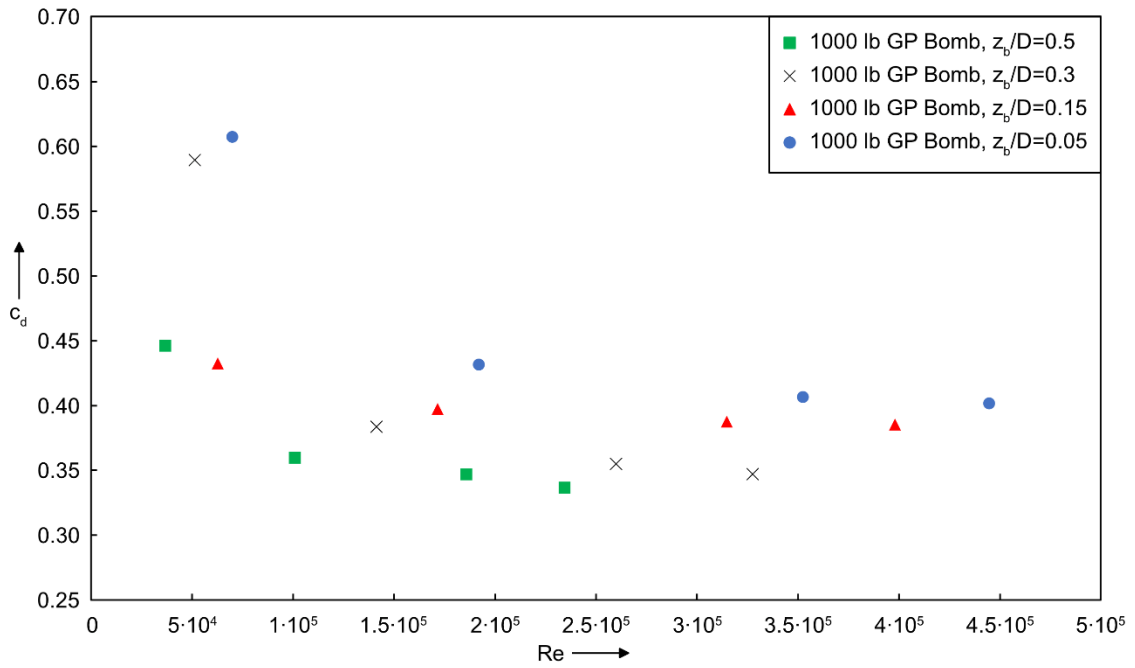


Fig. 63: Measured drag coefficient of the 1000 lb GP Bomb.

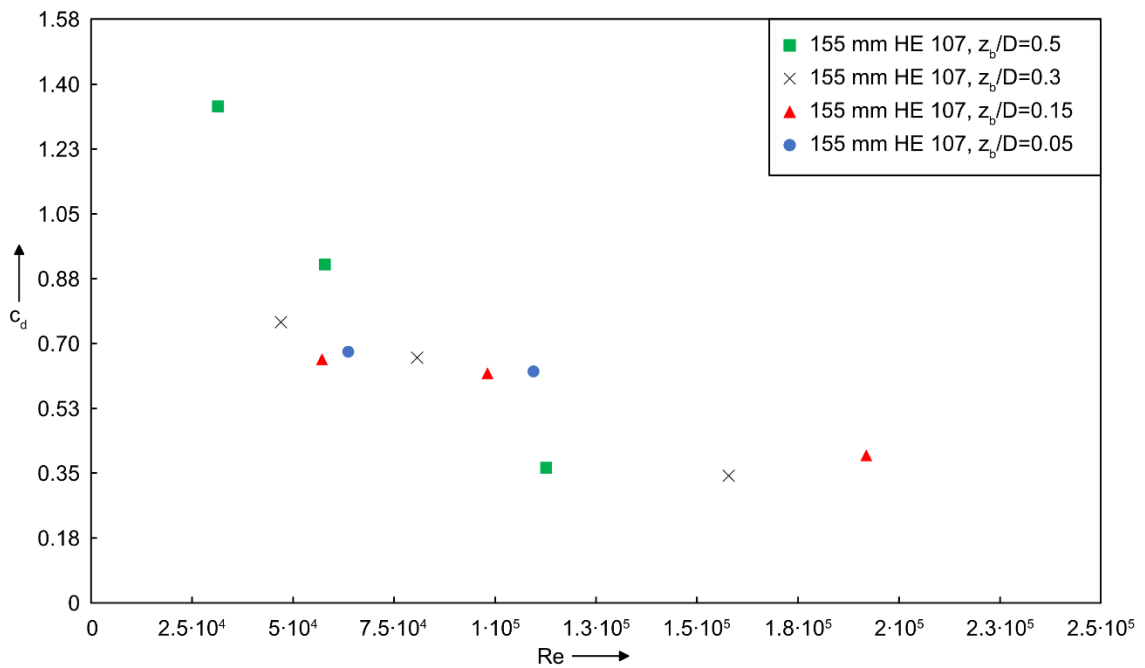


Fig. 64: Measured drag coefficient of the 155 mm, HE 107.

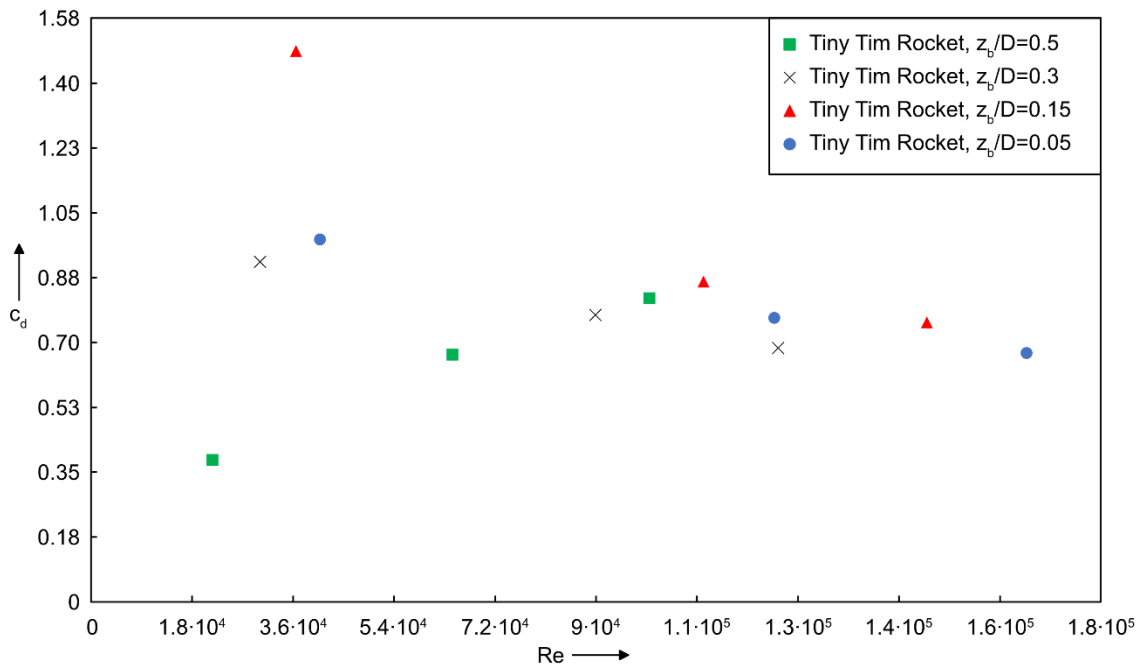


Fig. 65: Measured drag coefficient of the Tiny Tim Rocket.

4.3.2 Drag and lift from CFD

In Fig. 66 to Fig. 68, the drag coefficients for the different objects, burial depths and Reynolds number are plotted.

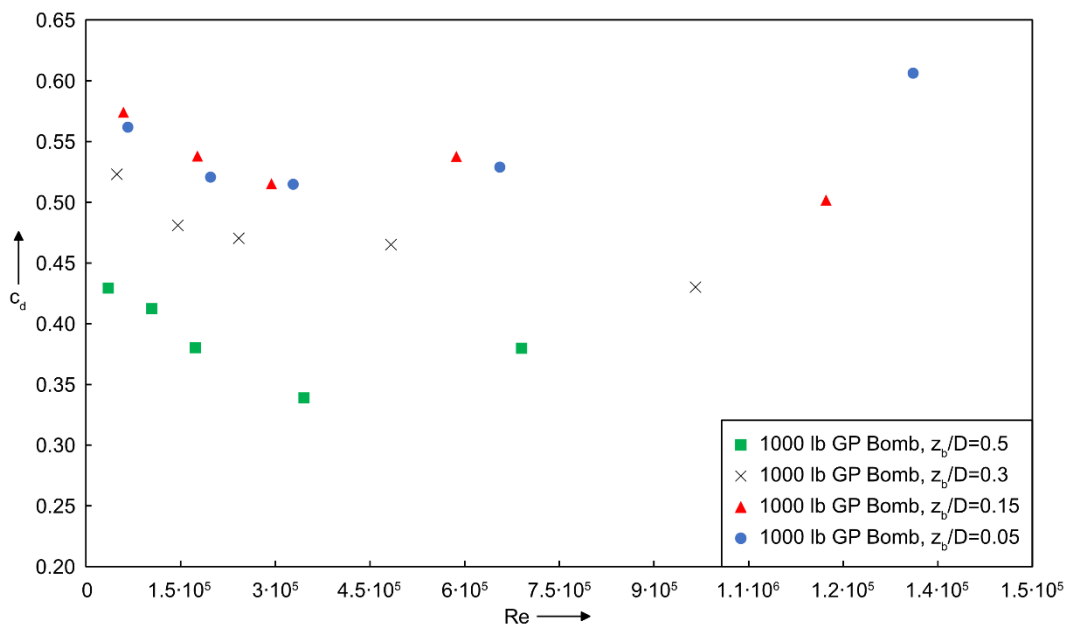


Fig. 66: Drag coefficient of the 1000 lb GP Bomb from CFD.

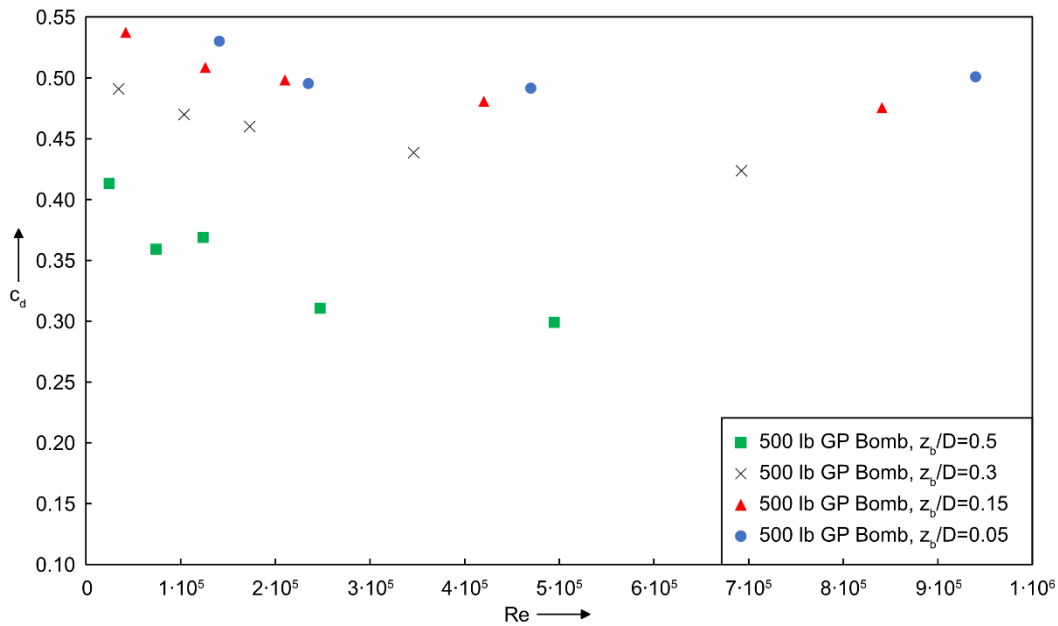


Fig. 67: Drag coefficient of the 500 lb GP Bomb from CFD.

Compared to the wind tunnel experiments, the results of the CFD are very similar and are in the range of about $c_d \approx 0.5$. Due to the change of the objects' geometry when changing the burial depth, a dependency of the drag coefficient on the burial depth of the objects also arises. This correlation occurs for all objects and must be taken into account.

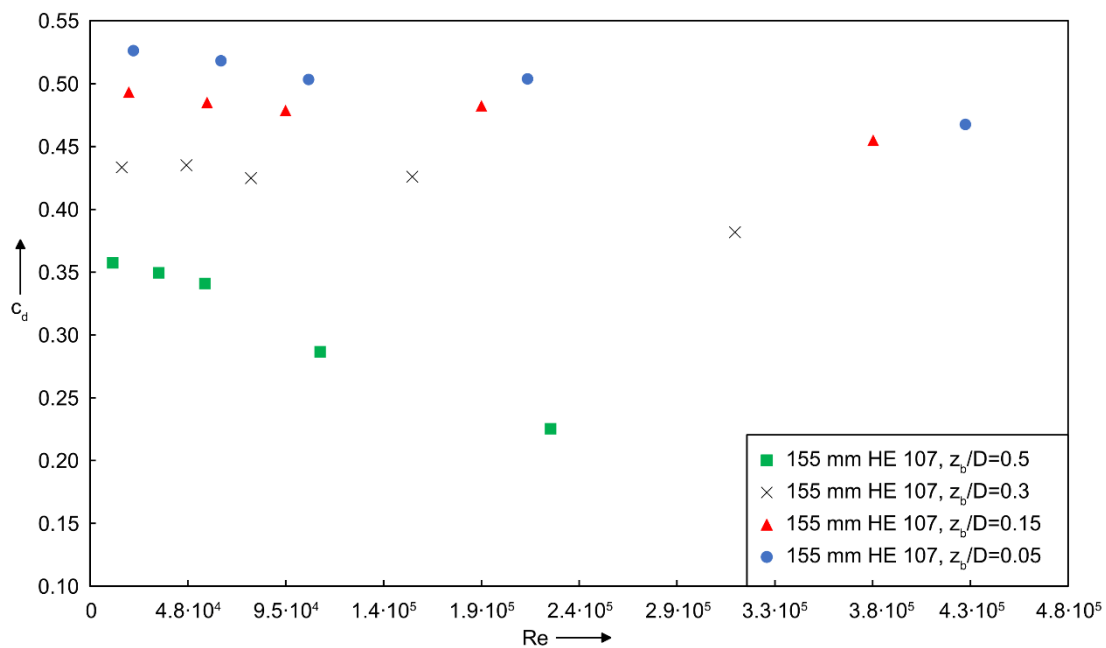


Fig. 68: Drag coefficient of the 155 mm, HE 107 from CFD.

In Fig. 69 to Fig. 71, the corresponding lift coefficients are plotted. As expected, the lift coefficient increases with increasing Reynolds number. However, the dependency of the lift coefficient on the burial depth is also evident.

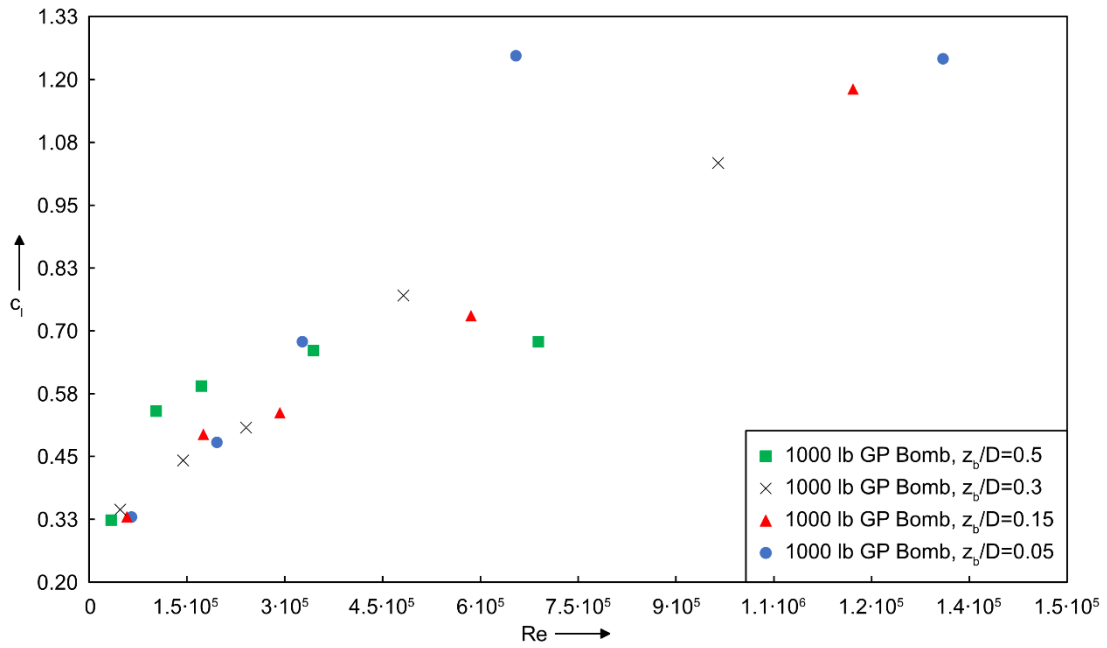


Fig. 69: Lift coefficient of the 1000 lb GP Bomb from CFD.

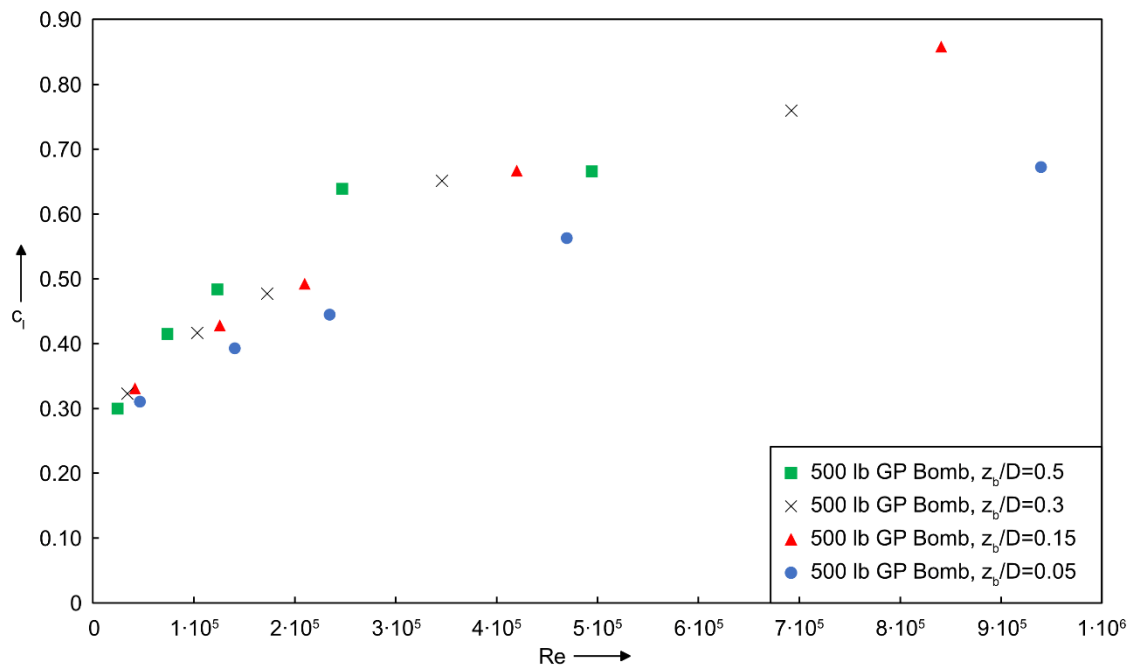


Fig. 70: Lift coefficient of the 500 lb GP Bomb from CFD.

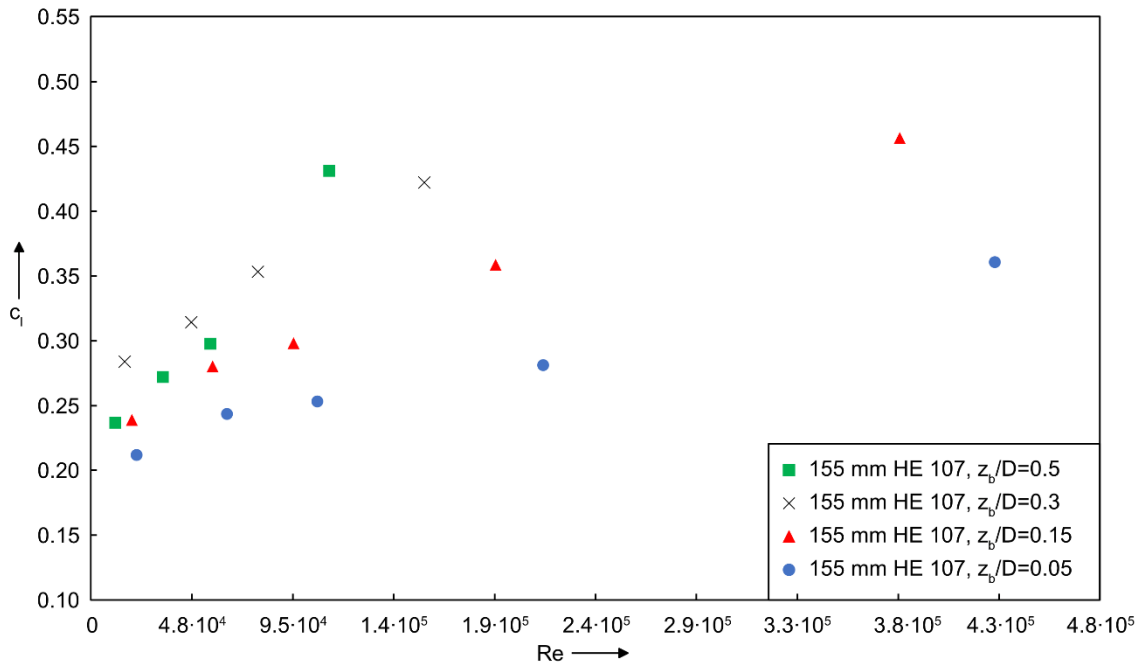


Fig. 71: Lift coefficient of the 155 mm, HE 107 from CFD.

4.3.3 Comparison of CFD and the wind tunnel experiments

The experiments in the wind tunnel were mainly intended to validate the numerical simulations or to reveal errors. Fig. 72 contains both, the drag coefficient of the 1000 lb GP Bomb from CFD and from the experiments.

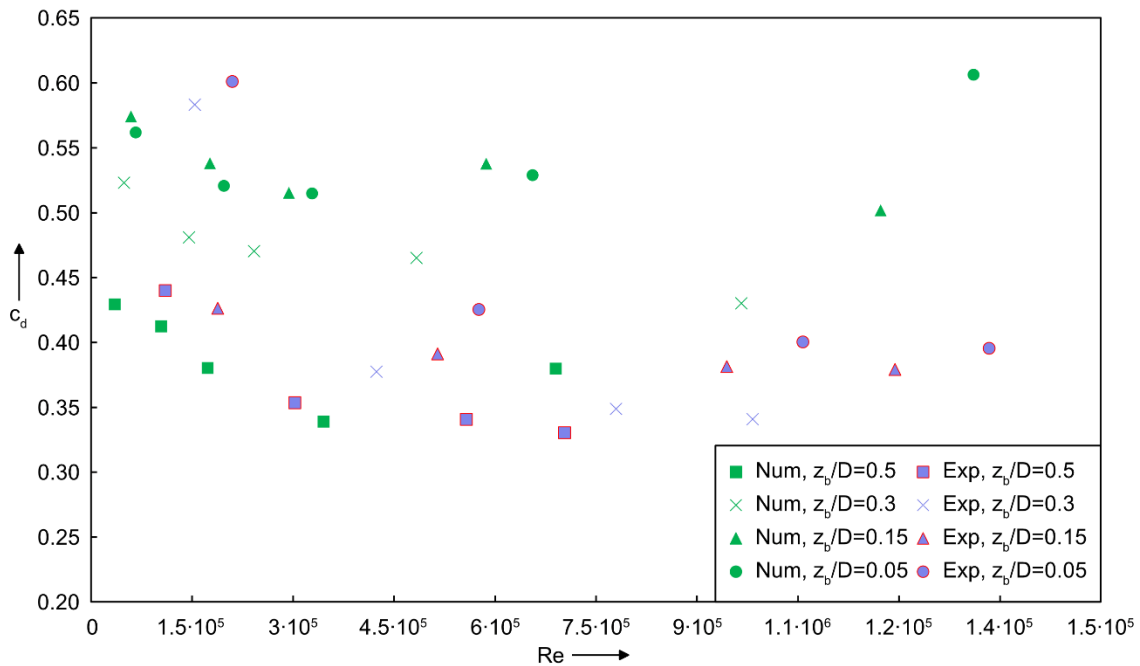


Fig. 72: Comparison of the results from CFD and the experiments for the 1000 lb GP Bomb

Comparing the results from CFD and the experiments, a high similarity of the data sets is noticeable. The effect of the drag crisis also occurs in the CFD datasets, which leads to the conclusion that the turbulent boundary layer was simulated correctly. Basically, the drag coefficient from the measurements in the wind tunnel is slightly smaller in direct comparison

to the numerical simulation at the burial depths of $z_b/D = 0.05$ to $z_b/D = 0.3$, but larger at $z_b/D = 0.5$. Small deviations can occur in the numerical simulation due to the meshing or the models used. In the wind tunnel, a slightly turbulent inflow and a small vibration of the end plate could lead to errors. However, the results show very good agreement. For this reason, the CFD results can be used to also determine the lift coefficients, which was subject to larger uncertainties in the wind tunnel due to the method of using a turntable.

4.3.4 Calculation of the polynomials for drag and lift

This chapter describes how both the numerical and the experimental results of the lift and drag coefficients can be transferred into the UXOmob software. It was particularly important to consider the dependence of the coefficients

$$c_d \text{ and } c_l = f(Re, z_b) \quad [99]$$

on the Reynolds number as well as on the burial depth during transfer. The dependence on the Reynolds number as well as on the burial depth can be explained by the changing geometry of the objects during burial.

The first step for the transfer of the results into the UXOmob program was to find a suitable function, which represents the results in the best possible way. As a simple set of curves is not able to represent the results, a more complex procedure was used. Fig. 73 exemplarily shows the polynomials found for the drag coefficient from CFD of the 1000 lb GP Bomb burial depths of $z_b/D = 0.05$ and $z_b/D = 0.5$.

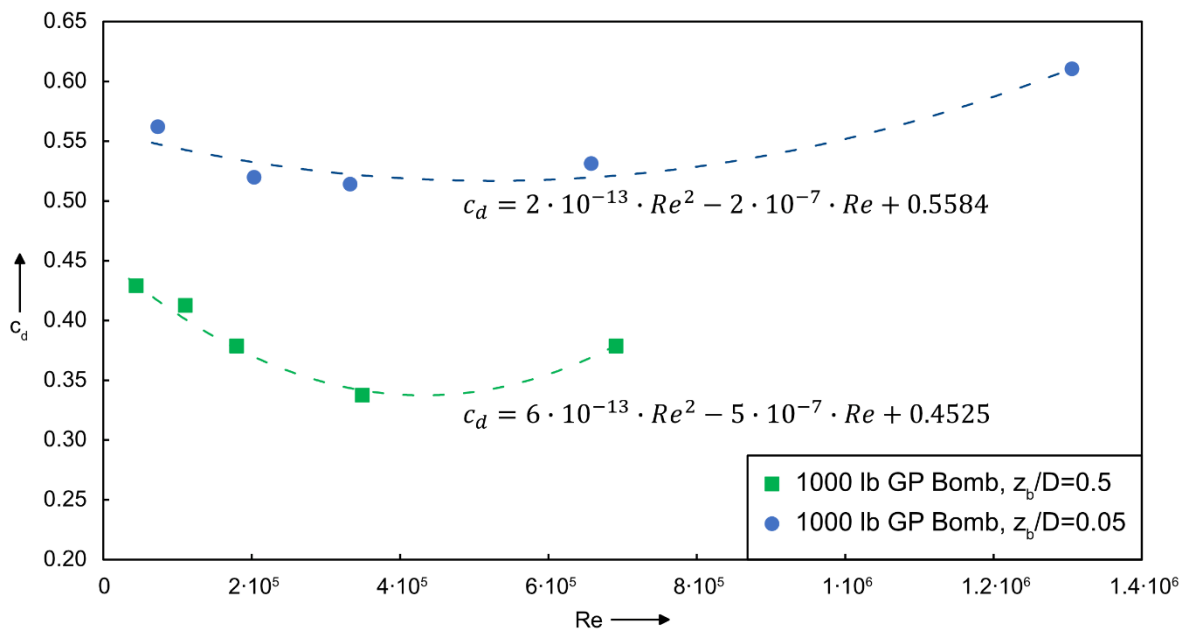


Fig. 73: Polynomials for the drag coefficient from CFD of the 1000 lb GP Bomb.

Using the polynomials, a further classification of all summands or subtrahends was then made (see Fig. 74).

$$c_d = \begin{matrix} \mathbf{a} & \mathbf{b} & \mathbf{c} \\ 2 \cdot 10^{-13} \cdot Re^2 & - 2 \cdot 10^{-7} \cdot Re & + 0.5584 \\ 6 \cdot 10^{-13} \cdot Re^2 & - 5 \cdot 10^{-7} \cdot Re & + 0.4525 \end{matrix}$$

Fig. 74: Classification of the functions into the coefficients a, b and c.

For each of these non-constant coefficients, a separate function was derived (see Fig. 75, to Fig. 77). Referring to Fig. 74, Fig. 75 shows the individual values for coefficient a.

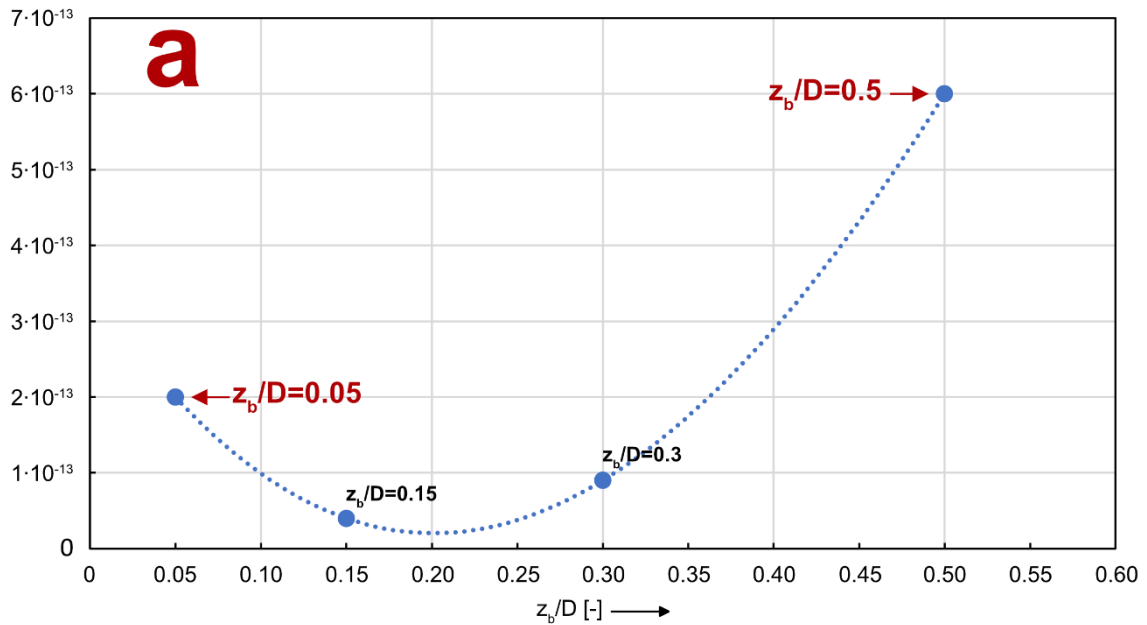


Fig. 75: Determined polynomial for the coefficient a at different burial depths.

This procedure was carried out in the same way for the coefficients b and c separately. As can be seen, their behavior differs significantly.

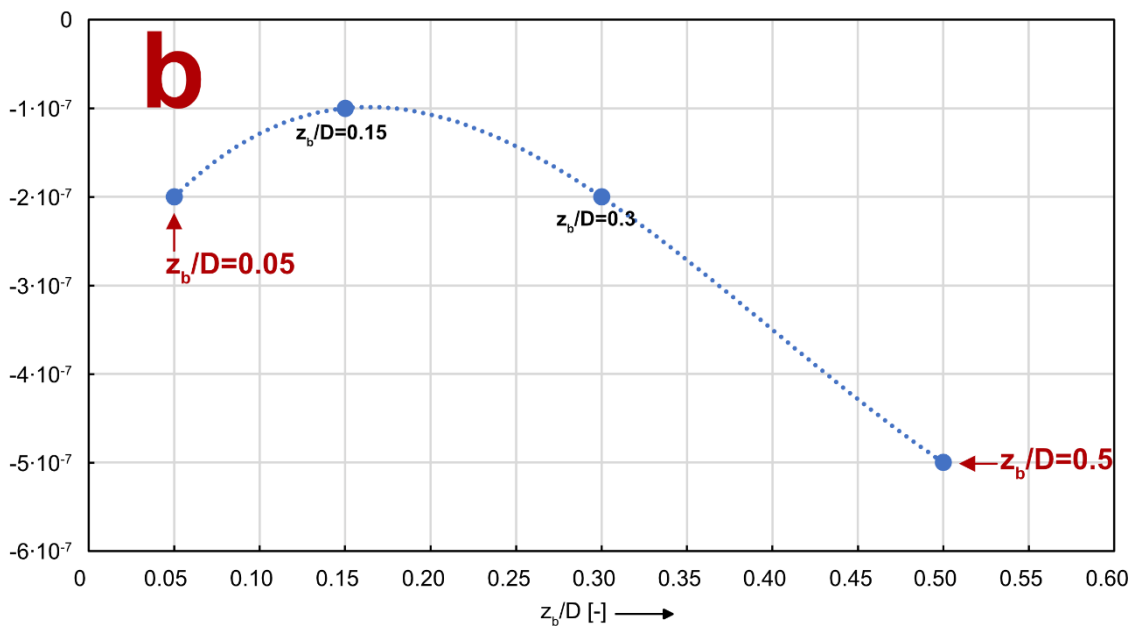


Fig. 76: Determined polynomial for the coefficient b at different burial depths.

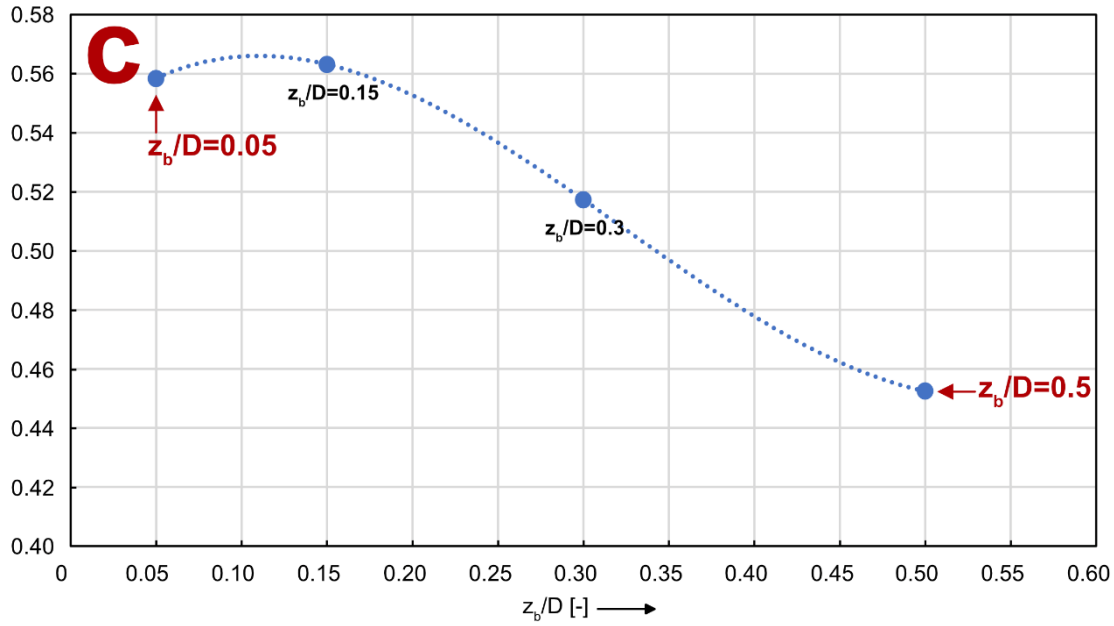


Fig. 77: Determined polynomial for the coefficient c at different burial depths.

A polynomial was then calculated again for each of the coefficients a , b and c , to represent the points in the best possible way. The equations for the coefficients are shown in the following equations:

$$a(z_b) = -3.111 \cdot 10^{-18} \cdot z_b^3 + 9.289 \cdot 10^{-16} z_b^2 - 3.357 \cdot 10^{-14} \cdot z_b + 3.45 \cdot 10^{-13} \quad [100]$$

$$b(z_b) = 9.524 \cdot 10^{-12} \cdot z_b^3 - 1.143 \cdot 10^{-9} \cdot z_b^2 + 2.976 \cdot 10^{-8} \cdot z_b - 3.214 \cdot 10^{-7} \quad [101]$$

$$c(z_b) = 3.032 \cdot 10^{-6} \cdot z_b^3 - 2.932 \cdot 10^{-4} \cdot z_b^2 + 0.005359 \cdot z_b + 0.5386 \quad [102]$$

Due to the fact that a quadratic polynomial was found for the relation equation shown in Fig. 73, the Eqs. [100] to [102] can now be substituted into a quadratic polynomial. The basic equation thus is:

$$c_d = a(z_b) \cdot Re^2 + b(z_b) \cdot Re + c(z_b). \quad [103]$$

After inserting the Eqs. [100] to [102] into Eq. [103], the result for the drag coefficient of the 1000 lb GP Bomb is found as:

$$\begin{aligned} c_d = & (-3.111 \cdot 10^{-18} \cdot z_b^3 + 9.289 \cdot 10^{-16} \cdot z_b^2 - 3.357 \cdot 10^{-14} \cdot z_b + 3.45 \cdot 10^{-13}) \cdot Re^2 \\ & + (9.524 \cdot 10^{-12} \cdot z_b^3 - 1.143 \cdot 10^{-9} \cdot z_b^2 + 2.976 \cdot 10^{-8} \cdot z_b - 3.214 \cdot 10^{-7}) \cdot Re \quad [104] \\ & + (3.032 \cdot 10^{-6} \cdot z_b^3 - 2.932 \cdot 10^{-4} \cdot z_b^2 + 0.005359 \cdot z_b + 0.5386) \end{aligned}$$

The same procedure was applied to all objects for the results of the CFD simulations and the wind tunnel experiments.



The following are the polynomials for the individual objects:

1000 lb GP Bomb:

$$c_d = (-3.111 \cdot 10^{-18} \cdot z_b^3 + 9.289 \cdot 10^{-16} \cdot z_b^2 - 3.357 \cdot 10^{-14} \cdot z_b + 3.45 \cdot 10^{-13}) \cdot Re^2 + (9.524 \cdot 10^{-12} \cdot z_b^3 - 1.143 \cdot 10^{-9} \cdot z_b^2 + 2.976 \cdot 10^{-8} \cdot z_b - 3.214 \cdot 10^{-7}) \cdot Re + (3.032 \cdot 10^{-6} \cdot z_b^3 - 2.932 \cdot 10^{-4} \cdot z_b^2 + 0.005359 \cdot z_b + 0.5386) \quad [105]$$

500 lb GP Bomb:

$$c_d = (1.587 \cdot 10^{-17} \cdot z_b^3 - 7.937 \cdot 10^{-16} \cdot z_b^2 + 1.071 \cdot 10^{-14} \cdot z_b + 1.643 \cdot 10^{-13}) \cdot Re^2 + (-3.81 \cdot 10^{-12} \cdot z_b^3 - 2.095 \cdot 10^{-10} \cdot z_b^2 + 1.543 \cdot 10^{-8} \cdot z_b - 3.714 \cdot 10^{-7}) \cdot Re + (-6.667 \cdot 10^{-8} \cdot z_b^3 - 1.533 \cdot 10^{-5} \cdot z_b^2 - 2.212 \cdot 10^{-3} \cdot z_b + 0.5782) \quad [106]$$

155 mm, HE 107

$$c_d = (9.714 \cdot 10^{-17} \cdot z_b^3 - 6.99 \cdot 10^{-15} \cdot z_b^2 + 1.282 \cdot 10^{-13} \cdot z_b - 7.786 \cdot 10^{-13}) \cdot Re^2 + (-2.629 \cdot 10^{-11} \cdot z_b^3 + 1.288 \cdot 10^{-9} \cdot z_b^2 - 1.121 \cdot 10^{-8} \cdot z_b - 7.286 \cdot 10^{-8}) \cdot Re + (8.286 \cdot 10^{-7} \cdot z_b^3 - 5.476 \cdot 10^{-5} \cdot z_b^2 - 2.714 \cdot 10^{-3} \cdot z_b + 0.5397) \quad [107]$$

4.3.5 Added mass coefficient

Since the calculation of the added mass is a numerical calculation, a mesh independence study was performed (see Fig. 78). It is shown that about 6000 triangles in the STL are sufficient for a representative mesh.

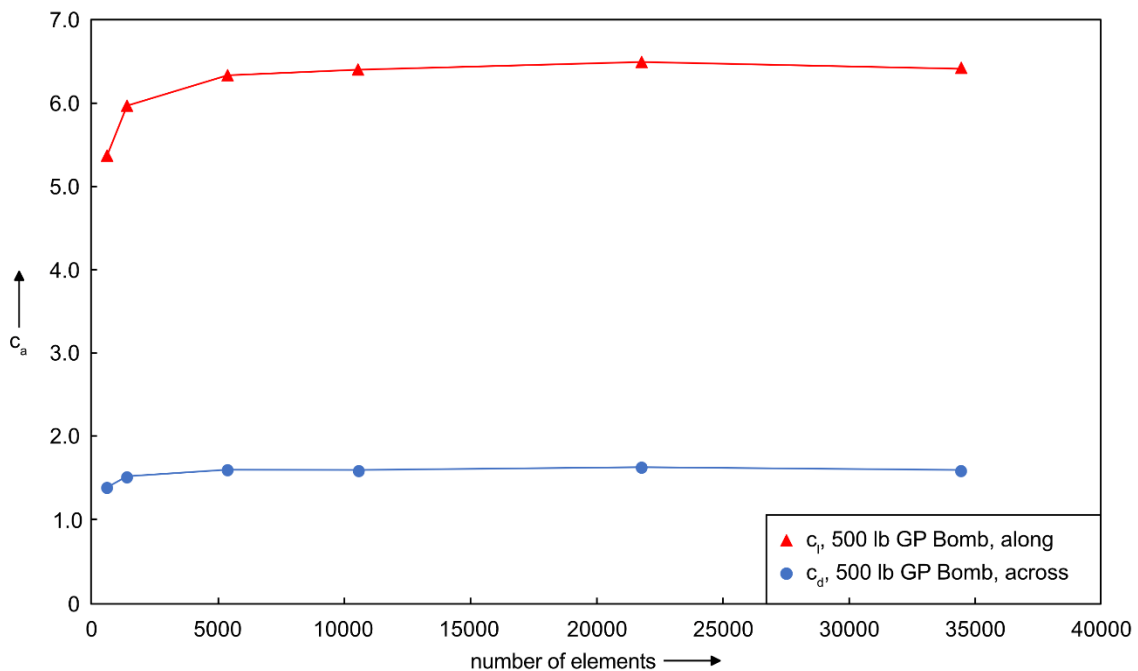


Fig. 78: Mesh convergence for the 500 lb GP Bomb at a burial depth of $z_b/D=0.05$.

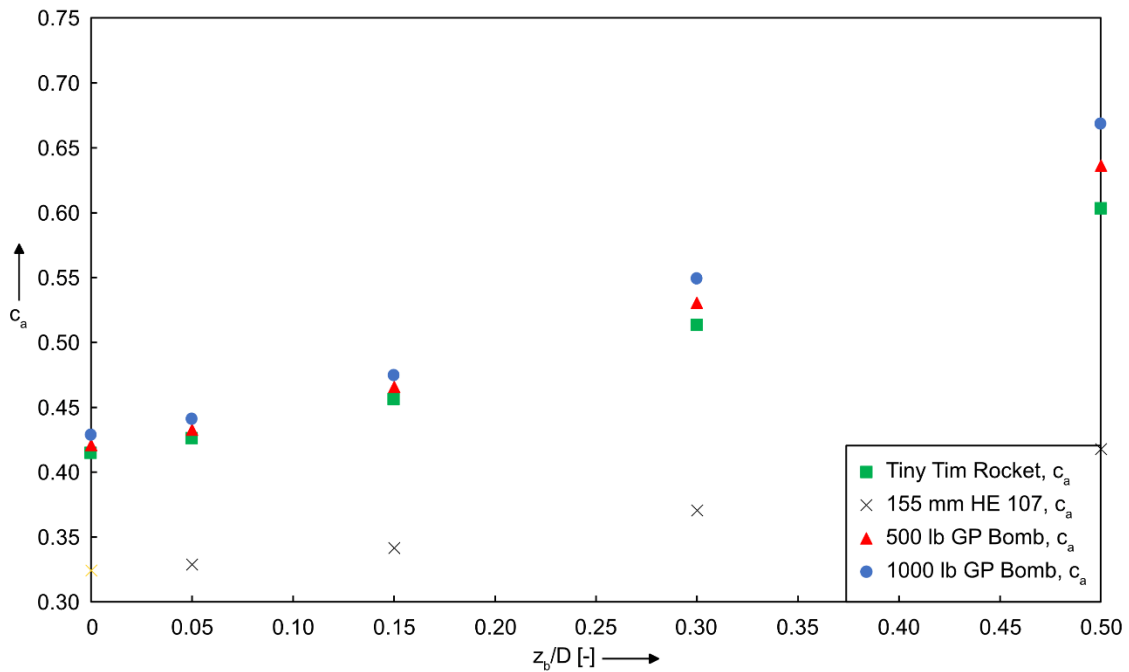


Fig. 79: Added mass coefficients.

Fig. 79 shows the results for the objects being oriented with their main axis perpendicular to the incident flow direction. It can be clearly seen that the added mass coefficient depends on the size of the objects. Again, polynomials were derived, representing the results of the simulation. These polynomials are shown in the Tab. 11 for the individual objects.

Tab. 11: Polynomials for the added mass coefficients.

object	added mass polynomial
155 mm, HE 107	$c_a = 0,0145 \cdot z_b^2 - 0,0411 \cdot z_b + 0,1777$
Tiny Tim Rocket	$c_a = 0,0263 \cdot z_b^2 - 0,065 \cdot z_b + 0,372$
500 lb GP Bomb	$c_a = 0,0315 \cdot z_b^2 - 0,0838 \cdot z_b + 0,3991$
1000 lb GP Bomb	$c_a = 0,0365 \cdot z_b^2 - 0,1012 \cdot z_b + 0,4272$

4.3.6 Conclusion on drag and lift and added mass

As shown above, the drag and lift coefficient in general are not constant. Implementing Eq. [104] into the burial and mobilization model allows to quantify their value during a wave cycle. The result is shown in Fig. 80 for the 500 lb GP Bomb and two burial depths.

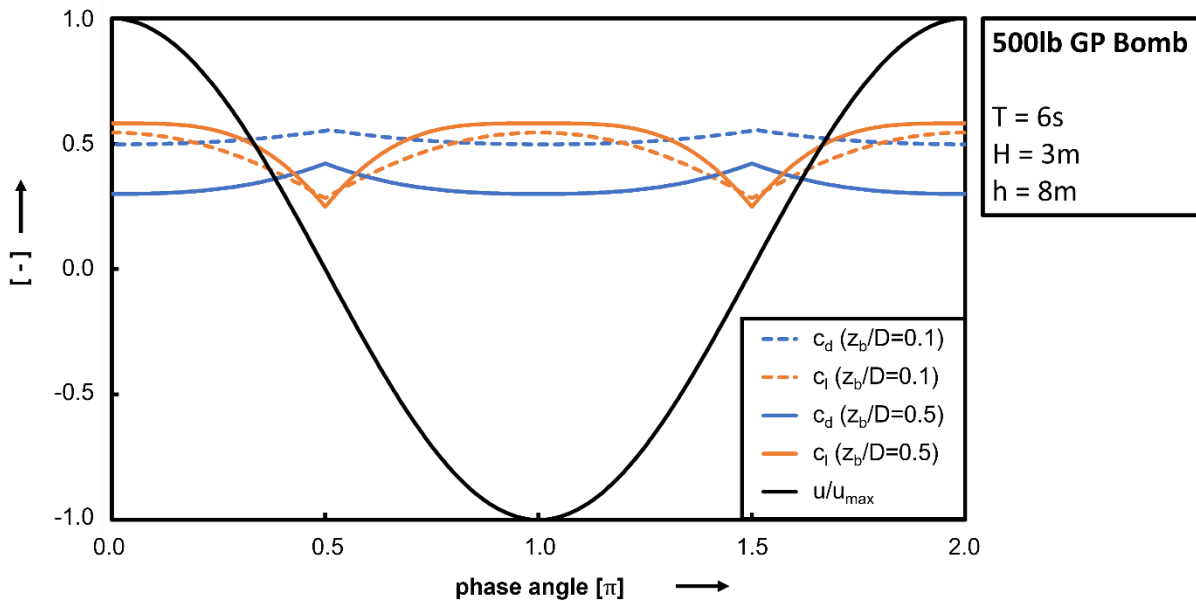


Fig. 80: Lift and drag coefficient during a single wave cycle.

The applied wave was a Stokes's 3rd order wave with the wave parameters described in Fig. 80. The black line shows that horizontal orbital velocity, approaching the object. During this single wave cycle, values of $0.30 < c_l < 0.55$ and $0.26 < c_l < 0.58$ are found. Thus, the simple assumption of $c_d = c_l = 0.5$ is not too bad.

As the dimensionless coefficients itself can just give tendency, the resulting loads have to be observed as well. For this purpose, Fig. 81 again shows the horizontal orbital velocity as a black line but also shows the sum of all hydrodynamic loads on the object F_{tot} in the orange graph. Obviously, the total loads on the object do not reach their maximum at maximum orbital velocity but within a region of the maximum orbital current acceleration. For a better understanding, the relative contribution of the drag force F_d , which depends on the orbital velocity, is shown in the blue dashed line. The relative contribution of the Froude-Kryloff Force F_{FK} and the added mass force F_{am} are shown in green dashed lines. Comparing all three loads, ends up in two conclusions:

1. The contribution of the hydrodynamic is relatively low in strongly wave-dominated regimes.
2. The contribution of the Froude-Kryloff Force is larger than the contribution of the added mass force, both contributions themselves are stronger than the contribution of the drag force and they occur during times of strong acceleration of the orbital current.

The overall conclusion from this is, that the absolute contribution of the drag and lift forces is low and thus, the small variability of the drag and lift coefficient can be neglected. Although the correct polynomials are now known and implemented, it might be sufficient to follow the simple assumption of $c_d = c_l = 0.5$.

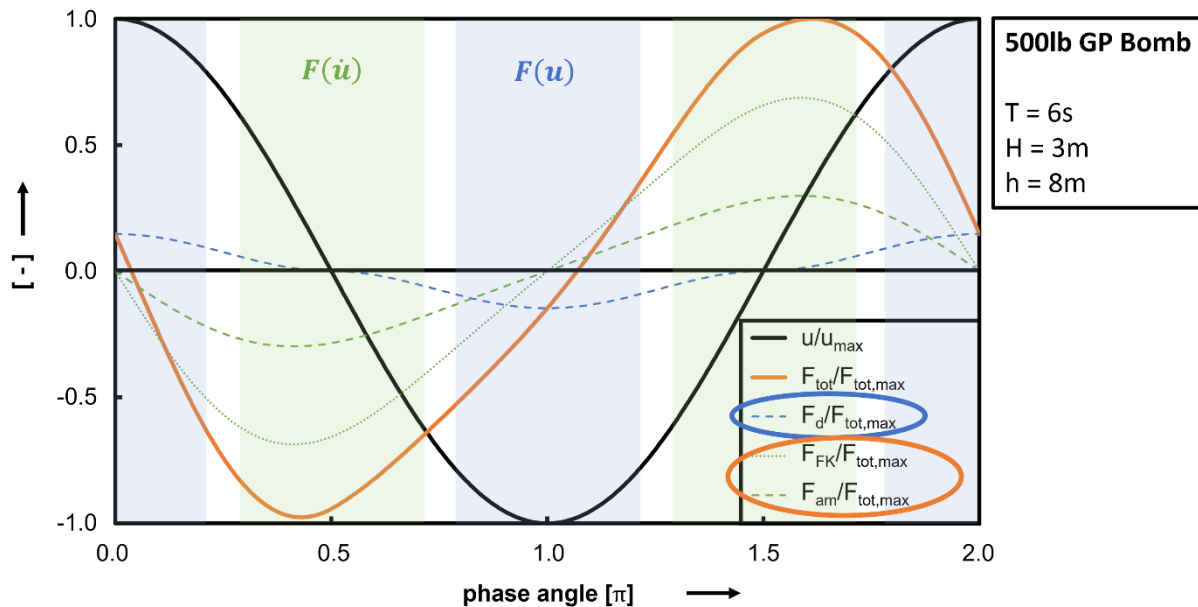


Fig. 81: Loads on an object during a single wave cycle.

A good knowledge of the added mass coefficient and its variability is a key to a good simulation. Furthermore, a good knowledge of the volume of the individual object is important as the Froude-Kryloff force as well as the added mass force are derived by multiplying with the objects' volume.

4.3.7 Rolling resistance coefficient

As the drag, lift and added mass coefficient were investigated during this project, the only remaining unknown dimensionless coefficient in Eq. [23] is the rolling resistance coefficient c_r . Comparing the results of the mobilization simulation with experimental investigations and observations show that this coefficient has a major influence on the results and often is used to tune/calibrate the models. Although the rolling resistance for wheels and tires on roads and sand is very well known, there are no results for any object on seabed sediments. It is assumed that the value of the rolling resistance on seabed sediments differs significantly from those on land roads. However, an experimental investigation is possible although it is may be very expensive in real scale to obtain appropriate quality measurements.

4.4 TELEMAC Simulations

4.4.1 Currents

Modelled free surface water elevation is compared with tide predictions based on the measured levels (NOAA, 2010). The comparison is carried out on 11 locations along the coast and in the vicinity of tidal inlets (Fig. 82). There is generally a good agreement in phase and amplitude between model results and the tide predictions (Fig. 83 to Fig. 86). The error is generally lower than 10 cm. And some of the errors are caused by a surge due to strong wind and wave conditions, which is accounted for in the model, but not in the tidal predictions. This is most noticeable in Ankona (bottom panel in Fig. 85)

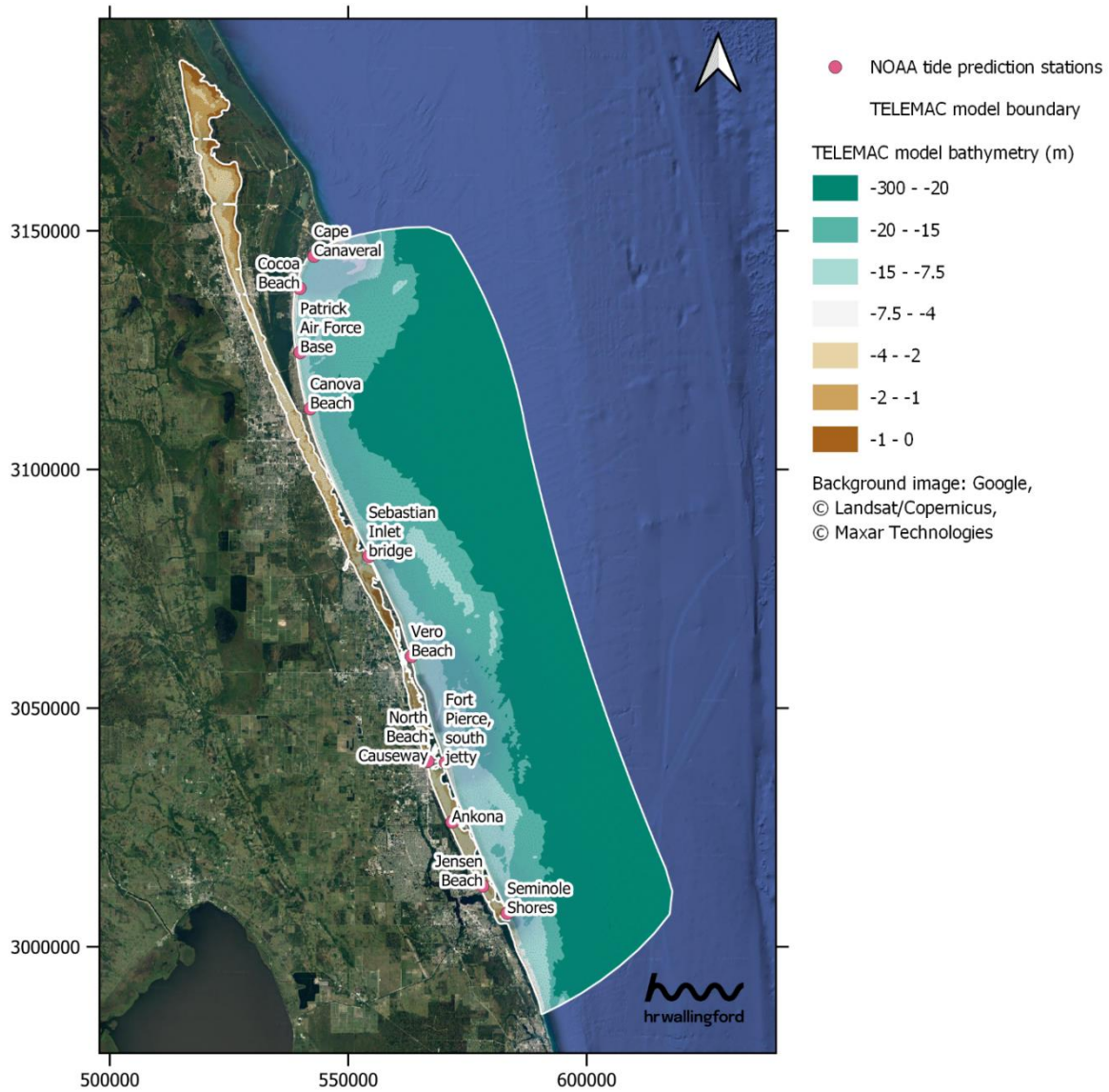


Fig. 82: Locations of measurement stations used in the tidal levels comparison.



Fig. 83: Comparison of water levels predicted by the model and by the NOAA tidal predictions at Cape Canaveral, Cocoa Beach and Patrick Airforce Base.

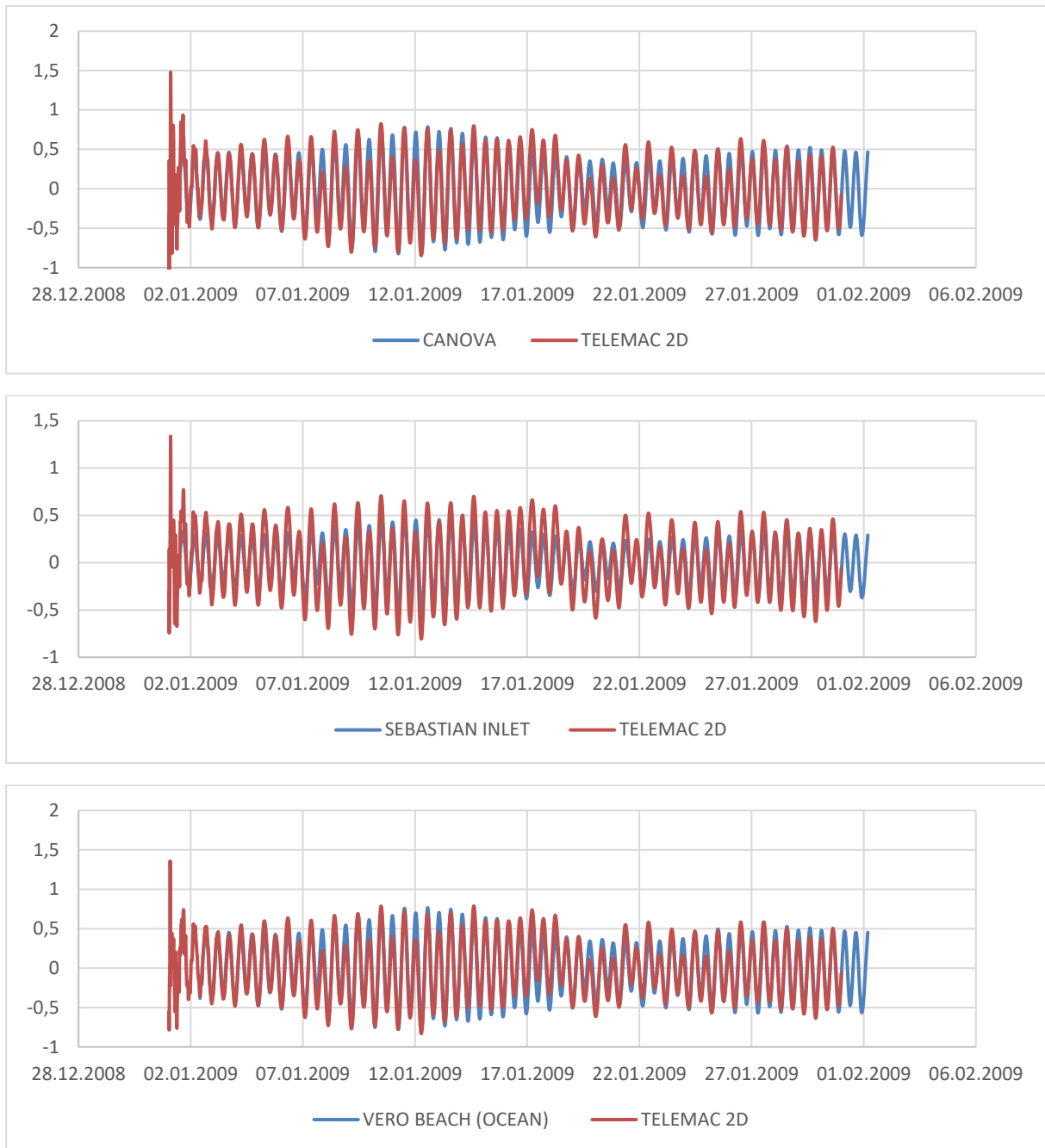


Fig. 84: Comparison of water levels predicted by the model and by the NOAA tidal predictions at Canova, Sebastian Inlet and Vero Beach.



Fig. 85: Comparison of water levels predicted by the model and by the NOAA tidal predictions at North Beach, Fort Pierce and Ankona.

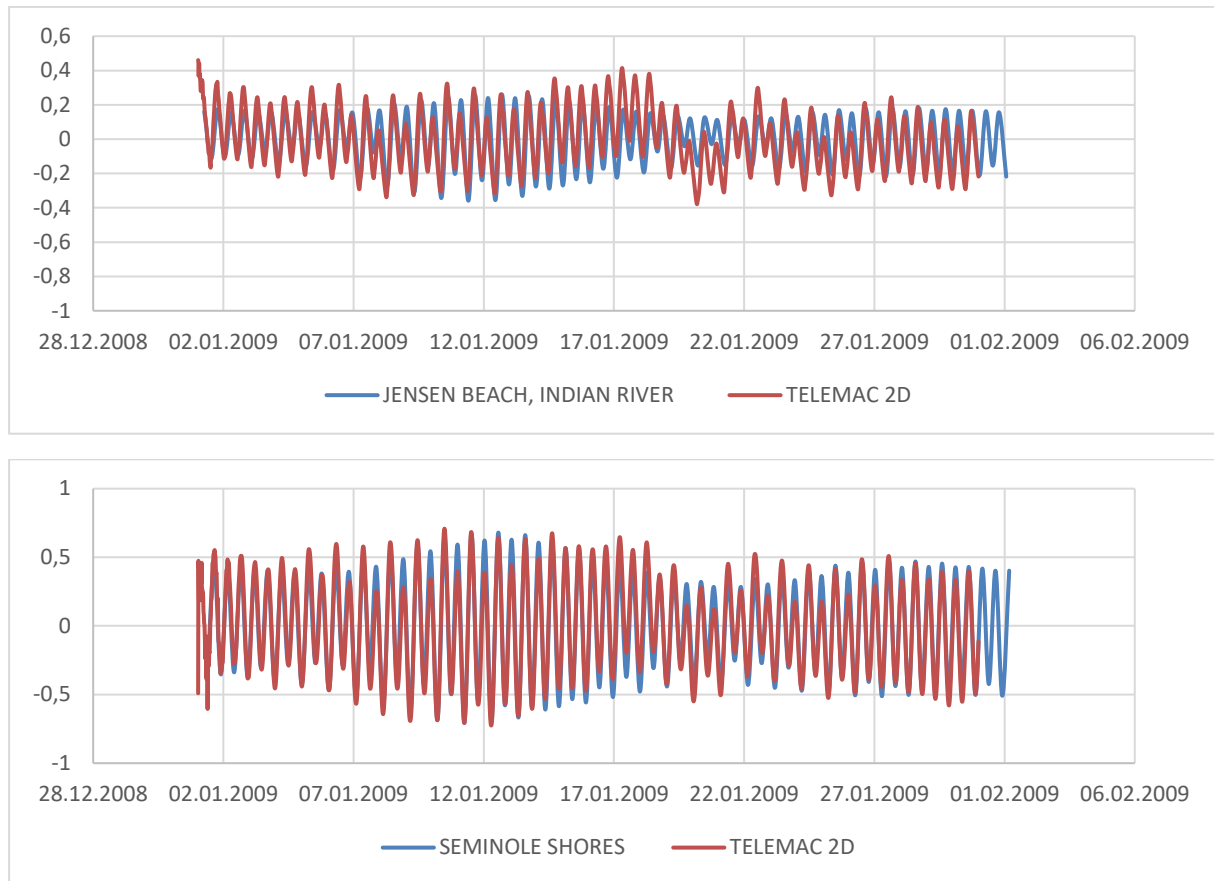


Fig. 86: Comparison of water levels predicted by the model and by the NOAA tidal predictions at Jensen Beach and Seminole Shores.

4.4.2 Waves

The wave predictions are compared with the measured data from the Datawell Waverider buoy offshore of Fort Pierce (Fig. 87). The comparison shows that the model generally predicts the measurements of significant wave height (H_s), peak wave period (T_p), and mean wave direction (Dir) at the Waverider buoy off the coast of Fort Pierce (see Fig. 88). The modelled wave energy density spectra is also in the range of the measurement spectrum (see Fig. 89). The model reproduces the bimodal spectrum, even though the separation is not as clear in the model as it is in the measured data.

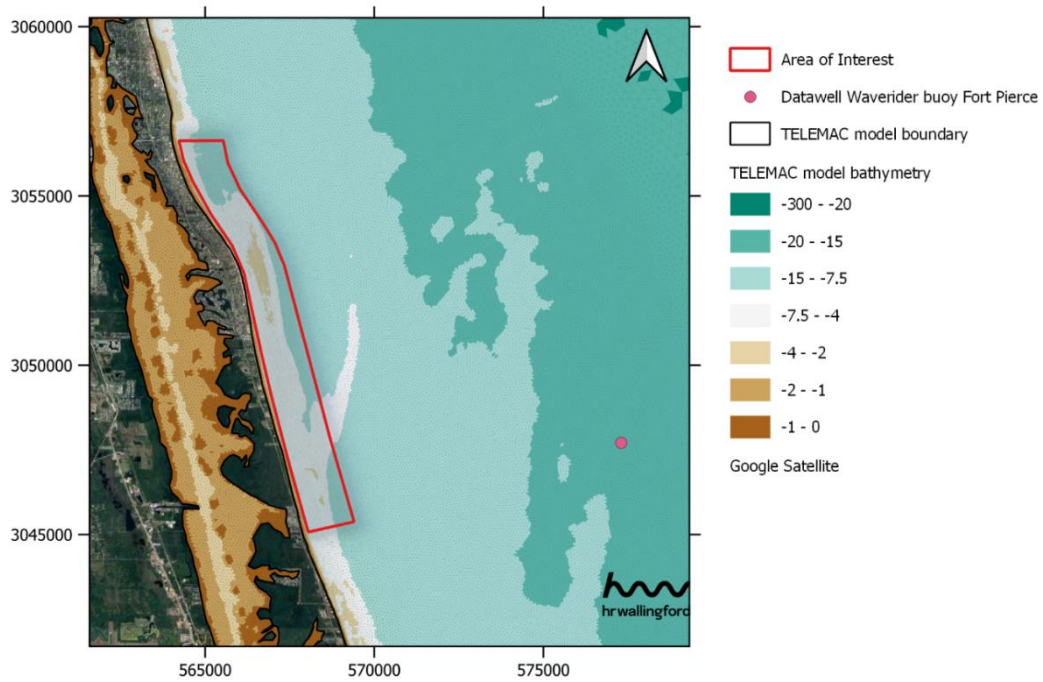


Fig. 87: Location of the Waverider buoy offshore of Fort Pierce.

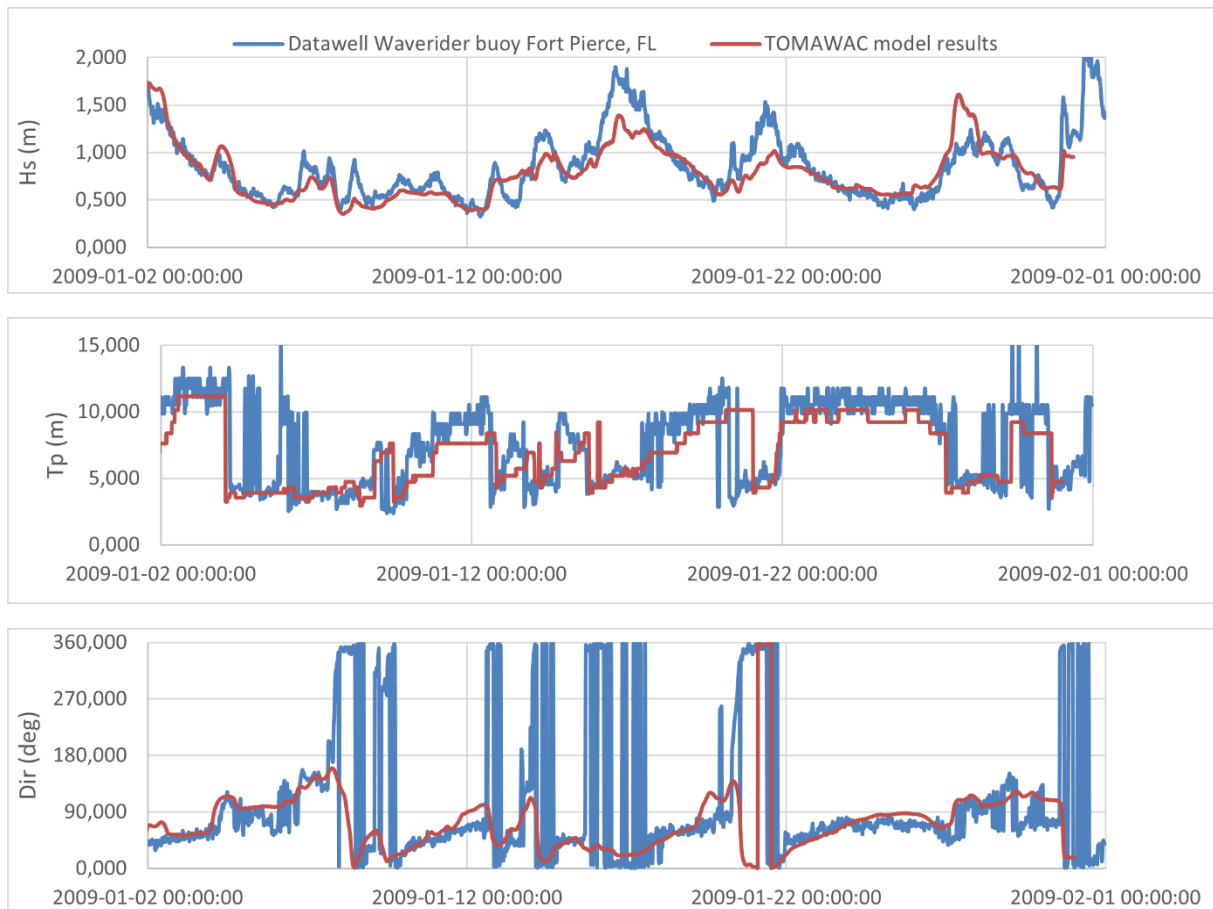


Fig. 88: Comparison between measured and predicted significant wave height (top); peak period (middle) and wave direction (bottom).

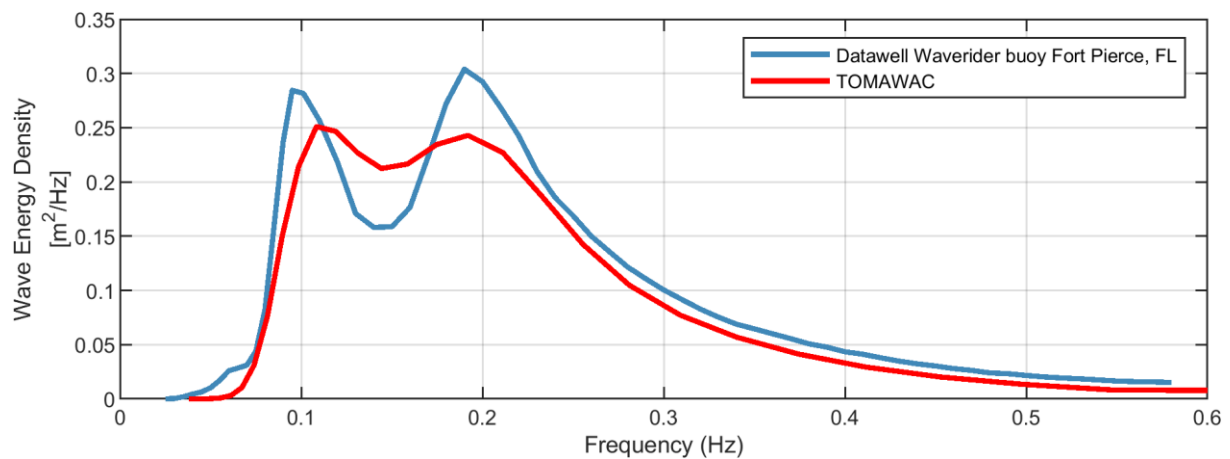


Fig. 89: Comparison between measured and predicted significant wave spectrum.

4.4.3 Sediments

The morphological results are within the range of the variability in of the measurements. A simulation representing the conditions during hurricane Matthew and qualitative comparison with available LiDAR data from (OCM-Partners, 2023b) and (OCM-Partners, 2023a) indicates that the model agrees with erosion and deposition patterns observed along the beach and over offshore sand bars and shoals (Fig. 90). The bed evolution patterns, of both the model and the measurements, are characteristic of beach lowering, bedform migration and erosion of shoal areas.

A quantitative comparison also showed that the simulated mean bed evolution along the shoreline (-0.9 m) matches well the measured value (-0.12 m). The standard deviations were found to be 0.27 m and 0.24 m for model results and measurements respectively, which is also in agreement with the shoreline changes for the region reported by (Birchler et al., 2019). These values were drawn from Fig. 91 (top), which was itself calculated from the zonal averages (solid lines) and standard deviations (shaded areas) of pixels falling within rectangular sample polygons drawn along the shoreline (see Fig. 91, bottom). The sample polygons are spaced at intervals of 90 m and have a cross-shore length of 300 m, their centroids are aligned with the coastline and their longest edges protrude 150 m onshore and 150 m offshore.

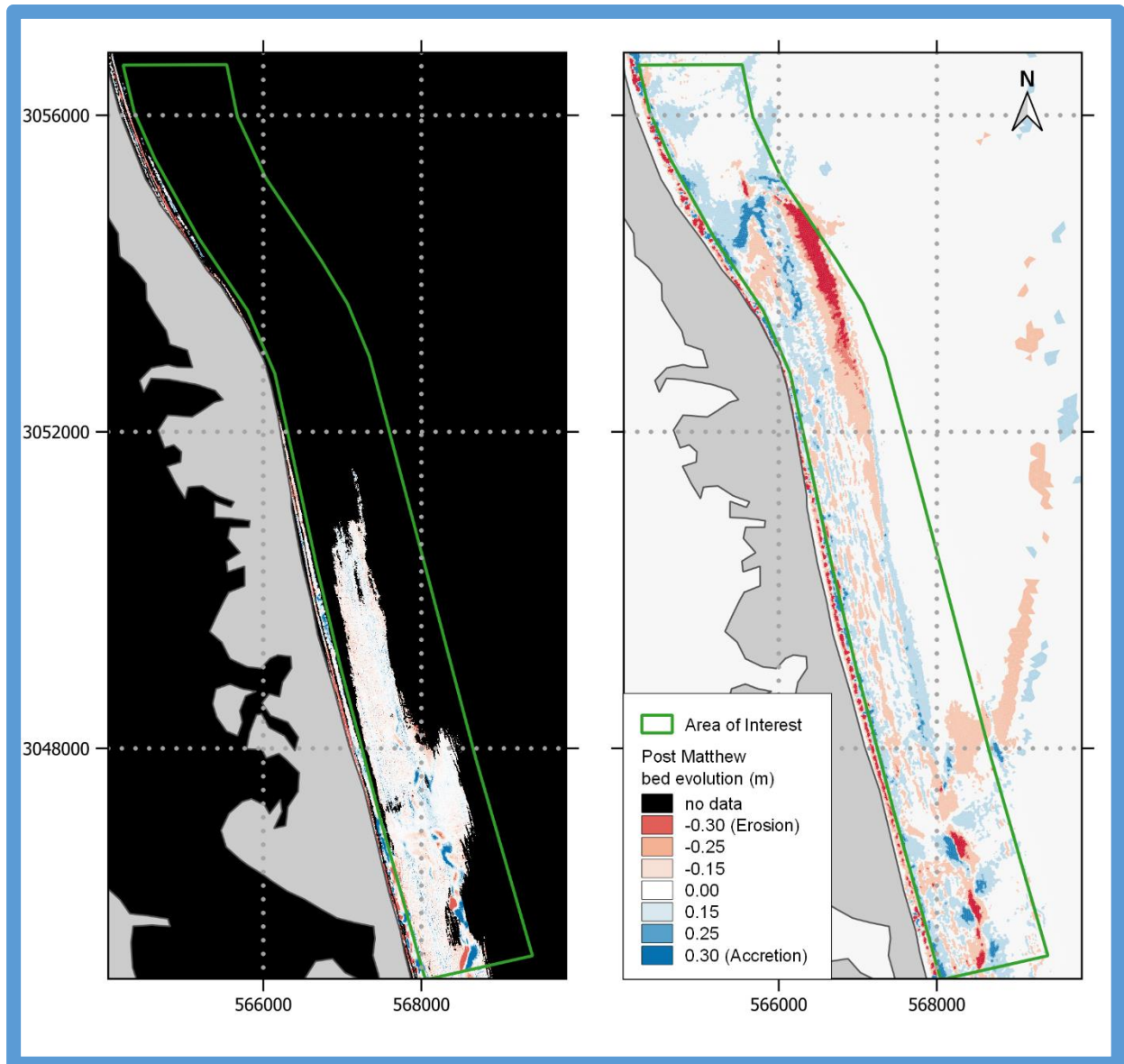


Fig. 90: Qualitative comparison of measured bed elevation changes(left) and modelled bed evolution (right). The sources for the measurements data are: (OCM-Partners, 2023b) and (OCM-Partners, 2023a).

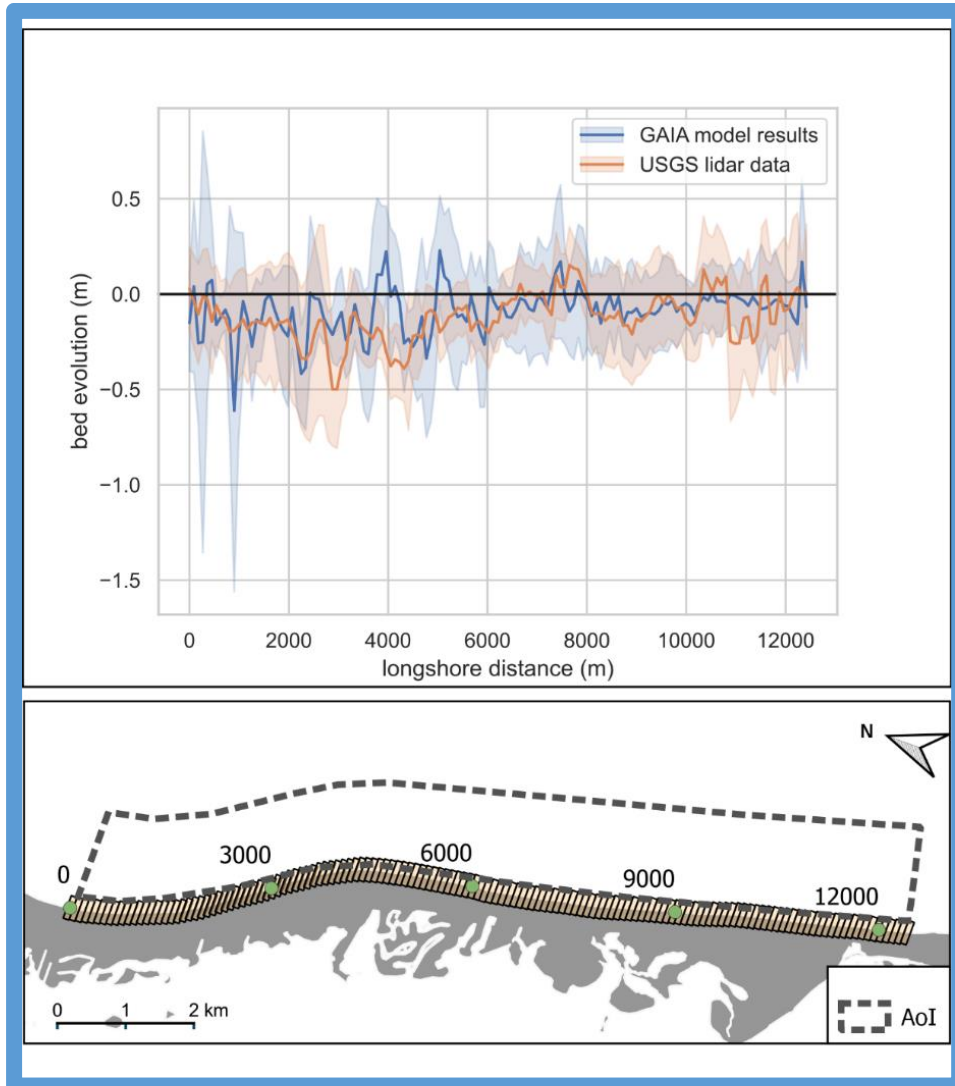


Fig. 91: Quantitative comparison of longshore bed evolution from measurements and model results. Top, bed evolution profile, the solid lines are the zonal average and the shaded areas are the standard deviation. Bottom, local coordinates and sample polygons used to calculate the zonal statistics. The sources for the measurements data are: (OCM-Partners, 2023b) and (OCM-Partners, 2023a).

4.4.4 Simulation of monthly metocean and morphodynamics conditions of 2016

The TELEMAC-2D, TOMAWAC and GAIA modelling train was used for simulating the waves, currents and morphodynamics of the whole year of 2016 (Fig. 92).

The average significant wave heights were about 0.5 m in summer, increasing to about 1 m in autumn, winter and spring. During storms, the significant wave height increased to 2 m in summer (e.g., during June 2016); 2.5 m in winter and spring; and 4.5 m during the autumn. For all the simulated months of 2016 the peak wave period oscillated between wind waves (5 s) and swell (10 s) (Fig. 92, central panel). The wave direction was consistent throughout the year, and most of the waves came from a sector between northeast and east (Fig. 92, bottom panel).

The largest morphodynamics changes of 2016 occur during Hurricane Matthew (October), followed by significant changes, although of lower magnitude and extension, throughout the rest of the autumn season (November and December), during winter (January,



February and December) and during April of 2016. The areas where most elevation changes occur are the beach, and shoal ridges located approximately 2 km from the beach (see Fig. 93).

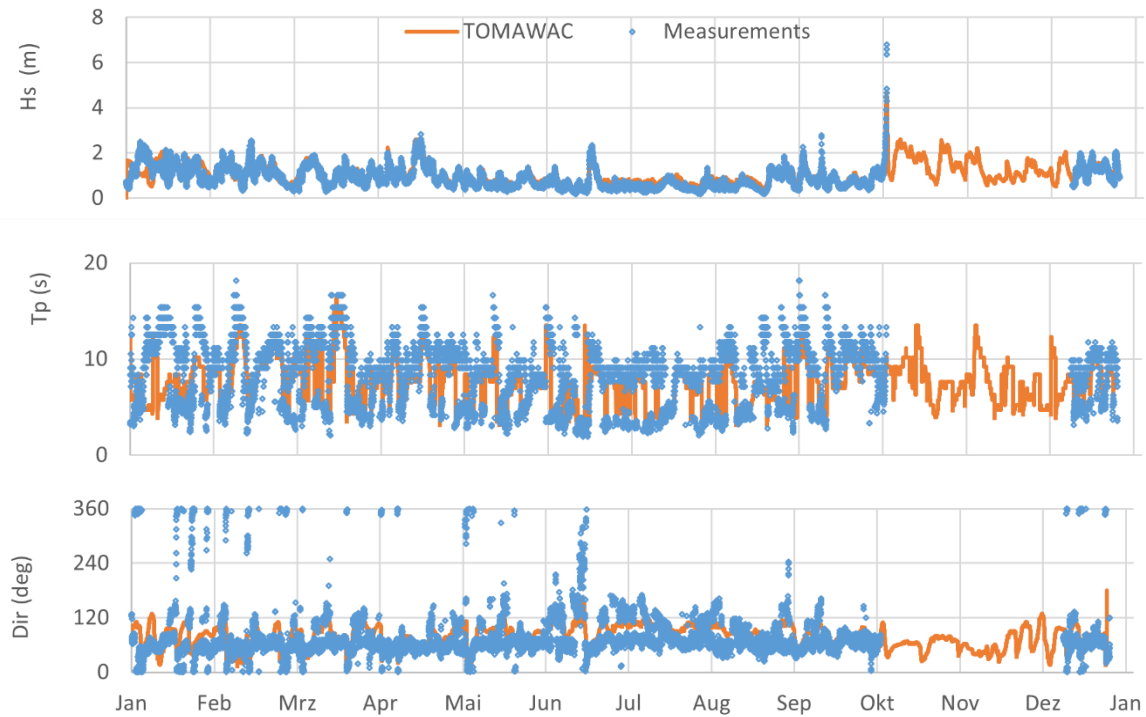


Fig. 92: Modelled and measured wave conditions at the Fort Pierce station, Florida, throughout 2016. Top: significant wave height. Middle: peak wave period. Bottom: mean wave direction.

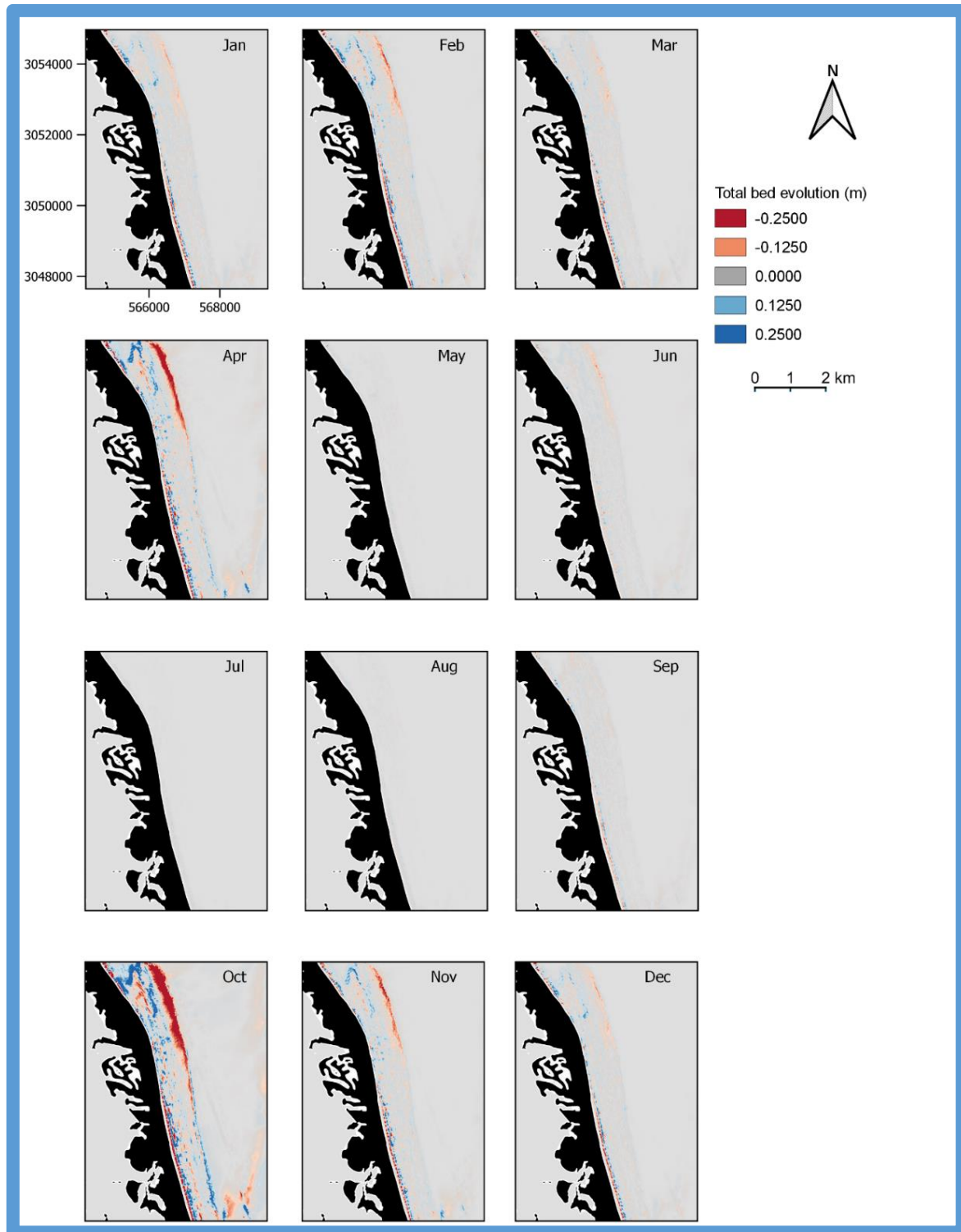


Fig. 93: Monthly total bed evolution modelled for 2016.

4.4.5 Conclusion

The model for flows, waves and sediment transport has been set up for the Fort Pierce AoI using inputs from site data. Model results have been presented for water levels, waves, and sediments. These show a realistic behavior when compared to predicted tides, measured waves and available bed elevation measurements.



Finally, a hydrodynamics and morphodynamics dataset was generated by running the model for the entire year of 2016. This provides a suitable input for large scale UXO mobilization and burial simulations.

4.5 Examples of the model-classification

Examples of the classification tables are included in Fig. 94 and Fig. 95. Fig. 94 relates to the original DRAMBUIE model (Whitehouse, 1998) although subsequent modifications and improvements have been suggested. The literature on that is being reviewed to bring out the main points of those modifications.

SERDP Project:	MR21-1081	HR Wallingford Ref:	DES1288	Status:	Ongoing/Complete		
Model classification table UXO and DMM burial and mobilization (v4)							
Reference	Whitehouse 1998						
Overview							
Model type	Burial	Mobilization	Migration				
Object type	Cylinder	Bomb	Sphere	Tapered cylinder	Frustrum	Other	
BM: Burial model							
BM1-Process	Impact	Scour	Liquefaction	Shoreline change	Bedform migration		
BM2-Forcing	Currents	Tidal	Waves	Wave+current	Breaking waves	Swash	Gravity
BM3-Basis	Deterministic	Time-varying					
BM4-Object density explicit	Yes	No					
BM5-Object orientation to flow	90 degrees	0 degrees	Variable				
BM6-Soil	Granular	Cohesive					
BM7-Morphology	Flat bed	Ripples	Megaripples	Dunes	Shoreface		
BM8-Scour feature	Depth	Lateral extent	Profile	Time evolution			
BM9-Object settlement	Yes	No					
BM10- Soil failure process	Included	Not-included					
BM11-Validated	Lab data	Field data					
MM: Mobilization model							
MM1-Forcing	Currents	Tidal	Waves	Wave+current	Breaking waves	Swash	Gravity
MM2-Basis	Deterministic	Time-varying					
MM3-Object density explicit	Yes	No					
MM4-Object orientation to flow	90 degrees	0 degrees	Variable				
MM5-Soil	Granular	Cohesive	Fixed bed				
MM6-Morphology	Flat bed	Ripples	Megaripples	Dunes	Shoreface	Furrows	
MM7-Initial condition	% Buried	% buried with scour profile	No burial				
MM8-Resistance	Sliding	Rolling	Pivot	Suction			
MM9-Mobilization step	Deterministic	Phase-resolving	Migration predictor				
MM10-Validated	Lab data	Field data					

Fig. 94: Model review classification table (v4) showing example of burial model.



SERDP Project:	MR21-1081	HR Wallingford Ref:	DES1288	Status:	Ongoing/Complete		
Model classification table UXO and DMM burial and mobilization (v4)							
Reference	Menzel et al 2018						
Overview							
Model type	Burial	Mobilization	Migration				
Object	Cylinder	Bomb	Sphere	Other			
BM: Burial model							
BM1-Process	Impact	Scour	Liquefaction	Shoreline change	Bedform migration		
BM2-Forcing	Currents	Tidal	Waves	Wave+current	Breaking waves	Swash	Gravity
BM3-Basis	Deterministic	Time-varying					
BM4-Object density explicit	Yes	No					
BM5-Object orientation to flow	90 degrees	0 degrees	Variable				
BM6-Soil	Granular	Cohesive					
BM7-Morphology	Flat bed			Megaripples	Dunes	Shoreface	
BM8-Scour feature	Depth	Lateral extent	Profile	Time evolution			
BM9-Object settlement	Yes	No					
BM10- Soil failure process	Included	Not-included					
BM11-Validated	Lab data	Field data					
MM: Mobilization model							
MM1-Forcing	Currents	Tidal	Waves	Wave+current	Breaking waves	Swash	Gravity
MM2-Basis	Deterministic	Time-varying					
MM3-Object density explicit	Yes	No					
MM4-Object orientation to flow	90 degrees	0 degrees	Variable				
MM5-Soil	Granular	Cohesive					
MM6-Morphology	Flat bed	Ripples	Megaripples	Dunes	Shoreface		
MM7-Initial condition	% Buried	% buried with scour profile	No burial				
MM8-Resistance	Sliding	Rolling	Pivot	Suction			
MM9-Mobilization step	Deterministic	Phase-resolving	Migration predictor				
MM10-Validated	Lab data	Field data					

Fig. 95: Model review classification table (v4) showing example of mobilization model.

Once the classification task is completed in the project, the models will be summarized and intercompared to draw out the main features of the existing Burial and Mobilization models that can be extracted to underpin the development of the new model being developed in this project.

Following the successful implementation in year 1 of the existing Burial model of (Whitehouse, 1998), extended with methods of (Soulsby, 1997), into the Mobilization model of (Menzel, et al., 2019) further development has taken place in year 2. The Burial model will be compared to a wider set of data than was available at the time of publication and extended to include parameterizations for a range of different object types and the effect of object density in the scour-induced settlement process. This extension will ensure a flow through of object parameters at the burial prediction stage to the migration predictions which already include object density as well as dimensions. Effects of non-horizontal beds will be included following the pivot analysis type of equation proposed for sands and gravels (Whitehouse, et al., 2000) and rolling and sliding models (Ali & Dey, 2016).

5 Conclusions to Date

The AoI and OoI were defined in cooperation with CEHNC. The available environmental data were acquired, and their usability is validated. The existing mobilization model was applied on the AoI for the OoI. It was shown that the existing model is applicable but the available wave data cannot be used directly. Thus, additional investigation on the wave parameters in the AoI were necessary. A very fruitful site meeting at Fort Pierce took place on 8th December 2022 in cooperation with CEHNC and CESAJ, representing the site manager and the supporting engineers. Requirements and deliveries for the site manager and the engineering department were agreed on.

As the specialist for the Lattice Boltzmann Simulation, Dr. Helen Morrison, left the project, another approach was found to deliver morphodynamics data. It was decided to run



TELEMAC simulations at HR Wallingford to deliver reliable data for the morphodynamics and additionally get the required spatial wave data. The simulation was set up and successfully tested by comparing the results of a test simulation, covering January 2009 with measured data. The data export was also tested and the exchange format was agreed on. A one year simulation for 2016, including hurricane Matthew was finalized.

The burial model of Whitehouse was successfully combined with the wave model of Menzel by writing a new software tool UXOmob 4.0 as shown in Sections 3.5 and 4.1.

The Go/No-Go decision point 1 at the end of FY 1 was:

Is it possible to include DRAMBUIE into the mobilization model?

- Yes: Go on as planned
- No: Include mobilization model into DRAMBUIE

As DRAMBUIE is a wave-averaged model and the mobilization model is phase-resolved in the wave cycle, it was possible to include DRAMBUIE into the mobilization model without any complications.

Thus it was shown that it is possible to include DRAMBUIE into the mobilization model.

Within FY 2, great progress was achieved. The dimensional lift, drag and added mass coefficient were derived from extensive wind tunnel experiments and numerical simulations. Thus, the quality and validity of the mobilization simulation is massively improved. As a main result from these investigations, polynomials for all coefficient and objects were derived. It was also shown that the lift and drag coefficient can be assumed as fixed numbers for a simple approach.

A new software design was introduced, based on the MVC design pattern. Based on this, the existing software was transferred to C++ and a huge increase in performance was already achieved.

The Go/No-Go decision point 2 at the end of FY 2 was:

Is it possible to match the timescales of the mobilization model, the burial model and the model for seabed morphology?

- Yes: Go on as planned
- No: Alternative approach needs to be found (maybe running the models in parallel)

Based on the new software design, a variable bathymetry was implemented as shown and discussed in Section 4.2. As described in Section 3.13, the performance of the software was massively increased and the design was adapted to handle huge time series of spatial data. The TELEMAC simulation, presented in Section 4.4 is now able to deliver the required input data of spatial wave and morphodynamics time series.

Thus it was shown that it is possible to match the time scales of the mobilization model, the burial model and the model for seabed morphology.

As an improvement of the burial model of Whitehouse, the adapted model of Soulsby was implemented. This new burial model is called DRAMBUIE 2.0. The main focus however was on a new approach, using a neural network for the equilibrium burial depth. A sensitivity analysis was performed to define the most important variables and the ANN was trained with



literature data. A time stepping model was developed, which includes the equations of (Friedrichs, et al., 2018). This completely new burial model is DRAMBUIE 3.0.

The last development step of the software will be the inclusion of wave spectra into the burial and mobilization model. The team has been in communication with Joe Calantoni and Allison Penko, including at the SERDP-ESTCP symposium in fall 2022, about obtaining UNMES or pyUNMES from the Munitions Response Library. This has been required early in 2023 to be able to include UNMES in the cross-validation exercise. Granting of access to the UNMES model was key to the next part of the model intercomparison. Unfortunately, access was denied. However, a comparison to the sub models (e.g. MM from MR-200417) and other models will be done.

As the design of the new software is very modular, it now allows to implement different burial and mobilization models as well as bathymetry and morphodynamics data from different sources such as Delft3D, TELEMAC or measurements. It also allows to implement further wave models and wave spectra.

For validation purposes, 1:1 lab experiments on the wave-induced burial and mobilization of UXO were performed by an external project in June 2022 and are going to be published in 2024. Thus, the applicability of the model can be proved.



6 Literature Cited

- Airy, G. B., 1845. *Tides and Waves, Encyclopedia Metropolitana*, §192: 241-496. s.l.:s.n.
- Ali, S. & Dey, S., 2016. Hydrodynamics of sediment threshold. *Physics of Fluids*, 28(7), p. 075103.
- Army, D. o. t., 2012. *Revised Inventory Project Report*, Atlanta: US Army Corps of Engineers.
- Battjes, J. A. & Janssen, J. P. F. M., 1978. Energy loss and set-up due to breaking random waves.. *Coastal Engineering*.
- Benedet, L., Finkl, C. & Klein, A. H., 2003. Morphodynamic classification of beaches on the Atlantic coast of Florida: Geographical variability of beach types, beach safety and coastal hazards. Issue Special Issue 39.
- Bhatnagar, P., Gross, E. & Krook, M., 1954. Model for Collision Processes in Gases. I. Small Amplitude Processes in Charged and Neutral One-Component Systems.. *Physical Review*, 94(3), pp. 511-525.
- Bilskie, M. V., Bacopoulos, P. & Hagen, S. C., 2019. Astronomic tides and nonlinear tidal dispersion for a tropical coastal estuary with engineered features (causeways): Indian River lagoon system.. *Estuarine, Coastal and Shelf Science*, Issue 216, pp. 54-70.
- Birchler, J. J., Doran, K. S., Long, J. W. & Stockdon, H. F., 2019. Hurricane Matthew: Predictions, observations, and an analysis of coastal change.. *US Department of the Interior, US Geological Survey*.
- Bleck, R., 2002. An oceanic general circulation model framed in hybrid isopycnic-Cartesian coordinates.. *Ocean Modelling*, 4(1), pp. 55-88.
- Bösch, F., Chikatamarla, S. S. & Karlin, I., 2015. Entropic multirelaxation lattice Boltzmann models for turbulent flows. *Physical Review E*, 92(4), p. 043309.
- Boussinesq, J., 1871. Théorie de l'intumescence liquide, appelée onde solitaire ou de translation, se propageant dans un canal rectangulaire. *Comptes Rendus de l'Académie des Sciences* 72, p. 755–759.
- Buczowski, B., Reid, J. & Jenkins, C., 2020. Sediments and the sea floor of the continental shelves and coastal waters of the United States—About the usSEABED integrated sea-floor-characterization database, built with the dbSEABED processing system. *U.S. Geological Survey Open-File Report*, p. 14.
- Budinski, L. et al., 2020. steady flow simulation using the curvilinear multiple-relaxation-time lattice Boltzmann method: Danube River case study. *Journal of Hydraulic Research*, 58(2), p. 204–217.
- Cataño-Lopera, Y. A., Demir, S. T. & Garcia, M. H., 2007. Self-burial of short cylinders under oscillatory flows and combined waves plus currents.. *IEEE J. Ocean. Eng.* 32 (1), pp. 191-203.



- Cavaleri, L. & Rizzoli, P. M., 1981. Wind wave prediction in shallow water: Theory and applications.. *Journal of Geophysical Research: Oceans*, 86(C11), pp. 10961-10973.
- CEHNC, 1996. *Final Engineering Evaluation/Cost Analysis Action Memorandum Former Ft. Pierce Naval Amphibious Training Base*, s.l.: s.n.
- CEHNC, 2007. *Archives Search Report Ft Pierce Naval Amph Base*, Fort Pierce: s.n.
- CEHNC, 2021. *DRAFT Remedial Investigation/Feasibility Study Report*, s.l.: s.n.
- CERC, 1984. *Shore Protection Manual*, Vicksburg, Mississippi: US Army, Corps of Engineers,.
- Chassignet, E. P. et al., 2007. The HYCOM (hybrid coordinate ocean model) data assimilative system.. *Journal of Marine Systems*, 65(1–4), p. 60–83.
- Chopard, B., Pham, V. & Lefèvre, L., 2013. Asymmetric lattice Boltzmann model for shallow water flows. *Computers & Fluids*, Volume 88, pp. 225-231.
- Clauss, G., Lehmann, E. & Östergaard, C., 1992. *Offshore Structures*. 1st ed. Hrsg. London: Springer.
- Coastal Data Information Program (CDIP), 2022. *Coastal Data Information Program (CDIP)*. [Online]
Available at: <http://cdip.ucsd.edu/themes/cdip?pb=1&u2=s:134:st:1&d2=p70>
[Accessed 27 January 2022].
- Coor, J. L., Beauvais, C. & Ousley, J. D., 2015. ROSS/OSSI (ROSSI): A coastal management tool for offshore sand sources. *The Proceedings of the Coastal Sediments*.
- Dorschner, B. et al., 2016. Entropic Multi-Relaxation Time Lattice Boltzmann Model for Complex Flows. *Journal of Fluid Mechanics*, pp. 623-651.
- Duerr, A. E. S. & Dhanak, M. R., 2012. An Assessment of the Hydrokinetic Energy Resource of the Florida Current. *IEEE Journal of Oceanic Engineering*, Issue 37(2), pp. 281-293.
- EAK, 1993. *Die Küste*, Heide in Holstein: Westholsteinische Verlagsanstalt Boyens & Co.
- Escobar, S., Whitehouse, R., Benson, T. & Knaapen, T., 2023. Hydro-morphodynamics modelling for the mobilization assessment of UXOs and DMMs.. *Proceedings of the 29th TELEMAC-MASCARET Users Conference 2023*..
- Ezer, T., 2020. Analysis of the changing patterns of seasonal flooding along the U.S. East Coast. *Ocean Dynamics*, Issue 70(2), pp. 241-255.
- Friedrichs, C., Rennie, S. & Brandt, A., 2016. Self-burial of objects on sandy beds by scour: A synthesis of observations, in: *Scour and Erosion*. CRC Press, pp. 179-189.
- Friedrichs, C., Rennie, S. E. & Brandt, A., 2018. *Simple Parameterized Models for Predicting Mobility, Burial and re-exposure of underwater munitions*. SERDP Final Report MR-2224, s.l.: Virginia Institute of Marine, Science, William & Mary.
- Gaul, L., Kögl, M. & Wagner, M., 2003. *Boundary element methods for engineers and scientists : an introductory course with advanced topics*. Berlin: Springer.



- Habel, R., 2001. *"Künstliche Riffe" zur Wellendämpfung*. Berlin: Dissertation an der Technischen Universität Berlin, Institut für Schiffs- und Meerestechnik, Mensch-und-Buch-Verlag.
- Hartmann, F., 1987. *Methode der Randelemente*. Heidelberg: Springer.
- Hasselmann, K. et al., 1973. Measurements of wind-wave growth and swell decay during the Joint North Sea Wave Project (JONSWAP). *Ergänzungsheft 8-12*.
- Hasselmann, S., Hasselmann, K., Allender, J. H. & Barnett, T. P., 1985. Computations and parameterizations of the nonlinear energy transfer in a gravity-wave spectrum. Part II: Parameterizations of the nonlinear energy transfer for application in wave models. *Journal of Physical Oceanography*, 15(11), pp. 1378-1391.
- Hedges, T. S., 1995. Regions of validity of analytical wave theories. *Proc. Inst. Civ. Eng., Water, Maritime and Energy* 112, pp. 111-114.
- Hedjripour, A., Callaghan, D. & Baldock, T., 2016. Generalized transformation of the lattice Boltzmann method for shallow water flows. *Journal of Hydraulic Research*, April, Volume 54, pp. 1-18.
- He, X., Zou, Q., Luo, L. & Dembo, M., 1997. Analytic solutions of simple flows and analysis of nonslip boundary conditions for the lattice Boltzmann BGK model. *Journal of Statistical Physics*, 87(1-2), pp. 115-136.
- Jonsson, L., 1966. Wave Boundary Layers and Friction Factors.. *Coastal Engineering Proceedings*, 1(10), 9.
- Karlin, I. V., Bösch, F. & Chikatamarla, S., 2014. Gibbs' principle for the lattice-kinetic theory of fluid dynamics. *Physical Review E*, 90(3), p. 031302.
- Komen, G. J. et al., 1996. *Dynamics and modelling of ocean waves*. s.l.:s.n.
- Komen, G. J., Hasselmann, K. & Hasselmann, S., 1984. On the existence of a fully developed wind-sea spectrum.. *Journal of Physical Oceanography*, 14(8), p. 1271-1285.
- Kornev, N., 2009. *Schiffstheorie I*. Aachen: Shaker.
- Korotkin, A., 2009. *Added Masses of Ship Structures*. 1st ed. Hrsg. Netherlands: Springer.
- Korteweg, D. & de Vries, G., 1895. On the change of form of long waves advancing in a rectangular canal, and on a new type of long stationary waves. *Philosophical Magazine Series 5*, 39:240, pp. 422-443.
- Kourafalou, V. H. & Kang, H., 2012. Florida Current meandering and evolution of cyclonic eddies along the Florida Keys Reef Tract: Are they interconnected?. *Journal of Geophysical Research: Oceans*, Issue 117(C5).
- Krüger, T. et al., 2017. *The Lattice Boltzmann Method*. Springer International Publishing.
- Laplace, P.-S. M. d., 1776. *Suite des recherches sur plusieurs points du système du monde (XXV-XXVII)*. s.l.:M'm. Présentés Divers Savans Acad. R. Sci. Inst. France, pp. 525-52 (Sur les Ondes, pp. 542-52).



- Latt, J. et al., 2021. Palabos: Parallel Lattice Boltzmann Solver. *Computers and Mathematics with Applications*, Volume 81, pp. 334-350.
- Le Méhauté, B., 1976. *An Introduction to Hydrodynamics & Water Waves*. New York, Heidelberg, Berlin: Springer-Verlag.
- Lewandowski, E., 2004. *The dynamics of marine craft : maneuvering and seakeeping*. Singapore: World Scientific Pub Co Inc..
- Li, J. et al., 2017. Feature selection: A data perspective. *ACM Computing Surveys (CSUR)*, Issue 50 (6), pp. 1-45.
- Li, S., Huang, P. & Li, J., 2015. A modified lattice Boltzmann model for shallow water flows over complex topography. *International Journal for Numerical Methods in Fluids*, 77(8), pp. 441-458.
- Liu, H. & Zhou, J., 2014. Lattice Boltzmann approach to simulating a wetting—drying front in shallow flows. *Journal of Fluid Mechanics*, February, Volume 743.
- Lord Rayleigh F.R.S., J. W. S., 1876. On Waves. *Philosophical Magazine Series 5, Volume 1, Issue 4*, pp. 257-279.
- Madsen, P. A. & Sørensen, O. R., 1993. Bound waves and triad interactions in shallow water.. *Ocean Engineering*, 20(4), p. 359–388.
- Malcherek, A., 2010. *Gezeiten und Wellen*. Wiesbaden: Vieweg + Teubner.
- Massel, S. R., 1999. *Fluid Mechanics for Marine Ecologists*. Berlin: Springer.
- McCarthy, D. A., Lindeman, K. C., Snyder, D. B. & Holloway-Adkins, K. G., 2020. Nearshore hardbottom reefs of east Florida and the regional shelf setting. *Islands in the Sand*, pp. 23-43.
- McDonald, J. R. et al., 1998. *MTADS MAPPING AND ORDNANCE INVESTIGATION AT THE FORMER FT. PIERCE AMPHIBIOUS BASE*, Washington D.C.: Naval Research Laboratory.
- Menzel, P., Drews, A., Otto, C. & Schütt, C., 2019. Mobilisation of UXO, caused by hydrodynamics. *Proceedings of the 5th Underwater Acoustic Conference and Exhibition UACE 2019*, Volume 5.
- Menzel, P. et al., 2018. Towards a general prediction-model for the current-induced mobilisation of objects on the sea floor. *Ocean Engineering*, Volume Volume 164, pp. 160-167.
- Morison, J. R., O'Brien, M. P., Johnson, S. A. & Schaaf, S. A., 1950. the force exerted by surface waves on piles. *Petroleum Transactions AIME Vol.189*, pp. 149-154.
- Morrison, H. & Leder, A., 2018. Sediment Transport in Turbulent Flows with the Lattice Boltzmann Method. *Computers & Fluids*, April, Volume 172.
- Munk, W. H., 1944. *Proposed uniform procedure for observing waves and interpreting instrument records*, s.l.: Scripps Institution of Oceanography (declassified U.S. Govt. document).



National Centers for Environmental Information, 2022. *NOAA NESDIS H05027*. [Online] Available at: <https://www.ngdc.noaa.gov/nos/H04001-H06000/H05027.html> [Accessed 27 January 2022].

National Centers for Environmental Information, 2022. *NOAA NESDIS H05032*. [Online] Available at: <https://www.ngdc.noaa.gov/nos/H04001-H06000/H05032.html> [Accessed 27 January 2022].

National Data Buoy Center, 2022. *National Data Buoy Center*. [Online] Available at: https://www.ndbc.noaa.gov/station_page.php?station=41114 [Accessed 27 January 2022].

NOS, 2021. United States Coast Pilot 4 - Atlantic Coast: Cape Henry, Virginia to Key West, Florida.

OCM-Partners, 2023a. *2016 USACE Post-Matthew Topobathy Lidar: Southeast Coast (VA, NC, SC, GA and FL)*. <https://www.fisheries.noaa.gov/inport/item/49616>, s.l.: s.n.

OCM-Partners, 2023b. *2016 USACE NCMP Topobathy Lidar DEM: Florida East Coast.*, s.l.: s.n.

Ousley, J. D., Kromhout, E., Schrader, M. H. & Lillycrop, L. S., 2014. *Southeast Florida sediment assessment and needs determination (SAND) study.*, s.l.: s.n.

Peng, Y., Zhang, J. M. & Zhou, J. G., 2016. Lattice Boltzmann Model Using Two Relaxation Times for Shallow-Water Equations. *Journal of Hydraulic Engineering*, 57(3), p. 06015017.

Pierson, W. J. J. & Moskowitz, L. A., 1964. Proposed Spectral Form for Fully Developed Wind Seas Based on the Similarity Theory of S. A. Kitaigorodskii. *Journal of Geophysical Research*, Issue 69, pp. 5189-5190.

Rennie, S., Brandt, A. & Friedrichs, C., 2017. Initiation of motion and scour burial of objects underwater. *Oceanic Engineering*, Volume 32, pp. 282-294.

Rodríguez, E. L. & Dean, R. G., 2009. A sediment budget analysis and management strategy for Fort Pierce Inlet, Florida. *Journal of Coastal Research*, Issue 25(4), pp. 870-883.

Salmon, R., 1991. The Lattice Boltzmann method as a basis for ocean circulation modeling. *Journal of Marine Research*, May, Volume 57, pp. 503-535.

Smith, N. P., 2001. Seasonal-scale Transport Patterns in a Multi-inlet Coastal Lagoon. *Estuarine, Coastal and Shelf Science*, Issue 51(1), pp. 15-28.

Soulsby, R., 1995. Bed shear-stresses due to combined waves and currents. *Advances in Coastal Morphodynamics*, pp. 4-20 to 4-23.

Soulsby, R., 1997. *Dynamics of Marine Sands: a manual for practical applications*. London: Thomas Telford.

Stokes, G. G., 1847. On the Theory of Oscillatory Waves. *Trans. Camb. Phil. Soc.*, 8, pp. 441-455.



Tassi, P. et al., 2022. GAIA - a unified framework for sediment transport and bed evolution in rivers, coastal seas and transitional waters in the TELEMAC-MASCARET modelling system. *Environmental Modelling and Software*.

Tavouktsoglou, N., Harris, J., Simons, R. R. & Whitehouse, R. J. S., 2017. Equilibrium Scour-Depth Prediction around Cylindrical Structures.. *Journal of Waterway Port Coastal and Ocean Engineering*. 143, pp. 1-19.

Toffolon, M. & Vignoli, G., 2007. Suspended sediment concentration profiles in nonuniform flows: Is the classical perturbative approach suitable for depth-averaged closures?. *Water Resources Research*, 43(4)..

Tolman, H. L., 1991. A third-generation model for wind waves on slowly varying, unsteady, and inhomogeneous depths and currents.. *Journal of Physical Oceanography*, 21(6), p. 782–797.

Ursell F.R.S., F. J., 1953. The long-wave paradox in the theory of gravity waves. *Proceedings of the Cambridge Philosophical Society* 49 (4), Volume 49 (4), pp. 685-694.

USACE NCMP Topobathy Lidar, 2022. *InPort Metadata Catalog*. [Online] Available at: <https://www.fisheries.noaa.gov/inport/item/49722> [Accessed 27 January 2022].

USACE, 1998. *Completion Report for Beach Barrier Removal Project*, Jacksonville, Florida: United States Army Corps of Engineers.

Van Thang, P. et al., 2010. Study of the 1D lattice Boltzmann shallow water equation and its coupling to build a canal network. *Journal of Computational Physics*, September, Volume 229, pp. 7373-7400.

Voropayev, S. I., Testik, F. Y., Fernando, H. J. S. & Boyer, D. L., 2003. Burial and scour around short cylinder under progressive shoaling waves. *Ocean Engineering Volume 30, Issue 13*, pp. 1647-1667.

Walter, G. & Herms, G., 2004. *Einführung in die Behandlung von Meßfehlern*. s.l.:Universität Rostock.

Whitehouse, R., 1998. *Scour at marine structures - A manual for practical applications*. London: Thomas Telford.

Whitehouse, R., Soulsby, R. & Damgaard, J., 2000. Discussion of “Inception of Sediment Transport on Steep Slopes”. *Journal of Hydraulic Engineering*, July, pp. 553-555.

Whitehouse, R., Soulsby, R., Roberts, W. & Mitchener, H., 2000. *Dynamics of Estuarine Muds: a manual for practical applications*. London: Thomas Telford.

Wilkens, R. & Richardson, M., 2007. Mine burial prediction: a short history and introduction. *Institute of Electrical and Electronics Engineers Journal of Oceanic Engineering*, 32(1), pp. 3-9.

Zanke, U. C. E., 2002. *Hydromechanik der Gerinne und Küstengewässer*.. Berlin: Parey Buchverlag.



Zhou, J., 2002. A lattice Boltzmann model for the shallow water equations. *Computer Methods in Applied Mechanics and Engineering*, 191(32), pp. 3527-3539.

Zhou, J., 2004. *Lattice Boltzmann Methods for Shallow Water Flows*. s.l.:Springer.

Zhou, J., 2011. Enhancement of the LABSWE for shallow water flows. *Journal of Computational Physics*, January, Volume 230, pp. 394-401.

Zhou, J. & Liu, H., 2013. Determination of bed elevation in the enhanced lattice Boltzmann method for the shallow-water equations. *Physical review. E, Statistical, nonlinear, and soft matter physics*, August, Volume 88, p. 023302.



Appendix A. The Lattice Boltzmann Method (rejected)

During this project, the lattice Boltzmann method (LBM) shall be used to enable accurate simulations of the coastal morphology in the wave shoaling zone (i.e. transitional and shallow water, Fig. 13) and combine this with the mobilization of UXO within these areas. The results will provide valuable insight into the physical processes behind seabed morphodynamics and the subsequent mobilization and migration of UXO and can then be used to improve and extend the area of applicability of the mobilization software presented in Section 3.8.

A.1 Introduction to the lattice Boltzmann method

The lattice Boltzmann method solves the discretized Boltzmann equation:

$$f_i(\vec{x} + \vec{c}_i, t + 1) = f_i(\vec{x}, t) + \Omega_i, \quad [108]$$

where f_i are particle probability distribution functions (PPDFs) corresponding to a discrete set of velocity vectors \vec{c}_i which span the lattice at the grid points \vec{x} . Furthermore, t denotes the overall simulation time steps and Ω_i represents the collision term, which depends on the chosen collision model. In the above equation, the lattice spacing is $\Delta x = 1$ and the time step is $\Delta t = 1$, such that the lattice velocity is given by $c = \Delta x / \Delta t = 1$. The density ρ and the velocity $\vec{u}(\vec{x}, t)$ of the fluid are obtained via the 0th and 1st order moments of the PPDFs, respectively:

$$\rho(\vec{x}, t) = \sum_{i=0}^{q-1} f_i(\vec{x}, t), \quad [109]$$

$$\vec{u}(\vec{x}, t) = \frac{1}{\rho} \sum_{i=0}^{q-1} \vec{c}_i f_i(\vec{x}, t). \quad [110]$$

Here, q denotes the number of discrete velocity vectors that are used to construct the chosen lattice. As an example, Fig. 96 shows the two-dimensional D2Q9 lattice, which consists of $q = 9$ velocity vectors (including the null vector \vec{c}_0).

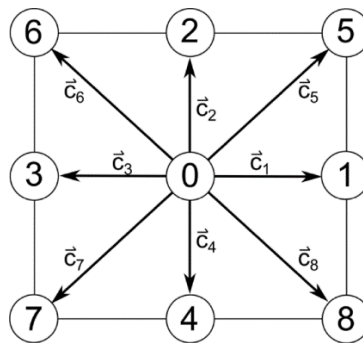


Fig. 96: D2Q9 lattice with corresponding velocity vectors \vec{c}_i

The so-called single-relaxation time Bathnagar–Gross–Krook (BGK) collision model, which is based on and named after the collision model of (Bhatnagar, et al., 1954), approximates the collision term by introducing a local equilibrium $f_i^{eq}(\vec{x}, t)$ and a relaxation time τ :

$$\Omega_i = -\frac{1}{\tau} [f_i(\vec{x}, t) - f_i^{eq}(\vec{x}, t)]. \quad [111]$$



The equilibrium distribution is given by a Hermite series expansion of the Maxwell-Boltzmann distribution (the dependency on \vec{x} and t is henceforth dropped to allow for better readability):

$$f_i^{eq} = \rho t_i \left(1 + \frac{\vec{u} \cdot \vec{c}_i}{c_s^2} + \frac{(\vec{u} \cdot \vec{c}_i)^2 - c_s^2 (\vec{u} \cdot \vec{u})}{2c_s^4} \right). \quad [112]$$

Here, t_i are lattice specific constants and c_s is the speed of sound, which relates the pressure p to the density via $p = c_s^2 \rho$. For most velocity sets, $c_s = 1/\sqrt{3}$ in lattice units.

The more commonly known Navier-Stokes equations can be recovered from the lattice Boltzmann equation via the Chapman-Enskog expansion, resulting in an explicit relationship between the relaxation time τ and the fluid viscosity ν in lattice units

$$\nu = c_s^2 \left(\tau - \frac{1}{2} \right). \quad [113]$$

Hence, given a chosen velocity set (e.g. D2Q9), a discretised domain, an initial set of PPDFs at each lattice point and an appropriately scaled fluid viscosity (e.g. via the Reynolds number $Re = UL/\nu$, where U is the characteristic velocity and L the characteristic length of the problem at hand), each time step of the simulation consists of the following algorithm:

1. Collide

- Compute ρ and \vec{u} via Eq. [109] and Eq.[110].
- Compute the local equilibria f_i^{eq} via Eq. [112].
- Compute the post-collision PPDFs via Eq. [108] and Eq. [111]:

$$f_i(\vec{x}, t)^* = f_i(\vec{x}, t) - \frac{1}{\tau} [f_i(\vec{x}, t) - f_i^{eq}(\vec{x}, t)] \quad [114]$$

2. Stream:

- Stream all post-collision PPDFs to their respective next lattice points, according to their corresponding velocity vectors \vec{c}_i :

$$f_i(\vec{x} + \vec{c}_i, t + 1) = f_i(\vec{x}, t)^* \quad [115]$$

It is worth pointing out that the characteristic velocity U in lattice units should be chosen such that the maximum local velocity in the simulation always fulfils the low Mach number condition $|\vec{u}_{max}| \ll c_s$, in order for the Chapman-Enskog expansion to hold and the simulation to remain stable. At the same time, larger lattice velocities mean that each simulation time step of $\Delta t = 1$ corresponds to a larger physical time step, thus reducing the required simulation time. In practice, the scaling is typically chosen such that $|\vec{u}_{max}| < 0.2$ (Krüger, et al., 2017).

A.2 High Reynolds number flows

For high Reynolds number flows, the low Mach number condition would dictate extremely high resolutions in order to avoid the fluid viscosity ν becoming too small ($\nu \rightarrow 0$ in lattice units, i.e. $\tau \rightarrow 0.5$). In practise though, such high resolutions are extremely costly and not always necessary for the desired simulation. Hence, for cases where $\tau \rightarrow 0.5$, different collision models to the single-relaxation time BGK model are often used. One such collision model is the

entropic multi-relaxation time lattice Boltzmann model (or KBC model), as introduced by (Karlin, et al., 2014) and (Bösch, et al., 2015). In this case, the particle probability distribution functions f_i are separated into a kinetic part k_i , a part which contains the shear stress s_i and a higher order component h_i : $f_i = k_i + s_i + h_i$. The collision term then becomes

$$\Omega_i = \frac{1}{\tau} \left[(s_i^{eq} - s_i) + \frac{\gamma}{2} (h_i^{eq} - h_i) \right], \quad [116]$$

where s_i^{eq} and h_i^{eq} are obtained from an equilibrium state of f_i^{eq} and γ is an additional relaxation time for the higher order moments, the so-called entropic stabilizer. It is computed locally to increase the numerical stability of the simulation without modifying the hydrodynamic limit. As the kinetic part k_i depends only on the locally conserved variables, $k_i - k_i^{eq} = 0$, and it is therefore not considered in the collision term. As shown by (Karlin, et al., 2014), γ can be approximated as follows:

$$\gamma = 2\tau - 2(1 - \tau) \frac{\sum_i \Delta s_i \Delta h_i / f_i^{eq}}{\sum_i \Delta h_i \Delta h_i / f_i^{eq}}, \quad [117]$$

where $\Delta s_i = s_i - s_i^{eq}$ and $\Delta h_i = h_i - h_i^{eq} = f_i - f_i^{eq} - \Delta s_i$. If the simulation is sufficiently resolved, then $\gamma \approx 2$ and Eq. [116] becomes Eq. [111], effectively resulting in the BGK collision model. The entropic multi-relaxation time collision model has shown excellent results in the presence of boundaries and for both resolved and under-resolved cases (Dorschner, et al., 2016). At the same time, unlike several other multi-relaxation time collision models, it requires no tuning of parameters before the simulation is run. Furthermore, as demonstrated in (Morrison & Leder, 2018), the exact expression of s_i can be used and modified accordingly to simulate both the fluid flow and the sediment transport, whereas the latter is then based on the advection-diffusion equation.

A.3 Lattice Boltzmann/advection-diffusion model for sediment transport

Within the project, the sediment transport is simulated using the lattice Boltzmann/advection-diffusion (LB/AD) model. The current state of the model and, in particular, the methods used to simulate erosion and accumulation on the seafloor are detailed in (Morrison & Leder, 2018). Hence, the following shall provide only a brief overview of the LB/AD model itself. The model, as the name suggests, is used to solve the advection-diffusion equation of an arbitrary quantity ζ :

$$\frac{\partial}{\partial t} \zeta + \nabla \cdot (\vec{u} \zeta) = D_0 \nabla^2 \zeta \quad [118]$$

with the advection velocity \vec{u} and the diffusion coefficient D_0 . In LB/AD, Eq. [108] is still used, whereas the PPDFs are typically denoted as g_i instead of f_i , in order to distinguish between the LBM for the solution of the Navier-Stokes equations and the LB/AD model. For the case where the LB/AD model is used to simulate the sediment transport in a flow this is particularly important, as both the LBM for fluid flows and the LB/AD model are then run alongside each other.

LB/AD models require a smaller velocity set and are thus typically run using the D2Q5 lattice in 2D and the D3Q7 lattice in 3D, which are subsets of the D2Q9 and D3Q27



lattices, respectively, where the diagonal velocity components are omitted. The equilibrium term is also simplified, as it need not contain any second-order velocity terms:

$$g_i^{eq} = t_i \zeta \left(1 + \frac{1}{c_s^2} \bar{c}_i \cdot \bar{u} \right). \quad [119]$$

Here, $\zeta = \sum_i g_i$. Using the single-relaxation time collision model, it can be shown that the model solves the advection-diffusion equations given the following relation between the diffusion coefficient and the relaxation time τ :

$$D_o = c_s^2 \left(\tau - \frac{1}{2} \right). \quad [120]$$

As already mentioned, the simulation of sediment transport in a fluid flow requires running two simulations simultaneously: the LBM simulation for the fluid and the LB/AD simulation for the sediment transport. In this case, ζ denotes the volume fraction of the sediment in the flow and the advection velocity \bar{u} is given by the local velocity from the fluid flow simulation \bar{u}_{fl} and an additional settling velocity w_s :

$$\bar{u}(\vec{x}, t) = \bar{u}_{fl}(\vec{x}, t) + w_s \bar{e}_z, \quad [121]$$

where \bar{e}_z is the unit vector in z -direction and it is assumed that gravity acts in the negative z -direction ($\vec{g} = -g\bar{e}_z$). The diffusion coefficient of the LB/AD simulation is defined via the Schmidt number $Sc = \nu/D_o$. Setting $Sc = 1$ thus results in the same relaxation parameters for both the fluid flow and the sediment transport simulations.

So far, the fluid flow and the sediment transport simulations are only coupled by using the simulated fluid velocity as the advection velocity in the LB/AD model. A valuable extension of the overall model will be the addition of a buoyancy force term in the fluid flow simulation, which will account for the varying density of the fluid based on the amount of sediment in the flow and will thus introduce a two-way coupling:

$$\vec{F} = \left(\frac{\rho_p - \rho}{\rho} \right) \zeta \vec{g} \quad [122]$$

with the particle density ρ_p and the fluid density ρ .

A.4 Lattice Boltzmann shallow water approach

The previous section has shown that the LBM is not restricted to solving only the Navier-Stokes equations, but that it can also be used to simulate problems governed by other sets of equations. Another such example is the lattice Boltzmann model for shallow water equations (LABSWE), as first described by (Salmon, 1991) and subsequently applied by (Zhou, 2002). The 2D shallow water equations describe the evolution of depth-averaged quantities and are thus valid for cases where the horizontal scale is much larger than the water depth and the vertical acceleration can be neglected. They are given as

$$\frac{\partial h}{\partial t} + \frac{\partial(hu_\alpha)}{\partial x_\alpha} = 0, \quad [123]$$

$$\frac{\partial(hu_\alpha)}{\partial t} + \frac{\partial(hu_\alpha u_\beta)}{\partial x_\beta} = -g \frac{\partial}{\partial x_\alpha} \left(\frac{h^2}{2} \right) + \nu \frac{\partial^2}{\partial x_\beta \partial x_\beta} (hu_\alpha) + F_\alpha, \quad [124]$$

where h is the water depth, t is the time, u_α is the depth-averaged velocity component in α -direction, $g = 9.81 \text{ m/s}^2$ is the gravitational acceleration, ν is the kinematic viscosity and F_α is the sum of all forces in α -direction. When bed slope and bed friction are considered, F_α is given as follows:

$$F_\alpha = -gh \frac{\partial z_e}{\partial x_\alpha} - \frac{\tau_{b\alpha}}{\rho}, \quad [125]$$

where z_e is the seafloor elevation, ρ is the water density and $\tau_{b\alpha}$ is the bed shear stress in α -direction:

$$\tau_{b\alpha} = \rho C_b u_\alpha \sqrt{u_\beta u_\beta}. \quad [126]$$

C_b is the bed friction coefficient, which can be estimated via $C_b = g/C_Z^2$, where $C_Z = h^{1/6}/n_b$ is the Chezy constant with the Manning's coefficient n_b . Inserting this estimation into Eq. [125] results in

$$F_\alpha = -gh \frac{\partial z_e}{\partial x_\alpha} - \frac{gn_b^2}{h^{1/3}} u_\alpha \sqrt{u_\beta u_\beta}. \quad [127]$$

In general, F_α may also contain Coriolis forces and the wind shear stress.

Using the D2Q9 lattice (Fig. 96) and the BGK collision model, the LABSWE is described by still using Eq. [114] for the collision step, whereas now the following relationships hold instead of Eq. [109] and [110]:

$$h(\vec{x}, t) = \sum_{i=0}^{q-1} f_i(\vec{x}, t), \quad [128]$$

$$h\vec{u}(\vec{x}, t) = \sum_{i=0}^{q-1} \vec{c}_i f_i(\vec{x}, t). \quad [129]$$

The equilibrium distribution function is also no longer defined by Eq. [112], but is now, following (Salmon, 1991) and (Zhou, 2002), given by

$$f_i^{eq} = \begin{cases} h \left(1 - \frac{5gh}{6} - \frac{2u_\alpha u_\alpha}{3} \right), & i = 0 \\ t_i h \left(\frac{3gh}{2} + 3c_{i\alpha} u_\alpha + \frac{9}{2} c_{i\alpha} c_{i\beta} u_\alpha u_\beta - \frac{3}{2} u_\alpha u_\alpha \right), & i \neq 0 \end{cases} \quad [130]$$

with the lattice weights $t_i = 1/9$ for all non-diagonal components ($i = 1, 2, 3, 4$) and $t_i = 1/36$ for all diagonal components ($i = 5, 6, 7, 8$) (and $t_0 = 4/9$).

Furthermore, the streaming step now has to include the forcing term, which has thus far not been done consistently throughout the LABSWE literature. Both (Salmon, 1991) and (Zhou, 2002) modify the streaming step as follows:

$$f_i(\vec{x} + \vec{c}_i, t + 1) = f_i(\vec{x}, t)^* + \frac{1}{6} c_{i\alpha} F_\alpha. \quad [131]$$

Note that here, for consistency, $\Delta t = 1$ and $\Delta x = 1$, which is not the case in the respective references and must thus be considered when converting the respective units into lattice units. The factor $1/6$ in Eq. [131] is not justified by either author. In fact, (Zhou & Liu, 2013) later even admit to the fact that Eq. [131]. does not always generate accurate solutions and fails, for example, to simulate the flow over complex 2D bed topographies. By performing a detailed Chapman-Enskog expansion including the force terms, they eventually come to the conclusion that, given the equilibrium in Eq. [130], the bed slope force $F_{\alpha, slope}$ must be included by introducing a parameter C_i :

$$f_i(\vec{x} + \vec{c}_i, t + 1) = f_i(\vec{x}, t)^* + C_i c_{i\alpha} F_{\alpha, slope} + \frac{1}{6} c_{i\alpha} F'_\alpha \quad [132]$$

with $C_i = 1/3$ for non-diagonal components and $C_i = 1/12$ for diagonal components. All other forces apart from the bed force are included in F'_α and are still added by using the constant factor $1/6$. Comparing the parameter C_i with the various forcing schemes known from “traditional” LBM reveals that the bed slope force term in Eq. [132]. is effectively added via a weighted forcing scheme, as is used, for example, in (He, et al., 1997):

$$f_i(\vec{x} + \vec{c}_i, t + 1) = f_i(\vec{x}, t)^* + \frac{t_i}{c_s^2} c_{i\alpha} F_\alpha \quad [133]$$

In fact, several works regarding the LABSWE, such as van (Van Thang, et al., 2010) or (Li, et al., 2015), do indeed use Eq. [133] for all forces. In conclusion, Eq. [133] should certainly be preferred over Eq. [131], especially when a complex 2D seabed topography is to be expected.

Regardless of the forcing term used, it can be shown that the Chapman-Enskog expansion of the presented 2D LABSWE recovers the shallow water equations (Eq. [123] and Eq. [124]) in the limit of $1 \gg gh$ (in lattice units) with

$$\nu = \frac{1}{3} \left(\tau - \frac{1}{2} \right). \quad [134]$$

Note that while for the D2Q9 lattice, Eq. [113] is equal to Eq. [134], because $c_s^2 = 1/3$, c_s^2 does not actually appear in the Chapman-Enskog expansion of the LABSWE. The factor $1/3$ is instead directly obtained via the required term $\sum_i c_{i\alpha} c_{i\beta} c_{i\mu} f_i^{eq} = \frac{h}{3} (u_\alpha \delta_{\beta\mu} + u_\beta \delta_{\alpha\mu} + u_\mu \delta_{\alpha\beta})$. In fact, the limitation of $1 \gg gh$ is needed, because certain terms that cancel out in the Chapman-Enskog expansion of the LBM for the solution of the Navier-Stokes equations (due to $c_s^2 = 1/3$) do not cancel out in the expansion of the LABSWE. It is also worth mentioning that for 1D LABSWE the Chapman-Enskog expansion results in a different relationship between the kinematic viscosity and the relaxation time ($\nu = \tau - 0.5$), as was shown in detail by (Van Thang, et al., 2010). This again confirms that the factor $1/3$ in Eq. [134] is indeed not based on c_s^2 .

Furthermore, (Van Thang, et al., 2010) arrive at a set of numerical stability criteria for the LABSWE based on the ratio of the wave speed to the lattice speed $c = \Delta x / \Delta t$:



$$\Phi = \frac{\sqrt{gh}}{c} \quad [135]$$

and the Froude number

$$Fr = \frac{u}{\sqrt{gh}} \quad [136]$$

They are given as

$$Fr > 1 - \frac{1}{\Phi}, \quad [137]$$

$$Fr < \frac{1}{\Phi} - 1, \quad [138]$$

$$Fr < 1. \quad [139]$$

Hence, the hydraulics of the case to be simulated needs to ensure that $Fr < 1$ and therefore $\sqrt{gh} < u$, and the scaling of the velocity from physical units to lattice units must be chosen such that $\sqrt{gh} < 1 \pm u$ (from Eq. [137] and [138], using $c = 1$) and $gh \ll 1$ in lattice units.

Another aspect to be considered is the implementation of the bed slope force itself, as it contains a spatial derivative:

$$F_{\alpha,slope} = -gh \frac{\partial z_e}{\partial x_\alpha} \quad [140]$$

(Zhou, 2004) introduces a centered forcing scheme in order to ensure the correct solution of both stationary and flow problems. In its semi-implicit form, the centered forcing scheme is written as follows:

$$f_i(\vec{x} + \vec{c}_i, t + 1) = f_i(\vec{x}, t)^* + C_i c_{i\alpha} F_{i\alpha,slope} + C_i c_{i\alpha} F'_{i\alpha} \quad [141]$$

$$\begin{aligned} F_{i\alpha,slope} &= F_{\alpha,slope} \left(\vec{x} + \frac{1}{2} \vec{c}_i, t \right) \\ &= -gh \left(\vec{x} + \frac{1}{2} \vec{c}_i, t \right) \partial_{x_\alpha} z_e \left(\vec{x} + \frac{1}{2} \vec{c}_i, t \right) \end{aligned} \quad [142]$$

$$F'_{i\alpha} = F'_{i\alpha} \left(\vec{x} + \frac{1}{2} \vec{c}_i, t \right) \quad [143]$$

The scalar product in Eq. [141] can be written out with the help of Eq.[142]:

$$\begin{aligned} c_{i\alpha} F_{i\alpha,slope} &= c_{ix} F_{ix,slope} + c_{iy} F_{iy,slope} \\ &= -g\bar{h} \left[\frac{z_e(\vec{x} + \vec{c}_i, t) + z_e(\vec{x} + c_{ix}, t) - z_e(\vec{x} + c_{iy}, t) - z_e(\vec{x}, t)}{2\Delta x} + \right. \\ &\quad \left. \frac{z_e(\vec{x} + \vec{c}_i, t) + z_e(\vec{x} + c_{iy}, t) - z_e(\vec{x} + c_{ix}, t) - z_e(\vec{x}, t)}{2\Delta x} \right] \\ &= -g\bar{h} \frac{z_e(\vec{x} + \vec{c}_i, t) - z_e(\vec{x}, t)}{\Delta x} \end{aligned} \quad [144]$$

with



$$\bar{h} = h\left(\vec{x} + \frac{1}{2}\vec{c}_i, t\right) = 1/2[h(\vec{x} + \vec{c}_i, t) + h(\vec{x}, t)] \quad [145]$$

Thus, with $\Delta x = 1$, Eq. [141] becomes

$$f_i(\vec{x} + \vec{c}_i, t + 1) = f_i(\vec{x}, t)^* - C_i g \bar{h}[z_e(\vec{x} + \vec{c}_i, t) - z_e(\vec{x}, t)] + C_i c_{i\alpha} F'_{i\alpha} \quad [146]$$

Eq. [141] is introduced by (Zhou, 2011) as the “enhanced LABSWE (eLABSWE)”, whereas it is not so much an enhancement as simply the computed form of Eq. [141]. Admittedly though, the computational overhead produced by this formulation is of course considerably lower than first computing the individual slope forces $F_{ix,slope}$ and $F_{iy,slope}$ and then using these to solve the scalar product in Eq. [141].

In summary, so far within this project, the eLABSWE by (Zhou, 2011) is used, alongside the weighted forcing scheme for all forces and not just, as in (Zhou & Liu, 2013), for the bed slope force:

$$f_i(\vec{x} + \vec{c}_i, t + 1) = f_i(\vec{x}, t)^* - \frac{t_i}{c_s^2} g \bar{h}[z_e(\vec{x} + \vec{c}_i, t) - z_e(\vec{x}, t)] + \frac{t_i}{c_s^2} c_{i\alpha} F'_{i\alpha} \quad [147]$$

Further theoretical work is currently being undertaken within the project to establish whether the LABSWE can be combined with the entropic multi-relaxation time collision model. While (Van Thang, et al., 2010) found that their D1Q3 LABSWE model remains numerically stable as long as $Fr < 1$, even when $\tau = 0.5$, the numerical stability is still limited at higher Reynolds numbers (and thus $\tau \rightarrow 0.5$) in other cases, for example in the presence of boundaries. Hence, there has been development in the literature to include higher order collision models in the LABSWE, such as the two-relaxation time (TRT) collision model (Peng, et al., 2016) and the multi-relaxation time (MRT) collision model (Budinski, et al., 2020).

Overcoming the limitation of the Froude number ($Fr < 1$) in LABSWE is another challenging task. (Chopard, et al., 2013) and (Hedjripour, et al., 2016) address this issue and introduce an asymmetric lattice Boltzmann scheme based on a Galilean transformation of the 1D LABSWE, thus enabling one-dimensional simulations of both subcritical and supercritical flow regimes. So far though, a 2D version of this approach was not yet found in the literature and (Hedjripour, et al., 2016) point out that an “extension of the proposed transformed scheme to two dimensions is more complicated”. Nevertheless, it might be worth pursuing this aspect within the upcoming months of the project.

A.5 LABSWE simulations of the extended AoI

As stated in Section A4, the current simulations are based on the eLABSWE of (Zhou, 2011) with the weighted forcing scheme of (He, et al., 1997). The method was implemented into the open-source lattice Boltzmann library Palabos (Latt, et al., 2021) and it was confirmed that the results from several simulation examples given in (Zhou, 2002) and (Li, et al., 2015) were comparable when the same simulation parameters were used. It should be pointed out though that the relaxation time τ in these examples was often arbitrarily set, most likely to ensure numerical stability, even though it should be, in principle, directly related to the kinematic viscosity and thus to the Reynolds number of the flow. Interestingly, the results given in both (Zhou, 2002) and (Li, et al., 2015) still agree well with the experimental data, even when the respective Reynolds numbers of the simulation and the experiment vary by up to an order

of 10^8 . This naturally poses the question to what extent the Reynolds number need be considered at all in LABSWE and shall thus be a subject of further investigation.

In order to use the implemented LABSWE to simulate the extended AoI, an input file for the bathymetry is needed. This was obtained by first transforming the rasterized and interpolated bathymetry dataset (Fig. 6) into UTM coordinates, then exporting an approximately 14 km x 14 km large field, rotating it by -15 degrees around the approximate center (17N 573103.8 m E 3051424.85 m N) and finally translating it by -565933 m in x-direction and -3044510 m in y-direction. Hence, the conversion between the (x, y) -coordinates of the simulation and the geographical coordinates (northing N and easting E) is given as:

$$x = (E - 573103.8) \cos(-15^\circ) - (N - 3051424.85) \sin(-15^\circ) + 7170.8 \quad [148]$$

$$y = (E - 573103.8) \sin(-15^\circ) + (N - 3051424.85) \cos(-15^\circ) + 6914.85 \quad [149]$$

A corresponding transformation backwards provides the geographical coordinates of the simulation's $(x, y) = (0, 0)$ point:

$$E(x, y) = (x - 7179.8) \cos(15^\circ) - (y - 6914.85) \sin(15^\circ) + 573103.8 \quad [150]$$

$$\Rightarrow E(0, 0) = 567967.034$$

$$N(x, y) = (x - 7179.8) \sin(15^\circ) + (y - 6914.85) \cos(15^\circ) + 3051424.85 \quad [151]$$

$$\Rightarrow N(0, 0) = 3042889.678$$

The rotation in the above transformation is chosen so that the shoreline is more or less aligned with the y-axis of the simulation.

$$N(x, y) = (x - 7179.8) \sin(15^\circ) + (y - 6914.85)$$

The resulting bathymetry dataset is finally resampled to a uniform grid and cropped to exclude resulting outliers at the corners. The final dataset that is read into the simulation consists of 279 x 279 sample points over a grid of approximately 14 km x 14 km and is shown in Fig. 97, together with the position of the waverider buoy ($x = 10267.1$ m, $y = 2239.6$ m).

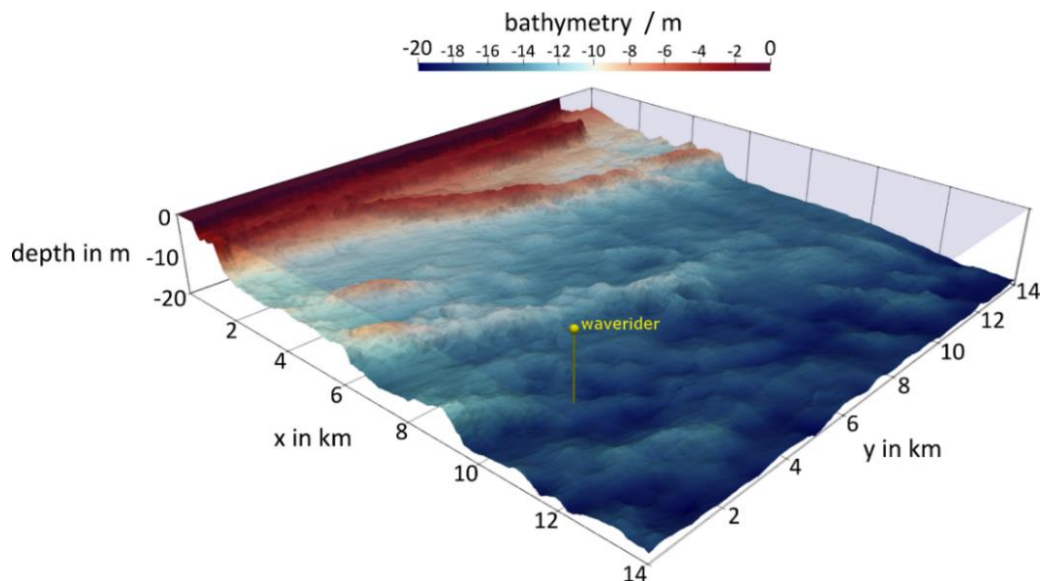


Fig. 97: The resulting bathymetry in the extended AoI after post-processing the two lead line datasets from 1930 (H05027 and H05032) and transforming the UTM coordinates to a uniform x-y grid.

Initial test simulations were run using this bathymetry input data with the aim of demonstrating the general ability of the implemented method to deal with real-life bathymetry data. For these initial simulations, the fixed reference level below the sea surface was set to $H_0 = 20$ m and the bed elevation, z_e , was set as $z_e = H_0 + D_{bathy}$, where D_{bathy} is the bathymetry, which is negative. In order to avoid having to include solid boundaries at this point, the initial water level was assumed to be 1 m higher than it is ($h = H_0 + 1 \text{ m} - z_e$), such that a bathymetry of 0 m (falsely) corresponded to an initial water height of $h = 1$ m. Obviously, future simulations will be able to deal with this, meaning that the lattice cells where $z_e = H_0$ will be assigned as solid and treated as such within the LBM. The simplest approach would be to use a bounce back condition, where the individual PPDFs f_i are swapped with their respective opposite PPDFs $f_i(\vec{c}_i = -\vec{c}_i)$, which effectively results in a local no-slip boundary condition. The simulation is resolved at a physical resolution of $\Delta x = 50$ m, the lattice velocity set to $\frac{\Delta x}{\Delta t} = 50$ m/s and the relaxation time chosen as $\tau = 1.3$. The simulation boundary at $y = 0$ m is treated as an inlet, with a temporally varying discharge $\vec{q}(x, t) = (0, q)^T$ of:

$$q(x, t) = \begin{cases} 0, & x < 7000 \text{ m} \\ \frac{q_0}{2} \left[1 + \sin\left(\frac{2\pi t}{T}\right) \right], & x \geq 7000 \text{ m} \end{cases} \quad [152]$$

where $T = 100$ s and $q_0 = 10 \text{ m}^2/\text{s}$. The boundaries at $x = 0$ m and $x = 14000$ m are set to free-slip (via specular reflection) and the boundary at $y = 14000$ m is treated as an outlet by fixing the water height to $h(x, y = 14000 \text{ m}) = H_0 + 1 \text{ m} - z_e(x, y)$. Other than the bed slope force, no other forces were included in the simulation.

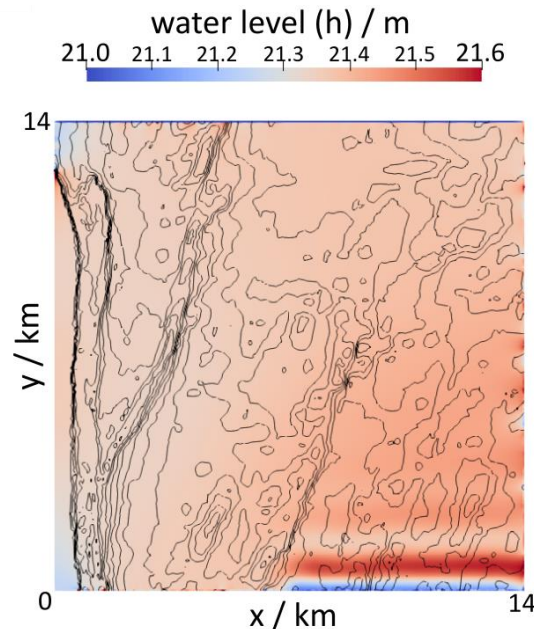


Fig. 98: Water level (m) at $t=2580$ s, obtained from the LABSWE test simulation using the extended AoI around Fort Pierce. The black contours visualize the bathymetry.

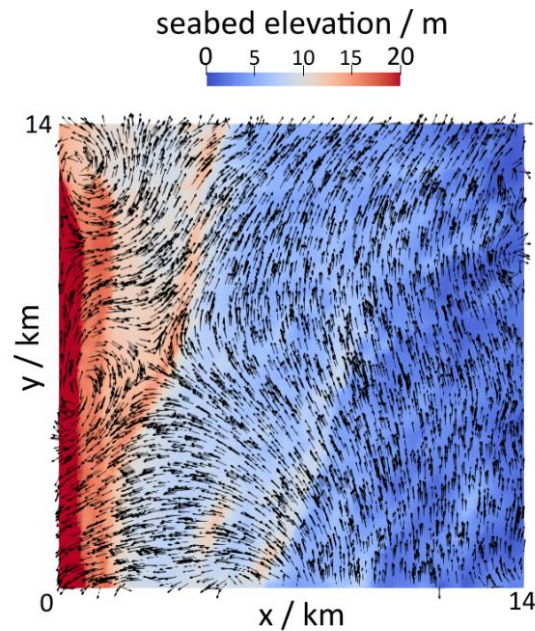


Fig. 99: Velocity vectors, scaled by a factor of 400, at $t=2580$ s, obtained from the LABSWE test simulation using the extended AoI around Fort Pierce. The underlying contour plot shows the bed elevation z_e , (m)

Fig. 98 depicts the water level in the extended AoI at $t = 2580$ s. As the presented simulation is meant as an initial proof of concept and the simulation parameters are chosen completely arbitrary, no detailed explanation of the results will be given. It can be pointed out though that the simulation is able to handle the input bathymetry data and remains stable. The resulting water level shows the effect of the varying discharge at the inlet (bottom right), but also some spurious effects at the other boundaries. Most notably, the water level increases significantly at the top left boundary where there is a significant jump in the bed elevation due to the fact that a bathymetry of $D_{bathy} = 0$ m is considered to be underwater. It will be interesting to see if this effect still occurs when $D_{bathy} = 0$ m is treated as land or, given larger velocities, whether similar effects might occur elsewhere in the simulation where the bed elevation varies significantly between the simulation cells. Furthermore, Fig. 99 shows the velocity vectors, scaled by a factor of 400, at the same time step ($t = 2580$ s). Most notable in this figure is that the velocity vectors are strongly affected by the sandbar: All incoming velocity vectors are deflected to stream along the sandbar. In the top left area behind the sandbar, which corresponds to the AoI, vortices have been formed and the flow shows a considerably different behaviour to the rest of the simulated area. In conclusion, although the presented simulation is meant purely as a proof of concept, it already demonstrates the need to accurately simulate the (extended) AoI and better understand the effect of the sandbar on the flow, and hence later also on the sediment transport and the burial and mobilization of UXO and DMM.

A.6 Results

Based on the information obtained from the Fort Pierce AoI, it was decided that the further development of the lattice Boltzmann simulations shall concentrate on three different scenarios which shall each focus on a different key aspect of interest:

1. Lattice Boltzmann shallow water simulations shall be used to simulate the AoI and the area beyond it, up to the location of the waverider buoy. The main aim of these simulations is to use the single-point statistical wave data to obtain a realistic



- temporally and spatially resolved estimate of the waves in the AoI. This data can then be used as input in the burial and mobilization model, as well as in further lattice Boltzmann simulations that focus only on the area within the AoI.
2. The bathymetry data of the Fort Pierce AoI suggests that no major changes to the bathymetry have occurred over the last 90 years. There is a near-shore sandbank at approximately 4-6 m depth though and a sandbar, which extends slightly offshore and north(east)wards from the southern end of the AoI, which could be subjected to seasonal variations. Morphodynamics simulations of the seafloor in the AoI shall thus be run using an enhanced sediment transport simulation approach with the lattice Boltzmann method based on the approach outlined in (Morrison & Leder, 2018).
 3. The effect of morphodynamics changes, varying wave conditions and other environmental parameters on the burial and mobilization of the various OoI shall further be investigated by including object mobilization in small-scale lattice Boltzmann simulations including sediment transport. The aim shall be to run a parameter study to help better understand the effects of various environmental parameters and scenarios.

At this point in the project, most work has gone into the first set of simulations (#1), which is reported on below. Additionally, some improvements have already been made to the underlying code of the sediment transport simulations (#2), but as these have not yet been used to produce any significant results, they will not be discussed further in this report.

A.7 Conclusion

During the first phase of the project, the applicability of the Lattice Boltzmann Method was investigated. It was shown that the method could be used but still requires massive improvements to keep up with current methods like TELEMAC and Delft3D. Unfortunately one of the very rare specialists in the Lattice Boltzmann Method, Dr. Helen Morrison, who was working on this project, left the team in early 2022. As it seemed to be impossible to find an adequate replacement to continue the work without creating a huge delay to the whole project, the decision was made to proceed without Lattice Boltzmann but with TELEMAC. The use of TELEMAC opens several advantages for the project. TELEMAC is already able to simulate the development of waves, entering shallow water and interacting with the seafloor. Furthermore, the system is well tested and widely proved in environmental current, wave and morphodynamics modelling and handling of huge input datasets from operational models. As HR Wallingford is using and developing TELEMAC continuously, the expertise is already available and can be applied to the project very fast without any additional training period. It was thus decided that the resources planned for the Lattice Boltzmann Simulation would now be used for the TELEMAC simulation and a more professional and sustainable implementation of the UXOmob software.